Technische Universität München

Fakultät für Chemie

Surface Modifications on Lithium-Ion-Battery cell components

Martin Johann Frankenberger

Vollständiger Abdruck der von der Fakultät für Chemie der Technischen Universität München zur Erlangung des akademischen Grades eines

Doktors der Naturwissenschaften (Dr. rer. nat.)

genehmigten Dissertation.

Vorsitzender: Prof. Dr. Tom Nilges

Prüfer der Dissertation: 1.   Prof. Dr. Hubert A. Gasteiger

                                              2.   Prof. Dr. Karl-Heinz Pettinger

"Most people would find the picture of our universe as an infinite tower of tortoises rather ridiculous, but why do we think we know better?"

Stephen Hawking, A Brief History of Time

Abstract

In this thesis, surface modifications of Lithium-Ion-Battery cell components based on electrode-separator lamination are studied. The technique is demonstrated to significantly improve C-rate stability, fast-charging capability as well as the fast-formation stability of graphite-$LiNi_{1/3}Mn_{1/3}Co_{1/3}O_2$ (NMC) cells. Fully-laminated cells show a reduction in C-rate drops of 3 %, 5 % and 12 % at 2 C, 3 C, 5 C-rate, respectively, compared to of 6 %, 11 % and 23 % for non-laminated cells.

Electrochemical impedance spectroscopy (EIS), was used to separate lamination effects between anode-separator and cathode-separator interfaces. Partial lamination at cathode side was found to induce an initial decrease in surface resistances of single cells, with no correlation to aging effects. In contrast, partial lamination at the anode side increases the residual capacity after 1500 fast-charging cycles to 84 %, compared to 75 % for non-laminated cells, which was also found to correlate to a reduction in surface resistance growth from + 8.4 $\Omega \cdot cm^2$ to + 5.9 $\Omega \cdot cm^2$.

The accumulation of solid electrolyte interphases (SEI) in graphite anodes at elevated formation rates (0.1 C, 1 C and 2 C) and cycling rates (1 C and 2 C) was investigated using EIS and neutron depth profiling (NDP). NDP reveals uniform lithium accumulations as function of depth with lithium situated at the surface of the graphite particles thus forming the SEI. Comparing NDP and EIS studies allowed to exclude surface resistance growth phenomena to arise from SEI growth in superior anode fractions.

Kurzfassung

Anhand von Graphit-$LiNi_{1/3}Mn_{1/3}Co_{1/3}O_2$ Zellen konnten deutliche Einflüsse der Prozesstechnologie Lamination auf die Ratenfestigkeit, das Schnell-Lade-Verhalten sowie die Schnell-Formierbarkeit nachgewiesen werden. Vollständige Lamination führt zu verringerten Einbußen bei erhöhten C-Raten von 3 %, 5 % und 12 % für 2 C, 3 C und 5 C-Rate, verglichen mit 6 %, 11 % und 23 % bei unlaminierten Zellen.

Mittels elektrochemischer Impedanzspektroskopie konnte der kathodenseitige Einfluss der Lamination als deutliche Verringerung der anfänglichen Oberflächenwiderstände von Zellen ermittelt werden, ohne signifikanten Einfluss auf deren weitere Zyklenfestigkeit. Durch anodenseitige Lamination hingegen konnte die verbleibende Zellkapazität nach 1500 Schnell-Lade-Zyklen auf 84 % erhöht werden, im Vergleich zu 75 % für unlaminierte Zellen, was sich auch in verringertem Wachstum der Oberflächenwiderstände von + 5,9 $\Omega \cdot cm^2$ statt + 8,4 $\Omega \cdot cm^2$ äußerte.

In Abhängigkeit von beschleunigter Formier- (0,1 C, 1 C, 2 C) und Zyklisier-Rate (1 C, 2 C) wurde zudem das Wachstum der Solid Electrolyte Interphase studiert. Hierzu wurden zyklisierte und vollständig entladene Graphit-Anoden post-mortem unter Einsatz von EIS und NDP charakterisiert. Lithium als Indikator der SEI wurde ausschließlich an der Oberfläche der Graphit-Partikel entdeckt. Der Vergleich von NDP- und EIS-Untersuchungen konnte einen Zusammenhang zwischen verringertem Wachstum der Oberflächenwiderstände und SEI-Wachstum in oberflächennahen Bereichen der Anode ausschließen.

Acknowledgement

This work has been carried out in collaboration between the Technology Center for Energy at the University of Applied Sciences Landshut and the Chair of Technical Electrochemistry at the Technical University of Munich.

I gratefully acknowledge and express my appreciation to Prof. Dr. Karl-Heinz Pettinger and Prof. Dr. Hubert Gasteiger for the opportunity to work in this research group and for their excellent supervision. Without any constraints, but always with valuable guidance, I got the chance to realize my own research ideas and to evolve this thesis according to my own interests.

I want to thank Markus Trunk, Dr. Stefan Seidlmayer, Dr. Ralph Gilles and their group members for their support in our joint neutron experiments at the FRM II.

Many thanks to Alexander Dinter, Dr. Sebastian Jankowsky, Dr. Madhav Singh, Christina Toigo, Dr. Benjamin Starke, Bernhard Springer, Hans-Konrad Weber, Jonathan Schubert, Jakob Veitl, Lukas Schaller, Martina Thurnreiter, René Müller, Andrea Sammereier, Viktoria Peterbauer, and my further colleagues at the TZE, for their endless patience in our discussions and for their support in realization of my research ideas, from raw concepts up to published research articles.

Special thanks to Elisabeth, Roland, Bernhard and Hans for checking spelling, grammar and document structure.

Finally, I conclude by thanking my family Barbara, Fritz, Elisabeth and Johannes for unconditional support at any time and in any situation in my life.

Content

1 Motivation and structure

Climatic change and its consequences are some of today's most discussed topics. A key instrument to reduce emissions of the greenhouse gas CO_2 is given by replacing energy production from combustion of fossil ressources by renewable ressources. This induces enormous expectations to energy storage technique, first to stabilize energy grids with regard to fluctuating energy production of renewable energy sources (stationary application), and second to enable electric vehicles to fully replace combustion vehicles (mobile application). The Lithium Ion Battery (LIB) concept is one of only very few concepts suitable to fulfill all demands both for stationary and mobile applications of energy storage techniques.

Yet the element position of lithium in the Periodic Table of Elements (PSE) can directly explain its superior choice as mobile species for electrochemical storage in battery applications. As an alcaline metal in the 1st main group in the PSE, lithium is most electronegative of all metals, thus enabling very high cell voltages. Aside, lithium is part of the 1st period in the PSE, hence it has the lowest weight of all metals, thus enabling highest energy densities. Due to its small ionic radius, given by its position both in 1st main group and 1st period in the PSE, lithium is capable to form intercalation compounds with a large variety of solid systems, which allows for fast kinetics in solid-state lithiation/delithiation reactions and consequently enables high power densities in battery applications.

After the first successful assembly of a dual-intercalation Lithium Ion Battery by Asahi Chemica in 1980s from a team lead by I. Kuribayashi and A. Yoshino,[1–4] the subsequent commercialization of the LIB was mainly driven by the Japanese companies Sanyo, Matsushita and Sony.[1] Their early concepts included carbon fibers as a lithium intercalation anode material, based on research of R. Yazami and Ph. Touzain,[1,5] as well as $LiCoO_2$ as a lithium intercalation cathode material, which was developed by J. B. Goodenough and co-workers,[1,6–8] completed by a polyolefin separator and a nonaqueous electrolyte ($LiClO_4$ in propylene carbonate).[1] Assembly of components was realized in discharged state to reduce their sensitivity to air and moisture, as was first demonstrated by M. S. Whittingham for Li-metal cells.[1,9] Despite enormous research efforts during the following decades on optimization of individual materials and assembly strategies, the basic structure of LIBs remains analogous until today. As a consequence, A. Yoshino, J. B. Goodenough and M. S. Whittingham were honored in 2019 by the Nobel Prize in chemistry, for their fundamental contributions in the development of the basic Lithium Ion Battery concept.

Compared to the well-established lead-acid battery technology, that shows specific energies of $33 - 42$ Wh/kg, energy densities of $50 - 70$ Wh/l, power densities of 180 W/kg, and lifetimes of $200 - 300$ cycles,[10–12] state-of-the-art lithium ion cells reach significantly higher numbers. LIBs reach specific energies of 250 Wh/kg and energy densities of 450 Wh/l for $LiCoO_2$/graphite cells,[10,12,13] power densities up to 3000 W/kg for $LiFePO_4$/graphite cells,[10,12,14] and more than 20000 cycles for cells using $Li_4Ti_5O_{12}$ anodes.[10,15,16]

Worldwide demand for Lithium Ion Batteries in 2017 lay at $100 - 125$ GWh, separating into $57 - 69$ GWh for electric vehicles, $45 - 50$ GWh for personal mobile applications and $1.5 - 5$ GWh for stationary energy storage. The annual growth rate for LIB demand lay around 25 %, forecasts state this growth rate to remain stable also in near future.[17,18] Further optimization of LIB concepts are expected to last at least for another $10 - 20$ years.[17] Today's most important challenges to state-of-the-art LIB technique concern energy density, power density, battery costs, and sustainability aspects.

While a variety of past research efforts focussed to cathode active materials,[6–8,19–26] anode active materials,[5,27–38] separator materials,[39–53] electrolyte components and electrolyte compositions,[54–68] very limited knowledge is given on electrochemical impacts of any surface and interface geometries in LIBs. Though, this research field might provide significant progress both in battery energy density as well as in reduction of battery costs by improvement of battery production techniques.

Main limitations to Lithium Ion Battery performance arise from kinetics and efficiency of the electrochemical reaction at the electrodes, as well as from charge and mass transport limitation aspects. Most important interfaces that limit charge and mass transport kinetics, are electrode – current collector and electrode – electrolyte interfaces.[69,70]

Therefore, tuning geometries at these areas could enable substantial progress to increase battery power density. Tuning electrode – current collector interface geometries might reduce delamination problems, induced by electrode volume changes during charge/discharge steps.[71] Increased electrode – electrolyte interface areas might reduce inhomogeneities, which was shown to reduce aging phenomena at high current rates.[72]

Special surface modification techniques that might be capable to fulfill these challenges, could be of modular design to fit into existing LIB production lines, therefore acting cost-efficient.

The described modifications would also directly address known limitations of excessively high-loaded electrodes. Any progress to enable LIB production for inclusion of higher loaded electrodes, would directly improve battery energy densities.

All these aspects inspired the research project SurfaLIB, which included pre-structuring of current collectors, plasma-etching of current collectors and electrodes, laser-structurung of electrodes, and plasma-based deposition of primer layers.

The SurfaLIB research project was carried out by cooperation of 5 industrial partners and 4 academic partners. At the Landshut University of Applied Sciences (UAS Landshut), major research related to the SurfaLIB project was responsibly realized by the thesis candidate.

This thesis was created to complement those studies, focusing to electrode-separator lamination as an additional and powerful surface modification technique beyond SurfaLIB.

The document is divided into several main sections.

Initially, special focus lies on essential theory. Starting with basic components of Lithium Ion Batteries (active materials, conductive additives, binder polymers, separators, electrolyte), important aspects as well as common representatives are discussed in detail. Subsequent focus lies on most important preparation techniques (electrode production and cell assembly), covering state-of-the-art LIB production types and characteristic limitations. Next topic are analysis techniques as used in this thesis, focussing to charge-discharge experiments (power test and lifetime test), Electrochemical Impedance Spectroscopy, Scanning Electron Microscopy (SEM) and Energy Dispersive X-ray analysis (EDX), as well as Neutron Depth Profiling. After introduction of raw materials, electrode and cell production, as well as analysis techniques, a literature review highlights important issues of LIB operation, with focus on aspects relevant for this thesis. Cathodic and anodic SEI concepts, formation processes and most important aging phenomena are discussed in detail. Final part of the theory chapter is a special focus onto experimental modification techniques, relevant for LIB production, as were studied in detail within the SurfaLIB project. This chapter finally places the lamination technique, main topic of this thesis, into a wider context of surface modification.

Second main part of the thesis, is the experimental chapter, presenting comprehensive information on sample production, operation parameters and data acquisition relevant for studies in this thesis. Substructure is analogous to the theory chapter, dividing into materials, electrode/cell production and analysis techniques.

Analysis and discussion section is divided into three main chapters, as arising from three published articles.

Central part is verification of a mechanistic model for the surface activity of the electrode-separator interface, specially designed to describe the electrochemical impact of the lamination technique. The electrode-separator interface characteristics are mainly driven by the interface pore situation. Depending on average pore size and pore size distribution, electrolyte bridges within the pores provide larger or smaller diffusion paths for Li^+ ions to jump from electrode pores into separator pores. The interface pore size homogeneity/inhomogeneity directly induces inhomogeneities on areal Li^+ ion current, that might at worst induce spots with increased possibility of lithium plating at elevated current rates or at low temperatures. Irreversible lithium plating will finally induce an acceleration in SEI growth, which should show up as accelerated capacity fading.

The first article (Laminated Lithium Ion Batteries with improved fast charging capability, https://doi.org/10.1016/j.jelechem.2019.02.030)[73] gives general insights into the electrode-separator interface situation. Cross-section EDX analysis is used to examine electrode-separator interface reorganization characteristics upon lamination. Electrochemical effects of the lamination technique on C-rate stability of non-calendered graphite-NMC 111 single cells are compared to permanent cell compression effects. Finally, the proposed mechanistic model is directly investigated by cycling tests at several charging rates, with different vulnerability for lithium plating.

The second article (EIS Study on the Electrode-Separator Interface Lamination, https://doi.org/10.3390/batteries5040071)[74] includes comprehensive EIS analysis for deeper insights into the lamination impacts at cathode side and anode side. Separate aspects of each electrode-separator interface are examined for their influence on internal resistance, capacity fading during cycling at fast-charging, and SEI growth.

Within the third manuscript (SEI growth impacts of lamination, formation and cycling in Lithium Ion Batteries, https://doi.org/10.3390/batteries6020021),[75] the ability of the lamination technique to modify SEI characteristics, is rechecked by characterizing fast-formation characteristics of non-calendered graphite-NMC 111 single cells. Sensitivity of manufactured cells onto accelerated formation rates and cycling rates is studied at several different routes. Comparative ex-situ studies (EIS and NDP) are included to provide more detailed insights in lamination driven SEI growth characteristics.

2   Theory

2.1   General terms

Some basic concepts, that are well-established in scientific context of LIBs, had fundamental importance to studies in this thesis, and should be therefore discussed in detail initially.

Lithium ion cell manufacturing processes for research aspects are typically realized in small batch numbers. Consequently, indidual cells might exhibit slightly variations in their nominal capacity. To maintain aging protocols comparable, charge and discharge currents are typically normalized to the individual cell capacity, using the C-rate concept[76]

$$C - rate \left[\frac{1}{h}\right] = \frac{i_{\text{charge/discharge}} \, [A]}{Q_{\text{nominal}} \, [Ah]} \qquad [1]$$

with charge/discharge current $i_{\text{charge/discharge}}$ and nominal capacity Q_{nominal}. E.g. charging a series of discharged lithium ion cells at 0.1 C-rate indicates application of individual charging currents to charge up to each cell's nominal capacity exactly within 10 h.

For the same reason, capacities of several cells are typically compared as specific capacities Q_{spec}

$$Q_{\text{spec}} = \frac{Q_{\text{meas}} \, [mAh]}{m_{\text{AM}} \, [g]} \qquad [2]$$

with measured capacity Q_{meas} and limiting active material mass m_{AM}.

Charge/discharge steps during LIB operation are usually evaluated by studying the coulombic efficiency q_{Ah}, or its reciprocal form charging factor f_{Ah}[76]

$$q_{\text{Ah}} = \frac{Q_{\text{discharge}}}{Q_{\text{charge}}} \qquad [3]$$

$$f_{\text{Ah}} = \frac{1}{q_{\text{Ah}}} \qquad [4]$$

with discharge capacity $Q_{\text{discharge}}$ and charge capacity Q_{charge}. q_{Ah} can act as a measure for the content of side reactions during LIB operation, and typically converges to 100 % at normal operation.[76,77]

State of charge (SOC) and Depth of Discharge (DOD) are well-established terms to scale electrochemical levels of lithium ion cells during operation. Terms are given as

$$DOD = \frac{Q_{\text{discharge-momentary}}}{Q_{\text{discharge-total}}} \qquad [5]$$

$$SOC = 1 - DOD \qquad [6]$$

with momentary discharge capacity at specific step $Q_{\text{discharge-momentary}}$ and total discharge capacity at specific step $Q_{\text{discharge-total}}$.

2.2   Electrode materials and cell components

Fundamental characteristics of Lithium Ion Batteries arise from their main components cathode, anode, separator and electrolyte. These components should be discussed in detail here.

2.2.1 Cathode materials

Cathode materials need to provide lithium intercalation host structures, with stable crystal lattices both in lithiated and delithiated state, at highly positive potentials against Li/Li$^+$. Transition metal based host lattices offer superior conditions for reversible storage of Li ions via intercalation reactions, due to high electronegativity and highly variable valence states provided by their d-orbitals.[23] Similar trends are given for transition metal phosphates, with potentials systematically shifted to higher voltages. Only very few elements can also provide long-term stability, low material costs, low toxicity and high sustainability. In present LIB applications, transition metal phosphates like $LiFePO_4$ (LFP) and $LiFe_{1/3}Mn_{2/3}PO_4$ (LFMP) or mixed crystals of transition metal oxides like $LiNi_{16/20}Co_{3/20}Al_{1/20}O_2$ (NCA) and $LiNi_{1/3}Mn_{1/3}Co_{1/3}O_2$ (NMC 111) are used typically. Transition metal phosphates reflect very stable performance in long-term cycling, as the lithiation/delithiation reactions are accompanied by phase-transition reactions, which induces stable potential plateaus along (de-)lithiation.[24,78–80] Though, one-dimensional Li solid state diffusion in transition metal phosphates drastically reduces ionic conductivity compared to transition metal oxides. Using transition metal phosphates as active materials requires reduction of particle sizes down to nm dimensions.[26,81–85] In transition metal oxides, an increase of the Ni content, e.g. $LiNi_{5/10}Mn_{3/10}Co_{2/10}O_2$ (NMC 532), $LiNi_{6/10}Mn_{2/10}Co_{2/10}O_2$ (NMC 622) or $LiNi_{8/10}Mn_{1/10}Co_{1/10}O_2$ (NMC 811), raises their specific capacity, while destabilizing their host lattice especially at elevated temperatures[86,87] or elevated cutoff voltages.[88]

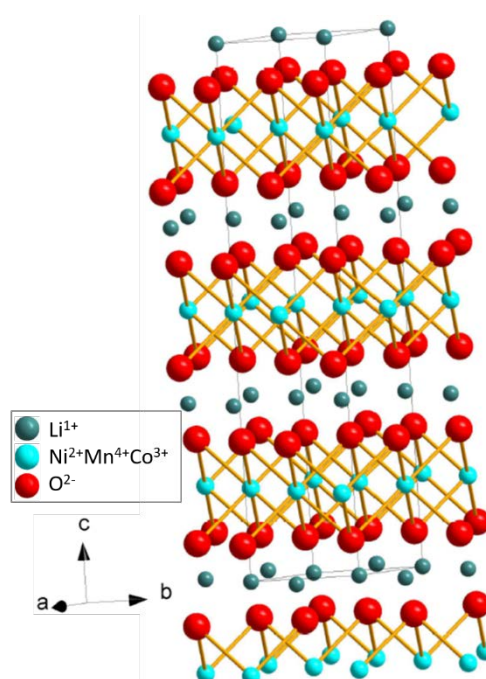NMC 111 reflects a $R\bar{3}m$ type host lattice in its fully lithiated state.

Fig. 2.1: $R\bar{3}m$ type NMC 111 crystal lattice (unit cell included) based on diffraction data by N. Yabuuchi and T. Ohzuku.[25]

Another visualization for the NMC 111 crystal lattice was presented by Y. Koyoma et al. in 2003, based on first principal calculations.[89] The $\left[\sqrt{3} \times \sqrt{3}\right]$R30°-type superlattice model gives more precise information on the separate positions of Ni^{2+}, Mn^{4+} and Co^{3+}.

Delithiation of the NMC crystal lattice changes interatomic distances. Initially, the a/b axis parameter (see Fig. 2.1) decreases, while the c axis parameter increases,[90] followed by a structural change to $P\bar{3}m1$ at low lithium contents.[90] Along delithiation from $Li_1Ni_{1/3}Mn_{1/3}Co_{1/3}O_2$ to $Li_{0.4}Ni_{1/3}Mn_{1/3}Co_{1/3}O_2$ the corresponding a/c relation of the $R\bar{3}m$ structure increases linearly by $\approx$ 3.5 %.[91] As for its linear change, the a/c relation can be used as a precise measure of the NMC 111 delithiation grade.[91] Delithiation of the NMC crystal below a minimum lithium content results in a crystal decomposition reaction, accompanied by oxygen release. The resulting oxidation of organic components within the electrolyte might cause spontaneous ignition, which is a critical safety issue for LIBs. So, identifying irreversible structural changes of NMC-type cathode materials and their precise relation to critical voltage levels is of major interest in current cathode research studies.[88,91–94]

NMC 111 is typically cycled within 3.0 V – 4.3 V vs. Li/Li+ to prevent structrural damages.[94] NMC 111 cathodes follow a characteristic voltage profile as shown in Fig. 2.2.
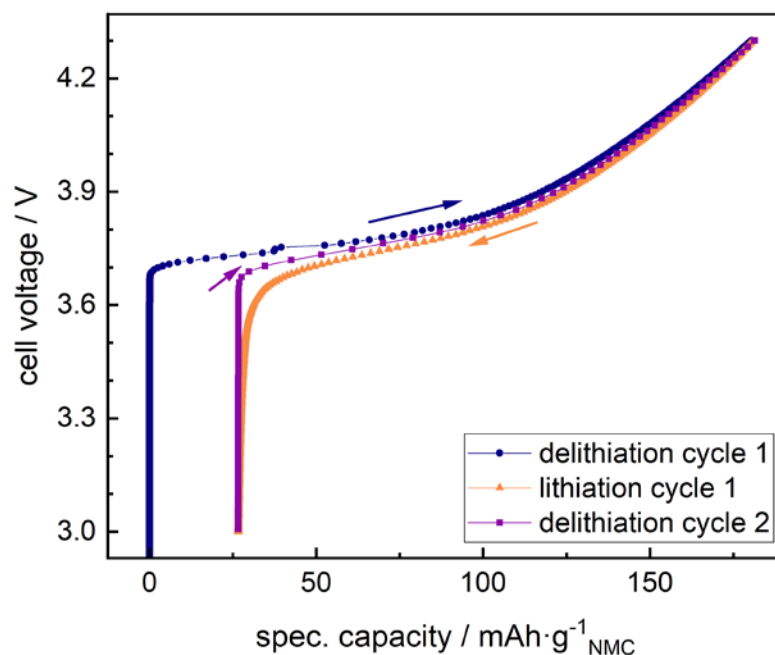

Fig. 2.2: NMC cathode cycling curves 3.0 – 4.3 V at 0.1 C-rate; data collected by half-cell (T-cell) experiment.

High cathodic potentials cause side reactions with common LIB electrolyte components, resulting in the formation of a passivation layer, that is known as the cathodic Solid Electrolyte Interphase (CEI). This phenomenon will be discussed more in detail in chapter 2.5.1.

2.2.2 Anode materials

Battery anode materials in general need to exhibit lowest electrochemical potentials, capable to store a maximum amount of mobile ions per volume and mass. Alkaline metals reveal lowest electronegativity of all element groups in the periodic table of elements, with lowest molar mass of all alkaline metals given for lithium. Therefore, favourable conditions for recharchable batteries would arise by use of metallic lithium as anode material. Though, recurring charge/discharge processes on metallic lithium anodes are challenging, due to its tendency to form dendritic lithium during the charging step.[95–97] Li dendrites grow permanently during continous charge/discharge cycles and increase the risk to form internal short circuits. Therefore, established LIB anode concepts are based on lithium intercalation materials (graphite, $Li_4Ti_5O_{12}$) or alloying materials (Si). Both graphite and spinel structured $Li_4Ti_5O_{12}$ (LTO) allow for reversible lithium intercalation/deintercalation reactions accompanied by minimal volume changes in the host lattice, which minimizes mechanical stress to electrodes and supports their long-term stability.

LTO , similar to cathodic transition metal phosphates like LFP or LFMP, reflects a stable potential plateau near 1.55 V vs. Li/Li$^+$ during (de-)lithiation, due to a reversible phase-transition reaction between spinel $Li_4Ti_5O_{12}$ ($Fd\overline{3}m$) and rock-salt $Li_7Ti_5O_{12}$ ($Fd\overline{3}m$) structure.[29,31,32,98–102]

Graphite or graphite composites are most frequently used as LIB anodes nowadays. Lithium intercalation into graphite occurs within several stages ($C_6 \cdots\rightarrow\cdots \rightarrow LiC_{18} \rightarrow LiC_{12} \rightarrow LiC_6$),[28,30,103] as indicated in Fig. 2.3.
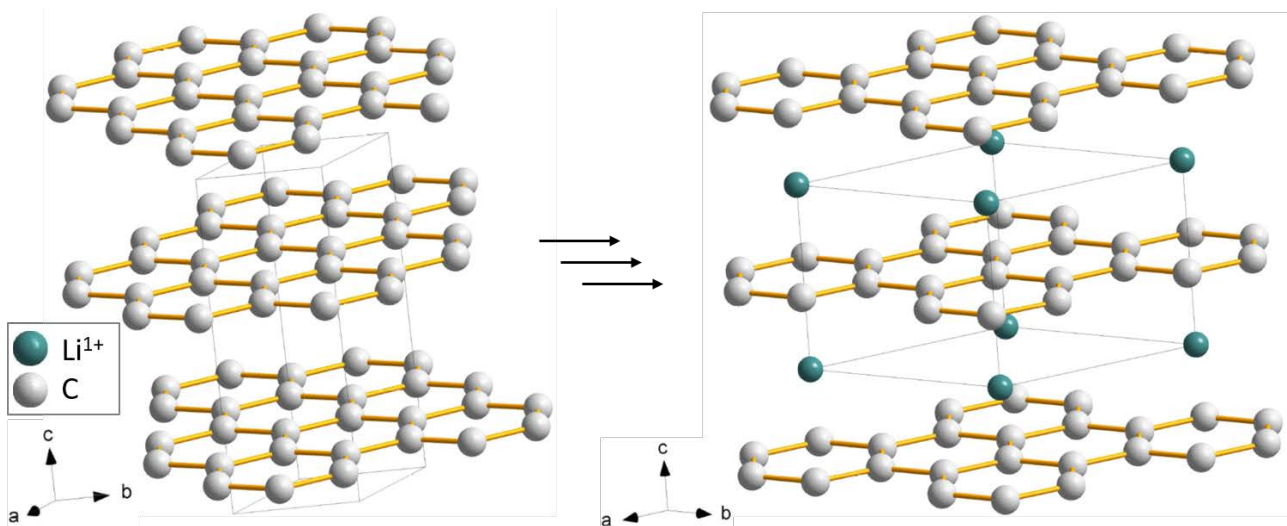

Fig. 2.3: Crystal structure change upon lithiation; $P6_3/mmc$ type graphite crystal lattice (unit cell included) according to D. D. L. Chung[27]; $P6/mmm$ type LiC$_6$ crystal lattice (unit cell included) based on diffraction data by K. Persson.[104]

Lithiation of graphite reveals low anodic potentials close to 0 V vs. Li/Li$^+$ in its fully lithiated state LiC$_6$. The typical voltage profile along graphite lithiation/delithiation is shown in Fig. 2.4.
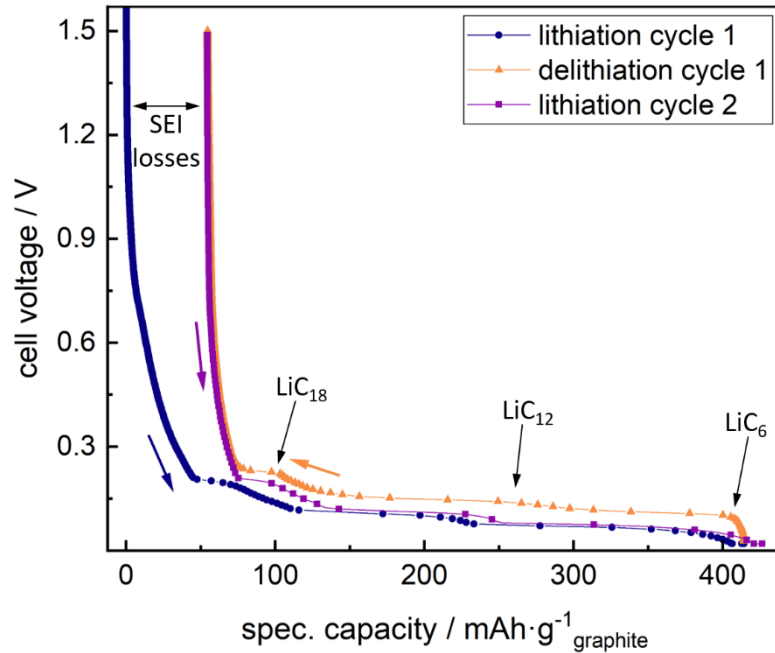
Fig. 2.4: Initial graphite anode cycling curves 0.02 – 1.5 V at 0.1 C-rate; data collected by half-cell (T-cell) experiment.

Cell overpotentials during LIB operation, possibly induced by lowered temperature or increased C-rates, might cause lithium plating at surfaces of lithiated graphite, i.e. deposition of metallic lithium, that cause known challenges of dendritic lithium as discussed above.

Anodic potentials close to Li/Li$^+$ potential cause side reactions with common LIB electrolyte components and induce formation of the Solid Electrolyte Interphase. This phenomenon will be discussed more in detail in chapter 2.5.1.

2.2.3 Conductive additives

A series of common LIB active materials exhibit limited electronic conductivity, e.g. layered oxides (NMC, NCA), phospates (LFP, LFMP) or LTO.[105–109] In electrodes composed of low conducting active materials, additional electron bridges must be provided furthermore by integration of highly conductive additives.[110] For the same reason, these active materials are typically used in small particle sizes or covered by carbon coatings.[26,81–85,111–113] Based on their high electronic conductivity, a series of sp^2-carbon based structures are most established as conductive additives, as listed in Tab. 2.1.

Tab. 2.1: Characteristics of conductive additives provided from literature and from supplier data sheets.

material	average particle size	BET [$m^2 \cdot g^{-1}$]
carbon black	$d \approx 150\,\mathrm{nm}$[114]	64
conductive graphites	$d_{50} \approx 3 - 4\,\mu m$	20
carbon nanotubes (CNT)	$d \approx 10\,\mathrm{nm}; l \approx 400\,\mu m$[115]	$25 - 34$[116]
vapor grown carbon fibers (VCGF)	$d \approx 200\,\mathrm{nm}; l \approx 10 - 20\,\mu m$[117]	$15 - 37$[117]
graphene nanosheets (GN)	$d \approx 6 - 8\,\mathrm{nm}; l \approx 15\,\mu m$	120

Grading nano-sized particles in terms of particle size is sometimes challenging, as for their trend to form superstructures. E.g. carbon black, principly composed of smallest primary particles (tenths of nm), always forms bigger mesostructures, known as aggregates (hundreds of nm). Carbon black aggregates again tend to form agglomerates (tenths of μm). Reversion of these processes is a main challenge for electrode production (more details in chapter 2.3.1).

Availability of conductive additive in a wide range of particle sizes allows for precise adjustment to any chosen active material at minimum contents, especially if combining several types of conductive additives to provide electron bridges at multiple scale lengths.[114,118] Though, the processable content of conductive additives is also limited to the chosen electrode processing technique, as particles of high Brunauer-Emmet-Teller (BET) surface area drastically increase the fluid viscosity of solvent based electrodes slurries,[114] which complicates both slurry preparation and coating issues and therefore raises mechanical difficulties for LIB production techniques.

Carbon black, which is most frequently used nowadays, can provide both high electronic conductivity as well as small particle size to operate well at low solid contents.[114] Though, its BET surface area is considerably high. Therefore, most cathodes and LTO anodes typically contain a mixture of conductive carbon and conductive graphites, to allow for limited fluid viscosity during electrode slurry preparation and maintain high electronic conductivity within the final electrode.[114]

2.2.4 Binder systems

Electrodes are typically manufactured by coating active materials, conductive additives and binder polymers onto metallic current collectors. The binder polymer must provide sufficient cohesion between electrode particles as well as adhesion to the metallic substrate, while staying inactive to any chemical species formed during LIB operation. Binder polymers also dominate electrolyte wetting aspects of LIB cells, arising from swelling aspects of binder polymers within the electrolyte solvents. Polyvinylidene difluoride (PVDF) based binders have been optimized for decades to meet most requirements.[119] Typically, organic solvents like N-methyl pyrrolidone (NMP), N-ethyl pyrrolidone (NEP) or acetone are used to form for electrode slurries during electrode production and to get removed subsequently after the coating process. Though, some obstacles for LIB operation remain upon PVDF-NMP systems. Use of NMP is environmentally harmful in case of accidental exposition, and obligatory solvent recovery processes are expensive due high evaporation temperature. PVDF-based electrodes were shown to suffer from inadequate drying conditions due to formation of binder gradients and increase of tortuosity.[120,121] Cathode side reactions like transition metal dissolution or cathode degradation reactions are intensified upon PVDF contact points and HF release.[122,123] So, significant efforts have been made to design fluorine-free and water-soluble binder polymers for enviromentally friendly and cheap electrode production. Sodium carboxymethylcellulose (CMC) and styrene butadiene rubber (SBR) have been shown to achieve comparable electrode performance for graphite, LTO or silicon anodes[124–128] as well as for $LiNi_{0.5}Mn_{1.5}O_4$ (LNMO), LFP or LFMP cathodes.[126,129,130] Alginate, guar gum, pectin and water-soluble PVDF-latex species have also been studied as water-soluble binders.[125,128,131,132] Binder systems used for water-based electrode slurries typically rely on separation of binder functions. While a first class of binder polymers (CMC, alginate) mainly ensures adhesion between electrode layer and current collector, a plasticizer (water-based SBR-latex) or a special binder (water-based PVDF-latex or derivatives) is used as a second class to reduce electrode slurry viscosity and to increase the electrode nano-elasticity.[124,127,133]

Latest research also addresses solvent-free electrode production for further cost reduction.[134,135]

2.2.5 Separators

Separators are sandwiched between anode and cathode to act as electronic insulation. Simultaneously, their microporous structure ensures ionic connectivity by liquid electrolyte bridges. Typically, thin polyolefin separators (< 30 µm) composed of polypropylen (PP), polyethylen (PE) or laminates of PP and PE are currently used in LIBs. Central aspects for the separator functionality arise from porosity (30 – 60 %) and pore size uniformity (0.03 – 0.1 µm).[136–139] Therefore, the production of commercial membranes used as LIB separators typically contains orientation steps to adjust porosity and tensile strength, which can be realized either in a dry process by melting, extrusion, annealing or stretching, or in a wet process (phase inversion process) using volatile solvents to control pore sizes.[39–41,44,136]

Inclusion of multiple (organic and inorganic) materials in separators is established as well, and can be achieved by forming multilayer compounds or by forming coated polymer fibers. A well-known example for multilayer separators was created to improve of safety issues of LIB operation. The trilayer PP-PE-PP laminate separator geometry includes a central PE layer within stable PP surfaces, which provides a shutdown mechanism in case of cell overheating, via pore-closure due to melting of the central PE layer. Increasing thermal stability of polyolefin was also demonstrated for inorganic (Al_2O_3, ZrO_2, zeolites) coating layers.

Use of pure nonwovens as separator in LIBs would require too high layer thickness to exclude electrical short circuits and ensure its insulating function. Though, nonwovens are frequently used as supporting matrices for stabilistation of additional separator components like organic or inorganic particles and coatings.

Coating and filling nonwovens with inorganic materials, can significantly improve safety and performance of LIBs. Both Al_2O_3 and ZrO_2 fiber coatings were demonstrated to increase thermal stability and to improve both nanoporosity and electrolyte wettability of separators.[43,45–49,51,140,141] Aside from metal oxides, latest studies also addressed metal hydroxides (flame retardant) or BN (Li dendrite growth inhibition) for separator modification.[50,53]

Special demands for separators arise, if the cell production should include the lamination step (more details in chapter 2.3.3). During lamination, heat and pressure are applied on the electrode-separator stack, to heaten all polymers (electrode binder, separator polymer) above glass transition and close to melting temperature. This state enables an interface connection, while the polymer viscosity is kept low enough to prevent the formation of an interface blocking layer by pore closure.

This process step can be achieved best, if all polymers both in electrodes and separator have similar melting points. As a consequence, known laminable systems of electrodes and separators are often purely based on PVDF. Though, a variety of common separators are composed of polyolefins, which either lack sufficient thermoplastic behavior for lamination (PP), or suffer from excessive shrinking trend at elevated temperatures (PE). Aside, common water-based binder systems lack thermoplastic behaviour as well (CMC). Enabling non-laminable systems for the lamination step can be achieved by additional bonding layers ontop of the separator, e.g. using bar-coating, spraying or electrospinning.[42,142]

2.2.6 Electrolytes

Lithium Ion Batteries rely on high energy density and power density upon using lithium as mobile ionic species.

Basic battery benefits arise from high cell potentials above 4 V between common cathode (NMC, NCA, LCO,) and anode materials (lithium metal, graphite). Though, choosing electrolyte solvents to avoid any side reactions in such high potential windows is challenging. Intrinsic stabilization of metallic lithium within chosen organic solvents, due to formation of a passivation layer, was found in early 1950s and later described as the Solid Electrolyte Interphase by E. Peled and Co-workers.[143] Relying on this stabilization mechanism, extensive research focused on investigation of organic solvents for stabilization of graphites in Lithium Ion Batteries.[144] Inorganic electrolyte solvents (Cl_2SO, SO_2) were developed as well for use in Lithium Ion Batteries.[144–147]

Beside providing electrochemical stability within typical cell voltages, electrolyte solvents are chosen to withstand the highly reductive potentials of lithium or lithiated graphite anodes and to allow for high ionic conductivity of Li^+ ions, so polar and aprotic solvents like ethers or esters are preferrable. High polarity is given for cyclic diesters like propylene carbonate (PC) or ethylene carbonate (EC),[144] so these solvents are of major interest for LIB electrolytes. Though, using pure propylene carbonate as electrolyte solvent is detrimental for graphite anodes, as for causing graphite exfoliation due to PC co-intercalation.[144,148] While EC reveals strongly beneficial issues in terms of forming stable SEI and providing high solvent polarity, processing at room temperature is impossible due to its high melting point at 36 °C.[149] So, common LIB electrolytes are composed of binary or ternary mixtures of EC and linear diesters like dimethyl carbonate (DMC), diethyl carbonate (DEC) and ethyl methyl carbonate (EMC).

Electrolyte dynamics are typically described by the well-known Newman approach,[150] based on four central parameters, that are electrical conductivity κ, binary diffusion coefficient $D_\pm$, activity coefficient $\gamma_\pm$ and transference number t_+.

$$\frac{\delta(\varepsilon\,c)}{\delta\,t}+\vec{\nabla}(\varepsilon\,c\,\overrightarrow{v_0})=\vec{\nabla}\cdot\frac{\varepsilon}{\tau}\left[D_\pm\left(1-\frac{\mathrm{d}\ln(c_0)}{\mathrm{d}\ln(c)}\right)\vec{\nabla}c\right]-\frac{\vec{\imath}\,\vec{\nabla}t_+}{z_+v_+\mathrm{F}} \tag{7}$$

$$\vec{\nabla}\varphi = -\frac{\vec{\imath}}{\kappa\frac{\varepsilon}{\tau}}+\frac{2\mathrm{R}T}{\mathrm{F}}\left(1+\frac{\mathrm{d}\ln\gamma_\pm}{\mathrm{d}\ln c}\right)(1-t_+)\vec{\nabla}\ln c \tag{8}$$

By integration of porosity ε, salt concentration c, kinematic viscosity v_0, current i, cation charge z_+, cation stoichiometric number v_+, Faraday constant F, potential φ and tortuosity τ, these equations describe mass conservation [7] and energy conservation [8] of electrolytes.

To achieve high Li^+ transference numbers, electrolyte conductive salts typically include complex anions, e.g. $LiPF_6$, $LiAsF_6$, $LiClO_4$ or $LiBF_4$, that distribute and stabilize their negative charge in a complex anion structure, therefore providing high anionic stability and low tendency to form solvent shells. Highest ionic conductivities in EC/DMC were reported for $LiPF_6$ and $LiAsF_6$.[62,144,151–154] As for the toxicity of both As(III) and As(0) oxidation

states, $LiPF_6$ is mostly used in LIBs today.[119,144] Similar to PVDF binder polymer issues, using $LiPF_6$ is problematic for layered oxide cathode materials as for possible cathode decomposition reactions induced by HF, that is formed from $LiPF_6$ in presence of H_2O.[91,155] Details on HF based cathode decomposition will be discussed in chapter 2.5.3. Further research focused on special conductive salts stable to H_2O side reactions like $Li^+[N(SO_2F)_2]^-$ (LiFSI) or $Li^+[N(SO_2CF_3)_2]^-$ (LiTFSI).[60,154,156–160]

Long-term cycling and C-rate stability of LIBs is strongly bound to the quality of the anodic passivation layer SEI, that is formed upon electrolyte decomposition during formation cycles; more details will be given in chapters 2.5.1 and 2.5.2. Additional stabilization of the SEI can be addressed using special electrolyte additives prone to reduction on the anodic surface. Typically, fluoroethylene carbonate (FEC), vinylene carbonate (VC) or their derivatives are used in LIB electrolytes for this purpose, using unsaturated monomers to induce polymerization under reductive conditions.[161–165] Also sulfur-, boron- and isocyanate-based additives are studied as additives for graphite anode stabilization.[58,68,166,167] For stabilization of high voltage cathode materials with potentials above 4.5 V vs. Li/Li^+ like $LiCoPO_4$, $LiNiPO_4$, $LiCoPO_4F$ or LNMO, special electrolyte additives were developed to stabilize LIB cathodes against oxidation reactions. Phosphorus-based, borate based or aromatic/heterocyclic additives are used for this issue.[66,67,166,168] Additives based on special redox shuttles are studied as battery overcharge protectors, like ferrocene-based structures, phenothiazines, piperinyl oxides and phenyl amines.[54–57,59,61,150,166,169,170]

Low temperature applications are typically realized by using special conductive salts like $LiBF_4$, or by including an additional solvent fraction of low-temperature stable solvents like PC, ethyl acetate or methyl butyrate.[144,171–173]

2.3   Electrode production and cell assembly

2.3.1 Electrode slurry preparation

Electrode slurry preparation is a fundamental tool to balance conflictive needs during electrode production. While important electrode properties like adhesive/cohesive forces, flexibility or electronic conductivity are bound to sufficient amount of inactive components (binder, conductive additives), energy density optimization requires their minimization. While established coating techniques limit processable fluid viscosities, cost reduction demands maximized solid contents within electrode slurries. High energy input during slurry preparation is necessary for crushing of agglomerates, and to ensure sufficient distribution of conductive additives.

Fulfilling all mentioned requirements is also challenging due to the strong differences in material characteristics (see Tab. 2.2).

Tab. 2.2: Characteristics of electrode raw materials given by monocrystal properties and supplier data sheets.

material	particle size [μm]	material density [g·cm^{-3}]	bulk density [g·cm^{-3}]
NMC	5 – 13	4.76	2.30
LFP	0.2 – 2	3.59	0.53
active graphite	10 – 46	2.26	0.92
LTO	0.7 – 1.6	3.49	1.20
carbon black	< 0.05	2.00	0.16
conductive graphite	1.6 – 6	2.26	0.06

As a consequence, optimized electrode formulations are directly bound to the chosen preparation strategy. Large efforts in past research addressed slurry preparation optimization.

Numerous studies emphasized strong influences of carbon black to LIB cathodes. Early findings by R. Dominko et al. showed a strong correlation of carbon black distribution and cathode polarization, mainly depending on the slurry preparation technique.[110] Subsequently, detailed investigations of slurry preparation strategy influences on electrode properties and performance were carried out within the German research cluster ProZell.[174] Evolving studies revealed important process-structure-characteristics relationships, like an optimum level of carbon black dispersion for ideal cathode performance,[175] or highest solid content formulations to be achieved upon including extruders.[176]

In total, a wide range of different slurry preparation strategies has been demonstrated successfully.

Both direct mixing of all solid components (active material, conductive additives and binder) with solvent or binder solution, as well as sequential fusion of solids with solvent or binder solution were studied in detail.[177,178] Electrode slurry preparation was demonstrated on discontinous devices like dissolvers, kneaders or planetary mixers, as well as on continous devices like extruders.[179–182] Additional filtering systems might be integrated for additional extraction of agglomerates.

If using kneaders for electrode slurry production, special sequences are applied.

After premixing active materials, conductive additives and PVDF binder, the solvent gets added sequentially to the mixture, as shown in Fig. 2.5. The slurry preparation process is divided into premixing phase, kneading phase and dilution phase. Main energy input is realized during the kneading phase, also known as KATANERI.[183] High shear rates and elevated temperature ensure homogenous distribution of conductive additives and sufficient crushing of agglomerates. Sufficient degassing can be finally achieved by vacuum steps.

Fig. 2.5: Electrode slurry preparation using a kneader; (a/b) premixing phase; (c) kneading phase; (d) dilution phase.

2.3.2 Coating techniques and issues

Preparation of electrode coatings represents a crucial manufacturing step for LIB production. Homogenous coatings with uniform coating thickness as well as optimized pore structure and high adhesion to current collectors are necessary for high energy density, high power density and minimized aging of LIBs. Wet electrode slurries are typically coated onto current collector foils using doctor-blade, slot die, reverse roll or comma bar coating.[184,185] Drying is usually carried out inline, using drying tunnels based on various drying techniques like conduction, convection or infrared radiation. To control electrode porosity and increase energy density, electrodes are typically compressed after the drying step using calendering technique,[184,185] which can significantly improve the performance of electrodes, as shown for layered oxide cathodes, phosphate cathodes, graphite anodes or Si/C anodes.[71,186–191]

Recent studies identified significant influences of coating methods on electrode performance and aging. Microstructural electrode inhomogeneities were shown to induce large overpotentials and subsequently increase the possibility for lithium plating.[192] Influences of inadequate drying processes were shown to induce binder migration and tortuosity increase; arising negative influences on electrode kinetics have been discussed in detail.[120,121,193,194]

Nevertheless, state-of-the-art electrode production uses accelerated coating processes up to 50 m·min^{-1} and shortened drying processes below 2 min.[185,195] For further increase of specific energy and energy density of LIBs, production issues and possible stabilization techniques of electrode coatings with increased thicknesses up to 200 µm were demonstrated on laboratory scale.[196–199]

Electrodes used for studies discussed in this work, were prepared by doctor-blade coating electrode slurries in a roll-to-roll process, including convective and conductive drying in an inline two-step drying tunnel. The coating procedure is shown in Fig. 2.6.

Fig. 2.6: Roll-to-roll electrode coating process including doctor-blade coating and inline drying tunnel.

SEM micrographs of as-prepared graphite anodes and NMC 111 cathodes show homogenous distribution of conductive additives between active material particles (see Fig. 2.7).
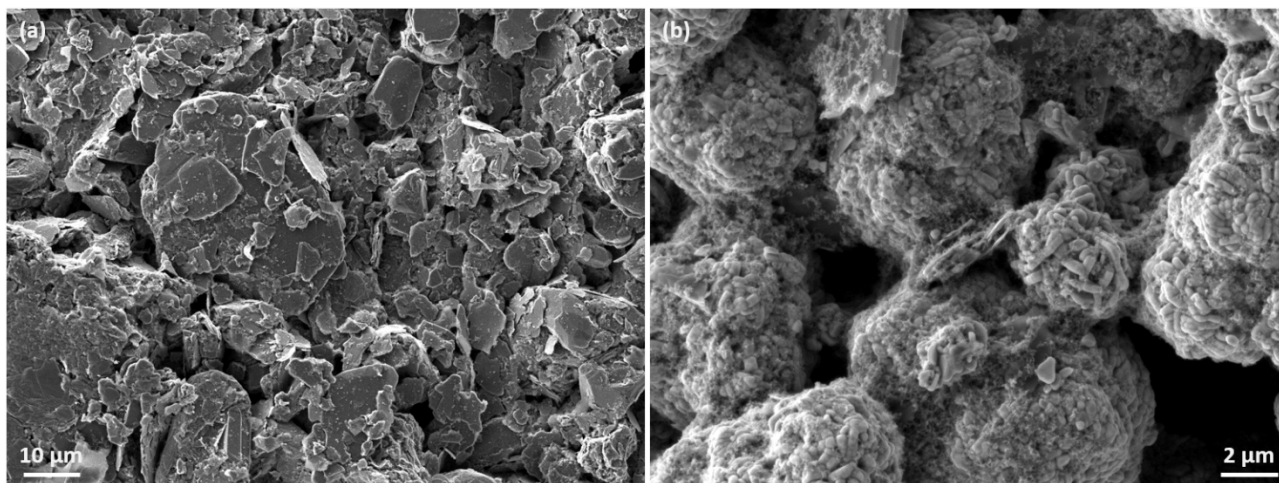

Fig. 2.7: Exemplary plain view SEM micrographs; (a) graphite anode; (b) NMC 111 cathode.

2.3.3 Cell assembly techniques

a) Half-cell assembly

For individual analysis of anodes or cathodes previous to full cell assembly, electrodes are frequently studied in half-cell geometry. Using lithium metal as counter electrode (CE) provides a reasonably stable source for infinite amount of active lithium, which limits the performance of charge/discharge steps only to capacity and kinetics of the working electrode (WE). Including a reference electrode (RE) for operation in three-electrode geometry additionally minimizes influences of ohmic overpotentials to the cell voltage curve (see Fig. 2.8a).

The T-cell setup is a well-known approach for half-cell measurements of lithium ion electrodes in three-electrode geometry (see Fig. 2.8b).
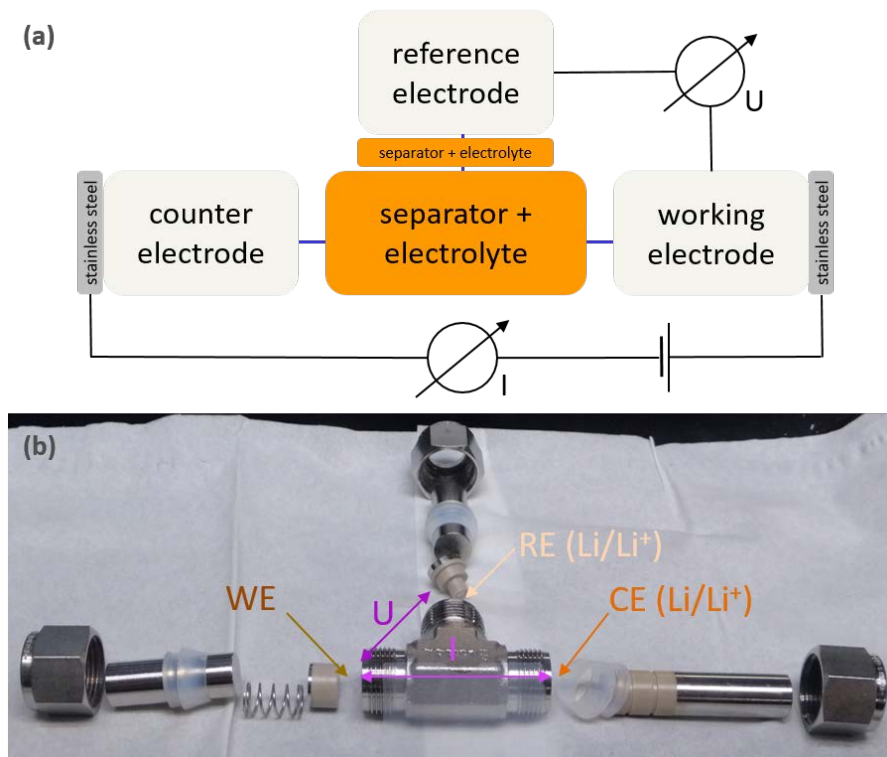
Fig. 2.8: Half-cell setup for operation in three-electrode geometry; (a) schematics (b) T-cell components.

b) Full cell assembly

Production of LIB packs with recognizable capacity requires large amounts of electrode material. Electrode layers are typically produced in sub-mm diameter. Bundling of the basic anode-separator-cathode unit can be realized using continous material processing by winding to form cylindrical or prismatic cells.[184] Cell aging effects arising from inevitable stress evolution in this geometry were studied in detail.[200,201]

Another approach is based on cutting separator, anode and cathode into separate units, which are either combined into stacks by alternating insertion of double-side coated anodes and cathodes into a continous separator unit (Z-folding technique), or by direct stacking of cut anode/separator/cathode units using single-sheet stacking.[184] Comparison of these cell assembly techniques is given in Fig. 2.9 and Fig. 3.3.
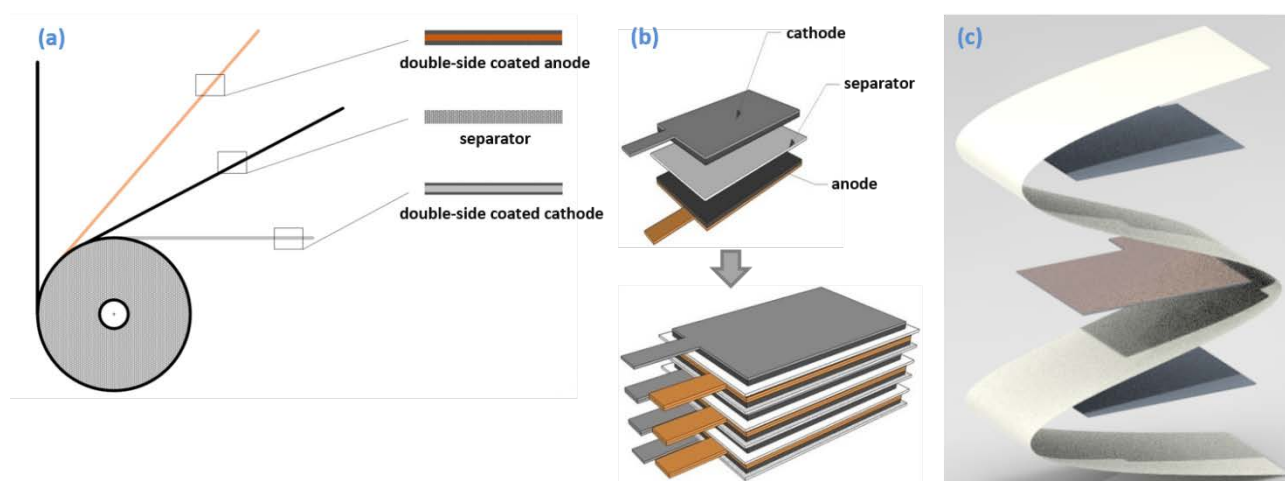
Fig. 2.9: Schematics for cell assembly; (a) cylindric winding; (b) stacking; (c) Z-folding; reproduced with permission of M. Thurnreiter and L. Schaller.

The stacking approach can be accelerated by the lamination technique, which pre-fuses three (anode-separator-cathode) or five (cathode-separator-anode-separator-cathode) single units into single cell or bicell stacks, for acceleration both of stacking process and production speed.[202] The lamination technique also allows for a combination of stacking and winding principles by prelaminating anodes and cathodes to a continous separator unit.[203] Implementations of the lamination technique into LIB production were patented (earliest in 1995) in several modifications during the past decades.[204–214] The technique was also expanded to supercapacitors for minimization of air bubbles and wrinkles during electrode production.[215] Lamination is also used for transfer of electrode layers between collector foils.[216]

Cell stacks are typically housed in multilayer pouch foil (polypropylene-aluminum-polyamide) or in rigid metal housings (aluminum, stainless steel) and subsequently filled with electrolyte under exclusion of H_2O. Pouch cells are typically evacuated twice, after the electrolyte filling step and after the formation step.

2.4   Analysis techniques

2.4.1 Charge/discharge cycling – Power test & Lifetime test

Lifetime tests and power tests are common methods for validation of cell capacity, cell dynamics and cell degradation of LIBs.[10] Repeated charging and discharging of a cell at identical C-rate within either partial or full voltage range (Lifetime test) can provide both the cell capacity at normalized conditions, as well as direct information on capacity fading with cycle number. An estimation on the fraction of unwanted side reactions can be extracted from the Coulombic efficiency. Power tests (C-rate tests) are performed by charging and discharging a cell at various C-rates, typically by increasing charging rate and/or discharging rate at every third or fifth cycle. This technique may allow for direct insights on the slowest limiting factor (i.e. electronic conductivity, ionic conductivity, Li^+ ion transport kinetics, solid state diffusion) of a specific system. Separation of constant current and constant voltage fractions (more details in Fig. 2.10) can provide additional information to separate specific aging phenomena.

A well-known profile of charge/discharge experiments for research issues, is applying a two-step charging protocol. A constant current (CC) charging section – until reaching the upper cutoff voltage – is followed by a constant voltage (CV) charging section – charging at the upper cutoff voltage, until the charging current drops below a certain level. Discharging is typically performed by a CC discharge step until reaching the lower cutoff voltage.

Relaxation periods between charge and discharge steps might be integrated to allow for further in-line analysis during extended charge-discharge experiments, e.g. for assumption of internal resistance (further information in chapter 5.6).

Along the described cycling structure, full cell voltage and current follow a characteristic profile, as shown in Fig. 2.10.
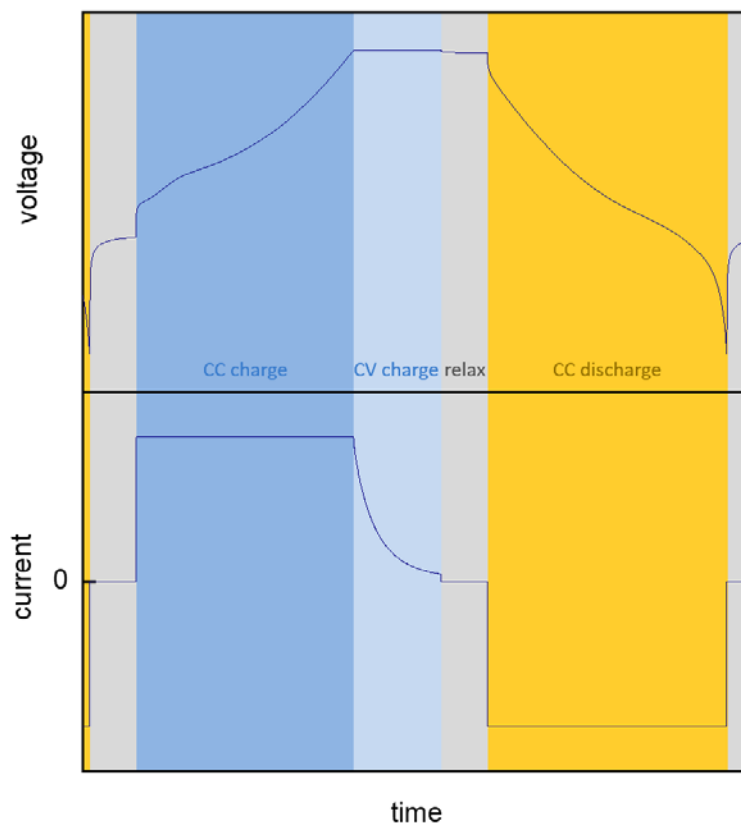
Fig. 2.10: Graphite-NMC full cell voltage profile and current profile during cycling; protocol steps highlighted by background color; CC charge (blue), CV charge (pale blue), relaxation (grey), CC discharge (yellow). Data conducted in two-electrode geometry.

Exemplary evolution of the individual potentials of anode/cathode/full cell for a graphite-NMC 111 cell upon cycling, are shown in Fig. 2.11.
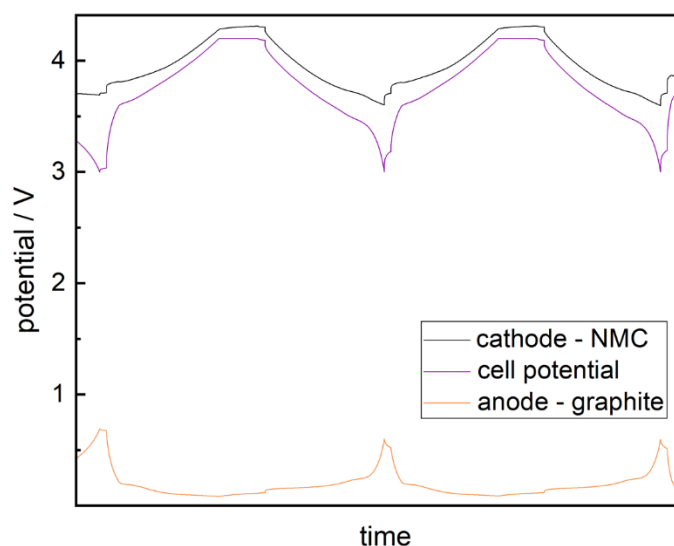

Fig. 2.11: Potential trend of a graphite-NMC 111 cell following a CCCV charging / CC discharging protocol. Data conducted in three-electrode (T-cell) geometry.

2.4.2 Electrochemical Impedance Spectroscopy

Electrochemical Impedance Spectroscopy is a common technique to separate physical, chemical and electrochemical processes (e.g. mass transport, diffusion, chemical reactions, adsorption/desorption processes, charge-transfer), according to their response on electrical excitation in an alternating electrical field. The discussed phenomena show individual dependencies to the frequency of the electrical excitation. The resulting frequency-dependent response is known as complex resistance or impedance Z

$$Z = \frac{u}{i} = \frac{\hat{u}}{\hat{i}} e^{j(\phi_u - \phi_i)} = \hat{Z} e^{j\phi_Z} \qquad [9]$$

with imaginary number j, complex voltage u, complex current i, momentary resistance $\hat{Z}$, momentary voltage $\hat{u}$, momentary current $\hat{i}$, and phase angles ϕ_Z, ϕ_u, ϕ_i.

The physical interaction to the frequency is mathematically treated by introducing a time dependent phase angle

$$\phi(t) = \omega t + \phi_0 \qquad [10]$$

which is described in terms of time independent phase angle ϕ_0, angular frequency ω and time t.

The angular frequency ω is proportional to the frequency f.

$$\omega = 2\pi f \qquad [11]$$

Electrical excitation is typically performed by sine-wave oscillation of the potential (Potentiostatic Electrochemical Impedance Spectroscopy – PEIS) or of the current (Galvanostatic Electrochemical Impedance Spectroscopy – GEIS). Real electrochemical cells are usually described by an equivalent circuit consisting of several ideal elements: capacitor C, ohmic resistance R, inductor L, or constant phase element CPE. Using the formulations given in Tab. 2.3, frequency dependencies and responses can be studied by equivalent circuit analysis.

Tab. 2.3: Fit elements used for EIS equivalent circuit diagrams.[217]

Element	$Z(\omega t)$	Fit parameters
Ohmic Resistance R	R	R
Capacitor C	$\dfrac{1}{j\omega C}$	C
Inductor L	$j\omega L$	L
Constant Phase Element CPE	$\dfrac{1}{Q(j\omega)^\alpha}$	Q, α
Warburg Element Z_W	$\dfrac{A_W}{\sqrt{\omega}} + \dfrac{A_W}{j\sqrt{\omega}}$	A_W

The Constant Phase Element (CPE) was introduced as a special case circuit element,[217–222] describing non-ideal behaviour of real samples. The CPE is designed as a transition between ohmic resistance ($\alpha = 0$) and capacitor ($\alpha = 1$). The Warburg Element, created to describe diffusion processes, is a special case of the constant phase element with a fixed phase angle of 45 ° ($\alpha = 0.5$).

Combinations of these elements in equivalent circuit diagrams obey Kirchhoff's circuit laws for real resistors:

- series connection

$$Z = Z_1 + Z_2 \tag{12}$$

- parallel connection

$$\frac{1}{Z} = \frac{1}{Z_1} + \frac{1}{Z_2} \tag{13}$$

The Randles equivalent circuit (Fig. 2.12) was developed to describe single-step charge-transfer processes with diffusion of reactants to the interface,[217,223] including solvent resistance R_S, charge-transfer resistance R_{CT}, double layer capacitance C_{DL} and Warburg Element Z_W.
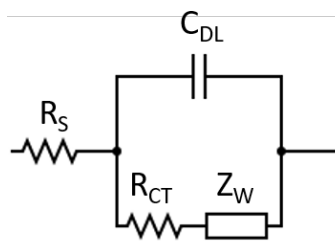
Fig. 2.12: Randles equivalent circuit.

The Randles equivalent circuit is commonly used to describe the EIS response of a single electrode in LIB cells. EIS measurements are usually visualized in a Nyquist diagram, by plotting active resistance (x-axis) Z' vs. negatively mirrored reactance (y-axis) $-Z''$. The Nyquist diagram for a Randles circuit is shown in Fig. 2.13.
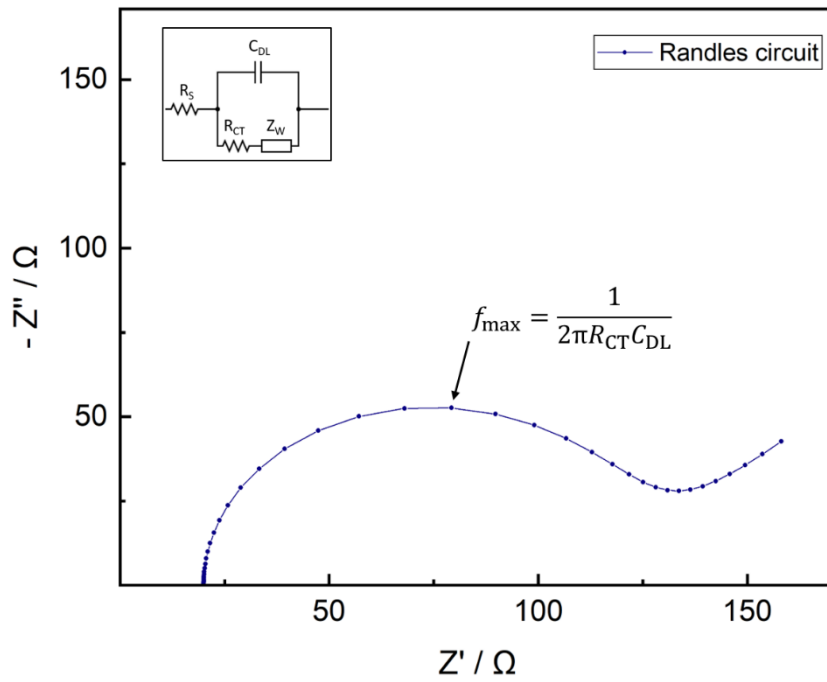
Fig. 2.13: Randles circuit simulation (100 kHz – 1 Hz); $R_S = 20\ \Omega$, $C_{DL} = 25\ \mu F$, $R_{CT} = 100\ \Omega$, $A_W = 100\ \Omega \cdot s^{-0.5}$.

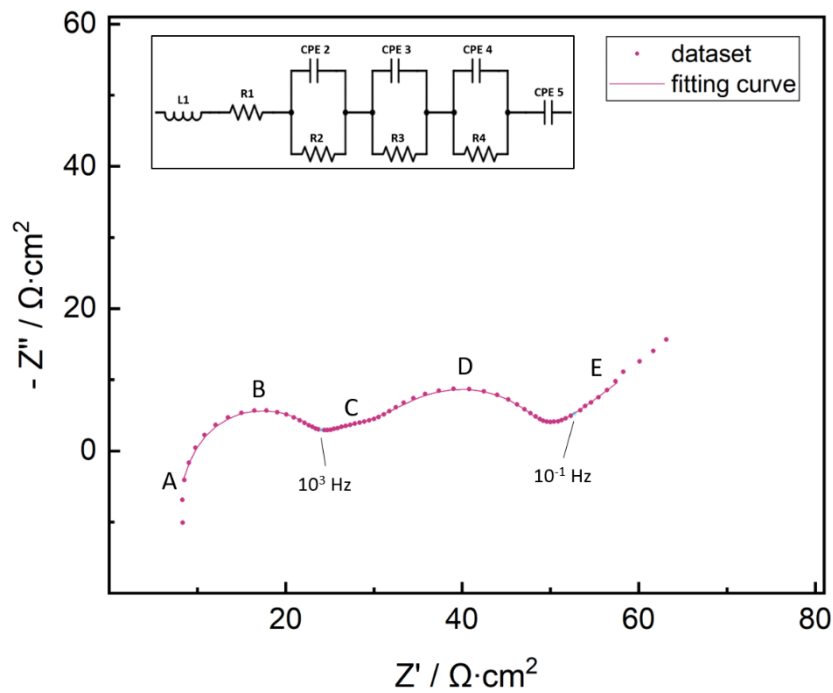A typical EIS response of graphite-NMC 111 single cells, as studied in this thesis, is shown in Fig. 2.14.

Fig. 2.14: Impedance measurement of non-laminated graphite-NMC 111 full cell; EIS (100 kHz–10 mHz) along charging step, 6th cycle; data points at 10^3 Hz and 10^{-1} Hz highlighted in pale blue; equivalent circuit model integrated.

The integrated equivalent circuit shown in Fig. 2.14 is a common model used to study the EIS response of graphite-NMC full cells.[224] Highest frequency responses (section A), represented by inductance element L1 and electronic resistance R1, are mainly driven by electrolyte resistance, and contain small setup side influences from cell tabs, welding points, channel contacts and cables. Three subsequent R-CPE elements (sections B – D) arise from surface resistance, anodic graphite charge-transfer reaction and cathodic NMC charge-transfer reaction. Lowest frequency response (section E) is dominated by diffusion characteristics, typically split into closed and open Warburg regimes.

Correct interpretation of the EIS response of LIB cells is sometimes impossible without further information. The surface resistance semicircle is typically considered to mainly depend on two separate limiting interfaces, which are the anodic SEI layer and interface contacts between cathode particles and cathodic current collector.[225] Charge-transfer signals from NMC cathode and graphite anode tend to overlap in this geometry.[226–229] Within the Warburg signal contribution, typically used to quantify solid state diffusion phenomena,[230] its two sections (open and closed Warburg) might sometimes be hard to differentiate.

For further insights into EIS response of LIB cells, several strategies have been demonstrated. Studying their temperature dependence, might allow for a more precise separation of the anodic SEI contribution.[224,231] Though, changing temperature of cells throughout EIS analysis might change their subsequent cycling behaviour. Measuring EIS in three-electrode-geometry,[229] based on cell geometry change by inclusion of specialized reference electrodes[232,233] might enable signal separation of anodic and cathodic charge-transfer reactions.

Further details on EIS signal interpretation will be given in the results and discussions section (chapter 5).

2.4.3 Scanning Electron Microscopy and Energy Dispersive X-ray analysis

Highest resolution of any microscopic applications, aside from lens aspects, is bound to the wavelength of the signal carrier. Compared to typical wavelengths of visible light (400 – 800 nm), accelerated electrons have drastically lowered de Broglie wavelenths ($E_{e^- - \mathrm{kinetic}} = 5\mathrm{keV} \rightarrow \lambda_{e^-} = 17\,\mathrm{pm}$). Aside, penetration depth into dense matter is much lower for electrons than for photons, what increases the sensitivity of electrons to surface aspects.

Both trends enable surface screening with focused electron beams as a powerful tool for high resolution microscopy applications. Scanning Electron Microscopy setups (see Fig. 2.15) basically consist of electron source, electron lensing systems and electron detectors, that allow for separation of elastically scattered electrons, inelastically scattered electrons, secondary electrons and Auger electrons.
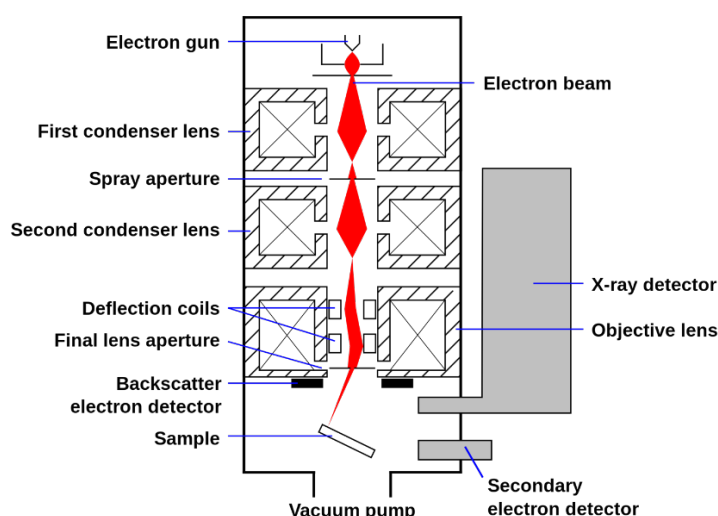
Fig. 2.15: Schematics of scanning electron microscopy. Reproduced from Wikimedia Commons.[234]

Electron radiation might knock out electrons from inner shells of surface layer atoms, which either induces X-ray radiation or Auger electron emission.
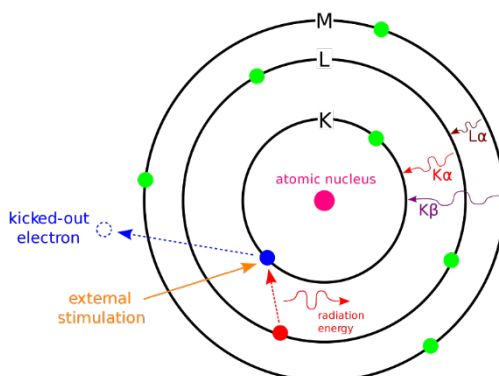
Fig. 2.16: Schematics of energy dispersive X-ray radiation. Reproduced from Wikimedia Commons.[235]

The resulting X-ray radiation is bound to discrete orbital transitions, and allows for precise differentiation between sensitive elements. So, combining EDX with SEM allows to create element maps of analyzed surfaces.

Scanning Electron Microscopy needs for high electronic conductivity of the sample surface. Samples of low surface conductivity are therefore sometimes covered with a thin conductive layer by Au sputtering.

In contrast to conventional SEM setups, that use heated W-cathodes as electron source, a Field-Emission Scanning Electron Microscope (FE-SEM) has a specialized electron source. In this case, the electric field induces electron tunneling from the small electrode tip (cold W-cathodes or Schottky-cathodes) into the microscop chamber. Field-Emission Scanning Electron Microscopy allows to study surfaces with high resolution at considerably low acceleration voltages, which reduces the energy input on the studied sample. This allows to study sensitive structures like biomolecules or free-standing polymer strings without surface sputtering.

2.4.4 Neutron depth profiling

The neutron depth profiling technique is a well-established technique for quantification of the concentration of several specific nuclei.[236] Neutron irradiation to materials containing NDP sensitive nuclides induces nuclear decomposition, followed by emission of charged particles with specific kinetic energy.

^{3}He, ^{6}Li, ^{7}Be, ^{10}B, ^{14}N, ^{17}O, ^{22}Na, ^{33}S, ^{35}Cl, ^{40}K and ^{59}Ni are sensitive to the NDP technique.[236] If charged particles pass dense matter, their kinetic energy is reduced. Given knowledge on the energy loss of ions passing specific materials, as collected in the SRIM software package,[237] can be used subsequently for precise depth analysis of the nuclear reaction position in a given sample. As for its high sensitivity to lithium, the NDP technique is of high interest for LIB research.

$$^6\text{Li} + \text{n} \rightarrow \ ^4\text{He}^{2+}(2055 \text{ keV}) + \ ^3\text{H}^+(2727 \text{ keV}) \qquad [14]$$
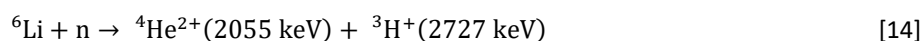
The NDP technique was successfully used to study the lithium distribution within electrodes in operando or to elucidate specific lithium transport phenomona.[238–242] NDP was also demonstrated as a powerful tool for analysis of anode aging phenomena, by quantifying inactive lithium immobilized in the anodic SEI.[77,243,244]

2.4.5 Statistics for data analysis

Validity of any scientific results and conclusions might be limited due to sample deviation, measurement errors or fluctuations of the setup environment.

Appropriate data analysis depends on the data distribution structure, which might have symmetrical or non-symmetrical shape. Exemplary symmetrical distributions are given by the normal distribution,[245,246] uniform distribution,[245,247] logistic distribution,[246,248,249] Laplace distribution[247,250] or Cauchy distribution.[247,250] Probability density functions are given as

<div align="center">uniform distribution[245,247]</div>

$$f(x) = \begin{cases} \dfrac{1}{b-a} & a \leq x \leq b \\ 0 & x < a \lor x > b \end{cases} \tag{15}$$

<div align="center">logistic distribution[246,248,249]</div>

$$f(x) = \frac{e^{-\frac{x-\alpha}{\beta}}}{\beta \left(1 + e^{-\frac{x-\alpha}{\beta}}\right)^2} \tag{16}$$

<div align="center">Laplace distribution[247,250]</div>

$$f(x) = \frac{1}{2\sigma} e^{-\frac{|x-\mu|}{\sigma}} \tag{17}$$

<div align="center">Cauchy distribution[247,250]</div>

$$f(x) = \frac{1}{\pi} \cdot \frac{s}{s^2 + (x-t)^2} \tag{18}$$

Same symmetric probability density functions are visualized in Fig. 2.17.
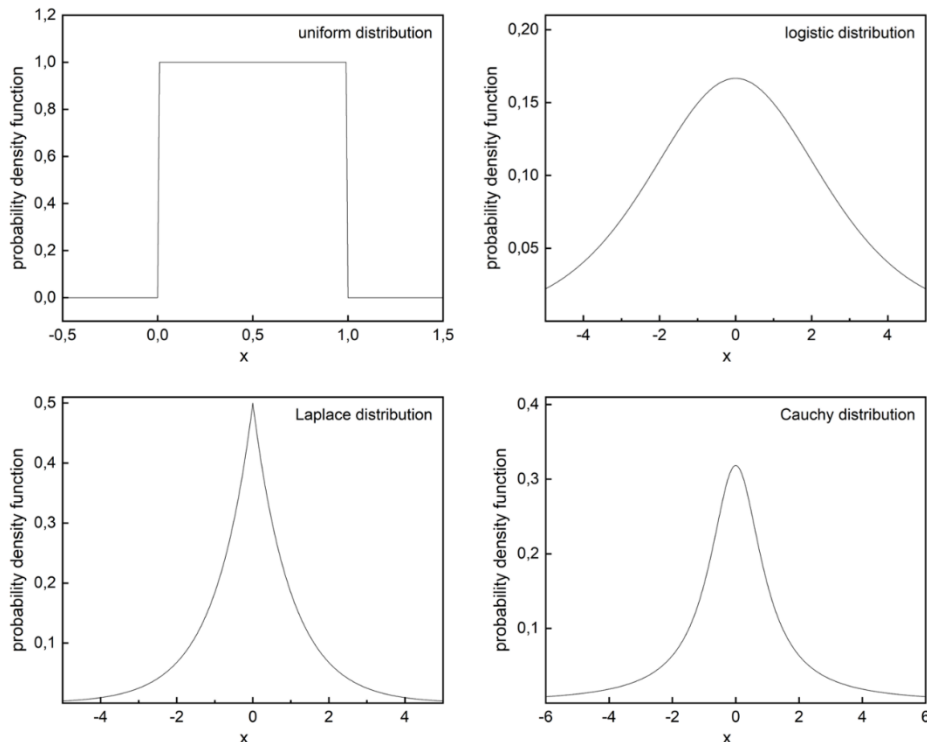
Fig. 2.17: Probability density functions for symmetrical data distributions; equal distribution [15] for $a = 0$ and $b = 1$; logistic distribution [16] for $\alpha = 0$ and $\beta = 1.5$; Laplace distribution [17] for $\mu = 0$ and $\sigma = 1$; Cauchy distribution [18] for $s = 1$ and $t = 0$.

The Gaussian/normal distribution[245,246] is given as

$$f(x) = \frac{1}{\sigma\sqrt{2\pi}} e^{-\frac{(x-\mu)^2}{2\sigma^2}}$$

[19]

and is a basic structure for the creation of common analysis tools. The expectation/mean/average of the normal distributed dataset x_k with $k = 1 \ldots n_x$ datapoints is described as[251]

$$E\{x\} = \mu_x = \frac{1}{n_x}\sum_{k=1}^{n_x} x$$

[20]

with expectation $E\{x\}$ and mean μ_x. The expectation can be used for determination of the variance σ_x^2.[251]

$$\sigma_x^2 = \frac{n_x}{n_x - 1}E\{(x - E\{x\})^2\} = \frac{1}{n_x - 1}\sum_{k=1}^{n_x}(x_k - \mu_x)^2$$

[21]

Standard deviation σ_x and standard error s_x are given as[251]

$$\sigma_x = \sqrt{\sigma_x^2}$$

[22]

$$s_x = \frac{\sigma_x}{\sqrt{n_x}}$$

[23]
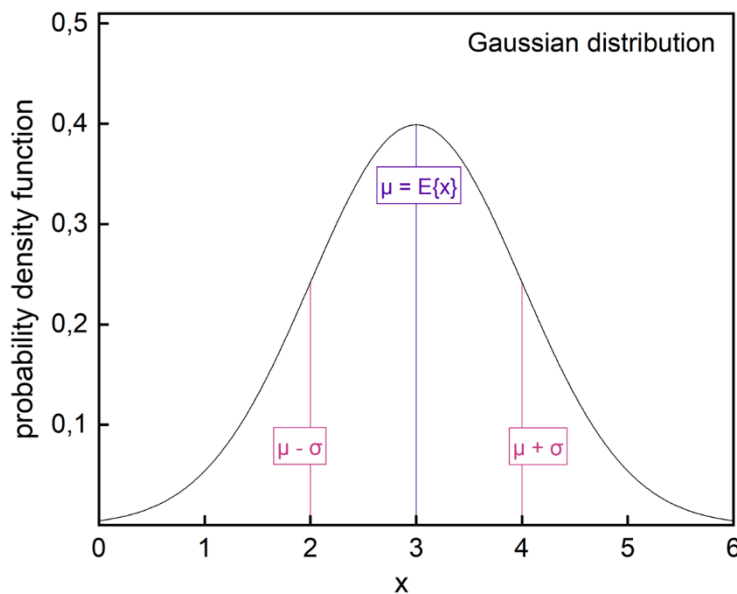
Fig. 2.18: Probability density function for Gaussian/normal distribution [19] for $\mu = 3$ and $\sigma = 1$.

An important characteristic of the Gaussian distribution is the probability of 68.26 % to find a random chosen datapoint of x_k within the range $\mu_x \pm \sigma_x$.

Examples for normal distributed datasets, are cell capacities at power tests and lifetime tests.

In case of normal distributed data, two datasets a and b (large data size of at least 30 indepently chosen datapoints per dataset) arising from two data populations might be tested on deviating means μ_a and μ_b using the t-test

$$\text{t-test}^{252}$$

Null hypothesis $H_0: \mu_a - \mu_b > $ hypothesized value

$$t = \frac{\text{E}\{dataset\ a\} - \text{E}\{dataset\ b\}}{\sqrt{\dfrac{\sigma_a^2}{n_a} + \dfrac{\sigma_b^2}{n_b}}}$$

[24]

with sample datasizes n_a and n_b. Typically, the null hypothesis is rejected if the t-test result exceeds a specific significance level like $p = 0.05$.

A different situation arises in case of non-symmetrical data distribution. An indepently chosen dataset can be checked on normal distribution using the Anderson-Darling-test, Ryan-Joiner-test or Kolmogorov-Smirnov-test.[253]

Typical non-symmetrical data distributions are exponential distribution,[245,247] gamma distribution,[248] lognormal distribution[248,250] or Weibull distribution.[248,254] Probability density functions are

$$\text{exponential distribution}^{245,247}$$

$$f(x) = \begin{cases} \lambda e^{-\lambda x} & x \geq 0 \\ 0 & x < 0 \end{cases}$$

[25]

$$\text{gamma distribution}^{248}$$

$$f(x) = \begin{cases} \dfrac{b^p}{\Gamma(p)} x^{p-1} e^{-bx} & x > 0 \\ 0 & x \leq 0 \end{cases}$$

[26]

$$\text{lognormal distribution}^{248,250}$$

$$f(x) = \begin{cases} f(x) = \dfrac{1}{\sqrt{2\pi}\sigma x} e^{-\frac{(\ln(x)-\mu)^2}{2\sigma^2}} & x > 0 \\ 0 & x \leq 0 \end{cases}$$

[27]

$$\text{Weibull distribution}^{248,254}$$

$$f(x) = \begin{cases} \lambda \cdot k \cdot (\lambda \cdot x)^{k-1} e^{-(\lambda x)^k} & x > 0 \\ 0 & x \leq 0 \end{cases}$$

[28]

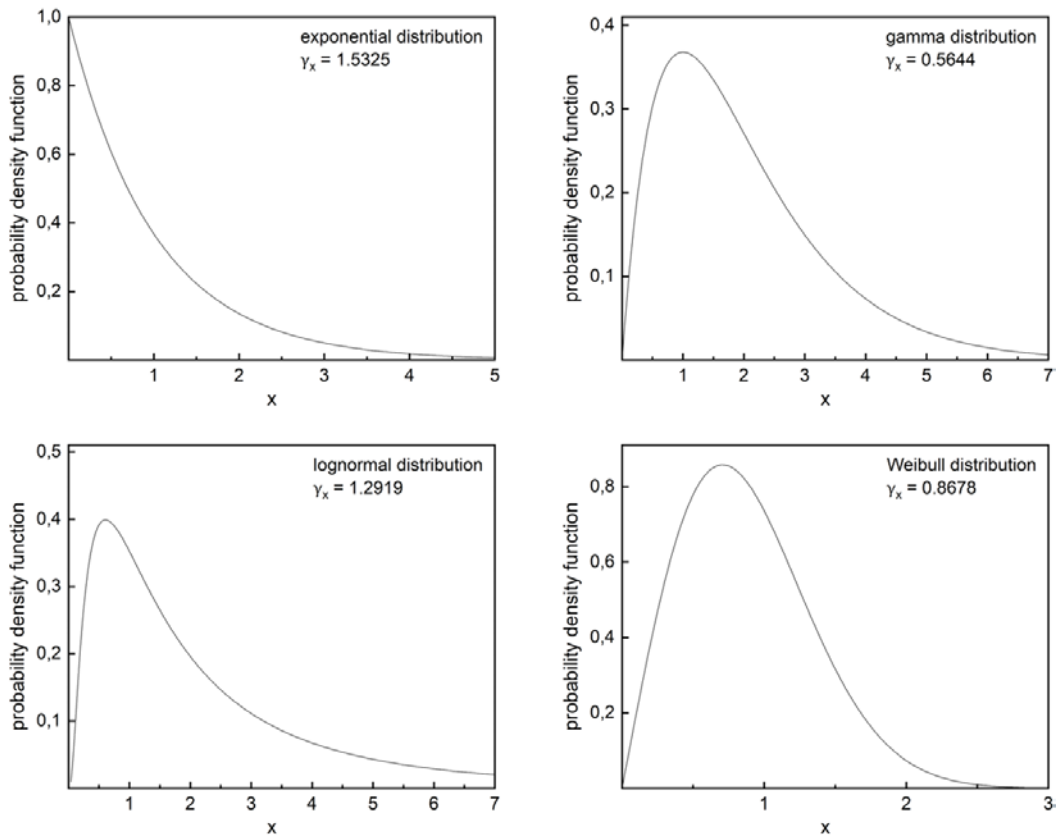These examples for non-symmetrical probability density functions are shown in Fig. 2.19.

Fig. 2.19: Probability density functions for non-symmetrical data distributions; exponential distribution [25] for $\lambda = 1$; gamma distribution [26] for $b = 1$ and $p = 2$; lognormal distribution [27] for $\mu = 0.5$ and $\sigma = 1$; Weibull distribution [28] for $\lambda = 1$ and $k = 2$.

Non-symmetrical data distribution is typically studied by separating left-skewness or right-skewness. A known approach for grading the skewness γ_x is[255]

$$\gamma_x = \frac{E\{(x - E\{x\})^3\}}{\sigma_x^3} \tag{29}$$

For symmetrical data distributions, the skewness γ_x is zero. Negative results for γ_x indicate left-skewness, i.e. datapoints are spread out more to the left of the mean than to the right, while positive results for γ_x indicate right-skewness.

A variety of well-established statistical analysis methods requires normally distributed datasets. For this purpose, non-normal or non-symmetrical distributed datasets are sometimes transformed by linear, logarithmic, or square-root transformation to get normal-distributed data.

Though, several analysis methods like t-test might simply get exchanged by similar analysis methods, valid for free-distributed datasets. The Wilcoxon rank sum test (or Mann-Whitney U-test), similar to a t-test, gives information on the Null hypothesis (H_0: $\mu_a - \mu_b >$ hypothesized value) to be rejected above a specific significance level like $p = 0.05$, though is still valid for non-normal distributed datasets and also for smaller data size (< 30 datapoints).[256] The Kruskal-Wallis test might be used in case of three or more subgroups.[256]

Important application of the non-symmetrical statistics theory within this thesis, is EIS analysis of LIB cells. More details will be given in chapter 5.6.

2.5 Lithium Ion Battery aging phenomena

2.5.1 Anodic and cathodic Solid Electrolyte Interphase

During initial charge/discharge cycles of Lithium Ion Batteries, electrochemical reactions between electrolyte and electrodes form passivation layers both on graphite anodes and layered oxide cathodes. Anodic potentials during lithiation of graphite form a highly reductive regime, which reduces both conductive salt anions as well as solvent molecules, until a covering layer of reaction products is formed, enclosing all active particles and thick enough to act as electronic insulator. This passivation mechanism was first described in 1979 by E. Peled et al. as the Solid Electrolyte Interphase for stabilization of alcaline metals in organic solvents.[143] The reduction reactions of solvent molecules, anions and electrolyte impurities occur competitive and form a very complex passivation layer. Despite extensive research activities on the SEI, there is still no complete model that fully describes structure, formation, and dynamics of the SEI during battery operation. Generally, the SEI is separated into inorganic and organic regime.[257]

During initial SEI formation, inorganic species like Li_2CO_3, Li_2O, LiF are concentrated close to the electrode/SEI interface, forming a thin and compact layer.[258–260] Common SEI precursors are chosen to support formation of this initial layer. Such precursors need to provide high standard electrode potential and high exchange current density for reduction, as given for AsF_6^- (conductive salt anion) or for CO_2. The latter can also be formed during the charging step after decomposition of liquid additives like VC or FEC.[65]

Subsequently, a more porous and structurally open layer of semicarbonate and polyolefine species is formed via solvent reduction and subsequent polymerisation.[258] SEI growth was shown to occur only at the SEI/electrolyte interface.[258] Tunneling of electrodes through preformed SEI layers as driving mechanism for further reduction reactions was calculated to stop latest at ≈ 10 Å.[258,261] Further propagation of the reduction mechanism is assumed to be driven by mobile radicalic species (Li radical atoms, VC radical anions, open-EC radical anions), that can diffuse through the SEI layer.[258]

Advanced studies suggested several modifications to this simple SEI structure model, like the polymer-electrolyte-interface model, the solid-polymer-layer model or the compact-stratified-model.[258,262] Most evidence was found for the microphase distribution model.[258,263,264] According to this model, Li^+ ions pass the SEI along lattice defects and vacancies during LIB operation, which preferrably occurs along grain boundaries orthogonal to the anode surface.[258] This Li^+ ion diffusion mechanism was identified as rate-determining-step for SEI kinetics in case of undamaged SEI on lithium metal anodes.[258]

Analogously to anodic SEI formation on lithium metal, carbonaceous or silicon-containing anodes, surface film formation phenomena were also suggested for layered oxide cathodes in 1985.[265] This phenomenon is known as cathodic SEI or CEI. In 2002, D. Aurbach et al. studied the increase of the capacity fade of $LiCoO_2$ cathodes upon cycling at elevated temperatures or in $LiPF_6$ rich electrolytes, and found a significant increase in cathode impedance driven by surface phenomena (formation of LiF, $ROCO_2Li$ and further organic species)

on the $LiCoO_2$ particles.[266] Similarly, A. Würsig et al. studied influences of electrolye conductive salts, solvents and additives on surface film formation on $LiCoO_2$, $LiNiO_2$ and $LiMn_2O_4$ upon polymerisation reactions and reported preferrable surface film formation in presence of $LiPF_6$ and VC.[267] Using advanced analysis techniques, the CEI was later characterized in detail to mainly contain inorganic species like Li_2CO_3, CH_2OCO_2Li or LiF from conductive salt decomposition and solvent decomposition, as well as organic species like poly(ethylene glycol), poly(ethylene glycol) dimethyl ether or poly(ethylene glycol) ethyl methyl ether from oligomerisation reactions of solvent decomposition products.[268]

2.5.2 Formation cycles

The initial charge/discharge cycles of a lithium ion cell are called formation cycles. Especially for liquid electrolyte cells including lithium metal, carbonaceous or silicon-based anodes, these cycles are crucial for overall capacity and aging, as the SEI is formed especially during the first charging step. Formation of a homogenous and stable SEI covering all anodic active material particles is ideally limited to the formation cycles, to minimize irreversible capacity losses upon immobilization of active lithium in the SEI. As this process essentially defines the subsequent battery capacity and aging performance, the formation cycles are typically performed by the battery manufacturer under controlled conditions.

A common way for achieving a stable SEI with minimized subsequent SEI growth, is cycling lithium ion cells at low C-rates for two formation cycles. If fully cycled within the total voltage limits of the cell, the formation process can also act as a precise tool for quality control and grading of cells in terms of nominal discharge capacity, charging efficiency and internal resistance. These characteristics can be used as basic cell information for commercial purpose.[184,269] Though, formation for several cycles at low C-rates is time-consumig and therefore an expensive part of battery production.[184] Several different approaches have been developed to reduce costs of the formation step, which are explained below.

Specialized formation protocols apply slow C-rates only within small voltage ranges, precisely addressing the reduction reactions of SEI precursors and SEI forming molecules, while shifting the formation voltage limits to a smaller voltage range, while accelerating C-rates in insensitive voltage regimes.[165,270] Further stablilisation of fast-formation protocols was also achieved by modifying external cell pressure and ambient temperature.[271] Pre-lithiation techniques were developed to reduce inevitable first cycle losses to energy density and specific energy of LIBs upon cathodic active lithium immobilization during SEI formation.[272] Chemical[273–276] or electrochemical[277,278] techniques as well as electrode additives[279–285] or inclusion of metallic lithium[286–291] were demonstrated as strategies for pre-lithiation. Significant research also addresses development of artificial SEI layers on anode particles, both for safety aspects and for reduction of capacity fade.[292–295]

2.5.3 NMC cathode aging mechanisms

Layered oxide cathode materials are sensitive to several aging processes during LIB operation. Soon after introducing transition metal oxide materials as cathode materials, presence of HF was found detrimental to capacity fading and unintended increase of the impedance of layered oxide cathodes.[266] In LIBs, HF was mainly found to form via decomposition of $LiPF_6$ under presence of H_2O.[296,297]

$$LiPF_6 \rightarrow LiF + PF_5 \tag{30}$$

$$PF_5 + H_2O \rightarrow 2HF + POF_3 \tag{31}$$

Based on the assumption of acidic corrosion of transition metal oxides by HF,[296] the corrosion mechanism of NMC 111 was proposed to follow a mechanism analogous to Hunter's reaction.[91,298,299]

$$
\begin{aligned}
2Li_{(1-x)}Ni_{1/3}Mn_{1/3}Co_{1/3}O_2 + 4(1-x)HF \\
\rightarrow (3x-1)Ni_{1/3}Mn_{1/3}Co_{1/3}O_2 + 2(1-x)H_2O \\
+ (1-x)MnF_2 + 2(1-x)LiF + 2(1-x)Ni_{1/2}Co_{1/2}O_2
\end{aligned} \tag{32}
$$
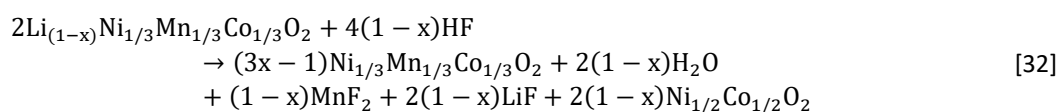
A second aging mechanism is immobilisation of active lithium in the anodic SEI, whereby cathode materials irreversibly loose active lithium.[300,301] Interatomic distances of transition metal oxide layers in the cathode crystal lattice of NMC were found to increase linearly in with delithiation (see chapter 2.2.1), which can be used as a direct measure for the residual lithium content in the crystal lattice.[91] Cathodic overpotentials during LIB operation were shown to arise from limited Li^+ transport kinetics within the cathodic active material particles.[92]

Increasing operation temperature and voltage ranges of graphite-NMC cells were shown to significantly accelerate cathode aging mechanisms.[88,93,94] Aging phenomena were found to arise from significant increase in impedance and polarisation of the cathode, which were assigned to structural changes of the cathode crystal lattices induced by considerable amount of oxygen release.[88] Cycling studies at elevated cutoff voltages by J. Kasnatscheew et al. revealed insignificant amount of transition metal dissolution, but substantial influence of kinetic limitations at layered oxide cathode material. Consequently, a lithiation/delithiation hindrance mechanism was suggested to drive this type of capacity fade.[93,94]

2.5.4 Graphite anode aging mechanisms

Several aging mechanisms, that limit performance and capacity of typical LIB anodes, have been studied in detail.

Processes that directly damage graphite if used as anode in LIBs were indentified soon after the introduction of initial LIB operating concepts. Detrimental effects arise if using pure PC as electrolyte solvent, as for its tendency for cointercalation between the graphene layers and therefore to induce graphite exfoliation.[148,166] Thus, appropriate choice of electrolyte solvents can minimize direct damage to graphite structures.[144,148,166] Anodic aging mechanisms present in current LIB systems typically arise from immobilization mechanisms of active lithium and consecutive reduction of the overall cell capacity.

Graphite anode inhomogeneities at different length scales were shown to induce significant overpotentials at common C-rates both at lithiation and delithiation step.[192] Increased overpotentials at local spots are problematic due to the possibility to locally undergo 0 V vs. Li/Li$^+$ in the lithiation step, followed by local dendritic deposition of metallic lithium (i.e. lithium plating), especially at low temperatures and high C-rates.[302,303] Similarly, local LiF rich fractions in the SEI were shown to accelerate lithium dendrite nucleation.[304] As long as the deposited lithium retains electronic contacts to the active material particle, such deposited lithium may get re-oxidized in the subsequent delithiation step (i.e. lithium stripping), resulting in no permanent loss of active lithium.[303] If plated lithium bursts through the SEI layer, metallic lithium consumes electrolyte to form a new Solid Electrolyte Interphase layer on the free lithium surface. If substantial amount of metallic lithium is deposited, parts exceeding the SEI forms kinks and might subsequently loose electronic contact to the active material particle, which results in irreversible loss for the system (formation of insulated lithium).[96,303] Both formation of SEI ontop of metallic lithium in addition to the graphitic SEI, as well as formation of insulated lithium fractions, substantially reduce the overall cell capacity.

Aside to SEI growth induced by metallic lithium, formation of cracks in the existing SEI will also induce SEI re-formation analogous to the SEI growth mechanisms described in chapter 2.5.1.[258] Cracks in the SEI might be formed upon gas release, or in case of significant volume changes of the anode materials during cycling.[258,305] Consequently, Si based anodes, which increase their particle volume up to 300 % during lithiation,[78] suffer severely from periodic SEI re-formation.[77,258] Deposition of transition metal ions like Ni^{2+}/Mn^{2+}/Co^{2+} species, released from the cathode lattice in presence of HF, were also shown to substantially increase capacity-fade via damaging the SEI and therefore inducing SEI growth in the latter charging steps.[91,296,306–309]

2.6   Surface modification techniques

LIBs have several surfaces and interfaces, that are known to influence the battery performance. The electrode-current collector interface is a critical bottleneck for the electron current, directly bound to quantity and electronic resistance of contact points. Volume changes of the electrodes during battery operation, upon crystal volume change between charged and discharged state, might induce contact losses at the electrode-current collector interface. This phenomenon is a crucial aging effect at long-term LIB operation, known as delamination. Delamination can be minimized by providing sufficient adhesion forces at the electrode-current collector interface.

Aside, anodic and cathodic charge-transfer reactions occur at the electrode-electrolyte interface and are therefore decisive parameters for battery kinetics and thermodynamics. Optimized charge-transfer characteristics are bound to optimal wetting of all electrode surfaces with sufficient electrolyte.

Finally, the diffusion of Li$^+$ through the electrolyte between anode and cathode is directly bound to electrolyte diffusion path lengths. Therefore, optimizing porosity and minimizing tortuosity both in anode, cathode and separator, are key parameters for optimal battery performance especially at accelerated C-rates.

In 2008, M. Gaberscek et al. reported the surface resistance of LFP cathodes to mainly depend on the electrode-current collector interface contacts.[225] Consequently, increasing the number of contact points between cathode and current collector by electrode calendering is frequently reported to significantly reduce surface resistances.[71,186] Increasing the surface roughness of the cathodic Al current collector was shown to reduce cathode surface resistances, and consequently to improve the C-rate stability upon reduced polarisation effects, as demonstrated for cathodes with low mass-loading based on NMC 111, LCO or NCA.[310–312]

The SurfaLIB research project (project number 03ET6103C, Federal Ministry for Economic Affairs and Energy, Germany) focused to several modification techniques either on current collectors or on electrode surfaces, aiming to improve the electrochemical performance of LIBs based on thick electrodes. Focus lay on preceding or in-line modification of current collectors, laser structuring or plasma-based etching of current collectors and electrodes, as well as plasma-based deposition of primer layers.

a)   Current collectors with modified topography

A possible transfer of the current collector surface enlargement strategy to anodes was studied in detail. Polarisation limitation, driven by electrode-current collector interface geometry, was identified as a minor limitation for graphite anodes, as shown in Fig. 2.20.[313,314]
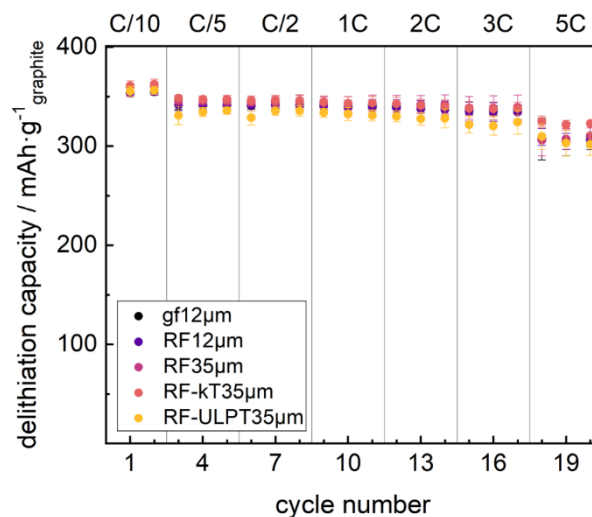
Fig. 2.20: Delithiation rate tests of graphite anode (≈ 2.0 mAh·cm⁻²) half-cells, comparing several Cu current collectors with varied surface roughness; reproduced from SurfaLIB report 2018-I/SurfaLIB final report.[313,314]

As discussed in section 2.3.2, major influences on the C-rate performance of graphite anodes arise from diffusion limitations of Li$^+$ in the electrolyte within the electrode pores.[192] Consequently, production aspects such as drying conditions, are superior key parameters for graphite anode performance.[120,121,193,194] Studies as part of the SurfaLIB project demonstrated the laser structuring of electrodes as a valid tool for improving C-rate performance of graphite anodes, upon accelerating Li$^+$ diffusion within optimized pore structures.[315] These findings correlate well to reports of W. Pfleging and co-workers on effects of laser structuring on the performance of thick-film electrodes in LIBs.[316–324]

b)　Plasma-based primer layers

Introducing primer layers on the current collector as additional layer beneath the electrode coating, is a valid strategy both to improve adhesive forces,[325] as well as to prevent corrosive side reactions that could damage the current collector.[325,326] To minimize resistances of the additional layer, primer layers are typically prepared as thin as possible, and composed of binder and carbon conductive agent,[325–330] or of conducting polymers.[325,331]

Despite the assumption, that introduction of an additional interlayer between electrode and current collector should naturally give an additional resistance upon limited conductivity, carbon coatings on aluminum have been demonstrated to reduce overall contact resistances[330] and improve the rate capability of cathodes,[329] and even minimize the necessity of conductive additives in cathode layers close to zero.[327] Based on Raman-studies of carbon coatings on current collectors and LFP particles, P. Swain et al. identified sp^2-bonded carbon species to significantly improve electrochemical properties, while sp^3-type carbon species induce large polarization effects.[332]

The SurfaLIB project studies focused on plasma-based application of carbon coatings to act as primer layers, which was successfully demonstrated to improve the rate capability both of graphite anodes and NMC 111 cathodes, as shown in Fig. 2.21.[314,333,334]
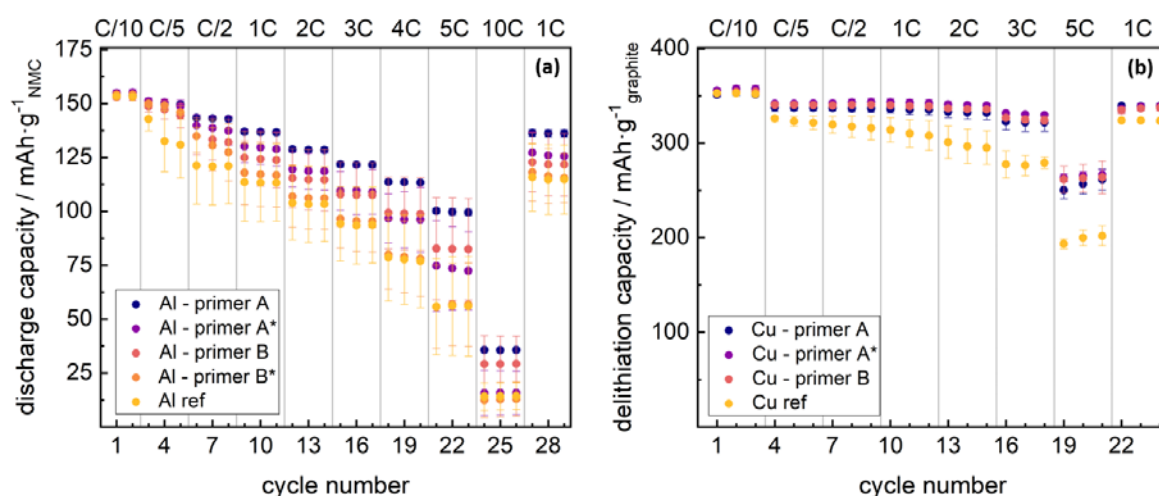
Fig. 2.21: Influence of plasma-based primer layers (acetylene precursor) on rate capability of Li ion electrodes, comparing thin primer layer (A), thin primer layer on pre-activated metal substrate (A*), thick primer layer (B), thick primer layer on pre-activated metal substrate (B*) and pristine current collector (Ref); (a) discharge rate tests of NMC 111 cathodes (≈ 1.8 mAh·cm⁻²) coated on Al; (b) delithiation rate tests of graphite anodes (≈ 2.3 mAh·cm⁻²) coated on Cu; reproduced from SurfaLIB report 2018-II / SurfaLIB final report with permission of J. Schubert.[314,333,334]

c)   Plasma-etching of current collectors and electrodes

Plasma processes are well-established in the production of LIBs.[335] Plasma spraying is frequently used for production of nano-sized active materials, such as layered oxide,[335,336] spinel type[335,337] or olivine type cathode materials,[335,338] or for production of binder-free electrode coatings.[335,338] Plasma techniques are also a well-known approach for preparation of carbon coatings on cathode particles for increase of their electronic conductivity.[335,339,340] Plasma-based techniques enable production of silicon nanoparticles,[335,341,342] silicon nanowires[343] or carbon coated silicon (core-shell) particles[335,344] for application as high capacity anode materials.

Plasma-based etching of polymeric structures can significantly increase its hydrophilicity, which is frequently used to improve electrolyte uptake characteristics of LIB separators,[335,345,346] or for production of composite separators by introducing metal oxide coatings (SiO_2, TiO_2, Al_2O_3) on polymeric matrices.[335,347–349]

Studies of the SurfaLIB project successfully demonstrated a temporary increase of the hydrophilicity of NMC 111 cathodes and graphite anodes upon etching with N_2 plasma. Arising from a limited time slot for the processability of single-cells comprising plasma-etched electrodes, several production strategies upon plasma-etching under normal atmosphere were compared in Fig. 2.22.[350]
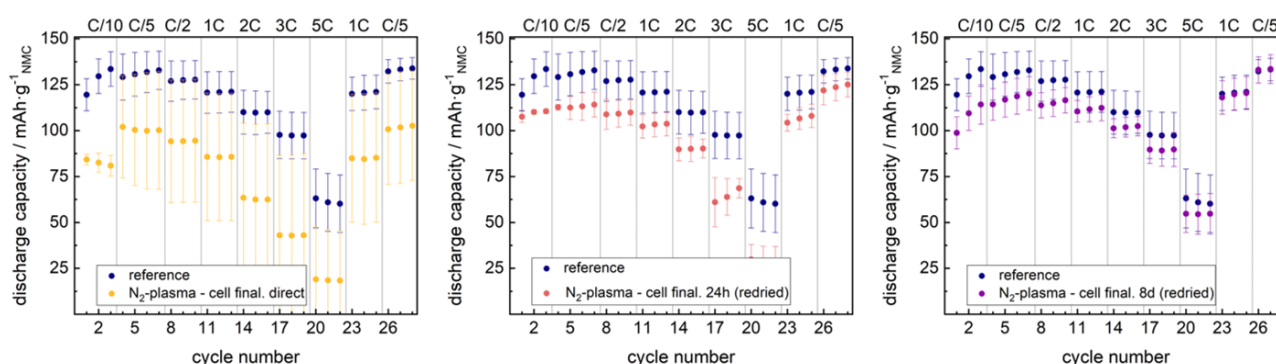
Fig. 2.22: Discharge rate tests of graphite (≈ 2.2 mAh·cm^{-2}) – NMC 111 (≈ 1.7 mAh·cm^{-2}) single cells comparing various time intervals between plasma-etching of electrodes and electrolyte filling; reproduced from SurfaLIB report 2019-II / SurfaLIB final report.[314,350]

Plasma-etching of separators was successfully demonstrated to increase ionic mobility of lithium ions and therefore to increase the rate capability of LIBs.[335,345,346] In contrast, the SurfaLIB project identified plasma-etching of lithium ion electrodes under normal atmosphere to reduce the discharge rate capability of graphite-NMC 111 cells upon significant H_2O uptake during air contact. Partial reversibility of the H_2O uptake influence was demonstrated by additional drying steps, while extended time separation between plasma-etching and electrolyte filling retired the electrochemical performance close to unpersuaded reference cells.

In total, the SurfaLIB project identified two processes to have most positive effects on the C-rate stability of graphite–NMC 111 single cells, which were laser structuring of graphite anodes and introduction of primer layers at any electrode – current collector interface. Modifying porosity and tortuosity of graphite anodes for reduction of Li$^+$ diffusion path lengths was shown to significantly reduce internal resistances and improve C-rate stability.[351] Aside, reduced transport limitations were demonstrated to lower the risk of Lithium plating, resulting in reduced capacity fade of graphite–NMC 111 cells.[351]

So, improving contacts at electrode – current collector interface, as well as anode porosity changes were found as a main influencing factor for C-rate capability of graphite–NMC 111 cells.

Lamination is a well-known manufacturing technique, capable both to improve interface contacts at electrode-current collector interface, as well as to modify porosities at electrode-separator interfaces. Findings of the SurfaLIB project predict significant influence of both lamination effects to electrochemistry of LIBs, even though this has never been subject to any scientific study previous to this thesis. For this reason, this thesis was developed to focus on the lamination technique as an expansion to surface modification studies beyond SurfaLIB studies.

3   Materials and Methods

3.1   Chemicals and devices

All chemicals used for PhD studies are listed in Tab. 3.1.

Tab. 3.1: List of used chemicals.

solids		
$LiNi_{1/3}Mn_{1/3}Co_{1/3}O_2$	NM-3102h	BASF TODA America, USA
graphite	MAGE3	HITACHI CHEMICAL, Japan
graphite	KS6L	IMERYS, Switzerland
graphite	SFG6L	IMERYS, Switzerland
carbon black	Super C65	IMERYS, Switzerland
polyvinylidene difluoride	Solef® 5130	SOLVAY, Italy
lithium	Li-foil 0.4 mm	GELON LIB, China
liquids		
N-methyl-pyrrolidone	N-methyl-pyrrolidone	Overlack, Germany
1M $LiPF_6$ in EC:EMC 3:7	Selectilyte LP57	BASF, USA
vinylene carbonate	Vinylene Carbonate E	BASF, USA
gases		
Argon	Argon 5.0	Westfalen, Germany

LP572 electrolyte was prepared by mixing LP57 electrolyte and vinylene carbonate in a mass ratio of 98/2 within an argon filled glovebox (MB20, H_2O and O_2 content < 0.1 ppm, MBraun, Germany).

3.2   Electrode preparation

Studies presented in this work were based on discontinous mixing within a kneader (TX-2, INOUE, Japan) both for anode and cathode slurries.

To ensure high comparability of electrodes and single cells within specific studies, large batches of electrode slurry with unique preparation characteristics were subsequently used for coating a maximum length of single sided electrode with comparable thickness, composition and microstructure. Compositions of any electrode batch used for PhD studies, are shown in Tab. 3.2.

Tab. 3.2: Compositon of electrodes.

component	function	solids percentage	overall percentage	mass [g]
NMC cathode #1				
NM3102-h	active material	93 %	55.8 %	558.0
Solef® 5130	binder	3 %	1.80 %	18.00
Super C65	conductive additive	3 %	1.80 %	18.00
KS6L	conductive additive	1 %	0.60 %	6.00
N-methyl-pyrrolidone	solvent	--	40.0 %	400.0
NMC cathode #2				
NM3102-h	active material	93 %	55.8 %	669.6
Solef® 5130	binder	3 %	1.80 %	21.60
Super C65	conductive additive	3 %	1.80 %	21.60
KS6L	conductive additive	1 %	0.60 %	7.20
N-methyl-pyrrolidone	solvent	--	40.0 %	480.3
graphite anode #1				
MAGE3	active material	90 %	45.0 %	421.2
Solef® 5130	binder	7 %	3.50 %	32.76
Super C65	conductive additive	2 %	1.00 %	9.36
SFG6L	conductive additive	1 %	0.50 %	4.68
N-methyl-pyrrolidone	solvent	--	50.0 %	468.1
graphite anode #2				
MAGE3	active material	90 %	41.4 %	345.6
Solef® 5130	binder	7 %	3.22 %	26.88
Super C65	conductive additive	2 %	0.92 %	7.68
SFG6L	conductive additive	1 %	0.46 %	3.84
N-methyl-pyrrolidone	solvent	--	54.0 %	450.8

Electrode slurries were prepared in a kneader (see Fig. 2.5), using sequences as shown in Tab. 3.3.

Tab. 3.3: Electrode slurry preparation sequences.

NMC cathode #1

step	solvent in batch	momentary solid content	kneader speed	temp.	duration
premixing	0.0 g	100 %	22.4 rpm	50 °C	10 min
premixing	40.0 g	94 %	22.4 rpm	50 °C	20 min
kneading	100.0 g	86 %	42.7 rpm	50 °C	60 min
kneading	200.0 g	75 %	63.0 rpm	50 °C	20 min
dilution	280.0 g	68 %	90.0 rpm	28 °C	60 min
dilution	400.0 g	60 %	90.0 rpm	20 °C	90 min
degassing – 150 mbar	400.0 g	60 %	22.4 rpm	20 °C	15 min

NMC cathode #2

step	solvent in batch	momentary solid content	kneader speed	temp.	duration
premixing	0.0 g	100 %	22.4 rpm	50 °C	55 min
premixing	56.1 g	93 %	22.4 rpm	50 °C	15 min
kneading	127.5 g	85 %	42.7 rpm	50 °C	40 min
kneading	222.4 g	76 %	63.0 rpm	50 °C	70 min
dilution	344.8 g	68 %	90.0 rpm	28 °C	30 min
dilution	480.3 g	60 %	90.0 rpm	20 °C	30 min
degassing – 150 mbar	480.3 g	60 %	22.4 rpm	20 °C	15 min

graphite anode #1

step	solvent in batch	momentary solid content	kneader speed	temp.	duration
premixing	0.0 g	100 %	22.4 rpm	50 °C	20 min
premixing	104.4 g	82 %	22.4 rpm	50 °C	15 min
kneading	182.2 g	72 %	42.7 rpm	50 °C	40 min
kneading	231.4 g	67 %	63.0 rpm	50 °C	100 min
dilution	336.3 g	58 %	90.0 rpm	28 °C	30 min
dilution	434.3 g	52 %	90.0 rpm	20 °C	15 min
dilution	468.1 g	50 %	90.0 rpm	20 °C	15 min
degassing – 150 mbar	468.1 g	50 %	22.4 rpm	20 °C	15 min

graphite anode #2

step	solvent in batch	momentary solid content	kneader speed	temp.	duration
premixing	0.0 g	100 %	22.4 rpm	50 °C	40 min
premixing	102.5 g	79 %	22.4 rpm	50 °C	10 min
kneading	158.0 g	71 %	42.7 rpm	50 °C	45 min
kneading	203.5 g	65 %	63.0 rpm	50 °C	100 min
dilution	301.7 g	56 %	90.0 rpm	28 °C	70 min
dilution	416.0 g	48 %	90.0 rpm	20 °C	20 min
dilution	450.8 g	46 %	90.0 rpm	20 °C	20 min
degassing – 150 mbar	450.8 g	46 %	22.4 rpm	20 °C	15 min

Slurry rheologies were determined by viscosimetry (DV3T, AMETEK Brookfield, Germany). Electrodes were coated roll-to-roll using doctor-blade coating and a two-step drying tunnel (see Fig. 2.6). Retention time of electrode coatings within the drying tunnel was ≈ 3 min. Al foil (Al 20 µm, GELON LIB, China) and Cu foil (Cu 15 µm, GELON LIB, China) were used as current collectors for NMC cathodes and graphite anodes, respectively. Chosen coating parameters are shown in Tab. 3.4.

Tab. 3.4: Electrode coating parameters.

electrode	slurry viscosity	gap	coating speed	drying tunnel temp. 1	drying tunnel temp. 2
NMC cathode #1	2213 mPa·s	100 µm	6.3 mm·s^{-1}	135 °C	150°C
NMC cathode #2	1692 mPa·s	140 µm	6.3 mm·s^{-1}	135 °C	150°C
graphite anode #1	18650 mPa·s	90 µm	4.0 mm·s^{-1}	135 °C	150°C
graphite anode #2	5320 mPa·s	135 µm	6.3 mm·s^{-1}	135 °C	150°C

3.3   Cell assembly

a)   Half-cell assembly

For half-cell measurements, electrodes were punched into circular disks of 10 mm diameter and dried at 110 °C under vacuum for 12 h. Half-cell electrode masses were detected using a high-resolution balance (MS105DU, Mettler-Toledo via Waagen-Service Schiefke, Germany). Half-cell measurements were carried out in three electrode geometry using a Swagelok type T-cell setup, assembled in an Argon filled glovebox. Lithium metal was used as reference and counter electrode. A glass fiber filter (grade 691, VWR-Avantor, USA) was used as separator. LP57 was used as electrolyte for NMC half-cell measurements, while LP572 electrolyte was used for graphite half-cell measurements. Half-cells were kept at room temperature over night before starting the electrochemical characterization.

Half-cell measurements were performed for each electrode used in publications (further details in Tab. 3.5). For each electrode, at least three half-cell measurements were performed to verify achievable capacities to correspond to supplier information on the processed active materials. Details shown in Fig. 3.1 and Fig. 3.2.
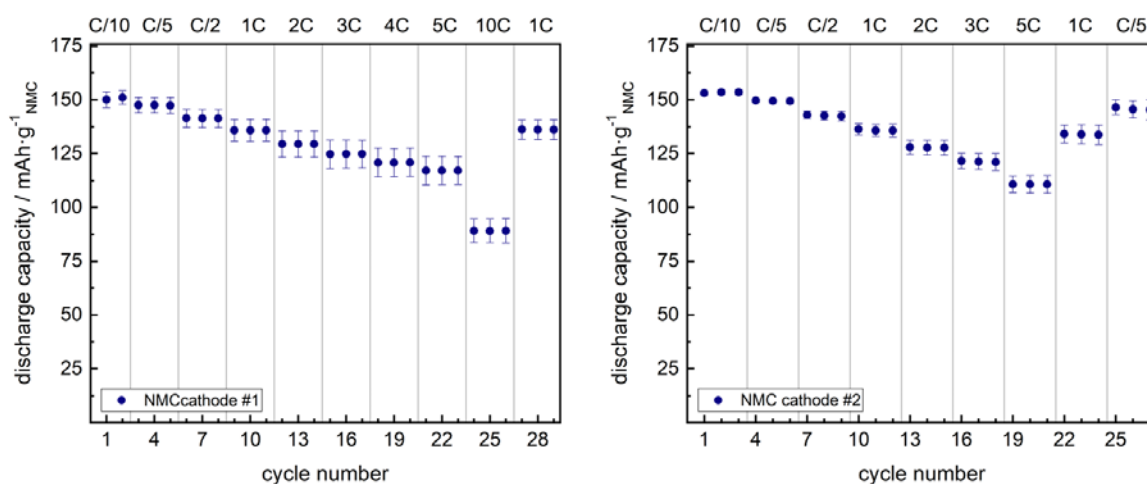
Fig. 3.1: Discharge capacities of PhD reference NMC cathodes (≈ 1.2 mAh·cm^{-2} and ≈ 1.3 mAh·cm^{-2}) in T-cell geometry during discharge rate test.
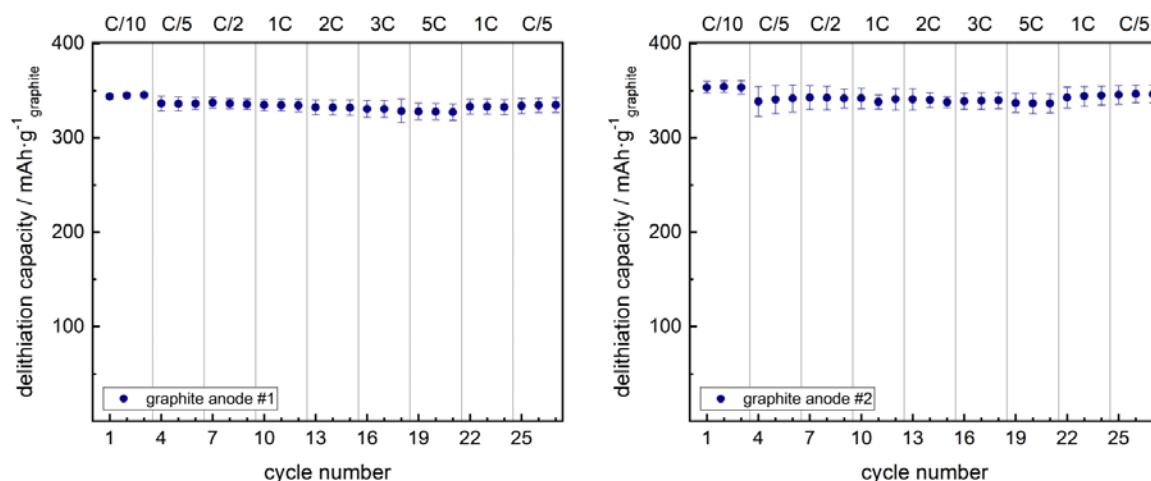
Fig. 3.2: Delithiation capacities of PhD reference graphite anodes ($\approx$ 1.3 mAh·cm^{-2} and $\approx$ 1.6 mAh·cm^{-2}) in T-cell geometry during delithiation rate test.

b)   Full cell assembly

For full cell preparation, cathodes and anodes were punched into sheets of 5 × 8 cm^2 and 5.4 × 8.4 cm^2, respectively, containing contact strips. Using separator sheets (5.8 × 8.8 cm^2), single cells were prepared by stacking anode-separator-cathode to form non-laminated, half-laminated or fully laminated stacks.

Full cell electrode masses were detected using a high-resolution balance (PH103S, Mettler-Toledo via Waagen-Service Schiefke, Germany). Punched anodes and cathodes were selected to provide highly comparable active material (AM) mass loadings and highly comparable balancing factors (areal capacity loading anode / areal capacity loading cathode) along performed studies. Details are presented in Tab. 3.5.

Tab. 3.5: Mass loadings and balancing factors of single cells.

research study [DOI]	anode AM mass [mg·cm^{-2}]	cathode AM mass [mg·cm^{-2}]	anode capacity [mAh·cm^{-2}]	cathode capacity [mAh·cm^{-2}]	anode/cathode balancing factor
10.1016/j.jelechem.2019.02.030	3.42 ± 0.16	6.72 ± 0.25	1.27 ± 0.06	1.13 ± 0.04	112.8 % ± 3.6 %
10.3390/batteries5040071	4.20 ± 0.23	8.38 ± 0.47	1.51 ± 0.08	1.30 ± 0.07	116.5 % ± 0.7 %
10.3390/batteries6020021	4.35 ± 0.13	8.68 ± 0.23	1.57 ± 0.05	1.35 ± 0.04	116.5 % ± 0.6 %

Lamination of stacks was performed using a lamination machine (BLE 282 D, MANZ Italy – former ARCOTRONICS Italia S.p.A., Italy) at the roll speed of 1.38 m·min^{-1}, at a line force of 157 N·cm^{-1} and a heating profile of 110 °C – 110 °C – 120 °C, with no fixed gap between the compressing steel-belts. Electrode-separator stacks were sandwiched within heat-resistant paper during the lamination step.

For preparation of partially laminated stacks, anode or cathode which should not get laminated were temporarily replaced by punched copper and aluminum sheets (for publication *Laminated Lithium Ion Batteries with improved fast charging capability* – see chapter 4) or by siliconized PET foil (for publication *EIS Study on the Electrode-Separator Interface Lamination* – see chapter 5) during lamination step.

After addition of Ni tabs and Al tabs (Al&Ni tabs, Gᴇʟᴏɴ Lɪʙ, China) to anode and cathode contact strips by ultrasonic welding, laminated/partially laminated/non-laminated single cells were housed in multilayer pouch foil (Laminate Al Pouch Film, Automotive Grade, Sʜᴏᴡᴀ Dᴇɴᴋᴏ Aᴍᴇʀɪᴄᴀ, USA) and dried under under vacuum at 110 °C for at least 12 h. An amount of 1500 µl of LP572 electrolyte was filled into each cell within an argon filled glovebox and sealed under vacuum. Electrolyte filled pouch cells were initially tempered at 60 °C for 60 min and kept at room temperature over night before starting any electrochemical characterization. The assembly route is indicated in Fig. 3.3.
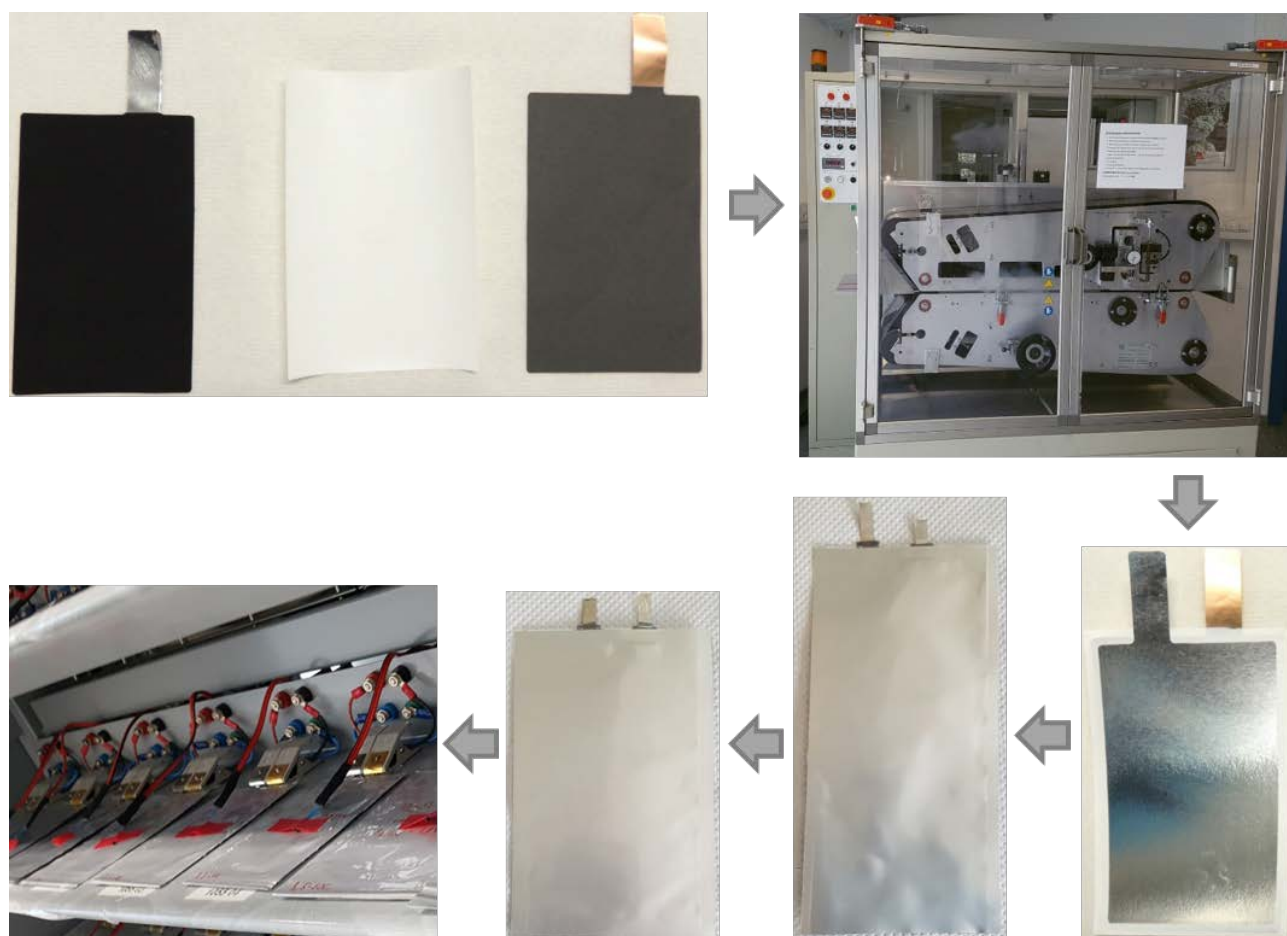
Fig. 3.3: Assembly route for laminated single cells.

To study the effect of additional cell compression, gravimetric force was applied to some cells by compressing each pouch cell stack with a weight of ~ 2.5 kg on top, while a polystyrol plate in between ensured homogeneous force distribution all over the active single cell area.

In total, 50 single cells were analyzed for 10.1016/j.jelechem.2019.02.030, while 21 single cells were analyzed for 10.3390/batteries5040071 and 111 single cells for 10.3390/batteries6020021.

3.4   Analysis techniques

Basic analysis of electrodes or cells prepared for scientific studies in this thesis, was realized by power tests for quantification of electrode kinetics/cell kinetics and lifetime tests for quantification of aging effects. Advanced insights in limiting aging phenomena were achieved using Electrochemical Impedance Spectroscopy and Neutron Depth Profiling. Valid analysis of single cell impedance measurements required fundamental understanding of non-symmetrical data statistics (more details in chapter 2.4.5).

3.4.1 Charge/discharge cycling – Powertest & Lifetime test

In the studies presented in this thesis, lifetime tests and power tests were performed on battery test systems (CTS-LAB, BaSyTec, Germany) using the provided control software (BaSyTest_V6.1.10.2, BaSyTec, Germany) for customized test procedures. The general charge/discharge structure as described in chapter 2.4.1 was implemented using a subroutine (see Fig. 3.4) within the final test routines (see Fig. 3.5 and Fig. 3.6).
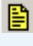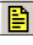
	Level	Label	Command	Parameter	Termination	Action	Registration	Comment
1			Start					U>1UBatMax&t>1s U<1UBatMin&t>1s I>1IBatMax&t>1s I<1IBatMin&t>1s
2			Cycle-start					
3			Charge	I=I_L1	U>Umax t>t_L1		U=5mV	Constant Current Charging
4			Charge	U=Umax	I<I_L2 t>t_L2		I=0.05mA	Constant Voltage Charging
5			pause		t>600s		t=10s	Relaxation
6			Discharge	I=I_E1	U<Umin t>t_E1		U=5mV	Constant Current Discharging
7			pause		t>600s		t=10s	Relaxation
8			Cycle-end	Count=Zyklen				
9			Stop					

Fig. 3.4: BaSyTest subroutine for cycling in CCCV charging/CC discharging mode.

For all full cell measurements, the voltage ranges were adjusted to 3.0 V – 4.2 V, while for NMC and graphite half-cell measurements the voltage ranges were adjusted to 3.0 V – 4.3 V and 0.02 V – 1.5 V, respectively. CV charging steps were continued until the charging current dropped below 0.05 C-rate.

For half-cell experiments, C-rate currents were calculated to fit to the theoretical capacity of the respective active material weight within each sample, using specific capacities for each processed active material as given by the supplier.

For the full cell experiments of 10.1016/j.jelechem.2019.02.030 and 10.3390/batteries5040071, formation was done by applying two cycles at 0.1 C-rate, calculated from NMC weight and specific NMC capacity as given by the supplier. The discharge capacity of the second formation cycle was chosen to act as nominal capacity for each cell. For further cycling processes, C-rates were calculated according to the measured nominal capacity of each cell.

While performing studies for 10.3390/batteries6020021, formation was done by applying two cycles at the respective C-rate of interest. Within this series, C-rate currents during formation and in any subsequent cycles, were calculated from NMC weight and specific NMC capacity as given by the supplier.

Using the subroutine shown in Fig. 3.4, test routines for full cells were prepared to outrun customized lifetime tests and power tests. Examplary protocols are shown in Fig. 3.5 and Fig. 3.6.
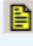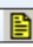
	Level	Label	Command	Parameter	Termination	Action	Registration	Comment
1			Start		T1>45°C		FirstPoint=1ms	U>1UBatMax&t>1s U<1UBatMin&t>1s I>1IBatMax&t>1s I<1IBatMin&t>1s
2			pause		t>12h		t=1min	electrolyte wetting period
3			@UP2018_VZ_NMC_Graphit_V1_0	Umax=4.2V Umin=3.0V I_L1=0.1CA t_L1=14h I_L2=0.05CA t_L2=3h I_E1=0.1CA t_E1=12h Zyklen=1				0.1C Formation cycle 1
4			@UP2018_VZ_NMC_Graphit_V1_0	Umax=4.2V Umin=3.0V I_L1=0.1CA t_L1=12h I_L2=0.05CA t_L2=3h I_E1=0.1CA t_E1=12h Zyklen=1				0.1C Formation cycle 2
5			@UP2018_VZ_NMC_Graphit_V1_0	Umax=4.2V Umin=3.0V I_L1=1CA t_L1=1.2h I_L2=0.05CA t_L2=3h I_E1=1CA t_E1=1.2h Zyklen=498				1C cycling
6			Charge	I=1CA	U>3.7V t>1h		U=5mV	final charge SOC20
7			Stop					

Fig. 3.5: Exemplary BaSyTest lifetime test routine – long-term cycling at 1 C-rate; 0.1 C formation included.
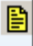
	Level	Label	Command	Parameter	Termination	Action	Registration	Comment
1			Start		T1>45°C		FirstPoint=1ms	U>1UBatMax&t>1s U<1UBatMin&t>1s I>1IBatMax&t>1s I<1IBatMin&t>1s
2			pause		t>60min		t=30s	temperature relaxation period
3			@UP2017_VZ_NMC_Graphit_V1_1	Umax=4.2V Umin=3.0V I_L1=0.2CA t_L1=6h I_L2=0.1CA t_L2=3h I_E1=0.2CA t_E1=6h Zyklen=4				0.2C Charge 0.2C Discharge
4			@UP2017_VZ_NMC_Graphit_V1_1	Umax=4.2V Umin=3.0V I_L1=0.2CA t_L1=6h I_L2=0.1CA t_L2=3h I_E1=0.5CA t_E1=2.4h Zyklen=3				0.2C Charge 0.5C Discharge
5			@UP2017_VZ_NMC_Graphit_V1_1	Umax=4.2V Umin=3.0V I_L1=0.2CA t_L1=6h I_L2=0.1CA t_L2=3h I_E1=1CA t_E1=1.2h Zyklen=3				0.2C Charge 1C Discharge
6			@UP2017_VZ_NMC_Graphit_V1_1	Umax=4.2V Umin=3.0V I_L1=0.2CA t_L1=6h I_L2=0.1CA t_L2=3h I_E1=2CA t_E1=0.6h Zyklen=3				0.2C Charge 2C Discharge
7			@UP2017_VZ_NMC_Graphit_V1_1	Umax=4.2V Umin=3.0V I_L1=0.2CA t_L1=6h I_L2=0.1CA t_L2=3h I_E1=3CA t_E1=24min Zyklen=3				0.2C Charge 3C Discharge
8			@UP2017_VZ_NMC_Graphit_V1_1	Umax=4.2V Umin=3.0V I_L1=0.2CA t_L1=6h I_L2=0.1CA t_L2=3h I_E1=5CA t_E1=0.24h Zyklen=3				0.2C Charge 5C Discharge

Fig. 3.6: Excerpt of exemplary BaSyTest power test routine – discharge rate test and charging rate test separated; formation step excluded.

3.4.2 Electrochemical impedance spectroscopy

In this work, PEIS measurements were carried out at 25 °C in a temperature chamber (± 1 °C, INCU-Line® IL 68R, VWR, Germany) with a potentiostat (PGSTAT204, Metrohm Autolab, Germany), using frequency ranges of 50 kHz – 10 mHz (10.1016/j.jelechem.2019.02.030 and 10.3390/batteries6020021) or 100 kHz – 10 mHz (10.3390/batteries5040071) and sinusoidal potential excitation with an amplitude of 10 mV$_{rms}$.
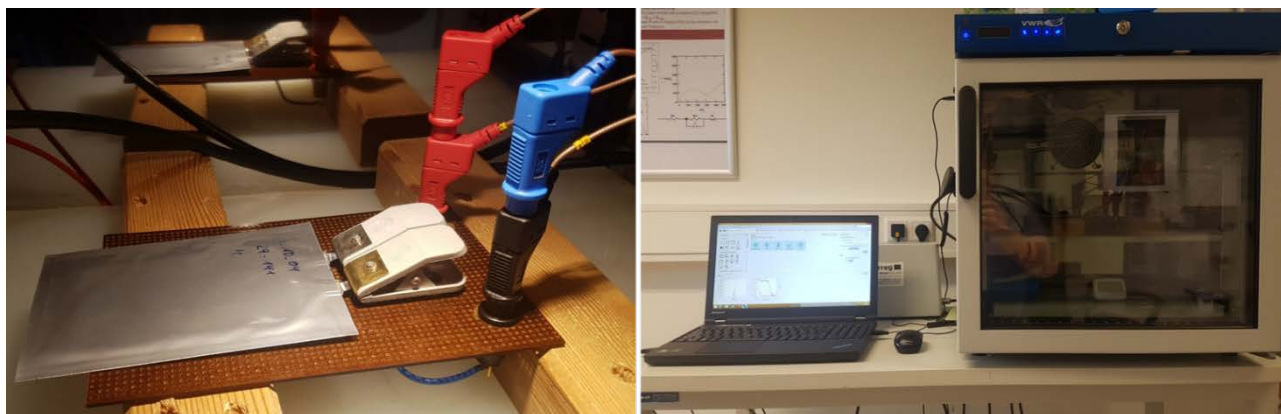
Fig. 3.7: EIS analysis setup.

EIS measurements were performed by charging the cells up to the respective cutoff voltage, followed by a controlled relaxation period of 2 h in open circuit voltage previous to each EIS measurement. Data fitting was performed using Z-fit as implemented in the BT-Lab software (BT-Lab V1.55, BioLogic SAS via Gᴀᴍᴇᴄ, Germany).

3.4.3 Porosity analysis

Porosities of separators and electrode layers were assumed by comparing their real volume with the minimal component volume given by the sample weight, extrapolating the theoretical densities of any raw components.

$$porosity = \frac{V_{\text{pores}}}{V_{\text{real}}} = \frac{V_{\text{real}} - V_{\text{components,minimal}}}{V_{\text{real}}} \qquad [33]$$

3.4.4 Scanning electron microscopy

Non-laminated single cell components were prepared for cross-section images with a handheld punch (clearance 4 µm, Nᴏɢᴀᴍɪ, Japan). Argon ion cutting on the fully laminated electrode-separator stack (EM TIC 3X, Leica, Germany) was performed by research partners at the Institute for Applied Materials – Energy Storage Systems (IAM-ESS) of the Karlruhe Institute of Technology (KIT), Karlsruhe, Germany. A Field-Emission Scanning Electron Microscope (Merlin Compact, Zeiss, Germany) with Energy Dispersive X-ray spectroscopy (EDX) was used to take cross-section images and EDX element mapping images of a single cell stack in laminated or non-laminated state.

3.4.5 Neutron analysis

For this work, fully delithiated graphite anodes were analysed post-mortem using NDP (see Fig. 3.8). Cells were opened and disassembled in an argon filled glovebox. For laminated stacks, the cathode was pulled off the anode-separator stack, while for non-laminated stacks, the graphite anode was extracted directly. All extracted anode/anode-separator samples were rinsed using EMC and dried subsequently under argon atmosphere to remove any lithium containing electrolyte residuals. For NDP measurements, circular samples with a diameter of 14 mm were punched out from the central parts of the anode sheets. The anode/anode-separator samples were studied with research partners at the N4DP setup at the PGAA facility of the Heinz Maier-Leibnitz Zentrum in Garching, Germany.
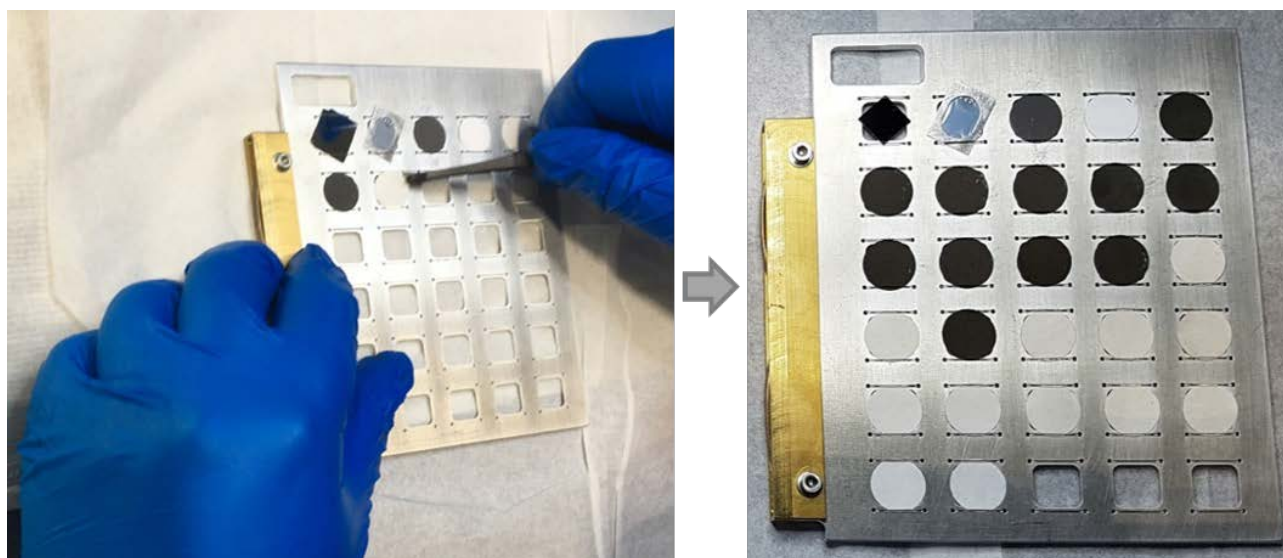
Fig. 3.8: Mounting of NDP samples in the NDP multiple sample holder.

NDP measurements were carried out at the FRMII neutron source of the Heinz Maier-Leibnitz Zentrum, using the Neutron-based four-Dimensional Profiling (N4DP) – Prompt Gamma-Ray Activation Analysis (PGAA) instrument (see Fig. 3.9). Details on the specialized NDP setup and the specialized electrode sample holder were described in literature.[243,352]

The anode/anode-separator samples were assembled in a vacuum chamber (10^{-5} mbar) facing the collimated cold neutron beam (12.6 mm^2, 3×10^9 n·cm^{-2}·s^{-1}) at an angle of 45 °. The cold neutron beam was adjusted to hit central parts of the anode/anode-separator samples; each sample was measured individually for 15 min. A nominal 7.5 µm thick Kapton® separation foil (DuPont, USA) was used to suppress signals from ^{4}He particles of the ^{6}Li(n,^{3}H)^{4}He reaction.
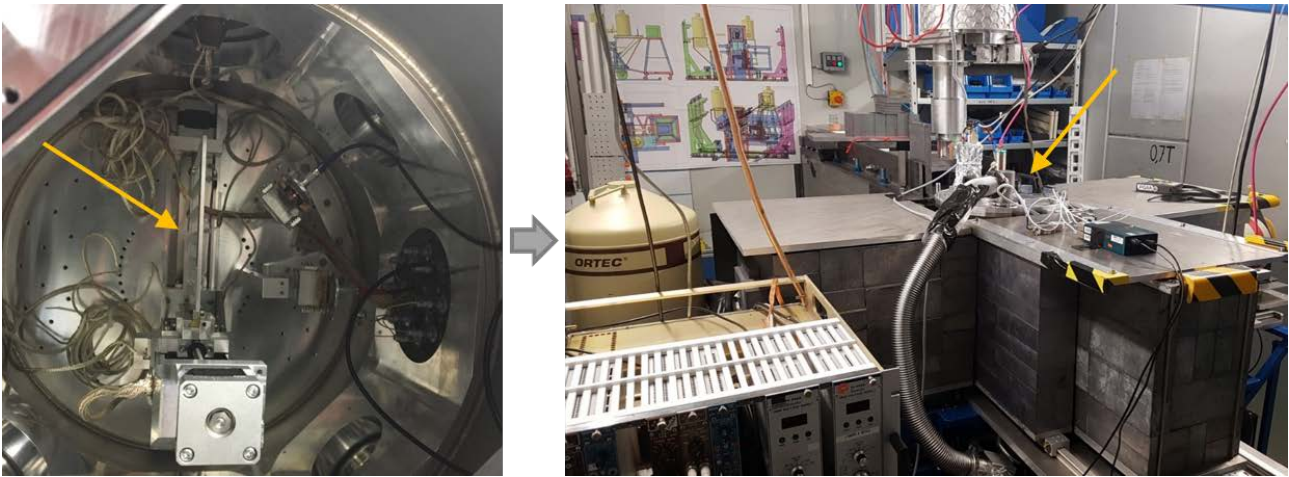
Fig. 3.9: Position of the NDP multiple sample holder in the N4DP-PGAA facility at the FRMII neutron source of MLZ.

4 Laminated Lithium Ion Batteries with improved fast charging capability

The article entitled *Laminated Lithium Ion Batteries with improved fast charging capability* by Martin Frankenberger, Madhav Singh, Alexander Dinter, Sebastian Jankowksy, Alexander Schmidt and Karl-Heinz Pettinger, published in the *Journal of Electroanalytical Chemistry*, 2019, Volume 837, Pages 151 – 158, is presented in this section.[73] This is a subscription article reprinted with permission of Elsevier. Copyright © 2019. (permanent weblink: https://doi.org/10.1016/j.jelechem.2019.02.030).

This study gives comprehensive insights in microstructural, morphological, and electrochemical effects on Lithium Ion Batteries, arising from the electrode-separator lamination technique. Application of the technique was demonstrated to significantly reduce the overall pore volume of the cathode-separator-anode compound, while maintaining interface diffusion channels. By surface adaption at microlevel, the separator links into anode and cathode surface, which reduces interface resistances of graphite-NMC 111 single cells. Simultaneous lamination at both interfaces was found beneficial to the C-rate stability of graphite-NMC 111 single cells, up to a level of replacing C-rate stabilization upon permanent external cell compression.[I] Lamination was found to reduce capacity fading along long-term cycling especially at fast-charging conditions.

Author contributions:

The author of this thesis manufactured all electrodes and test cells, designed and performed the electrochemical experiments, analyzed electrochemical and morphological data, visualized all data and drafted the manuscript. S. Jankowsky, M. Singh. and K.-H. Pettinger helped in designing the experiment agenda. V. Peterbauer assisted during cathode slurry preparation and coating process. A. Schmidt performed Argon ion cutting, while A. Dinter helped to perform the SEM experiments. M. Singh and K.-H. Pettinger helped in editing the manuscript.

[I] Though external compression (0.06 bar) on the evacuated pouch cells in this study was lower than minimum studied external cell compressions in comparable reports as done by J. Cannarella (0.50 bar)[353] or A. Barai (0.34 bar),[354] recognizeable effects of the cell compression were visible within the C-rate tests.

4.1   Abstract

The fast charge and discharge capability of Lithium Ion Batteries is improved by applying a lamination step during cell assembly. Electrode sheets and separator are laminated into one stack which improves the electrochemical performance as well as the stack assembly process. The effect of non-laminated and laminated interfaces on the reversible capacity during cycling are studied thoroughly in half-cell and full-cell configurations. The fully-laminated cells show a reduction in the capacity losses of 3%, 5% and 12% upon cycling at 2C, 3C and 5C-rate, respectively, while capacity losses of 6%, 11% and 23% are observed in non-laminated cells at the same C-rates. A significant reduction in the capacity fading at high C-rates is observed upon lamination. Additional compression is applied on the cells to compare the effect of lamination and compression on the cell performance. The laminated cells show an improvement in the fast charging capability in comparison to the non-laminated cells.

4.2   Introduction

More than 40 years after production of the first commercial lithium cell by Sanyo in 1970s,[355] the LIB technology has become a main contributor for the storage devices in the field of rechargeable batteries. LIB technology needs further improvement in terms of fast charging capability which can reduce the charging time from hours to minutes especially for the electric vehicle applications. Enormous research is going on to improve the cell components such as active materials,[356,357] electrolyte,[144] separator[141,358] and manufacturing steps[359] in order to increase the energy density, power density, lifetime and reduce the cost. The performance of Lithium Ion Battery electrodes has been improved by varying the thickness[197,199] and porosity of the electrodes,[198] controlling the stack pressure[303,353,360–362] and tuning the lithium ion diffusion paths in electrodes via modified manufacturing processes, for example by controlling the graphite particle orientation normal to the current collector surface during the coating step using a magnetic field,[209] or via laser structuring of graphite anodes, silicon/graphite anodes, NMC cathodes or $LiMn_2O_4$ cathodes.[315,318,363,364]

The laser structuring creates additional lithium ion diffusion pathways and increases the active surface area of thick NMC and graphite electrodes, thus enhances the discharge capacities at higher C-rates.[315,318] Besides, LIB cycling stability and aging mechanism can also be improved by varying the stack pressure,[303,353,360–362] which influences the distribution of SEI or plated lithium deposition on the graphite-separator interface.[192,360,361] It has been reported that the high stack pressure causes the higher capacity fade, so lower stack pressure is required to extend the life time. In addition, the non-uniform surface of the electrodes also induces non-uniform pressure at the interfaces among different electrode layers and the amplitude of the pressure varies during charging and discharging.[353] Non-uniform space among the electrodes and separator results in longer diffusion paths at the interfaces in the cell stacks, as shown in schematic Fig. 4.1a. In this regard, lamination technique stabilizes the electrode-separator interfaces, which shortens the lithium

diffusion paths at the interfaces as well as stabilizing the active surface area of the electrodes during cycling significantly (Fig. 4.1b), and thus homogenize the liquid phase concentration[315] of the lithium ions on the active material particle surface. The lamination technique provides the slight mobilization of the polymer binder chains both in the separator and electrode by applying heat and pressure which interlinks the electrode-separator interfaces and also maintains the surface porosity of the electrode and the separator. The necessity for mobilization of polymer binder chains in all components limits the choice of binder to thermoplastic polymers with similar melting points. Heat-induced polymer chain mobilization must not exceed the melting temperature of the polymer in order to prevent the production of a nonporous interface block.
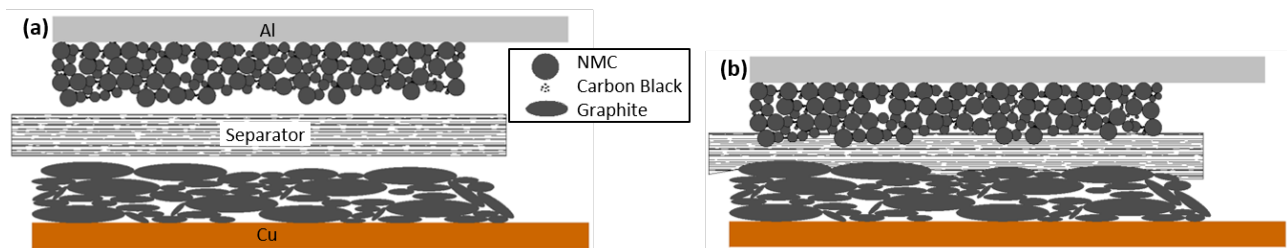
Fig. 4.1: Schematics of electrode-separator lamination technique; (a) non-laminated single cell stack (b) laminated single cell stack.

Lamination technique has been well known for some decades[205,207] for the stacking process simplification which reduces the defects occurring due to electrode misplacement at the anode-separator-cathode compound.[202] Lamination technology connects the interlayers, separator-cathode and separator-anode, physically by using a roller lamination machine and therefore, maximizes the physical and ionic contacts as well as minimizing the voids at the interfaces (Fig. 4.1).

First time, the lamination technology was used in the assembly process during the Lithium Ion Battery production in 1996.[207] Later specific roller lamination technique was reported as a binding technique to prevent the air bubbles and wrinkles within the laminated material for preparing the supercapacitor electrode on a current collector.[215] Winding and lamination technologies are typically used as state-of-the-art technologies in industrial LIB production lines.

The lamination technique is a simple and easy-to-apply technology, which simplifies the stacking process by reducing the number of components. The lamination process enables fast assembly speeds up to 100 m/min and therefore lowers the costs of the assembly process. Besides, the lamination technique improves the electrochemical performance of the cell, in terms of improving cycling stability, reducing aging effects and stabilizing cell performance even in case of vacuum reduction in the cell, in comparison to the above mentioned additional electrode modification technologies.

In this article, we present a detailed study of the electrode-separator lamination in full cell configuration at higher C-rates. This study will reveal the significant improvement in the fast charging and discharging capability of single cells after applying the lamination technique.

4.3   Experimental

4.3.1 Materials

Commercially available battery grade cathode material $LiNi_{1/3}Mn_{1/3}Co_{1/3}O_2$ (NM-3102 h, *BASF*, Germany – former *TODA AMERICA*, USA) and anode material graphite (MAGE3, *HITACHI CHEMICAL*, Japan) were used as active materials. Conductive carbon (Super C65, *IMERYS*, Switzerland – former *TIMCAL*, Switzerland), cathode conductive graphite (KS6L, *IMERYS*) and anode conductive graphite (SFG6L, *IMERYS*) were used as conductive additives. PVDF (Solef® 5130, *SOLVAY*, Italy) was used as binder. *N*-methyl-pyrrolidone (*Overlack*, Germany) was used as solvent. 1 M $LiPF_6$ – EC : EMC 3:7 w/w (Selectilyte LP57, *BASF*, Germany) and vinylene carbonate (Vinylene Carbonate E, BASF, Germany) were used as electrolyte. A laminate type aluminum pouch film (*SHOWA DENKO AMERICA*, USA) was used as housing of pouch cells. Pure lithium and glass microfibre filter (Glass Fibre Filter Grade 691, *VWR-avantor*, USA) were used for T-cells (half-cell). A self-standing inorganic filled (Al_2O_3) separator film with a PVDF/HFP Copolymer as binding agent, was used for the pouch cell (full-cell) configuration. All materials and substrates were used as received.

4.3.2 Electrode/separator preparation

The cathode was prepared by mixing NMC (93 wt%), PVDF (3 wt%), Super C65 carbon (3 wt%) and KS6L graphite (1 wt%) with NMP solvent to have a final solid content of 60 wt%. The anode was prepared by mixing MAGE3 graphite (90 wt%), PVDF (7 wt%), Super C65 carbon (2 wt%) and SFG6L graphite (1 wt%) with NMP to give a final solid content of 50 wt%. The electrode slurries were prepared in a planetary mixer (TX-2, *INOUE*, Japan) and were single-side coated by a doctorblade coater in a roll-to-roll process coating machine. Electrodes were dried inline in a two-step drying tunnel at the temperature range of 135-150 °C. Low electrode mass loadings were chosen to act as high capacity and high power reference system.[365] The averaged active mass loadings of cathode and anode electrodes were ~ 6.9 mg·cm^{-2} (1.13 mAh·cm^{-2}) and ~3.4 mg·cm^{-2} (1.28 mAh·cm^{-2}), respectively.

The cathode and anode capacity balancing factor was 1:1.14 in the full cells. The electrodes in full cell configuration have mass in the range of 0.245 – 0.278 g of NMC and capacity in the range of 0.041 – 0.047 Ah.

4.3.3 Cell preparation

The active areas of cathode and anode sheets were 5×8 cm^2 and 5.4×8.4 cm^2 within the pouch cell. Cathode, anode and separator were laminated to make a single stack by using a lamination machine (BLE 282 D, *MANZ Italy* – former *ARCOTRONICS Italia S.p.A.*, Italy) at the roll speed of 1.38 m·min^{-1}, using a line force of 157 N·cm^{-1} in the temperature range 100-120 °C.

To analyze the effect of lamination on the electrochemical performance of cathode and anode individually, cathode-separator stacks were laminated by laminating a copper-separator-cathode stack, later the copper

was replaced with the appropriate anode without any further lamination. Similarly, anode-separator stacks were laminated by laminating an aluminum-separator-anode stack, later the aluminum foil was removed from the stack, and replaced with the appropriate cathode without any further lamination. Nickel and aluminum tabs were welded onto the anode and cathode electrodes by ultrasonic welding. Pre-assembled pouch cell stacks were dried at 110 °C for 12 h under vacuum. The electrolyte amount of 500 µl for laminated cells and 750 µl for partially laminated/non-laminated cells is used within an argon filled glovebox (MB20, H_2O and O_2 content < 0.1 ppm, MBraun, Germany) and sealed under vacuum. The cells were kept at room temperature over night before starting the electrochemical characterization. To study the effect of additional cell compression, gravimetric force was applied to the cells by compressing each pouch cell stack with a weight of ~ 2.5 kg on top, while placing a polystyrol plate between the cell and applied weight for homogeneous force distribution along the active single cell area.

For half-cell measurements, the electrodes were punched into circular disks of 10 mm diameter and dried at 110 °C under vacuum for 12 h. Half-cell measurements were carried out in three electrode geometry using a Swagelok type T-cell setup, assembled in an Argon filled glovebox. Lithium metal was used as reference and counter electrode. LP57 was used as electrolyte for NMC half-cell measurements. A mixture of LP57 (98 wt%) and vinylene carbonate (2 wt%) was used as electrolyte for graphite half-cell measurements and for all full cell measurements. Half-cells were kept at room temperature over night before starting the electrochemical characterization.

4.3.4 Cell characterization

Electrochemical characterization was done with a battery tester (CTS-LAB, *BaSyTec*, Germany), using galvanostatic (CC) and potentiostatic (CV) modes for charging step and CC-mode for discharge step. For full cell measurements, the voltage ranges were adjusted to 3.0 V – 4.2 V, for NMC half-cell measurements the voltage ranges were adjusted to 3.0 V – 4.3 V, for graphite half-cell measurements the voltage ranges were adjusted to 0.02 V – 1.5 V. CV charging steps were continued until the charging current dropped below 0.05C rate. For the full cell experiments, formation was done by applying two cycles at 0.1C, calculated from the NMC weight and the theoretical NMC capacity of 168 mAh·g^{-1}. For the further cycling process, C-rates were calculated according to the measured nominal capacity of each cell, which is the discharge capacity of the second formation cycle (see supplementary information). For half-cell experiments, the C-rate currents were calculated to fit to the theoretical capacity of the active material weight within the samples, using a theoretical NMC capacity of 168 mAh·g^{-1} and a theoretical graphite capacity of 372 mAh·g^{-1}.

Non-laminated single cell components were prepared for cross-section images with a handheld punch (clearance 4 µm, *NOGAMI*, Japan). Argon ion cutting (EM TIC 3X, *Leica*, Germany) was used for the laminated electrode-separator stack. A field emission scanning electron microscope (FE-SEM) (Merlin Compact, *Zeiss*,

Germany) with energy dispersive X-ray spectroscopy (EDX) was used to take cross-section images and EDX element mapping images of a laminated single cell stack.

Porosities of separator and electrode layers were calculated by comparing their real volume with the minimal component volume given by the sample weight, using the theoretical densities of the components.

$$porosity = \frac{V_{\text{pores}}}{V_{\text{real}}} = \frac{V_{\text{real}} - V_{\text{components,minimal}}}{V_{\text{real}}} \qquad [33]$$

For impedance spectroscopy analysis, full cells were charged to 3.6 V at 0.1C rate directly after formation. Impedance measurements were carried out in a climate chamber (INCU-Line® IL 68R, *VWR-avantor*, USA) at 25 °C. After connecting to the potentiostat (PGSTAT204, Metrohm Autolab, Netherlands), the cells rested for 2 h at 25 °C prior to the measurement. Impedance analysis was done in potentiostatic mode in the frequency range of 50 kHz – 10 mHz using an amplitude of 10 mV. Data fitting was performed using Z-fit.

4.4   Results and Discussion

4.4.1   Morphological characterization

Fig. 4.2 shows the cross-section SEM images of the non-laminated single cell components NMC cathode, self-standing inorganic filled separator film and graphite anode.
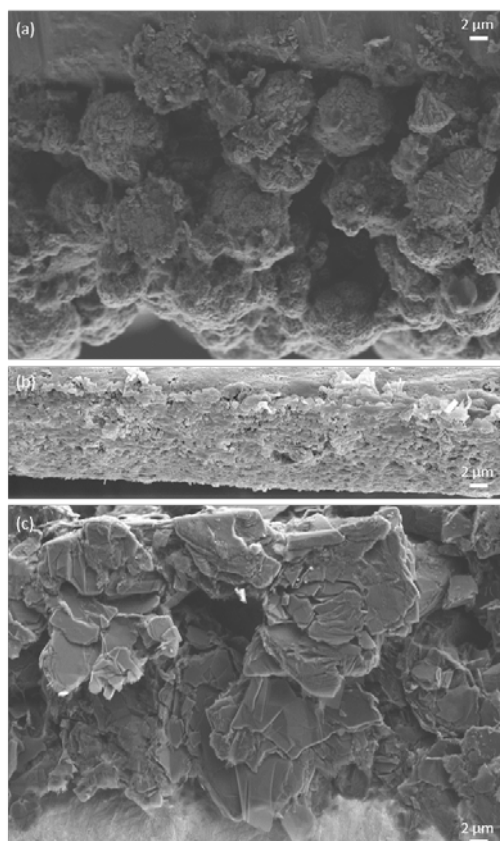
Fig. 4.2: Cross-section SEM images of non-laminated stack components; (a) NMC cathode; (b) self-standing inorganic filled separator film; (c) graphite anode.

Cross-section SEM and EDX images of a laminated single cell stack, containing NMC cathode, self-standing inorganic filled (Al_2O_3) separator film and graphite anode, are shown in Fig. 4.3.
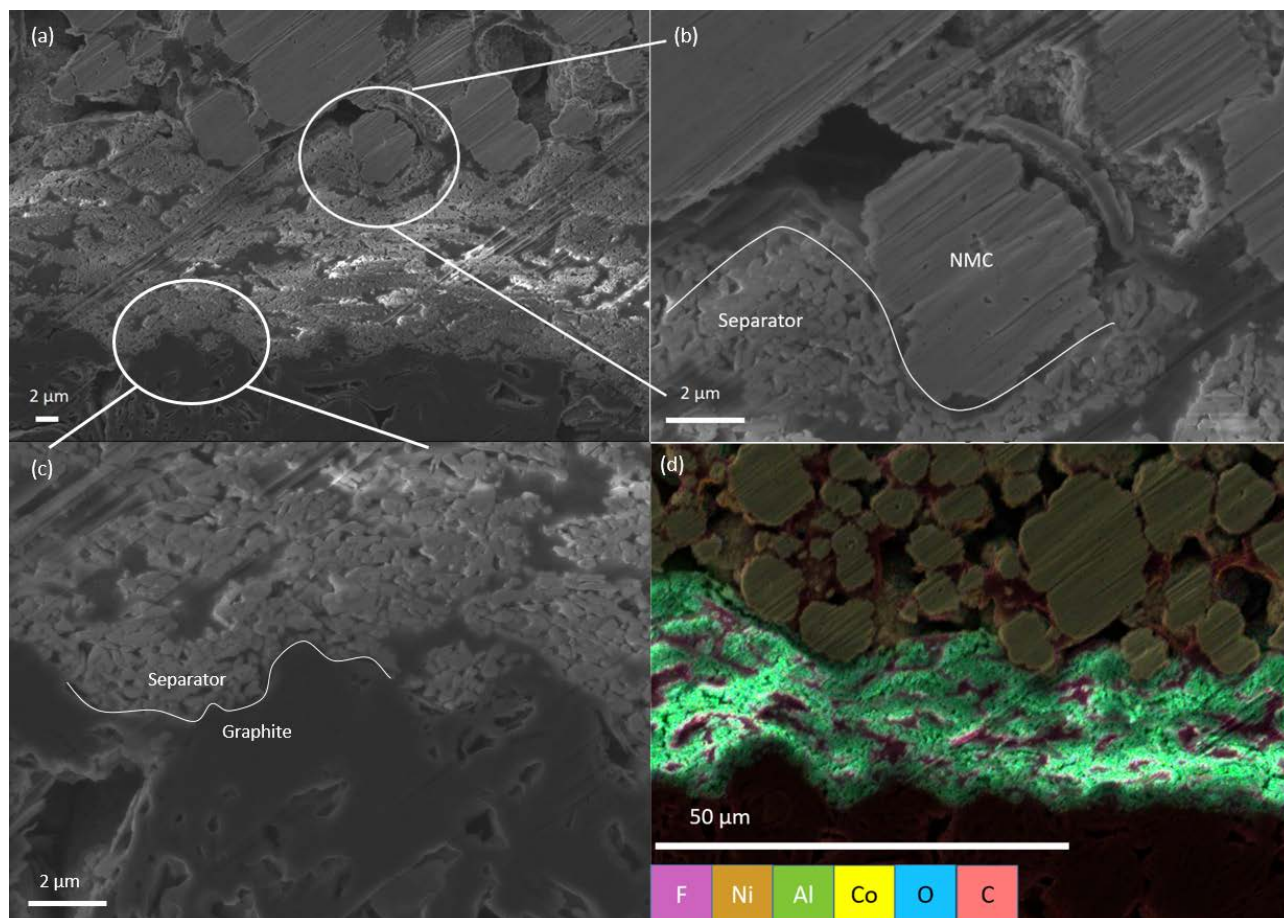
Fig. 4.3: Cross-section images of laminated single cell stack: NMC cathode in upper part, self-standing inorganic filled separator film in central part, graphite anode in lower part; (a, b, c) SEM image, recorded at a voltage of 5.0 kV and a working distance of 13 mm; (d) EDX element mapping image.

The cross-section images of interfacial linking with both electrodes clearly show the correspondence with the schematics, as shown in Fig. 4.1. No remaining voids are visible at the interfaces (cathode/separator and anode/separator interfaces) while the separator surface clings to NMC surface particles at the cathode side and to graphite surface particles at the anode side. The high magnification image, Fig. 4.3b and Fig. 4.3c, show that NMC/graphite particles and separator adhere perfectly after lamination. It could be mentioned that no damaging of active materials were found during the lamination process. In addition, lamination provides stabilized interfaces which minimize the interfacial resistances and reduce the capacity fading upon increasing the C-rates. The EDX image proves that the electrode and separator interface is well contacted. The EDX mapping shows the homogeneous distribution of alumina in the separator (Fig. 4.3d).

The overall pore volume within the active area of anode layer, separator and cathode layer in the single cell stack is reduced by ~ 66% upon lamination. Therefore, the overall porosity of the cathode-separator-anode stack decreases from ~ 54% down to ~ 30%. The SEM images show the pore volume loss to primarily occur via particle reorganization at the electrode-separator interface.

4.4.2 Half-cell measurements

NMC cathode and graphite anode are electrochemically tested in half-cell configuration versus lithium metal. Both electrodes reflect the nominal capacities as specified by the manufacturers, and show negligible capacity losses upon cycling at different C-rates (see Fig. 4.9 in Supplementary Information – SI). These optimized electrodes are used to study the effect of lamination and compression on the electrochemical performance in full cell configuration.

4.4.3 Full cell measurements

a) Electrochemical performance of laminated cells

To identify the influence of the electrode-separator lamination on the electrochemical performance, non-laminated cells are compared with fully laminated cells. Specific influence of the individual interface lamination of anode-separator and cathode-separator are studied by comparison of partially laminated stacks. The counter electrodes in non-laminated and partially laminated full cells are hold in position by the pouch foil housing in the evacuated cell.
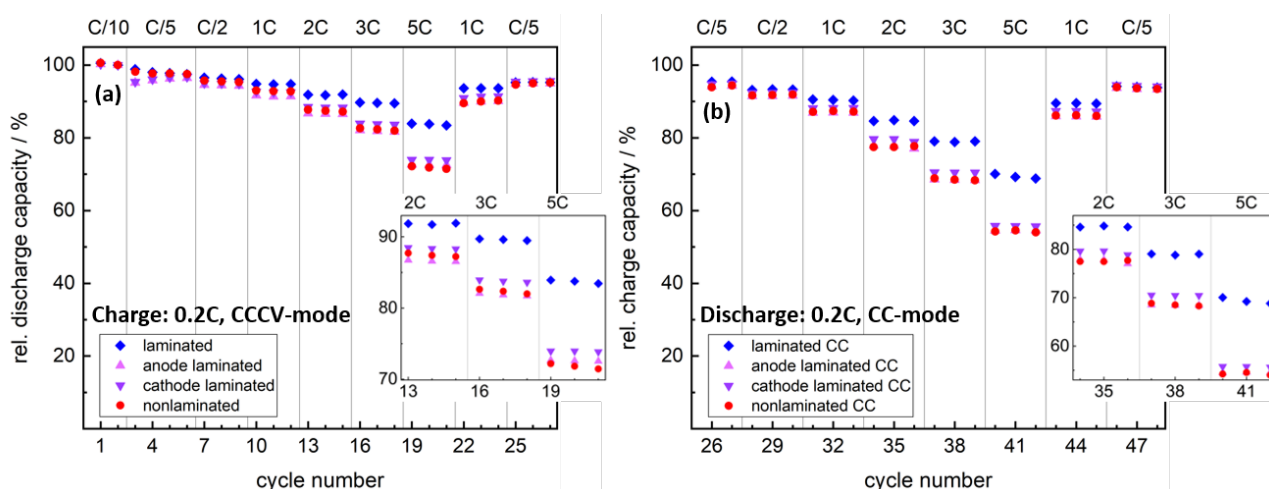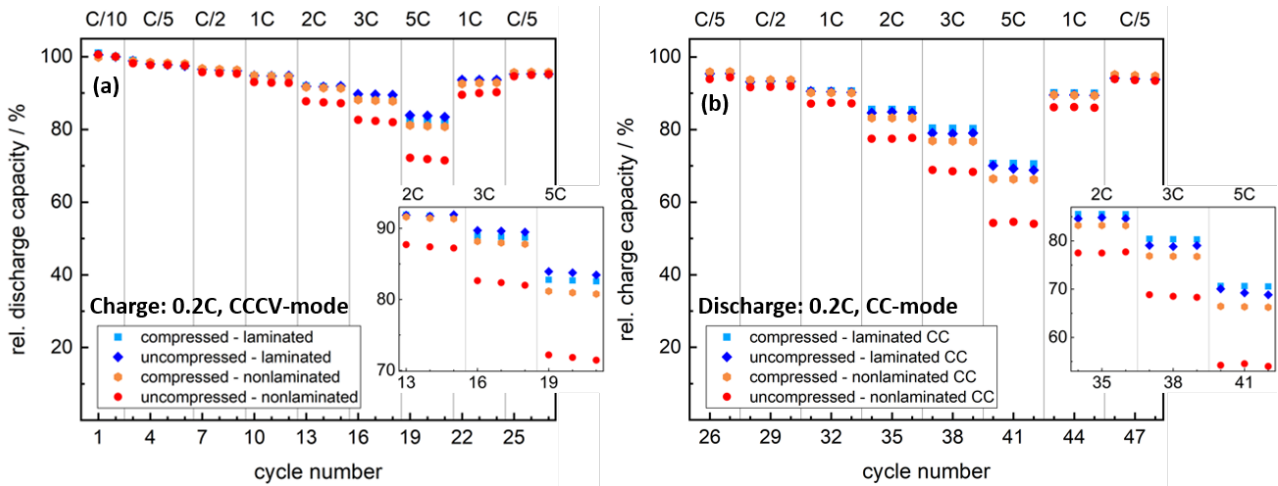

Fig. 4.4: C-rate tests of uncompressed single cells; (a) discharge capacities of discharge rate test, discharge rate per step as indicated, charge rate: 0.2C, CCCV-mode; (b) charge capacities at charge rate test (CCCV-mode; CC-charge fraction plotted), charge rate per step as indicated, discharge rate: 0.2C CC-mode.

To study the significant influence of the lamination on the charging and discharging capacities of the full-cells, the cells are charged at fixed C-rate while discharged at variable C-rates and vice-versa, as shown in Fig. 4.4. The charge-discharge curves of laminated and non-laminated cells at charge and discharge rate tests are given in Supplementary Information. From the relative discharge capacity graphs, Fig. 4.4a, it can be seen that the lamination process on both interfaces has significantly improved the capacities especially at higher C-rates. In addition, the overall electrochemical performance also improves at mild C-rates after lamination. The cells show that the difference in the discharge capacity values is not changing up to 0.5C rate, while at higher C-rates the discharge capacity ratio is significantly high. The non-laminated cell reveals 72% of the nominal capacity, while the laminated cell shows 84% of the nominal capacity at 5C rate. Besides, the cells

show hardly any influence of the C-rate on the charge/discharge capacities and recover the initial capacities even after cycling at 5C-rate. In addition, partially laminated cells such as anode-separator lamination and cathode-separator lamination also show slight improvement in the discharge capacity at high C-rates. It indicates that the advantages of the lamination can be only seen when the cell is fully laminated at both interfaces. The laminated cell at 5C-rate delivers even slightly higher discharge capacity in comparison to the non-laminated cell at 3C-rate.

Charge capacity graphs, Fig. 4.4b, indicate that charge rate tests show no significant difference in the cell performance, revealing 94 – 96% of the nominal capacity, at various C-rates especially upon applying CCCV-mode, which results from the same cutoff current 0.05C. Therefore any overpotential differences between the cells are neglected (see Fig. 4.14 in SI). On the other hand, the capacity fractions during charging in CC-mode show similar improvement in CC charge rate stability upon lamination, as observed in the discharge rate tests, Fig. 4.4a. The non-laminated cell charges 55% of the nominal capacity in CC-mode, while the capacity increases to 70% upon lamination at 5C charge rate. This indicates a clear improvement in the fast-charging capability of the cell upon electrode-separator lamination. As can be seen from Fig. 4.4, the CC-charge mode delivers slightly lower capacities in comparison to CC-discharge mode which could be due to the unequal kinetics of graphite lithiation and delithiation at different C-rates. Partially laminated cells reveal 55% of the nominal capacity upon anode laminated and cathode laminated stacks charged at 5C-rate in CC-mode. The results again prove that no improvement in the electrochemical performance of the cell is observed upon partial lamination in comparison to the non-laminated cell stack.

From the results of charge and discharge rate tests, it proves that the electrode-separator lamination technique improves the fast charging and discharging capability of the cell. Lamination process improves the pore structure at both interfaces, as shown in the SEM images in Fig. 4.3, which provides a better ionic network as well as physical contacts among the particles and separator at the interfaces. It would be worth mentioning here that the lamination shortens the ionic path length especially at the electrode-separator interfaces, thus improving the charge and discharge rate capability, see Fig. 4.4.

b) Influence of additional stack compression

In multilayer electrode stacks additional compression besides the vacuum effect is applied to the individual cells upon the gravimetric compression from the adjacent cells. In this regard, to investigate the effects of electrode-separator lamination in multilayer stack, additional analysis is necessary. To compare the effects of compression and lamination on the electrochemical performance in single cells, an additional gravimetric force is applied on the pouch cells. The internal cell pressure of the as-built cell with electrolyte is 43 mbar at 25 °C. Additional gravimetric cell pressure is realized at 143% of the internal cell pressure. Charge and discharge rate tests are performed with a corresponding single cell series of non-laminated cells and fully laminated cells after applying additional compression.

Fig. 4.5: C-rate tests of uncompressed and compressed single cells; (a) discharge capacities of discharge rate test, discharge rate per step as indicated, charge: 0.2C, CCCV-mode; (b) charge capacities at charge rate test (CCCV-mode; CC-charge fraction plotted), charge rate per step as indicated, discharge rate: 0.2C, CC-mode.

A comparison study is done to analyze the effect of additional compression along with lamination and non-lamination process, as shown in Fig. 4.5. The charge-discharge curves of laminated and non-laminated cells at charge and discharge rate tests in additional compressed and uncompressed states are given in SI. As it has been mentioned earlier, the non-compressed cells show differences in the C-rate stability. The non-laminated cell shows slight improvement in the C-rate stability after applying additional pressure to the cells, resulting in 80% of the nominal capacity at 5C discharge mode. In addition, the cells show hardly any influence of the C-rate on the charge/discharge capacities and recover the initial capacities even after cycling at 5C rate.

Discharge capacity values clearly indicate that the additional compression does not have an obvious effect on the laminated cells, while non-laminated cell shows significant improvement in the discharge capacity in comparison to the uncompressed non-laminated cell.

The charge capacities in CCCV-mode lie in the range of 94 – 96% of the nominal capacity along all cell geometries and C-rates (see Fig. 4.14 in SI), while the CC-charge capacities show the same trend like the discharge capacities. Additional compression on the non-laminated cell improves the charge rate stability in CC-mode and raises the capacity from 54% to 66% at 5C rate, while the laminated cell provides 70% of the nominal capacity in both non-compressed and compressed states at the same C-rate. From the results of discharge rate and charge rate capability tests, it is clear that the cell compression and lamination processes improve the cell performance. From the results it is clear that the additional compression also slightly improves the physical contacts among the electrode-separator interfaces. Lamination technology has advantages at microscopic level in comparison to the additional gravimetric cell compression. Lamination technique improves the pore structure upon mobilization of the polymer chains in the electrode and separator, resulting the better ionic network in addition to the better physical contacts at both interfaces. It has been reported that the cycling efficiency of lithium ion cells is strongly affected by applying additional

stack pressure.[303,353,360–362,366] The stabilization in the cycling efficiency was shown to arise from modified SEI growth at compressed state.[303,353,360–362,366]

c) Fast charging and fast discharging cycling test

Cycling studies are performed on non-laminated and fully laminated cells to evaluate the long-term effects of the indicated discharge and charge rate benefits in CC-mode at different C-rates. Fig. 4.6 shows comparison of the discharge capacities of the non-laminated and fully laminated cells.
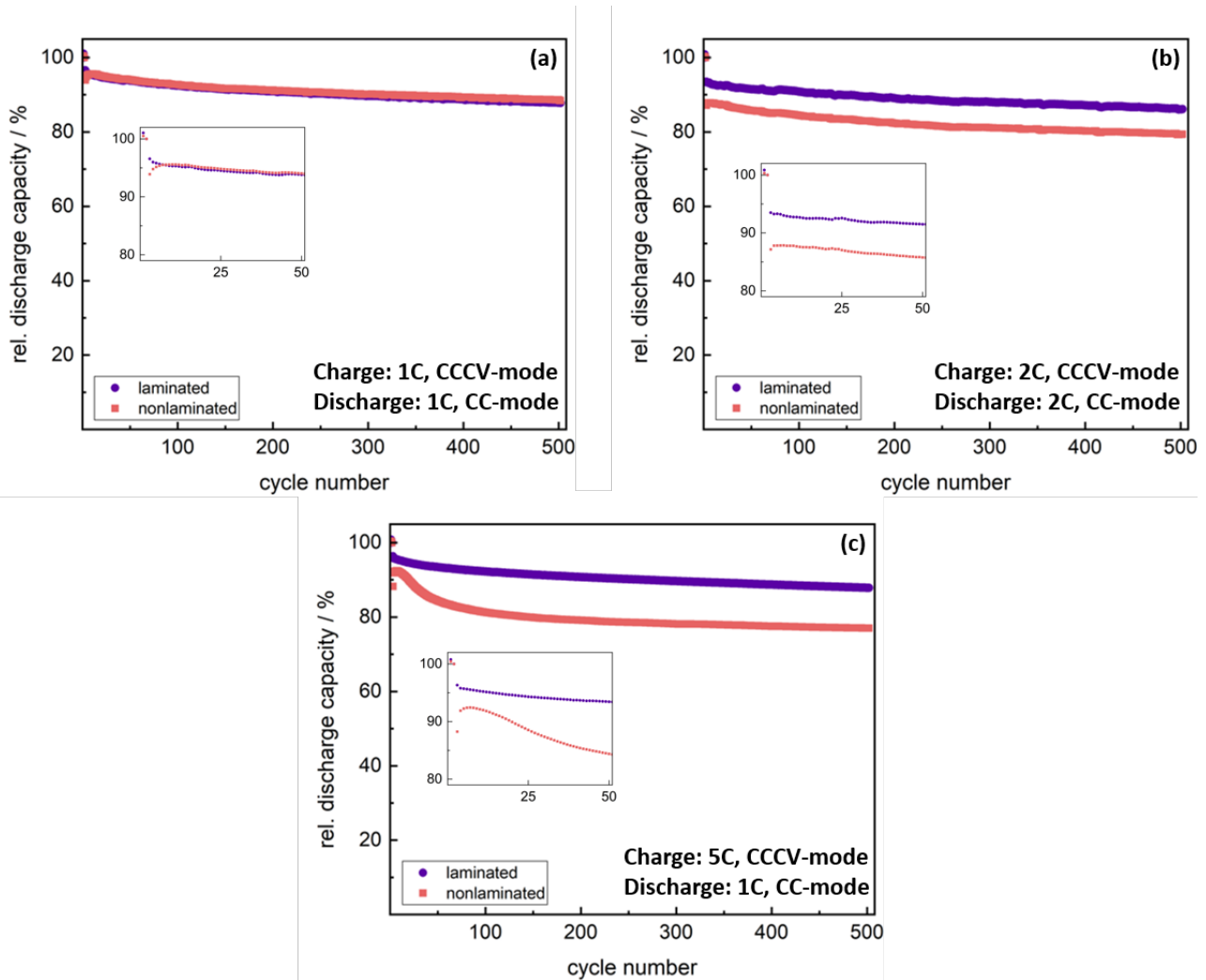
Fig. 4.6: Discharge capacity data of uncompressed laminated and non-laminated cells at different charge-discharge rates; (a) cycling at 1C-rate; (b) cycling ag 2C-rate; (c) cycling at 5C/1C-rate.

Fig. 6a shows the cycling data of non-laminated and laminated single cells at 1C rate. The non-laminated and fully laminated cells exhibit a maximum capacity of 95% of the nominal capacity. After 500 cycles, both cells give 88% of the nominal capacity. No difference in the initial capacity and fading rate is observed after cycling at 1C rate upon applying electrode-separator lamination.

The cycling data of non-laminated and laminated single cells at 2C rate is shown in Fig. 6b. The non-laminated and laminated cells show maximum discharge capacities of 88% and 93% of the nominal capacity, while after 500 cycles, the cells reveal 75% and 82% of the nominal capacity, respectively. The improvement in maximum

discharge capacity at 2C rate corresponds with the results of the discharge rate tests (Fig. 4.4a). The results of the cycling test at 2C rate indicate that the fading rate reduces slightly upon lamination, thus improving the aging mechanism at 2C rate.

In addition to charging and discharging at 2C rate, the cells are further charged at 5C rate in CCCV-mode in order to study the effect of long-term stability and fast charging capability, as shown in Fig. 4.6c. The non-laminated and laminated cells reach maximum capacities of 92% and 96% of the nominal capacity, respectively. As can be seen from the cycling curves, during the first 100 cycles, the non-laminated cell shows fast capacity loss, revealing 81% of the nominal capacity, compared to 92% of the laminated cell. After 500 cycles, the non-laminated cell reaches 77%, compared to 88% of the laminated cell. The results show that the laminated cell delivers the same capacity whether cycled at 1C or 5C charge rate, while the non-laminated cell shows clearly different aging effect on the same C-rates. As has been mentioned earlier, the lamination provides high active area for the lithium ions. It has been reported that lower stack pressure results in more swelling in the anode during cycling. Swelling in the repeated cycling decreases the active area as well as the electrical contacts.[360,361] Contact losses increase the resistance which can lead to local lithium plating and therefore induce subsequent SEI growth.[192] The results emphasize the theory of the lamination which influences the aging mechanisms related to the electrode-separator interface.

d) Impedance analysis

The Nyquist plots of laminated, partially laminated and non-laminated cells are shown in Fig. 4.7. The RQ-elements are assigned to represent the SEI-resistance (1st semicircle), charge-transfer resistance of anode (2nd semicircle), and charge-transfer resistance of cathode (3rd semicircle).[224] The full lamination step does not increase the charge-transfer resistances of NMC cathode and graphite anode. A change in the SEI resistance can be clearly seen in the graphs upon lamination. The partially laminated states show higher SEI resistance and charge-transfer resistances. The increased SEI resistance and charge-transfer resistances explain well the poor C-rate performance of the partially laminated cells, as shown in Section a). The partial lamination leads to poor contacts between separator and counter electrode at the respective non-laminated interface.
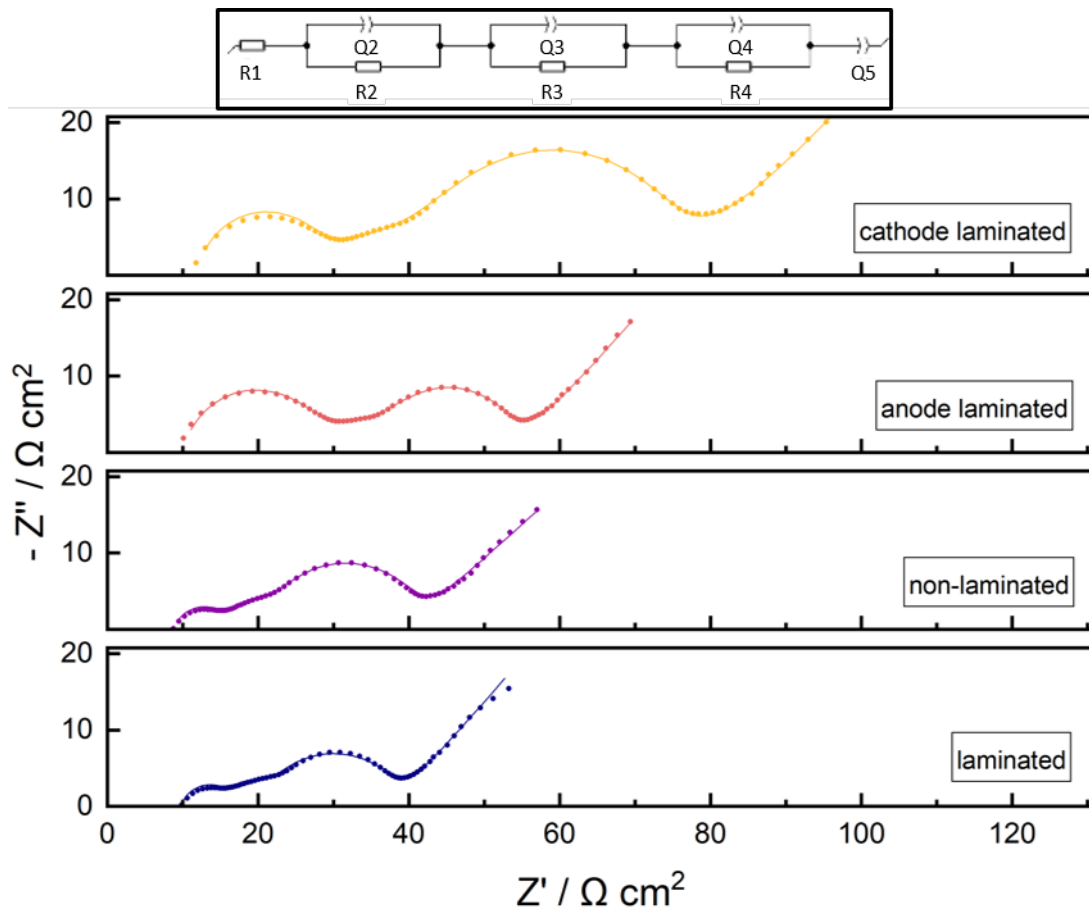
Fig. 4.7: Impedance data of non-laminated/partially laminated/fully laminated cells; EIS spectra (50 kHz – 10 mHz) of single cells collected at 25 °C in OCP at 3.6 V cell voltage after formation; equivalent circuit model used for data fit is indicated; measurement data is indicated as dots, fitting curves are indicated as straight lines.

To calculate the resistances (see Tab. 4.4 in SI), the data fit was performed by using the equivalent circuit model, as shown in Fig. 4.7. The SEI resistance reduces from 7 to 4 $\Omega \cdot cm^2$ after lamination in comparison to non-laminated state. The lamination technique stabilizes and homogenizes the electrode-separator interface, as well as decreases the overall cell porosity, therefore the electrolyte filled cells have better ionic contacts in total by homogenizing and reducing the pores. Besides due to the lower SEI resistance and overall resistance upon lamination, overpotentials in the laminated cells are lowered. This reduces the possibility of the anode potential at high C-rates to enable reductive side reactions with electrolyte and conductive salt, which accelerates the SEI growth.[367]

Therefore, SEI growth phenomena given by reductive side reactions are less likely to occur in laminated state than in non-laminated state. In this manner, EIS data emphasize that the improvement of laminated cells upon cycles at high C-rates arise from reduction of the further loss of electrolyte and active lithium in the SEI growth.[367] S. Müller et al. have reported that the local inhomogeneities in graphite anodes cause local overpotentials,[192] which give an additional stress in the interfacial region and further increase the possibility of reductive side reactions.[367]

4.5   Conclusion

The additional production step of electrode-separator interface lamination was successfully applied to a full cell of NMC/graphite, by using PVDF as binder both in electrodes and separator. Cross-section SEM measurements show successful interlinking through the particles and separator along both anode-separator and cathode-separator interfaces. Significant improvement in fast charging capacities in CC-mode and fast discharge capacities at accelerated C-rates are observed from the total interface lamination simultaneously at the cathode-separator interface and the anode-separator interface in comparison to the non-laminated cells or individually laminated cells with either cathode-separator interface or anode-separator interface laminated. The positive effect of lamination on the charge and discharge rate stability is correlated with applying an additional compression on the non-laminated cells. The study showed that additional compression also significantly improves the cell performances of all cells excepting laminated cells. EIS analysis indicates that the lamination process stabilizes the interfaces resulting in lower SEI resistance and overall cell resistance. Long-term cycling results of the laminated cells show significant reduction in the capacity fading upon continuously applying fast charging cycles which indicates that the losses arising from subsequent SEI growth reduce significantly upon lamination.

4.6   Acknowledgement

4.7   Supplementary Information

Supplementary data to this article can be found online at https://doi.org/10.1016/j.jelechem.2019.02.030.

4.7.1 Cell preparation

Fig. 4.8 shows the lamination modification to separator and electrodes in case of a single cell.
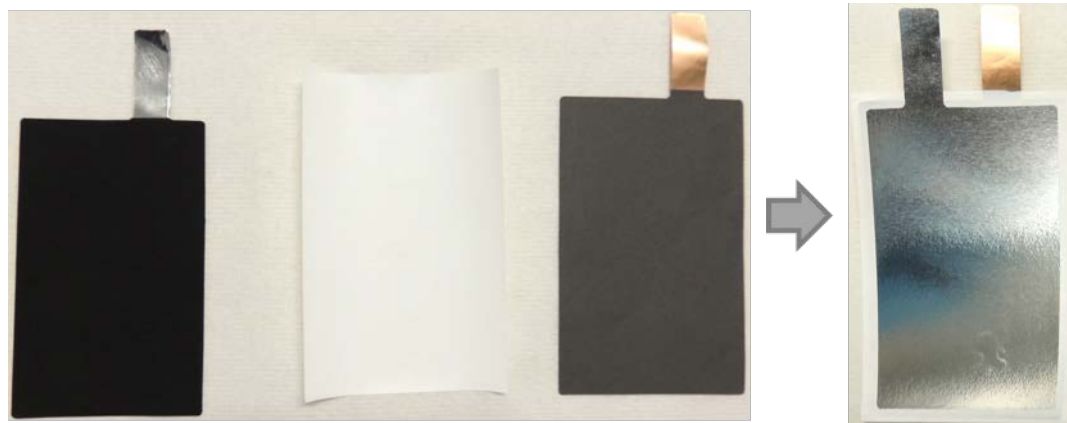
Fig. 4.8: Stacking effect of the lamination process in case of single cell.

4.7.2 Half-cell measurements

NMC cathode and graphite anode are electrochemically tested in half-cell configuration versus lithium metal. When the cells are charged and discharged repeatedly, NMC and graphite show stable capacities over the course of 3 cycles at each C-rate, as shown in Fig. 4.9.

Tab. 4.1: NMC cathode half-cell capacities.

discharge rate	C (spec) [mAh/g]
C/10	154
C/5	151
C/2	144
1C	138
2C	130
3C	125
4C	120
5C	116
10C	92
1C – 2nd	138

Tab. 4.2: Graphite anode half-cell capacities.

charge rate	C (spec) [mAh/g]
C/10	349
C/5	342
C/2	342
1C	342
2C	341
3C	340
5C	338
1C – 2nd	342
C/5 – 2nd	343

The cathode exhibited discharge capacities of 154 mAh·g^{-1}, 151 mAh·g^{-1}, 144 mAh·g^{-1}, 138 mAh·g^{-1}, 130 mAh·g^{-1}, 125 mAh·g^{-1}, 120 mAh·g^{-1}, 116 mAh·g^{-1}, 92 mAh·g^{-1} and 138 mAh·g^{-1} at C/10, C/5, C/2, 1C, 2C, 3C, 4C, 5C, 10C and 1C rate, respectively. After applying cycles at high C-rates like 5C or 10C, the NMC cathode

restores back to the initial capacity at 1C. On the other hand, the anode exhibited delithiation capacities of 346 mAh·g^{-1} at C/10 rate and ~ 340 mAh·g^{-1} at higher C-rates. NMC and graphite materials delivered discharge capacities in the same range as the manufacturers have specified. Both electrodes show stable and negligible capacity losses upon cycling at different C-rates. These optimized electrodes are used to study the effect of lamination and compression on the electrochemical performance in full cell configuration.
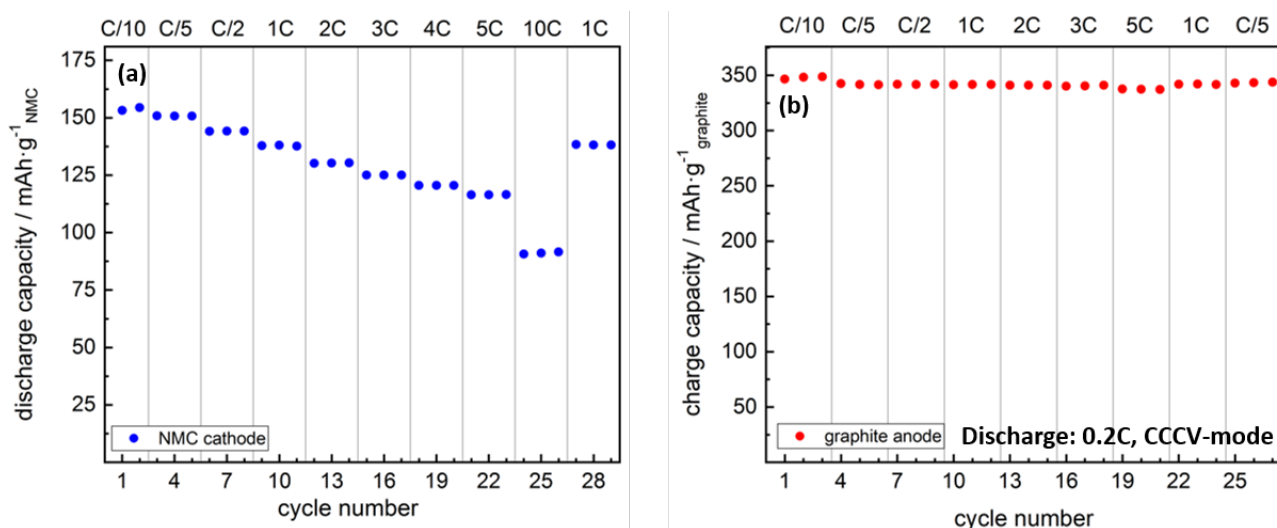
Fig. 4.9: Rate capability test in half-cell configuration: (a) NMC cathode; (b) graphite anode.

4.7.3 Full cell measurements

Electrochemical performance of laminated cells
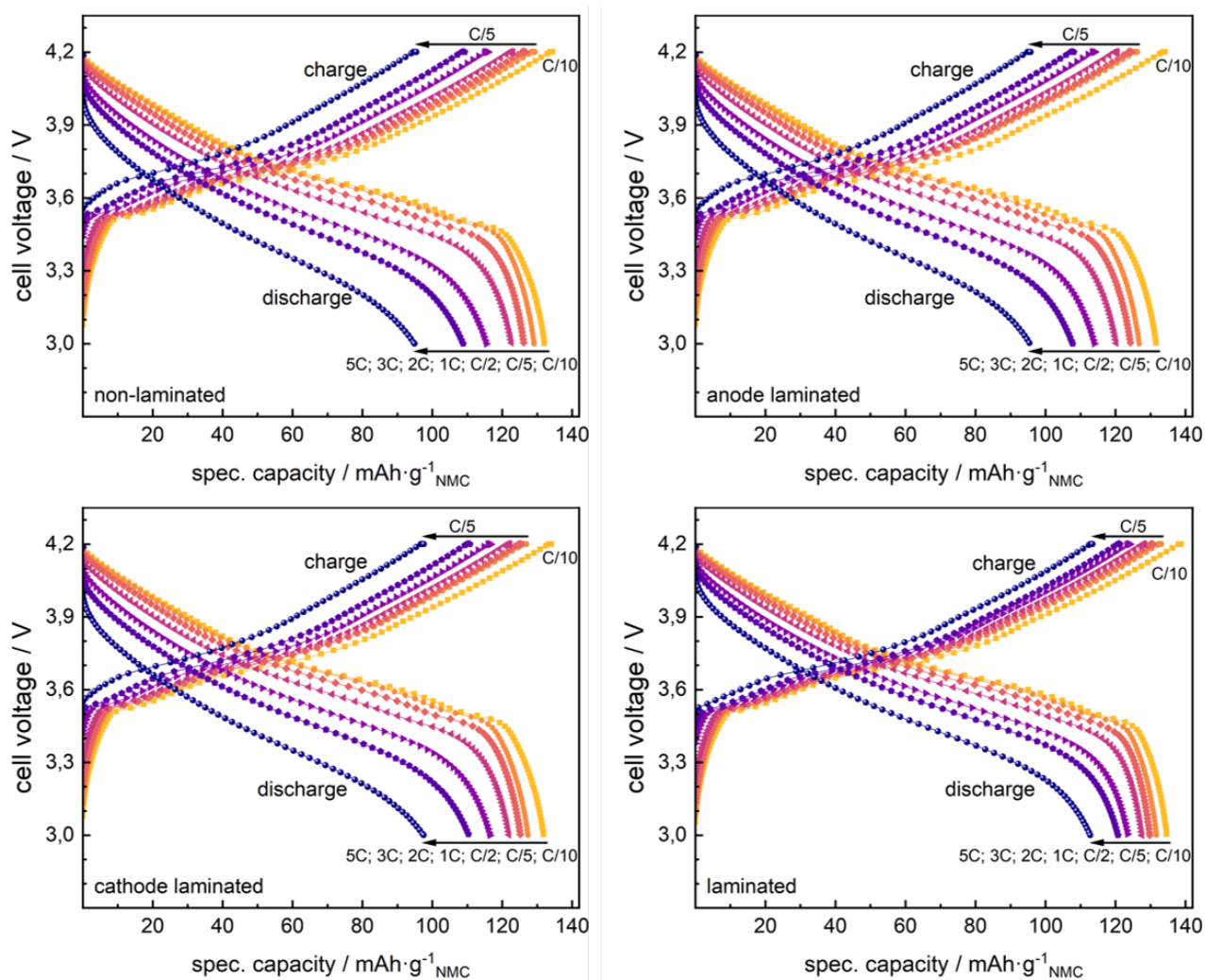
Fig. 4.10: Charge/Discharge profiles: uncompressed single cell discharge rate tests (a) non-laminated cell; (b) anode/separator laminated cell; (c) cathode/separator laminated cell; (d) fully laminated cell.

The charge-discharge cycles of laminated and non-laminated cells at discharge rate test are shown in Fig. 4.10. The non-laminated cell delivers the discharge capacities of 132 mAh·g^{-1} (100%) and 95 mAh·g^{-1} (100%) at C-rate of C/10 and 5C, respectively. Anode laminated and cathode laminated cells show no improvement in the discharge capacities at the same C-rates. On the other hand, the fully laminated cell exhibits 136 mAh·g^{-1} (103%) and 114 mAh·g^{-1} (120%). The charge discharge profiles show that the fully laminated cell exhibits significantly increased discharge capacities at accelerated C-rates in comparison to the non-laminated cell. From the discharge curves, Fig. 4.10, it can be seen clearly that the fully laminated cells reach the cutoff voltage of the CC discharging step at higher capacities upon increasing the C-rate in comparison to other partially laminated cells.
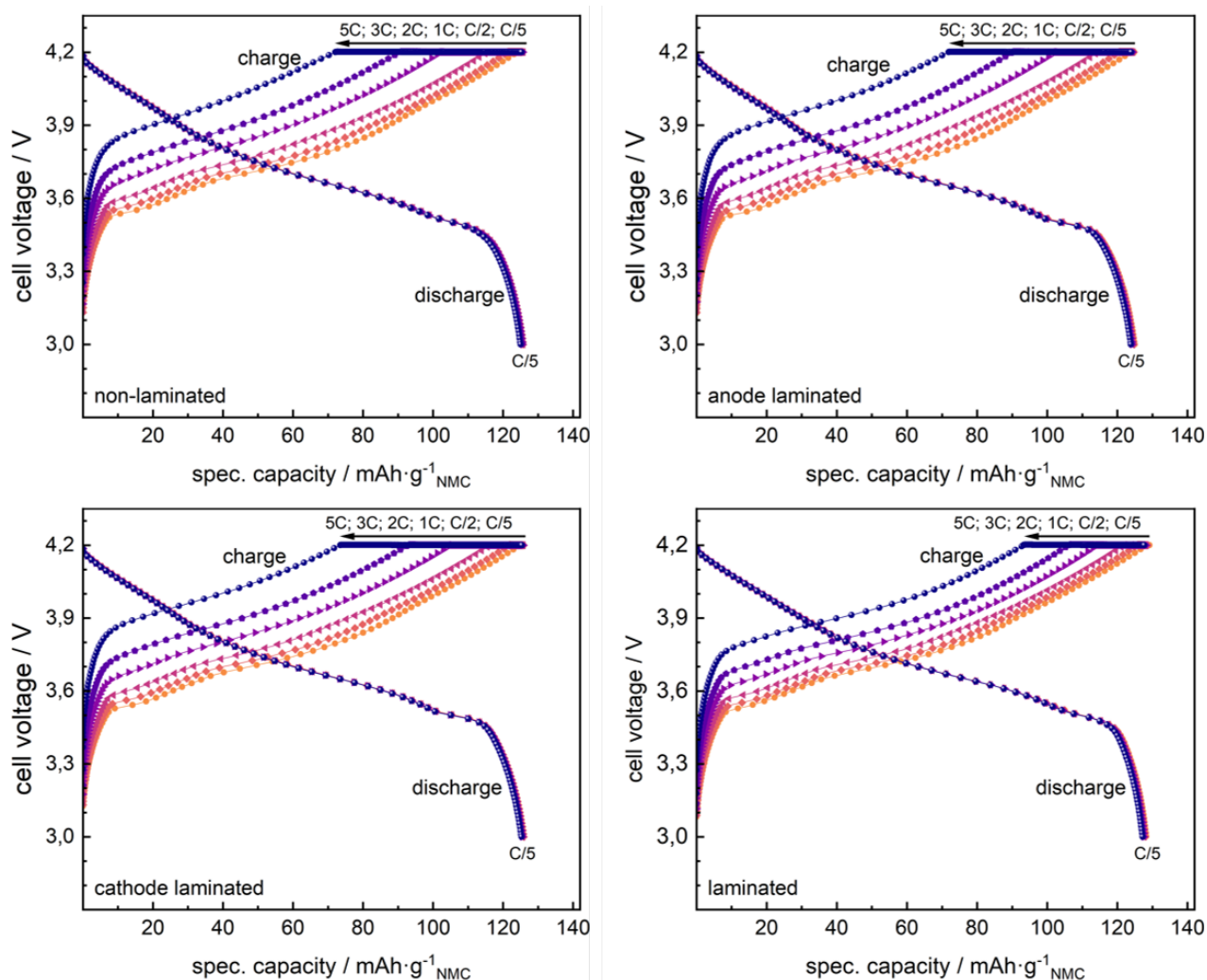
Fig. 4.11: Charge/Discharge profiles: uncompressed single cell charge rate tests (a) non-laminated cell; (b) anode/separator laminated cell; (c) cathode/separator laminated cell; (d) fully laminated cell.

The charge-discharge cycles of laminated and non-laminated cells at charge rate test are shown in Fig. 4.11. The non-laminated cell delivered the CCCV charge capacities of 124 mAh·g^{-1} (100%) and 124 mAh·g^{-1} (100%) at C-rate of C/5 and 5C, respectively. In contrast, the non-laminated cells delivered the CC charge capacities 124 mAh·g^{-1} (100%) and 70 mAh·g^{-1} (100%) at C-rate of C/5 and 5C, respectively. Anode laminated and cathode laminated cells show no improvement in the charge capacities. The fully laminated cell exhibits 129 mAh·g^{-1} (104%) and 128 mAh·g^{-1} (103%) at CCCV charge capacities for C/5 rate and 5C rate. Besides, at CC charge capacity, the fully laminated cell gives 129 mAh·g^{-1} (104%) and 95 mAh·g^{-1} (136%). The charge discharge profiles show that the fully laminated cell exhibits significantly increased CC charge capacities at accelerated C-rates in comparison to the non-laminated cell. The charge rate curves clearly show that the fully laminated cells reach the cutoff voltage of the CC charging step at higher capacities when increasing the C-rate in comparison to the non-laminated cells.

Influence of additional cell compression
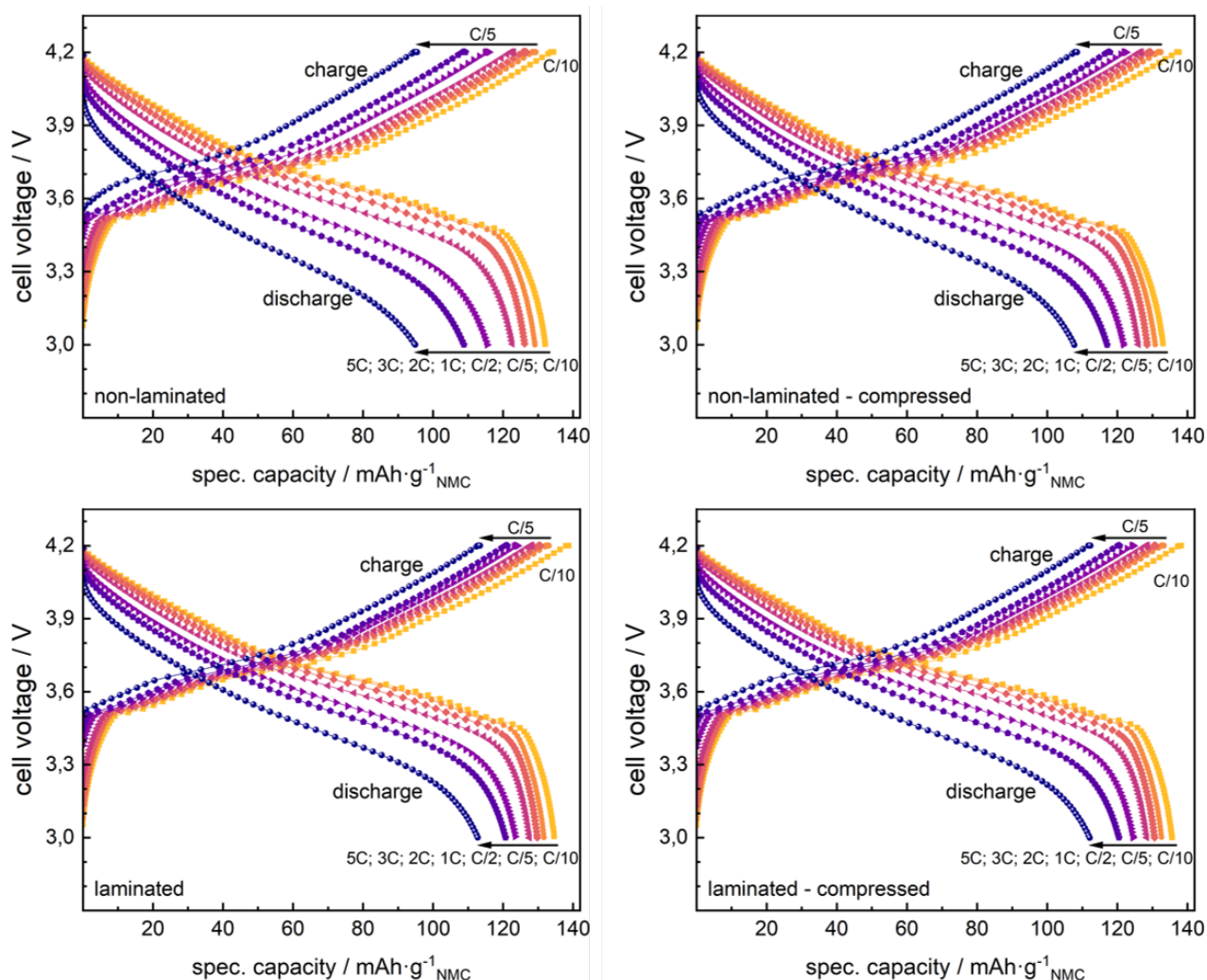
Fig. 4.12: Charge/Discharge profiles: additional compression on single cell – discharge rate tests; (a) non-laminated cell uncompressed; (b) non-laminated cell compressed; (c) fully laminated cell uncompressed; (d) fully laminated cell compressed.

The charge-discharge cycles of laminated and non-laminated cells at compressed and uncompressed states at discharge rate test are shown in Fig. 4.12. The non-laminated, uncompressed cell delivered the discharge capacities 132 mAh·g^{-1} (100%) and 95 mAh·g^{-1} (100%) at C-rate of C/10 and 5C, respectively. Additional compression to non-laminated cells provides a slight improvement in the discharge capacities of 133 mAh·g^{-1} (101%) and 108 mAh·g^{-1} (114%) at C-rate of C/10 and 5C, respectively. On the other hand, the fully laminated cell still overcomes this level at uncompressed state by giving the capacities of 136 mAh·g^{-1} (103%) and 114 mAh·g^{-1} (120%), while the compression of laminated cells does not significantly affect the discharge capacity at C/10 rate, 137 mAh·g^{-1} (104%) and 5C rate to 112 mAh·g^{-1} (118%) compared to the uncompressed state.
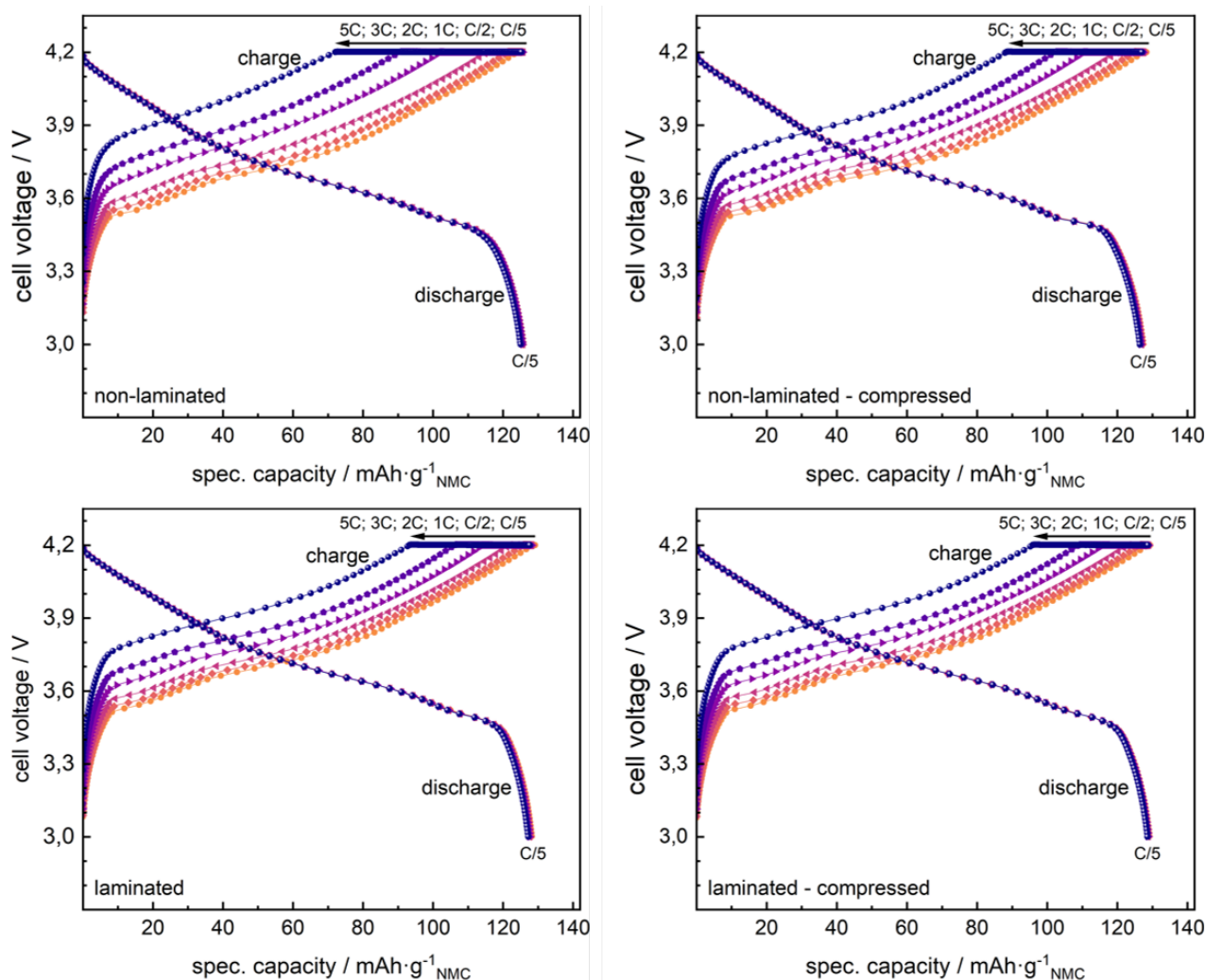
Fig. 4.13: Charge/Discharge profiles: additional compression on single cell – charge rate tests; (a) non-laminated cell uncompressed; (b) non-laminated cell compressed; (c) fully laminated cell uncompressed; (d) fully laminated cell compressed.

The charge-discharge cycles of laminated and non-laminated cells at compressed and uncompressed state at charge rate test are shown in Fig. 4.13. The non-laminated, uncompressed cell delivered the charge capacities 124 mAh·g^{-1} (100%) and 124 mAh·g^{-1} (100%) at C-rate of C/5 and 5C, respectively. In contrast, the non-laminated, uncompressed cells delivered the CC charge capacities 124 mAh·g^{-1} (100%) and 70 mAh·g^{-1} (100%) at C-rate of C/5 and 5C, respectively. Additional compression to non-laminated cells slightly increases the CCCV charge capacities to 128 mAh·g^{-1} (103%) and 127 mAh·g^{-1} (102%) at C-rate of C/5 and 5C, while CC charge capacities are clearly increased to 128 mAh·g^{-1} (103%) and 88 mAh·g^{-1} (126%) at C-rate of C/5 and 5C, respectively. On the other hand, the fully laminated cell again overcomes this level even at uncompressed state by giving the above mentioned CCCV charge capacities of 129 mAh·g^{-1} (104%) and 128 mAh·g^{-1} (103%), and the CC charge capacities of 129 mAh·g^{-1} (104%) and 95 mAh·g^{-1} (136%). Additional compression of laminated cells does not significantly affect the CCCV charge capacities as well as the CC charge capacities.

Charge rate tests

Charge rate tests were performed at different C-rates using CCCV charging mode. The following charge capacities were measured after full charging steps.
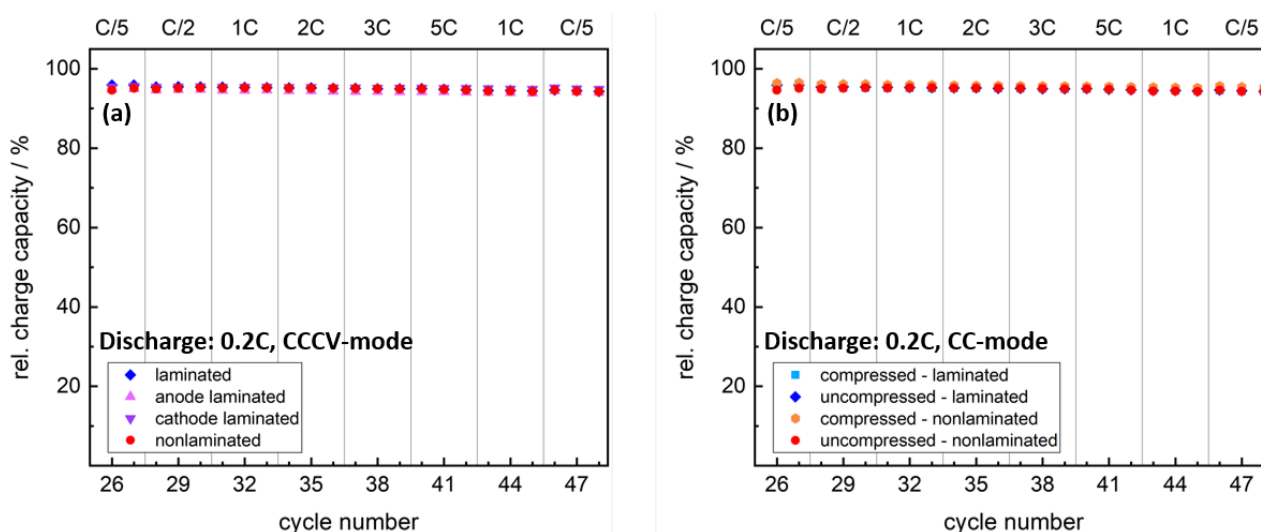
Fig. 4.14: Charge-rate tests of single cells – charge capacities (CCCV mode), charge rate per step as indicated, discharge rate: 0.2C CC-mode. (a) non-compressed cells non-laminated/partially laminated/fully laminated; (b) cells non-laminated/fully laminated in compressed and uncompressed state.

Normalization references used in Fig. 4.5, Fig. 4.6, Fig. 4.7 and Fig. 4.14

Tab. 4.3: Pouch cell normalization data.

analysis mode	cell	m (NMC) [g]	C (theo) [Ah]	C (abs dis 1st) [Ah]	C (abs dis 2nd) [Ah]
cycling 1C	laminated l2	0,2716	0,04562	0,03713	0,03674
cycling 2C	laminated l3	0,2641	0,04437	0,03620	0,03589
cycling 5C-1C	laminated l7	0,2762	0,04640	0,03772	0,03743
C-rate compressed	laminated l21	0,2511	0,04218	0,03440	0,03405
C-rate uncompressed	laminated l6	0,2688	0,04515	0,03639	0,03620
cycling 1C	non-laminated ul1	0,2706	0,04547	0,03588	0,03570
cycling 2C	non-laminated ul2	0,2744	0,04609	0,03658	0,03647
cycling 5C-1C	non-laminated ul7	0,2734	0,04593	0,03673	0,03658
C-rate compressed	non-laminated ul15	0,2446	0,04109	0,03251	0,03256
C-rate uncompressed	non-laminated ul3	0,2744	0,04609	0,03648	0,03625
C-rate uncompressed	anode laminated al4	0,2781	0,04672	0,03671	0,03661
C-rate uncompressed	cathode laminated kl4	0,2771	0,04656	0,03663	0,03654

Impedance spectroscopy – measurement series and fit parameters

Impedance analysis was performed on each three cells at laminated and non-laminated state to achieve reliable trends comparing the fitting parameters of each best cell. Partially laminated cells were studied at

each one cell for comparison. Fig. 4.15 gives the full measurement series at laminated and non-laminated state. The variation in the surface resistances, especially in the non-laminated cells, arise from the electrode surface roughness. The electrodes were used as-coated.
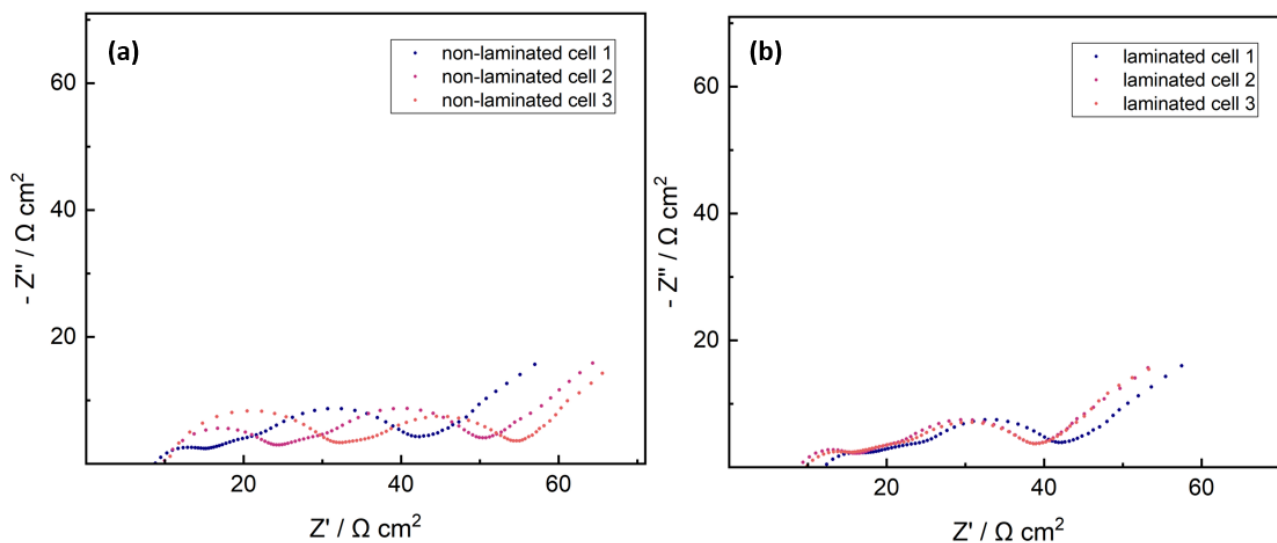
Fig. 4.15: EIS spectra (50 kHz – 10 mHz) of single cells collected at 25 °C in OCP at 3.6 V cell voltage after formation; (a) non-laminated cell series ; (b) laminated cell series.

Tab. 4.4 gives the fitting parameters for each measurement

Tab. 4.4: Impedance data – fit parameters.

	$R_{electronic}$ [$\Omega \cdot cm^2$]	R_{SEI} [$\Omega \cdot cm^2$]	$R_{CT-graphite}$ [$\Omega \cdot cm^2$]	R_{CT-NMC} [$\Omega \cdot cm^2$]
non-laminated cell 1	9	7	6	18
non-laminated cell 2	10	14	7	18
non-laminated cell 3	10	18	10	19
laminated cell 1	12	3	10	16
laminated cell 2	9	4	7	18
laminated cell 3	10	4	6	17
cathode laminated	11	22	13	33
anode laminated	9	21	11	14

5 EIS Study on the Electrode-Separator Interface Lamination

The article entitled *EIS Study on the Electrode-Separator Interface Lamination* by Martin Frankenberger, Madhav Singh, Alexander Dinter and Karl-Heinz Pettinger, published in *batteries*, 2019, Volume 5, Issue 4, Article No. 71, is presented in this section.[74] This is an open access article distributed under the terms of the Creative Commons Attribution Non-Commercial No Derivatives 4.0 License (permanent weblink: https://doi.org/10.3390/batteries5040071).

In this study, impacts of the electrode-separator lamination technique to the electrochemistry of Lithium Ion Batteries, was studied in detail using Electrochemical Impedance Spectroscopy. Studying the impedance response of graphite-NMC 111 single cells along varied State of Charge revealed significant reduction of the surface resistance arising from lamination at the cathode-separator interface, up to comparable levels of surface resistance reductions as demonstrated from cathode calendering. This surface resistance reduction was subsequently used as a normalization technique to the EIS response of graphite-NMC 111 single cells, allowing to monitor SEI growth phenomena directly from the normalized surface resistance signal.

The well-known reduction in capacity fade along fast-charging cycling, could therefore be attributed to a significant reduction in SEI growth, arising from lamination at the anode-separator interface.

Author contributions:

The author of this thesis manufactured all electrodes and test cells, designed and performed electrochemical experiments, analyzed and visualized any data and drafted the manuscript. M. Singh helped in designing the experiment agenda. A. Dinter and K.-H. Pettinger helped in editing the manuscript.

5.1   Abstract

This paper presents a comprehensive study of the influences of lamination at both electrode-separator interfaces of Lithium Ion Batteries consisting of $LiNi_{1/3}Mn_{1/3}Co_{1/3}O_2$ cathodes and graphite anodes. Typically, electrode-separator lamination shows a reduced capacity fade at fast-charging cycles. To study this behavior in detail, the anode and cathode were laminated separately to the separator and compared to the fully laminated and non-laminated state in single-cell format. The impedance of the cells was measured at different states of charge and during the cycling test up to 1500 fast-charging cycles. Lamination on the cathode interface clearly shows an initial decrease in the surface resistance with no correlation to aging effects along cycling, while lamination on both electrode-separator interfaces reduces the growth of the surface resistance along cycling. Lamination only on the anode-separator interface shows up to be suffcient to maintain the enhanced fast-charging capability for 1500 cycles, what we prove to arise from a significant reduction in growth of the Solid Electrolyte Interphase.

5.2   Introduction

Lithium Ion Battery technology has grown to a market leader in the field of rechargeable batteries in the last decades. LIBs are used as the energy source for portable devices and electric vehicles, as well as for stationary energy storage systems to ensure grid stability upon fluctuations from renewable energy sources. To improve the fast-charging capability as well as the travelling distance of the EVs, ongoing research mainly addresses the basic cell components like active materials,[368,369] electrolyte,[64] separator,[52,137,138,370] and manufacturing steps. Different manufacturing techniques, such as ultra-thick electrodes,[196–199] calendering process,[186] controlled stack pressure,[353,366] laser structuring[315,317,318,363,364,371] and lamination,[73] have been applied to increase the power density, energy density, lifetime and for cost reduction of LIBs. Typically, the calendering process improves the contact situation between the active material particles,[353] which leads to an increase of the rate capability as well. On the other hand, extensive calendering can break the active material particles and block the lithium ions at the electrode-electrolyte interface which makes the fast-charging capability problematic.[71,186]

The electrode-separator lamination technique is known for the simplification of the stacking process upon reducing the probability of stack component slipping in the anode-separator-cathode compound,[202] as well as accelerating the manufacturing speed. Besides, it can also improve the fast-charging capability and reduce the capacity fade at high C-rates.[73] This leads to the assumption that the detailed mechanisms that drive the fast-charging capability upon electrode-separator lamination are not completely understood so far, which inspired this study.

A recent study of lithium metal anodes showed that surface treatments for smooth lithium surfaces can significantly suppress lithium dendrite growth by modifying the surface topography and local surface chemistry, therefore lowering the Solid Electrolyte Interphase growth losses during cycling.[304] Similarly, it was shown that electrochemical polishing on alkali metal anodes, which yield ultra-smooth surfaces, provide ultra-thin SEI layers which possibly suppress dendrite growth along cycling.[372]

In our previous study, cross-section images gained by scanning-electron-microscopy clearly showed pore size reduction at both electrode-separator interfaces upon lamination.[73] Hence, the lithium ion diffusion paths can be expected to be shortened and homogenized at both electrode-separator interfaces. As a result, the ion current density distribution along the active area of the full cell gets equalized according to the ion path length homogenization on the electrode-separator interfaces. Equalizing the current density distribution reduces the possibility to locally reach exceptional high ohmic overpotentials, high enough to undergo the lithium deposition potential and cause local lithium dendrite formation, especially at high charging rates. Similar effects were found by S. Müller et al., who recently reported a clear correlation for graphite anode inhomogeneities at different scale lengths to possibly cause local overpotentials high enough to undergo the lithium deposition potential.[192]

To overcome some of the mentioned problems, the electrode-separator lamination technique provides proper contacts of separator and electrode at micro level. Suppression of ridges and wrinkles as well as reducing the probability to form cracks during cycling, analogously holds the potential to prevent dendrite formation and SEI growth. Validity of this assumption can be reasonably studied using electrochemical impedance spectroscopy.

To appropriately study the contribution of each electrode within a full cell using EIS, typically three electrode geometries are designed and used, which unfortunately requires special modifications to any kind of full cell design.[232,233] In case of two-electrode impedance spectroscopy, the distinction of each electrode contribution is challenging, but possible.[233] The EIS signal responses for $LiNi_{1/3}Mn_{1/3}Co_{1/3}O_2$ cathodes[71] or related structures[226] and graphite anodes[227,228] have yet been studied in detail. Using this information, the EIS signal of a graphite/NMC full cell could be considered well understood so far. Nevertheless, in literature the interpretation of the surface resistance semicircle reflects several further aspects. While the signal is often assigned to mainly depend on the SEI,[224,373] there are also studies that show separate influences arising from the electrode-current collector contact situation.[225] Therefore, reliable studies of SEI effects emerging from the surface resistance signal have to deal with a proper separation of the signal contributions.

To overcome this diffculty, EIS measurements are either driven at exceptional low temperatures,[224] which is problematic when aiming for aging studies purely based on cycling effects, or by introducing reference electrodes into the cell geometry.[232,233]

In this study, we will show the ability of the lamination technique to provide this signal separation even in a two-electrode geometry, and use the correlation to prove the enhanced fast-charging capability of laminated cells to arise from a reduction in SEI growth.

5.3   Results and discussion

5.3.1 Cathode-separator lamination effects

Single cells consisting of a NMC cathode, separator and graphite anode were studied via EIS in non-laminated/partially laminated/fully laminated state along varied state of charge after three formation cycles (C/10 rate) and two initial cycles at 1C rate. Fig. 5.1 shows the impedance spectra gathered upon different lamination modes.
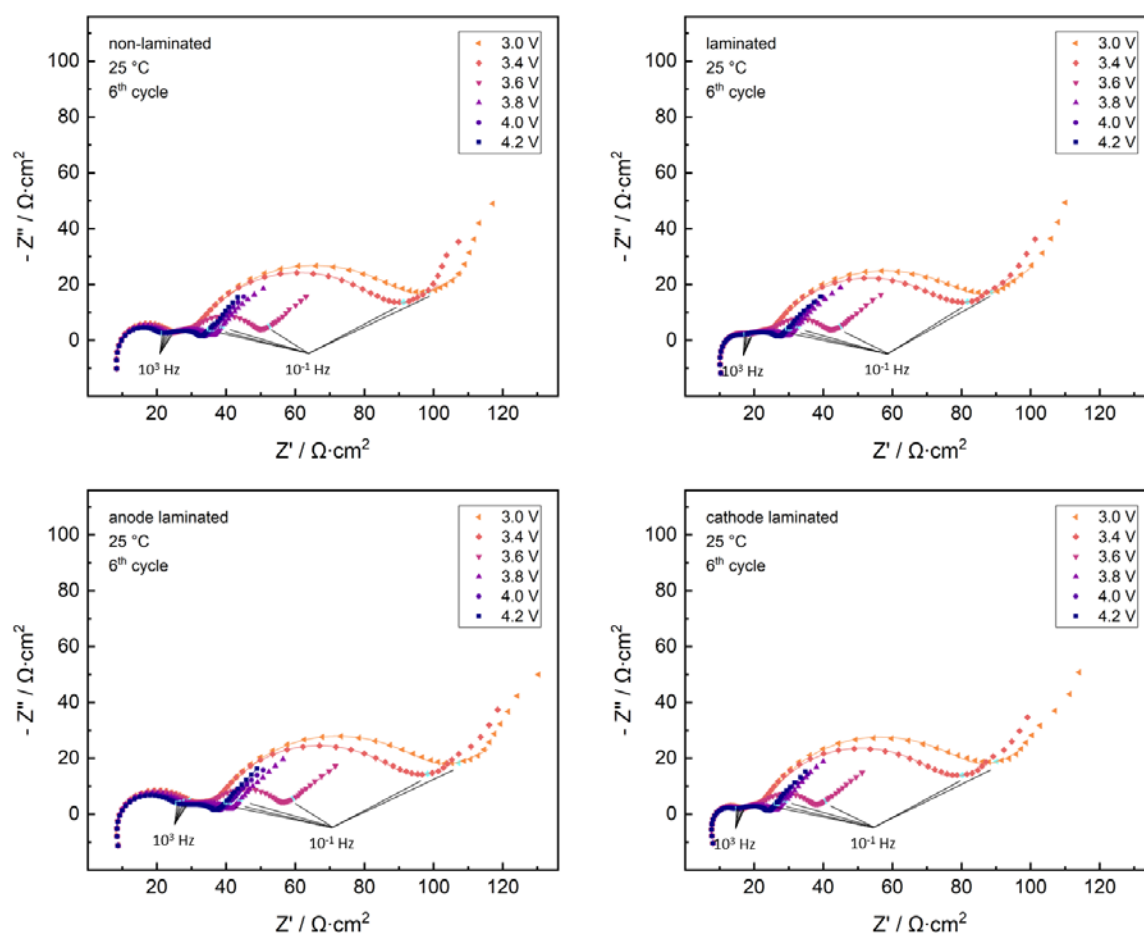
Fig. 5.1: Impedance measurements of laminated/partially laminated/non-laminated cells: EIS (100 kHz – 10 mHz) along charging step, 6th cycle; fitting curves indicated as solid lines; data points at 10^3 Hz and 10^{-1} Hz highlighted in pale blue.

The Nyquist plots uniquely show inductive behavior at the high-frequency regime, followed by three semicircles and the typical Warburg behavior at the lowest frequencies. For further studies, we characterize the three semicircles and the Warburg regime using the equivalent circuit model shown in Fig. 5.2.
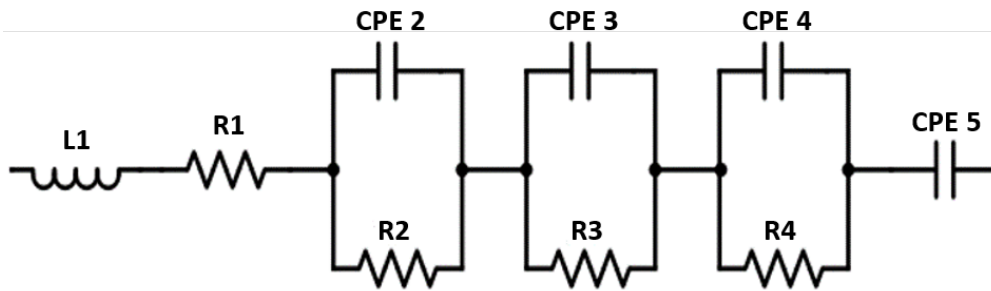
Fig. 5.2: Equivalent circuit model used for EIS fit analysis.

This common equivalent circuit model is frequently used in literature[224] to describe NMC/graphite full cells. In the highest frequency regime, the signal is dominated by inductive phenomena arising from the impedance measurement environment. Both inductance element L1 and the electronic resistance R1, considered to mainly arise from the electrolyte resistance, contain side influences from the setup, such as cell tabs, welding points, impedance channel contacts and cables. The first semicircle represents the surface resistance phenomena. The second and third semicircle are driven by the charge-transfer reactions of graphite anode and NMC cathode, respectively. Low frequency phenomena arise from solid state diffusion characteristics, that can be split into closed and open Warburg regime,[78] and therefore sometimes occurring as a consecutive series of slopes in the Nyquist presentation of the lowest frequency responses. As described above, signals from both charge-transfer reactions tend to overlap in this reference system as arising from the sum of the graphite anode and NMC cathode charge-transfer contributions.[226–229] For proper signal separation of these charge-transfer contributions, typically three-electrode cell designs are used involving reference electrodes. But in the case of NMC/graphite full cells, given knowledge on the separate EIS signal trends along SOC for the NMC cathode[374] or related composite materials,[226] and graphite anode[227,228] can be used to identify the individual full cell signal contributions to the charge-transfer resistance. It is well accepted that in case of LIB full cells the sum of the signal contributions of the separate electrodes define the EIS response in a two-electrode geometry.[229,375] I. Jimenez Gordon et al. described the signal contribution of graphite anodes in LIBs.[227,228] While the surface resistance contribution, arising from porosity aspects and SEI characteristics, stays independent from the SOC of the cell,[227] the charge-transfer signal of graphite decreases with increasing SOC, following a characteristic trend.[228] G. Liu et al. clarified the EIS trends of composite cathodes with respect to the amount and ratio of the conductive additive and PVDF binder, identifying separate mechanisms to drive the raise in impedance depending both on the ratio and on the total content of binder and conductive additive.[226] In the case of a ratio of 0.8:1 for acetylene black : PVDF, both for the total contents of 3.6% and 9%, they found a characteristic increase of the charge-transfer resistance with increasing depth of discharge. A drastic increase of the slope was found approaching 100% DOD.[226]

The highlighted data point set at 10^3 Hz in Fig. 5.1 lies close to the minimum between the first and second semicircle for all shown Nyquist datasets. As its relative position does not change with SOC for any cell, the surface resistance, that characterizes the first semicircle, can be considered independent from SOC. The

second highlighted data point series at 10^{-1} Hz lies within the Warburg regime at high SOC for all cells, shifting closer to the minimum between the third semicircle and Warburg regime with decreasing SOC. This behavior indicates a shift to lower time constants of the cathode charge-transfer process with decreasing SOC, which is a known effect on the charge-transfer resistance of NMC based full cells.[374]

Using the described correlations of the EIS signal response, the equivalent circuit analysis of the signals shown in Fig. 5.1 is unambiguous. As for the structure of the chosen equivalent circuit, the open Warburg behavior was excluded from the data fit. Results are presented in Fig. 5.3 and Fig. 5.4.
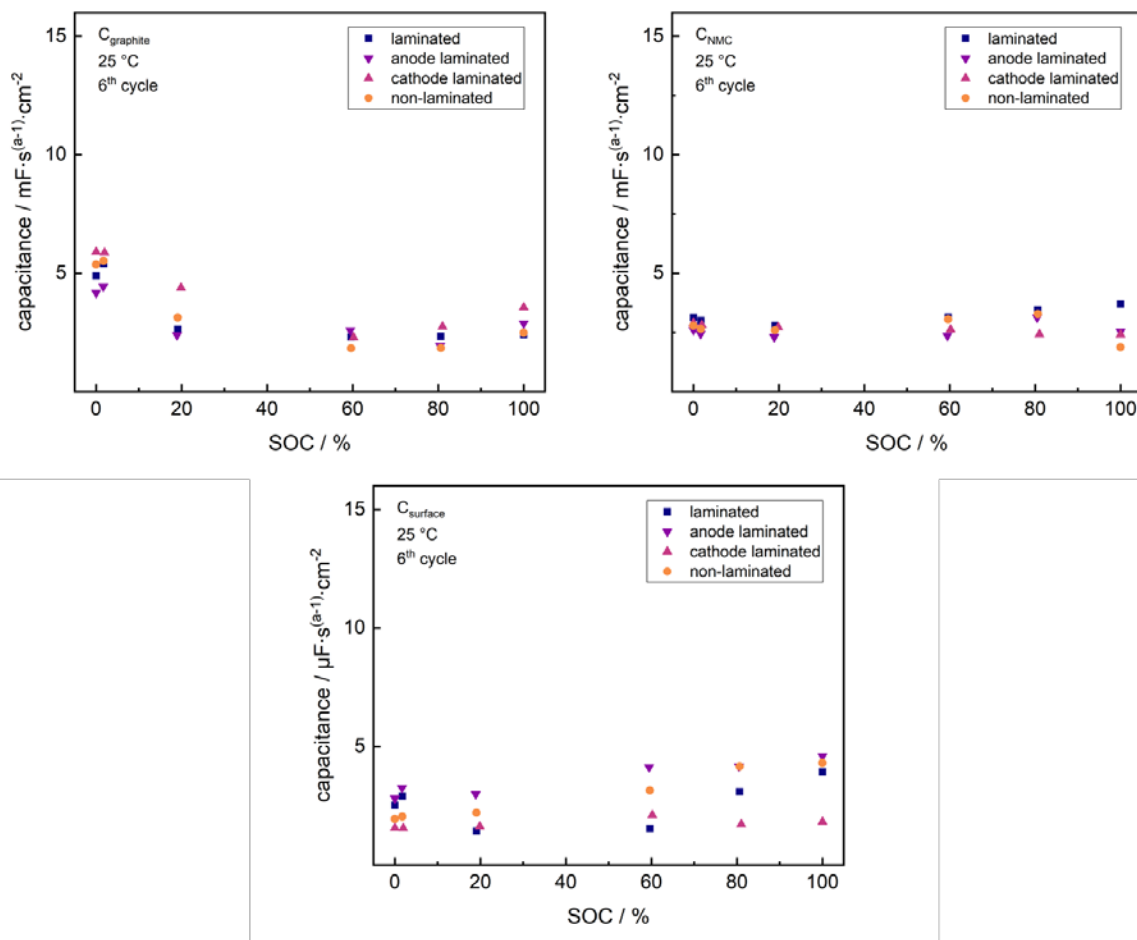
Fig. 5.3: EIS capacitance fit parameters of laminated/partially laminated/non-laminated cells along charging step, sixth cycle; data normalized to geometric electrode area.

As shown in Fig. 5.3, the capacitance fit parameters for the graphite anode and NMC cathode lie around $3 - 4$ mF·s$^{(a-1)}$·cm^{-2} with negligible dependence on SOC, which is in the range of typically reported values for EIS capacitance fit parameters, normalized to the geometric electrode area, of graphite anodes and composite cathodes in non-aqueous electrolytes.[376–378] The capacitance fit parameters of the surface resistance semicircle show no significant correlation to the SOC and lie around $3 - 5$ µF·s$^{(a-1)}$·cm^{-2} for all cells, which is in the range of double layer capacitances of non-aqueous electrolytes.[377] Further information can be extracted from the resistance fit parameters, shown in Fig. 5.4.
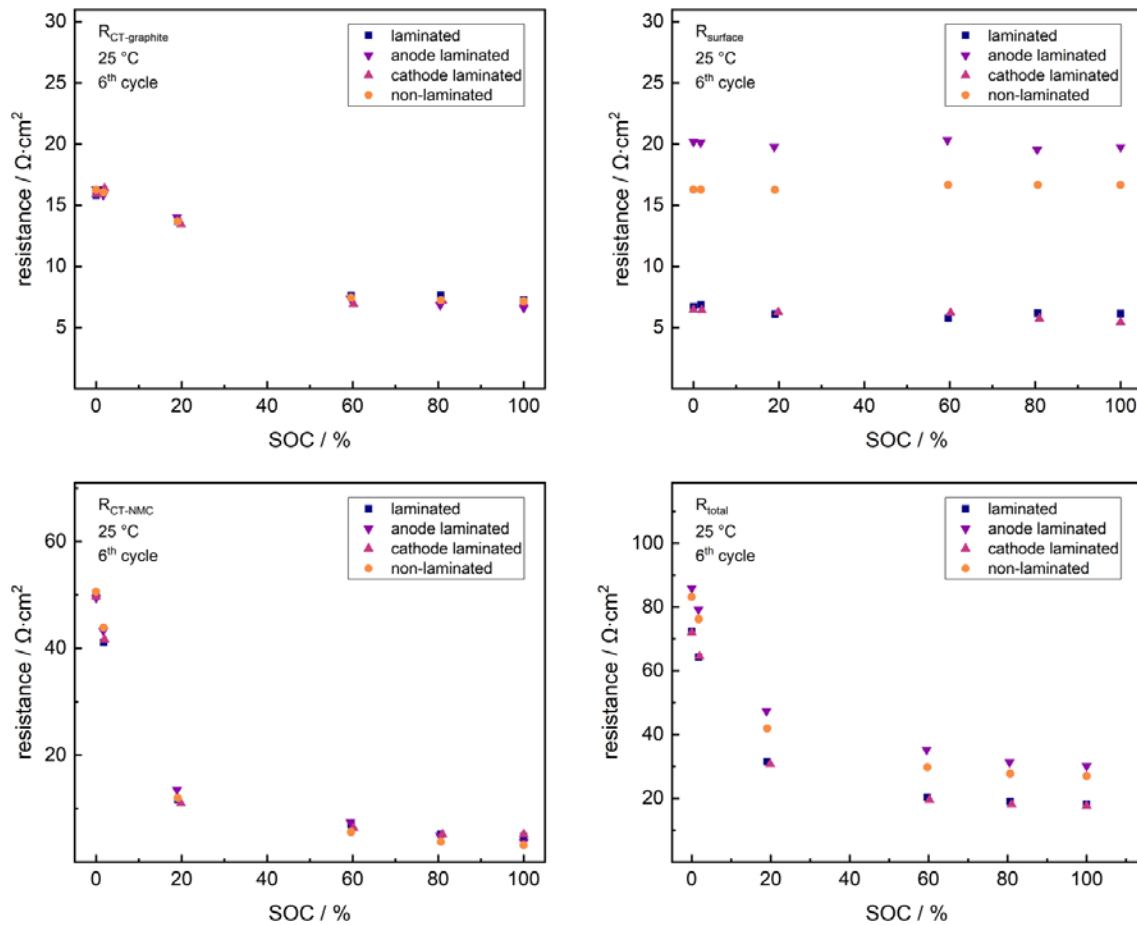
Fig. 5.4: EIS resistance fit parameters of laminated/partially laminated/non-laminated cells along charging step, sixth cycle; data normalized to geometric electrode area.

For all cells, the charge-transfer resistance signal for the graphite anode decreases initially down to ~ 14 $\Omega \cdot cm^2$ at 20% SOC. For SOC higher than 60%, the charge-transfer signals lie at a constant lower plateau at around ~ 7 $\Omega \cdot cm^2$. This trend of the graphite anode charge-transfer resistance was well-described by I. Jiménez Gordon et al.[227,228] As it can be seen, there is no significant difference between different lamination modes.

Analogously, a logarithmic drop of the NMC charge-transfer resistance along increasing SOC is found for all cells, with no correlation to any lamination mode. This logarithmic trend of the NMC charge-transfer signal is well-known.[226,379]

The first significant difference between the lamination modes can be found in the trends of the surface resistance. Both non-laminated cell ~ 16 $\Omega \cdot cm^2$) and anode-laminated cell (~ 20 $\Omega \cdot cm^2$) show relatively high surface resistance signals, whereas cathode-laminated and fully laminated cells both drop to a surface resistance signal around ~ 6 $\Omega \cdot cm^2$, especially at higher SOC. H. Zheng et al. found a similar drop of the surface resistance purely upon calendering NMC cathodes to different porosities, where also lowest resistances at around 5 $\Omega \cdot cm^2$ are reached.[71] This recognizable drop arises from porosity changes and contact optimization at the cathode side. As both lamination and calendering technique are applied previous to final cell assembly,

this surface resistance drop can act as a normalization for the starting conditions of the full cell surface resistance. After minimizing all well-known NMC cathode influences on the surface resistance as in the cathode-laminated and fully laminated state previous to cycling studies, any further changes on the surface resistance upon cycling uniquely arise from changes in the SEI.

5.3.2 Anode-separator lamination effects

Fig. 5.5 presents the results of non-laminated/partially laminated/fully laminated cells in the cycling test, when charging at 5C (CCCV mode) and discharging at 1C (CC mode). Recent studies on electrode-separator lamination showed a recognizable reduction in capacity fading upon fast-charging cycles at fully laminated state.[73]
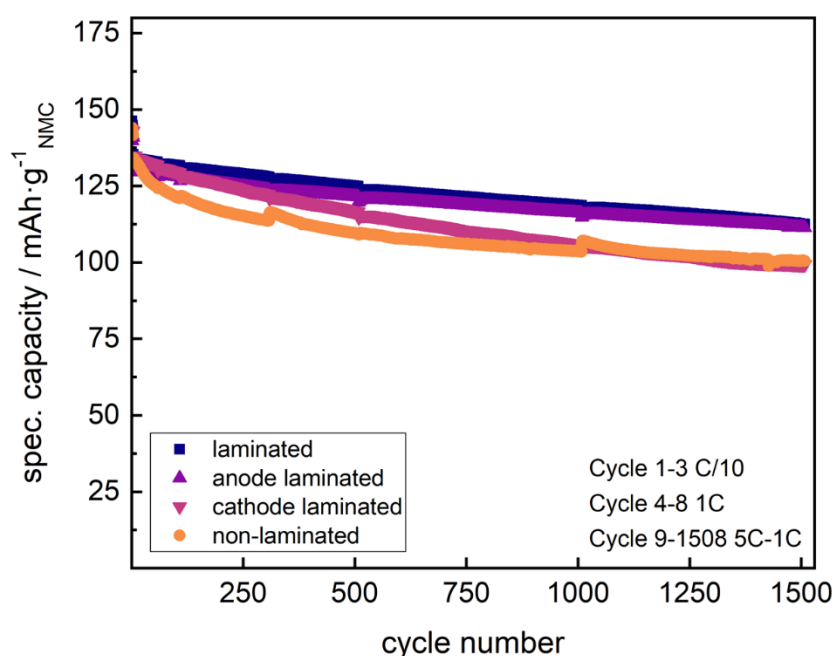
Fig. 5.5: Discharge capacity data of laminated/partially laminated/non-laminated cells in fast-charging cycle test; charge at 5C CCCV mode, discharge at 1C CC mode.

Both the non-laminated cell and cathode-laminated cell reveal severe capacity fading, decreasing from 133.0 mAh·g^{-1} (100%) and 133.4 mAh·g^{-1} (100%) at the 9th cycle, down to 100.4 mAh·g^{-1} (75.5%) and 99.3 mAh·g^{-1} (74.6%) at the 1508th cycle, respectively. Additionally, both laminated and anode-laminated cells show a reduced capacity fading, decreasing from 133.2 mAh·g^{-1} (100%) and 129.6 mAh·g^{-1} (100%) at the 9th cycle, down to 112.5 mAh·g^{-1} (84.6%) and 111.4 mAh·g^{-1} (83.7%) at the 1508th cycle, respectively. Capacity fade trends are summarized in Tab. 5.1.

Tab. 5.1: Capacity fade of laminated/partially laminated/non-laminated cells in the fast-charging cycle test.

Cycle Number	Laminated	Anode-Laminated	Cathode-Laminated	Non-Laminated
9	133.2 mAh·g^{-1}	129.6 mAh·g^{-1}	133.4 mAh·g^{-1}	133.0 mAh·g^{-1}
1508	112.5 mAh·g^{-1}	111.4 mAh·g^{-1}	99.3 mAh·g^{-1}	100.4 mAh·g^{-1}

From the cycling test results, there arise two unique conclusions. First, minimization of the surface resistance via cathode lamination cannot ensure a permanent reduction in capacity fading upon fast-charging cycles, as is shown from the cathode-laminated cell. Second, yet the partial lamination on the anode interface is suffcient to generate the well-known reduction of capacity fade during fast-charging cycles, as shown from the discharge capacity trend of the anode-laminated cell in Fig. 4.5. The data therefore show clearly that the fast-charging capability arises only from lamination at the anode interface, while the cathode interface does not affect the fast-charging aging mechanisms.

The cells studied at the fast-charging cycle test were also characterized with EIS along the cycling. Fig. 5.6 shows the trends of the respective datasets in the Nyquist plots.
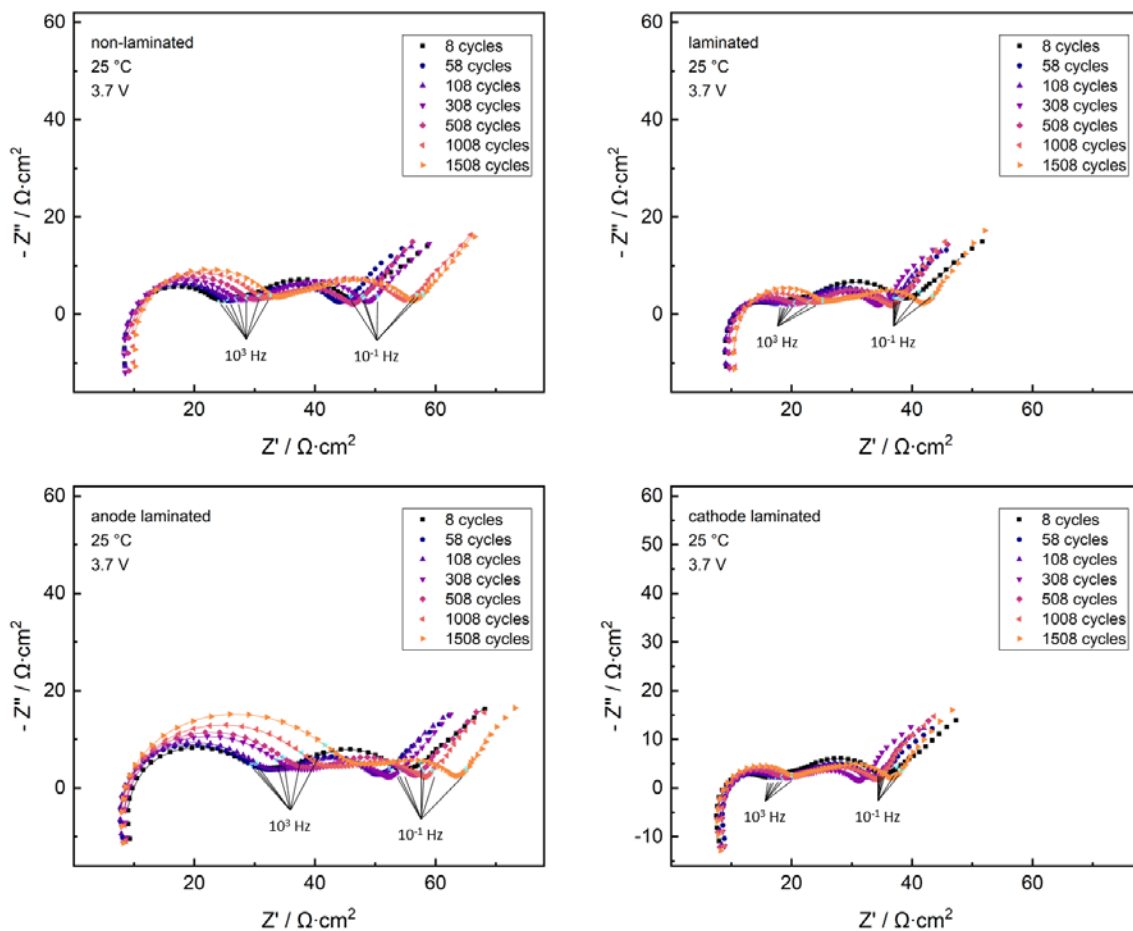
Fig. 5.6: Impedance measurements of laminated/partially laminated/non-laminated cells: EIS (100 kHz – 10 mHz) along fast-charging cycles; fitting curves indicated as solid lines; data points at 10^3 Hz and 10^{-1} Hz highlighted in pale blue.

Similar to Fig. 5.1, the highlighted data point set at 10^3 Hz in Fig. 5.6 lies close to the minimum between the first and second semicircle for all datasets, while the second highlighted dataset series at 10^{-1} Hz lies close to the minimum between the third semicircle and Warburg regime.

Both benchmark frequency datasets do not change in relative position within the Nyquist datasets along cycling, indicating a negligible change of the time constant with cell aging at the chosen conditions. This correlates well to findings by W. Waag et al. on NMC based full cells at moderate SOC.[374]

To exclude side influences from cathode interface phenomena to the surface resistance signal, EIS aging studies focused on SEI effects require a minimization of the surface resistance starting condition. As discussed above, lamination at the cathode-separator interface minimizes the surface resistance previous to cycling influences. Initially, both the cathode-laminated and fully laminated cell have smaller surface resistance semicircles, while anode-laminated and non-laminated cell reveal enlarged surface resistance semicircles. All cells reveal, that the surface resistance semicircle increases with rising cycle number, while no clear trend for the charge-transfer semicircles arises along cycling for any cell. Further insights can be extracted by studying the semicircles in the equivalent circuit fit.

Again, due to the structure of the chosen equivalent circuit, the open Warburg regime was excluded from the data fit. Fig. 5.7 shows the trends of the resistances and capacitances calculated uponthe fitting.
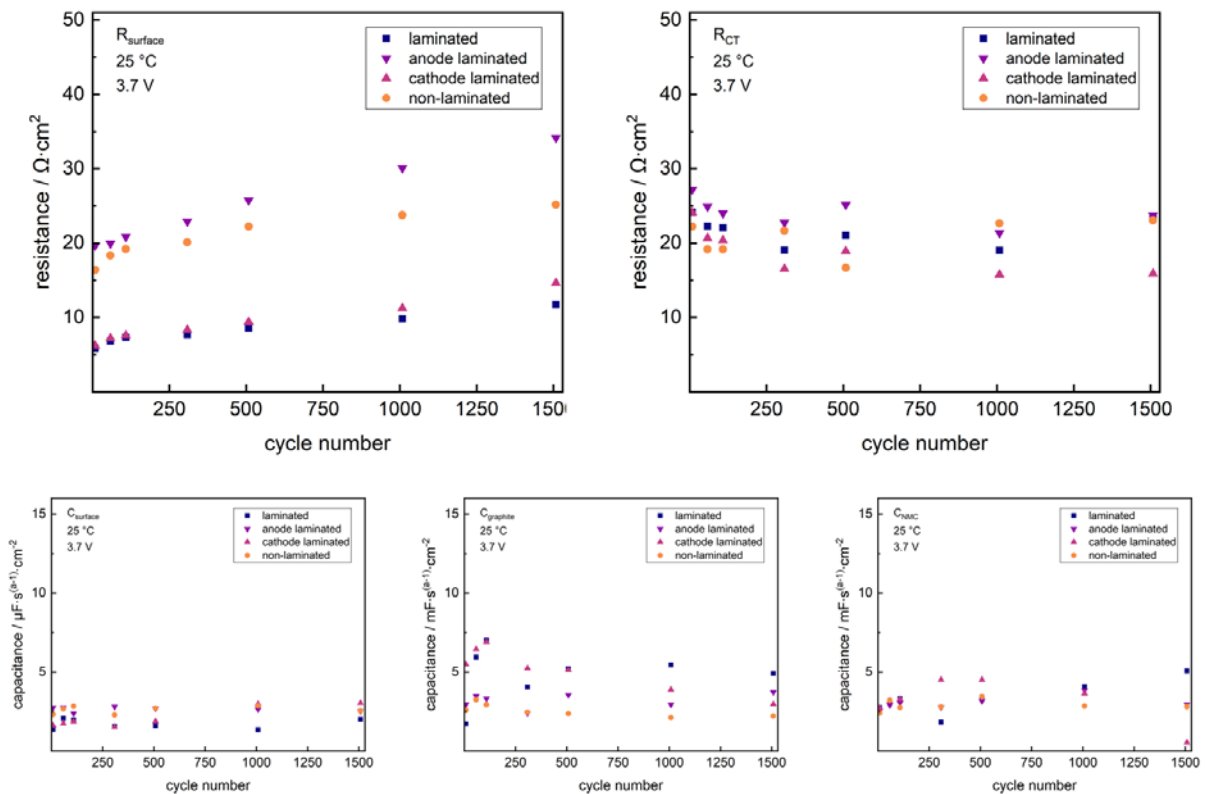
Fig. 5.7: EIS resistance fit parameters of laminated and non-laminated single cells along fast-charging cycles; data normalized to geometric electrode area.

As both charge-transfer signals have drastic overlap, only the sum of the fitted charge-transfer resistances can be studied. No clear trend on the charge-transfer resistance signal along cycling is found for any lamination mode. Although all surface resistance signals differ in starting values, as indicated in the Nyquist plots, they all increase upon cycling. Both the capacitance fit parameters for the graphite anode and NMC cathode $(3 - 4\,mF \cdot s^{(a\ 1)} \cdot cm^{-2})$ and the capacitance signals of the surface resistance semicircles $(\sim 3\,mF \cdot s^{(a-1)} \cdot cm^{-2})$ reveal no significant trend along cycling.

As discussed above, focusing on the SEI trends arising from the lamination modes requires minimization of the cathode influences on the surface resistance. Therefore, only the surface resistance signals of the cathode-laminated and fully laminated cell deliver unpersuaded information on the SEI changes.

As shown in Fig. 5.8, both cathode-laminated and fully laminated cells have a minimized surface resistance of 6.2 $\Omega \cdot cm^2$ and 5.8 $\Omega \cdot cm^2$ at the eigth cycle. The cathode-laminated cell increases in surface resistance up to 14.6 $\Omega \cdot cm^2$ after 1508 cycles, while the laminated cell dampens the surface resistance growth to 11.7 $\Omega \cdot cm^2$ after 1508 cycles. This trend in surface resistance clearly proves a reduction in SEI growth, which is specifically due to the lamination at the anode-separator interface.
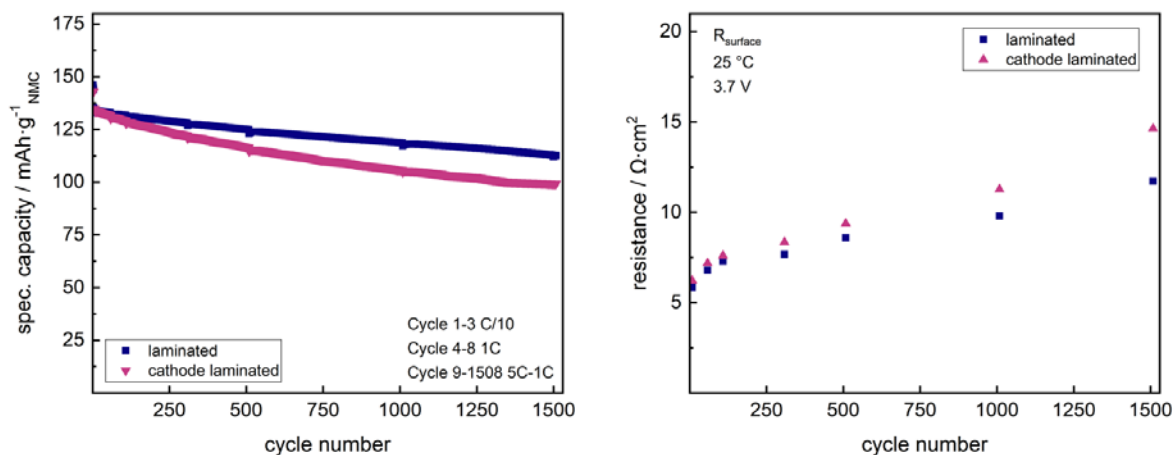
Fig. 5.8: Decrease of discharge capacity vs. increase of surface resistance of laminated and cathode-laminated single cells along fast-charging cycles.

5.4   Materials and methods

5.4.1 Electrode preparation

For preparation of anode slurries, MAGE3 graphite (HITACHI CHEMICAL, Sakuragawa, Japan), Solef® 5130 polyvinylidene difluoride (PVDF, SOLVAY, Milan, Italy), Super C65 carbon (IMERYS, Bodio, Switzerland) and SFG6L graphite (IMERYS) were mixed in a ratio of 90/7/2/1 with N-methyl-pyrrolidone (NMP, Overlack, Mönchengladbach, Germany) in a planetary mixer (TX 2, INOUE, Isehara, Japan), while for cathodes, $LiNi_{1/3}Mn_{1/3}Co_{1/3}O_2$ (NMC, NM-3102 h, BASF TODA America, Battle Creek, USA), PVDF (SOLVAY), Super C65 carbon (IMERYS) and KS6L graphite (IMERYS) were mixed in a ratio of 93/3/3/1 with NMP. Anode and cathode slurries were coated on copper foil (15 µm, GELON LIB, Hong Kong, China) and aluminum foil (20 µm, GELON LIB), respectively, by single-side coating on a doctor-blade coater in a roll-to-roll process coating machine, including inline drying in a two-step drying tunnel at the temperature range of 135 – 150 °C. The averaged active mass loadings of cathode and anode electrodes were ~ 8.4 $mg·cm^{-2}$ (1.30 $mAh·cm^{-2}$) and ~ 4.2 $mg·cm^{-2}$ (1.51 $mAh·cm^{-2}$), respectively. Cathodes and anodes were matched to have a capacity balancing factor of ~ 1:1.16 in all full cells.

5.4.2 Pouch cell preparation

Within the pouch cell, punched cathode, anode and separator (inorganic filled separator, 67% Al_2O_3 and 33% PVDF/HFP copolymer) sheets with the dimensions 5 × 8 cm^2, 5.4 × 8.4 cm^2 and 5.8 × 8.8 cm^2 were assembled. For the fully laminated state, stacks of cathode-separator-anode were laminated to form a single stack by using a lamination machine (BLE 282 D, MANZ Italy, former Arcotronics Italia, Bologna, Italy) at the roll speed of 1.4 $m·min^{-1}$, using a line force of 157 $N·cm^{-1}$ in the temperature range of 100 – 120 °C. For separate electrode-separator lamination, stacks of cathode-separator-PE carrier and anode-separator-PE carrier were laminated at identical parameters. Pre-assembled pouch cell stacks were dried under vacuum at 110 °C for 12 h. 1 M $LiPF_6$ in EC : EMC 3:7 w/w (Selectilyte LP57, BASF, Florham Park, USA) and vinylene carbonate (VC, Vinylene Carbonate E, BASF, Florham Park, USA), mixed in a ratio of 98/2, was used as electrolyte. The pre-assembled stacks were filled with 1000 µL electrolyte within an argon filled glovebox (MB20, H_2O and O_2 content < 0.1 ppm, MBraun, Garching, Germany) and sealed under vacuum. Before starting the electrochemical characterization, wetting of all pores was ensured by keeping the cells at room temperature for 24 h previous to starting the formation cycles.

5.4.3 Electrochemical characterisation

Electrochemical characterization was done with a battery tester (CTS-LAB, BaSyTec, Asselfingen, Germany) and a potentiostat (PGSTAT204, METROHM, Filderstadt, Germany). Cells were cycled between 3.0 V and 4.2 V, using a CCCV protocol for charging (constant current protocol followed by constant voltage protocol) with a CV termination below 0.05C rate, and CC protocol for discharging. Formation was done by applying three cycles at 0.1C, using the nominal capacity of the NMC in each cell, calculated from the specific NMC capacity of 155 mAh·g^{-1}, given by the supplier. After formation, the discharge capacity of the third formation cycle was taken as the nominal capacity for C-rate calculation of all following steps.

For EIS analysis along SOC, cells were first discharged to 3.0 V at 0.2C rate after the fifth cycle, to then charge the cell up to each point of investigation at 0.2C rate. For EIS analysis along cycling, cells were charged to 3.7 V at 1C rate previous to EIS measurements at each specific cycle. Comparable temperature (25 °C) in EIS measurements was ensured by measuring in a cooled incubator (INCU-Line® IL 68 R, VWR, Ismaning, Germany). Cells rested for 2 h at OCV prior to each EIS measurement. EIS measurements were carried out in the frequency range of 100 kHz – 10 mHz (potentiostatic mode) using an amplitude of 10 mV$_{rms}$. For EIS data fitting the Z-fit protocol, included in the BT-Lab software, was used (BT-Lab V1.55, BioLogic SAS via GAMEC, Illingen, Germany).

To ensure reproducibility of the study, for each cell assembly mode at least three cells were prepared and studied thoroughly. At each path, the performance of the respective cell with lowest initial impedance contributions and lowest capacity fade along 1500 fast-charging cycles is shown and discussed.

5.5 Conclusion

NMC/graphite full cells were studied in several lamination modes upon significant interface lamination effects revealed by EIS. Along variation of the SOC, both NMC cathode and graphite anode charge-transfer signals were found to stay independent from any lamination mode. The initial surface resistance gets minimized upon lamination at the cathode-separator interface previous to cycling influences.

Fast-charging cycling studies revealed a clear correlation of the reduction in capacity fade, to arise from lamination at the anode-separator interface. The surface resistance minimization via cathode-separator lamination was furthermore used to exclude cathode influences on the surface resistance signal evolution in cycling tests. Using this correlation, the cycling studies prove the fast-charging capability to arise from a reduction in SEI growth specifically arising from lamination at the anode-separator interface.

So, lamination at the cathode-separator interface is found to decrease the internal cell resistances, while lamination at the anode-separator interface reduces long-term aging phenomena during fast-charging cycles.

Author contributions

Conceptualization: M.F., M.S. and K.-H.P.; methodology: M.F. and M.S.; software: M.F.; validation: M.F. and A.D.; formal analysis: M.F. and A.D.; investigation: M.F.; data curation: M.F. and A.D.; Writing – Original draft preparation: M.F.;Writing – Review and editing: M.F., M.S., A.D. and K.-H.P.; visualization: M.F.; supervision: M.S. and K.-H.P.; project administration: M.F.; funding acquisition: K.-H.P.

Funding

Conflicts of interest

The authors declare no conflict of interest. The funders had no role in the design of the study; in the collection, analyses, or interpretation of data; in the writing of the manuscript, or in the decision to publish the results.

5.6   Addendum – Statistics on EIS analysis for LIBs

This section was not published previously in any form. Maximum possible number of comparable graphite-NMC 111 single cells, all prepared from identical electrode batches (reference anode #2 and reference cathode #2, see Tab. 3.3 and Tab. 3.4) were used for further statistical analysis.

A series of 31 laminated graphite-NMC 111 single cells with theoretical capacities of 0.04661 – 0.05713 Ah and an anode:cathode balancing factor of 116.7 % ± 0.7 % passed an identical formation protocol of 2 cycles at 0.1 C-rate. The same formation and cycling protocol was applied to 22 non-laminated cells with theoretical capacities of 0.04776 – 0.05555 Ah and an anode:cathode balancing factor of 116.6 % ± 0.6 %.

Internal resistances R_{DC} of all cells after the formation were calculated from the voltage drop at at the end of discharge steps, i.e., from the difference between the discharge cutoff voltage $U_{\text{dis−cutoff}}$ and the voltage after 10 minutes of OCV relaxtion $U_{\text{dis−10 min relaxation}}$, divided by the discharge current $i_{\text{discharge}}$:

$$R_{\text{DC}} = \frac{|U_{\text{dis−cutoff}} − U_{\text{dis−10 min relaxation}}|}{i_{\text{discharge}}}$$

[34]

Distribution of the sampled internal resistances for the described cell sets, as obtained by equation [34], are presented in Fig. 5.9.
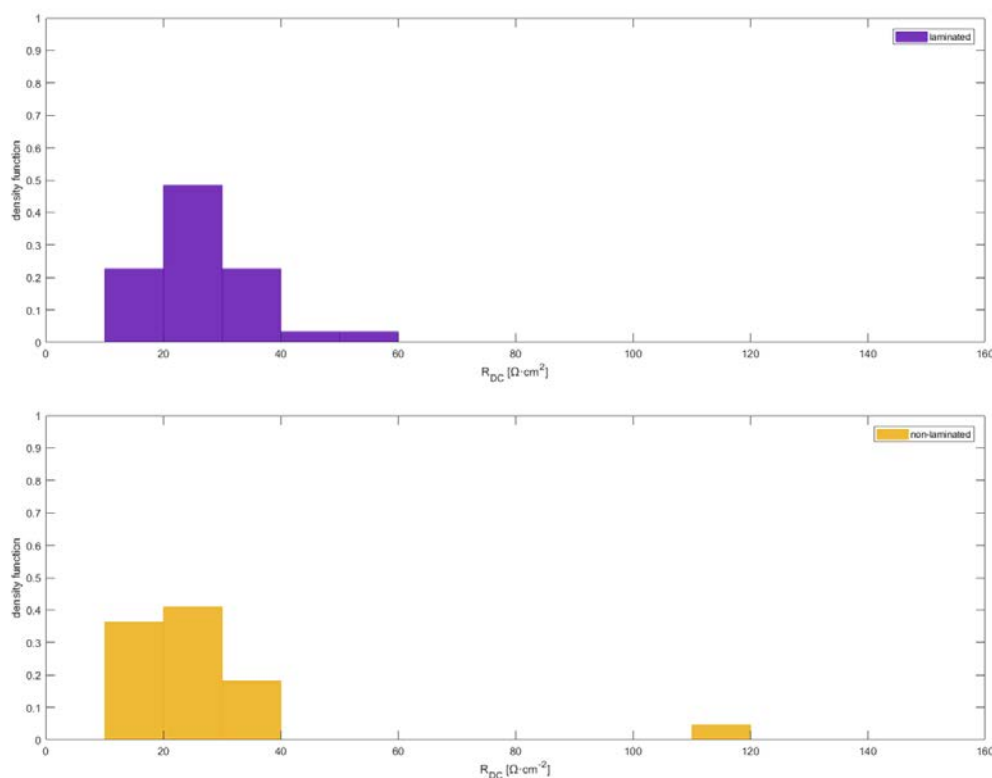
Fig. 5.9: Distribution of the sampled internal resistances R_{DC} of 31 laminated and 22 non-laminated graphite-NMC 111 single cells in fully discharged state after 2 formation cycles at 0.1 C-rate.

The mean of the resistance distributions in Fig. 5.9 is located at relatively low internal resistance values and the distribution is skewed towards a few very large values (see Tab. 5.2).

Similar analysis is possible on the surface resistances of as prepared graphite-NMC 111 single cells after formation. 15 laminated (theoretical capacities $0.04661 - 0.05655$ Ah; balancing $116.8\% \pm 0.8\%$) and 7 non-laminated cells (theoretical capacities $0.04776 - 0.05555$ Ah; balancing $116.4\% \pm 0.3\%$) were analyzed by EIS after formation, charging to 3.6 V at 0.1 C-rate and recording EIS data after a 2 h relaxation period at the open circuit potential..

The distribution of the measured surface resistances, as obtained by EIS fit analysis according to the equivalent circuit fit shown in Fig. 5.2, is presented in Fig. 5.10.
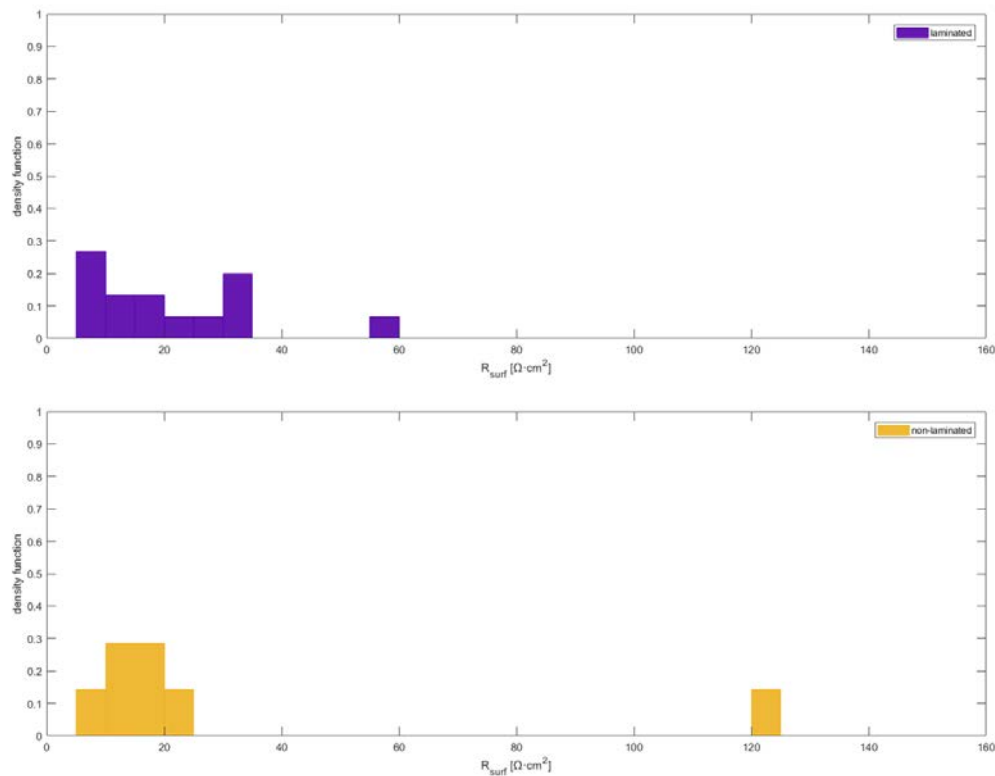
Fig. 5.10: Distribution of the measured surface resistances R_{surface} of 15 laminated and 7 non-laminated graphite-NMC 111 single cells charged to 3.6 V after 2 formation cycles at 0.1 C-rate.

Analogous to the distribution of the sampled internal resistances R_{DC}, the distribution of the surface resistances R_{surface} for laminated and non-laminated cells indicate a right-skewed non-symmetrical data distribution, with a mean value (see Tab. 5.2) at low internal resistance values.

For further analysis, mean μ (equation [20]) and standard deviation σ (equation [22]) are determined.

Tab. 5.2: Mean μ of R_{DC} and R_{surface} for laminated/non-laminated cells.

dataset	mean μ	standard deviation σ
R_{DC} – laminated	26.44	9.63
R_{DC} – non-laminated	27.07	21.05
R_{surface} – laminated	19.16	14.14
R_{surface} – non-laminated	30.03	40.14

Calculation of the standard deviation σ is bound to the prerequisite of normally distributed datasets for R_{DC} – laminated, R_{DC} – non-laminated, R_{surface} – laminated and R_{surface} – non-laminated, which is contradictive to their discussed non-symmetrical distribution appearance in Fig. 5.9 and Fig. 5.10. Consistent with this, $\sigma_{R_{\mathrm{DC}}-laminated}$, $\sigma_{R_{\mathrm{DC}}-non-laminated}$, $\sigma_{R_{\mathrm{surface}}-laminated}$ and $\sigma_{R_{\mathrm{surface}}-non-laminated}$ reveal extraordinarily high values.

For direct test on normal distribution, the datasets are evaluated by the Kolmogorov-Smirnov-test.

Tab. 5.3: Kolmogorov-Smirnov-test for R_{DC} – laminated, R_{DC} – non-laminated, R_{surface} – laminated and R_{surface} – non-laminated datasets; H_0: dataset has normal distribution; significance level $p_{\mathrm{significance}} = 5\,\%$.

dataset	p indicator	h indicator	null hypothesis
R_{DC} – laminated	$9.1521 \cdot 10^{-29}$	1	rejected
R_{DC} – non-laminated	$8.0393 \cdot 10^{-21}$	1	rejected
R_{surface} – laminated	$1.2681 \cdot 10^{-14}$	1	rejected
R_{surface} – non-laminated	$-1.1102 \cdot 10^{-15}$	1	rejected

Clearly, none of the datasets has a normal distribution, as already assumed by the histograms and by the standard deviation calculation.

More general analysis of the data distribution, is done by calculating their skewness γ using equation [29].

Tab. 5.4: Skewness γ of R_{DC} and R_{surface} for laminated/non-laminated cells.

dataset	skewness γ	probability density function structure
R_{DC} – laminated	1.7062	right-skewed
R_{DC} – non-laminated	3.9057	right-skewed
R_{surface} – laminated	1.0722	right-skewed
R_{surface} – non-laminated	1.9981	right-skewed

Both internal resistance R_{DC} and surface resistance R_{surface} datasets for laminated and non-laminated cells are clearly right-skewed.

The publication "EIS Study on the Electrode-Separator Interface Lamination" (chapters 5.1 – 5.5) dealt with differences on cell impedance of several cell datasets, e.g. surface resistance of laminated and non-laminated cells. So the achieved knowledge on the data distribution of the datasets R_{DC} – laminated, R_{DC} – non-laminated, R_{surface} – laminated and R_{surface} – non-laminated can now be used for further statistical analysis on the deviation of their means $\mu_{R_{\mathrm{DC}}-laminated}$, $\mu_{R_{\mathrm{DC}}-non-laminated}$, $\mu_{R_{\mathrm{surface}}-laminated}$ and $\mu_{R_{\mathrm{surface}}-non-laminated}$.

Though, due to the non-symmetrical data distribution, analysis of a significant deviation between the expectations of non-laminated and laminated cells in context of R_{DC} and R_{surface} characteristics, cannot be checked by a classical t-test, which would require sufficient datapoints (minimum 30 datapoints per set) and normal distribution within each dataset. Instead, the Wilcoxon ranksum test is used, which allows for analysis of a significant deviation between two subgroups, for freely distributed datapoints and limited data size.

Check of the null hypothesis (H_0: laminated non-laminated and laminated cell datasets have equal means) at a well established significance level of $p_{\text{significance}} = 5\,\%$ is shown in Tab. 5.5.[II]

Tab. 5.5: Wilcoxon rank sum test for test for R_{DC} and R_{surface} datasets; H_0: $\mu_{laminated} - \mu_{non-laminated} \leq p$; significance level $p_{\text{significance}} = 5\,\%$.

dataset	p indicator	h indicator	null hypothesis
R_{DC}	0.3912	0	accepted
R_{surface}	0.8325	0	accepted

In both cases for R_{DC} and R_{surface} datasets, the null hypothesis (H_0: $\mu_{laminated} - \mu_{non-laminated} \leq p$) cannot be rejected at the 5 % significance level. So, based on the Wilcoxon rank sum test, there is no significant difference between laminated cells and non-laminated cells in terms of R_{DC} and R_{surface}.

Therefore, the original assumption (internal resistance and surface resistance are lower for laminated cells than for non-laminated cells) cannot be supported statistically at this point.

Further insights might be achieved by transformation of the R_{DC} and R_{surface} datasets to get normal-distributed data.

Finally, it is clear that more detailed statistical analysis (based on larger data size) of the impedance trends of graphite-NMC 111 single cells with different lamination state, SOC and cycle number, as discussed in the publication "EIS Study on the Electrode-Separator Interface Lamination" (chapters 5.1 – 5.5), might lead to different conclusions.

[II] It should be noted that the h indicator of the used Matlab ranksum function refers to the inversed null hypothesis than commonly known $\left(H_0^{\text{Matlab}}: \mu_{laminated} - \mu_{non-laminated} \leq p \text{ instead of } H_0^{\text{common}}: \mu_{laminated} - \mu_{non-laminated} > p\right)$.

6   SEI growth impacts of lamination, formation and cycling in Lithium Ion Batteries

The article entitled *SEI growth impacts of lamination, formation and cycling in Lithium Ion Batteries* by Martin Frankenberger, Markus Trunk, Stefan Seidlmayer, Alexander Dinter, Johannes Dittloff, Lukas Werner, Roman Gernhäuser, Zsolt Revay, Bastian Märkisch, Ralph Gilles and Karl-Heinz Pettinger, published in *batteries*, 2020, Volume 6, Issue 2, Article No. 21, is presented in this section.[75] This is an open access article distributed under the terms of the Creative Commons Attribution Non-Commercial No Derivatives 4.0 License (permanent weblink: https://doi.org/10.3390/batteries6020021).

Given knowledge on lamination benefits for the fast-charging behaviour of lithium ion cells upon reduction in growth of the Solid Electrolyte Interphase, was expanded to studies on lamination impacts to fast-formation behaviour of graphite-NMC 111 single cells. Laminated and non-laminated cells were demonstrated to maintain similar capacity-fade up to 1C formation rate, while at formation and cycling at 2 C-rate, the electrode-separator lamination technique could significantly stabilize the cell aging at reduced capacity fading. Post-mortem Neutron Depth profiling indicated homogenous SEI growth for non-laminated cells at similar SEI amount for all studied formation and cycling rates. Superior anode fractions were found to reveal similar amount SEI both for laminated and non-laminated cells. Electrochemical impedance spectroscopy correlated the reduction in capacity fading of laminated cells to a significant reduction in surface resistance growth. This either indicates non-homogenous SEI growth for laminated single cells or significant influence of separate surface resistance phenomena.

Author contributions:

The author of this thesis manufactured all electrodes and test cells, designed and performed the electrochemical experiments, analyzed and visualized the electrochemical data and drafted the manuscript. S. Seidlmayer, A. Dinter and K.-H. Pettinger helped in designing the experiment agenda. S. Seidlmayer and M. Trunk helped in performing NDP measurements. M. Trunk, J. Dittloff, L. Werner, R. Gernhäuser, Z. Revay and B. Märkisch analyzed the NDP data and helped in visualization of the NDP data. M. Trunk, S. Seidlmayer, A. Dinter, Z. Revay, R. Gilles and K.-H. Pettinger helped in editing the manuscript.

6.1   Abstract

The accumulation of solid electrolyte interphases (SEI) in graphite anodes related to elevated formation rates (0.1C, 1C and 2C), cycling rates (1C and 2C), and electrode-separator lamination is investigated. As shown previously, the lamination technique is beneficial for the capacity aging in graphite-$LiNi_{1/3}Mn_{1/3}Co_{1/3}O_2$ cells. Here, surface resistance growth phenomena are quantified using electrochemical impedance spectroscopy (EIS). The graphite anodes were extracted from the graphite-NMC cells in their fully discharged state and irreversible accumulations of lithium in the SEI are revealed using neutron depth profiling (NDP). In this post-mortem study, NDP reveals uniform lithium accumulations as a function of depth with lithium situated at the surface of the graphite particles thus forming the SEI. The SEI was found to grow logarithmically with cycle number starting with the main formation in the initial cycles. Furthermore, the EIS measurements indicate that benefits from lamination arise from surface resistance growth phenomena aside from SEI growth in superior anode fractions.

6.2   Introduction

Lithium Ion Batteries are considered a reasonable energy-storage solution for electric vehicles and grid stabilization when introducing renewable energy sources.[78,119,380] Future requirements needs further increase of energy density, power density and reduction of costs. Substantial production costs arise from the formation cycles, realized by the supplier.[381] Initial cycles of LIBs based on graphite are required to form a stable protective layer covering all anode particles, what is typically done by applying specific time consuming procedures.[381] Implementation of accelerated formation protocols is therefore crucial for the cost-reduction of state of the art LIBs.[381]

Typical operating voltage ranges used for Lithium Ion Batteries based on graphite anodes and layered oxide $LiMO_2$ cathodes (with M = Ni, Co and Mn) are typically within 3.0 – 4.3 V.[91,94] During operation, carbon-based anodes undergo reduction potentials of typical electrolyte components[382] like ethylene carbonate, dimethyl carbonate, ethylmethyl carbonate, diethyl carbonate and $LiPF_6$, while typical composite cathodes exceed potentials inducing polymerization reactions of electrolyte components in the presence of electrolyte decomposition products.[268] Due to this issue, interphase layers of decomposition products form during operation between electrolyte and both electrode surfaces, first described by E. Peled as the solid electrolyte interphase.[143] Consecutively, electrolyte solvents and additives, as well as anode materials, were optimized to form stable, pin-hole-free anodic SEI layers during the first cycles.[164,383] Vinylene derived additives like vinylene carbonate or fluorinated solvents like fluoroethylene carbonate are frequently used as components optimizing SEI formation on graphite anodes or silicon based composite anodes.[161,162,165] Superior additive content of ≈ 2% VC was found for LCO/graphite cells.[163]

M. Meyerson et al. described impacts of the SEI chemistry on Li dendrite nucleation, identifying preferred Li nucleation sites at LiF-rich SEI regions.[304] I. Buchberger et al. studied several aging mechanisms of graphite-$LiNi_{1/3}Mn_{1/3}Co_{1/3}O_2$ cells with cycling at moderate conditions, elevated temperature or elevated cutoff voltage [5].[91] Traces of H_2O in the cell can release HF from $LiPF_6$ decomposition,[296,297] which induces cathode deformation and transition metal release, especially of Mn species, via corrosion reactions close to Hunter's reaction.[91,298,299] While losses of active cathode material have minor effects on capacity-fade, the transition metal deposition on the anodic SEI results in a significant increase of the SEI growth rate. Therefore the active lithium losses increase via lithium immobilization in the SEI, as well as the impedances both of NMC 111 cathode and graphite anode with cycling.[91] Similar aging phenomena at elevated cutoff voltages were shown by J. Kasnatscheew et al. for graphite-$LiNi_{5/10}Mn_{3/10}Co_{2/10}O_2$, graphite-$LiNi_{6/10}Mn_{2/10}Co_{2/10}O_2$ and graphite-$LiNi_{8/10}Mn_{1/10}Co_{1/10}O_2$ cells.[94] Recent studies reported minor influences of parasitic electrolyte oxidation reactions on NMC 111 cathodes at cutoff voltages below 4.6 V[63] and emphasized significant cathode capacity losses to arise mainly from partially reversible kinetic limitations due to changes in the crystal lattice of the NMC cathode particles,[93] in contrast to irreversible lithium losses induced by parasitic side reactions inducing SEI growth at graphite anodes.[91]

Influences of the formation protocol on the SEI in graphite-NMC 532 cells with 1.2 M $LiPF_6$ in EC : DEC (3:7) as an electrolyte, were studied by S. J. An et al.[270] By keeping the cell in high SOC during formation, they showed possible routes how to use accelerated formation rates up to C/5 while maintaining reduced surface resistances and lowered capacity fading along cycling.[270] Similarly, N. Rago et al. described an accelerated formation protocol up to C/5 rate for silicon/graphite-NMC 532 cells using FEC-rich electrolyte, applying C/20 rate only in a small voltage region. Despite indications for a significantly thicker SEI after accelerating the formation rate, their cells did not reveal additional capacity fading at 1C cycling.[165] Applying external pressure during operation was recently shown by H. H. Heimes et al. to considerably prolong CC charging phases at 1C formation rate of graphite-NMC 622 cells, similar to 1C formation at elevated temperature, but acting more cost effciently.[271]

M. B. Pinson and M. Z. Bazant created several theoretical models to fit and predict SEI growth, validated with published Lithium Ion Battery fade data.[384] Their porous electrode model clearly indicates a superior dependence of the SEI growth with time, while negligibly affected from the total number of charge/discharges cycles (in case of moderate anode thickness, charging rate and temperature).[384]

Neutron depth profiling was first shown by S. M. Whitney et al. as a valid technique to quantify both anodic SEI and cathodic solid electrolyte interphases.[241,242] M. S. Whitney et al. described the calendaric SEI growth with respect to temperature, and the CEI growth depending on the charge/discharge rate during cycling.[241] Hereafter, the NDP technique has been frequently used to study LIB aging aspects such as SEI trends on Si/graphite anodes,[77,243] degradation aspects of all-solid-state batteries[244] as well as in-situ lithium transport phenomena in LIBs.[238–240]

The lamination technique is well-known in the industrial production of LIBs for its benefits in increasing the production line speed of stacked cell compounds and for reducing reject rates due to the electrode-separator misplacement.[202] Technical aspects have been specified by several patent applications[205,207] and research reports on supercapacitor production techniques.[215] A detailed overview on the use of lamination in LIB production was given in our previous report.[73] While mechanical benefits of the lamination technique are well-known to the scientific community, electrochemical aspects remain mostly unclear. Recent studies on lamination revealed benefits especially on the fast-charging capability of graphite-NMC 111 cells.[73,74] The lowered capacity losses along fast-charging cycles were shown to arise from a significant reduction in SEI growth upon lamination at the anode-separator interphase.[74] The lamination technique was also shown to tune the C-rate stability of graphite-NMC 111 cells similar to application of external cell pressure during operation.[73]

Beneficial aspects of the electrode-separator lamination technique on the SEI growth at accelerated formation rates are investigated in this study.

6.3   Results and discussion

6.3.1 Capacity-fade phenomena

Graphite-NMC single cells in non-laminated/laminated state were cycled for 2 cycles at varied formation rates (0.1C, 1C and 2C) and at varied cycling rates (1C and 2C) for several subsequent cycles (8, 48, 98 and 498). Averaged discharge capacity trends for each formation/cycling path are shown in Fig. 6.1.
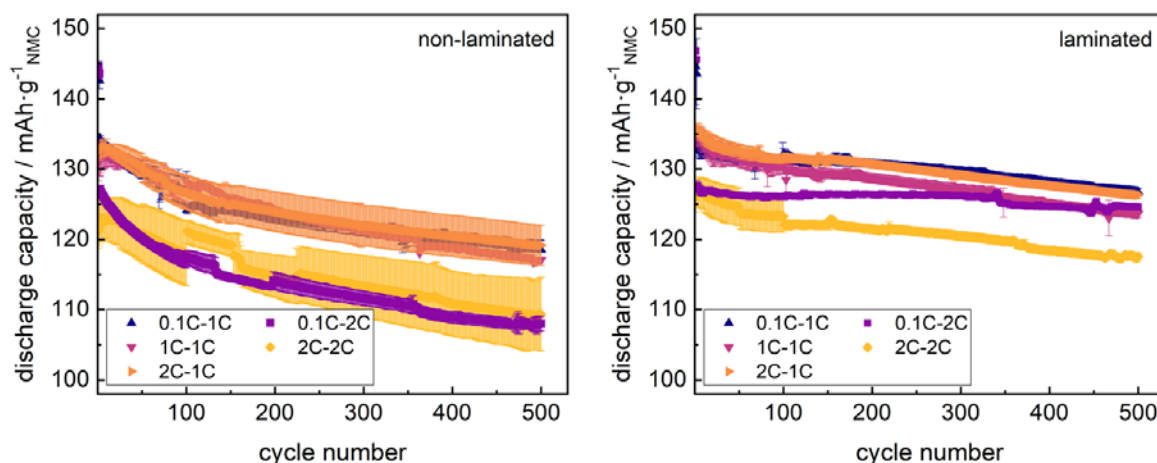
Fig. 6.1: Averaged discharge capacity data of non-laminated/laminated cells in cycling test (500 cycles) after varied formation rate (2 initial cycles); error bars indicated.

Due to temporary data acquisition issues with seven cells considered in Fig. 6.1, some cycling curves in Fig. 6.1 show an offset within cycles 101–211 due to a temporary reduction of representative datasets. These cycles however were excluded from further analysis.

Non-laminated cells cycled at 1C rate revealed similar capacity-fade along cycling, revealing ≈ 89% of the maximum discharge capacity after 500 cycles, with accelerated formation rates (1C and 2C) starting at slightly lower discharge capacities in the initial cycle, and ascending to the reference level of formation at 0.1C rate within the first 10 cycles. Increasing the cycling rate of non-laminated cells reduced both the maximum discharge capacity of the cells reached during cycling, as well as the residual capacity after 500 cycles (87%). Formation of non-laminated cells at 2C rate induced increased data spreading of the cell series, both for subsequent cycling at the 1C rate and 2C rate. Non-laminated cells both formed and cycled at the 2C rate, again revealed an inflection point of discharge capacity within the initial cycles, as well as significantly enhanced data spreading.

Laminated cells revealed no inflection point in the initial discharge capacities for any formation or cycling rate, while reducing the capacity losses within the first 500 cycles at 1C cycling (94% of maximum capacity) and 2C cycling. Laminated cells formed at 0.1C revealed the significantly lowest capacity losses at 2C cycling (98% after 500 cycles) and tended to reach similar capacity levels both at 1C and 2C cycling with increasing cycle number. Formation and subsequent cycling of laminated cells at 2C rate reduced the residual capacity

(94%) after 500 cycles. An increase of data spreading during cycling for cells formed at 2C rate was clearly dampened using laminated cells. All capacity-fade trends are summarized in Tab. 6.1.

Tab. 6.1: Averaged capacity-fade of non-laminated/laminated cells at varied formation/cycling rate.

mode – cycle number	0.1C-1C	1C-1C	2C-1C	0.1C-2C	2C-2C
Laminated – 10	133 mAh·g^{-1}	134 mAh·g^{-1}	135 mAh·g^{-1}	127 mAh·g^{-1}	126 mAh·g^{-1}
laminated – 500	127 mAh·g^{-1}	124 mAh·g^{-1}	126 mAh·g^{-1}	125 mAh·g^{-1}	118 mAh·g^{-1}
laminated – Δ	6 Ah·g^{-1}	10 mAh·g^{-1}	9 mAh·g^{-1}	2 mAh·g^{-1}	8 mAh·g^{-1}
non-laminated – 10	133 mAh·g^{-1}	134 mAh·g^{-1}	133 mAh·g^{-1}	125 mAh·g^{-1}	123 mAh·g^{-1}
non-laminated – 500	119 mAh·g^{-1}	117 mAh·g^{-1}	119 mAh·g^{-1}	108 mAh·g^{-1}	109 mAh·g^{-1}
non-laminated – Δ	14 mAh·g^{-1}	17 mAh·g^{-1}	14 mAh·g^{-1}	17 mAh·g^{-1}	14 mAh·g^{-1}

The given trends in the discharge capacity correlated to our previous studies on single cells in the laminated and non-laminated state. A possible increase of the formation rate up to 1C rate without significant obstacles is clearly shown for both assembly modes, which overcomes previous reports of stable fast-formation protocols given by S. J. An et al. or N. Rago et al., reporting maximum 0.5C rate formation protocols.[165,270] This underlines the validity of choosing vinylene carbonate as SEI precursor additive in the ratio of 2%, as suggested by Wang et al.[163]

It is well-known that the electrode-separator lamination technique can replace the application of external cell pressure to improve the C-rate stability.[73] The data shown in Fig. 6.1 and Tab. 6.1 now underline as well the ability of the lamination technique to stabilize cells at fast-formation up to the 2C rate, similar to known effects of external cell pressure stabilizing 1C formation of graphite-NMC 622 cells.[271]

Applying the electrode-separator lamination technique previous to cycling again proves as a valid modification for the reduction of capacity fading phenomena as reported in our previous studies,[73,74] and improves the cell performance at the 2C formation rate. As the SEI growth phenomena were shown to act as the main aging effect tuned by lamination at fast-charging protocols, the given cycling data indicate similar aging effects driving the modified cell performance at fast-formation.

6.3.2 SEI growth phenomena

Discharged graphite anodes from non-laminated cells were studied post-mortem with NDP after varied formation rates (0.1C, 1C and 2C), cycling rates (1C and 2C) and cycle numbers (2, 10, 50, 100 and 500). Pristine non-laminated and laminated graphite anodes (i.e., with no lithium content) were used to generate reference spectra. On the low-energy end of the spectra, one can see a region with high counts, which originates from low-energy beta particles and gamma photons produced during neutron capture.[352] This background was subtracted from all the spectra. This stripping technique does not work reliably at the lowest energies, i.e. for particles emitted near the anode/current collector interface, so this region was omitted from the further analysis. These spectra are shown in the supplementary materials. Lithium immobilized in

the SEI was revealed by detecting the energy of the ^{3}H particle of the ^{6}Li(n,^{3}H)^{4}He reaction. As described by M. Trunk et al.,[243] the lithium depth profiles were extracted from the NDP energy spectra using the SRIM software[237] taking into account the Kapton® separation foil and the composition of the pristine graphite anodes. The lithium depth profiles are shown in Fig. 6.2.
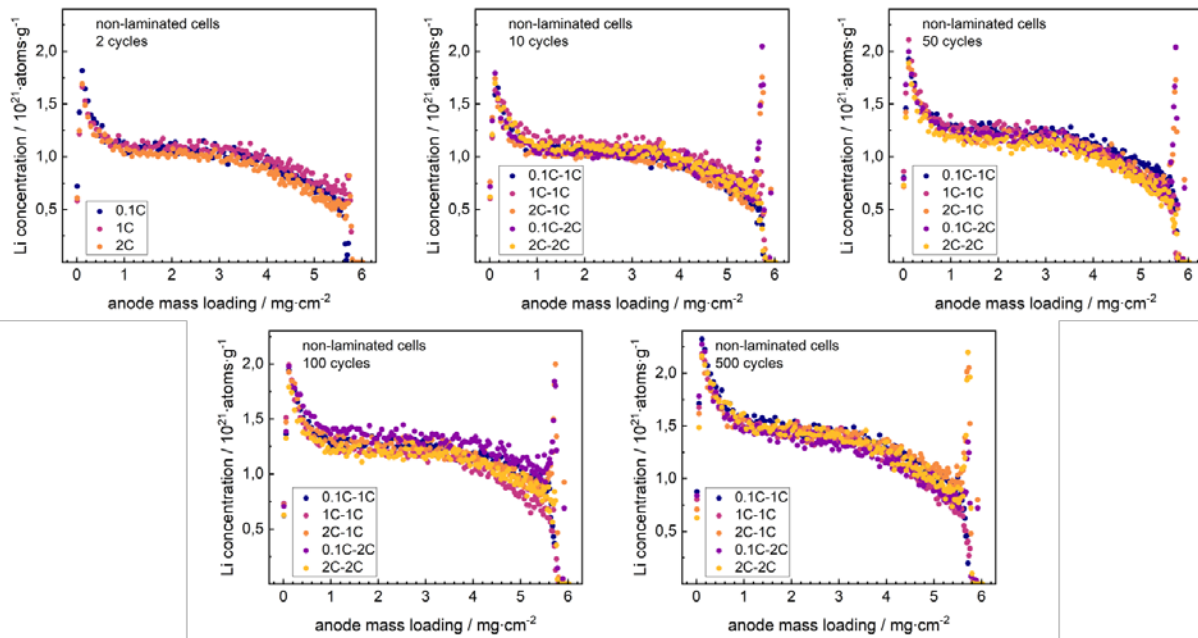
Fig. 6.2: Change of lithium depth profiles of delithiated graphite anodes along cycling, extracted from non-laminated cells along cycling (500 cycles total) after a varied formation rate (2 initial cycles).

The 2 cycles datasets represent the three separate formation rates. Further separation into five different formation/cycling modes starts at the 3rd cycle, when the C-rate change to the final cycling rate is first applied. As all other possible lithium contributions (lithiated graphite, cathode and electrolyte) were removed from the samples via fully discharging the battery and rinsing of the anode, the detected signal can be assigned to irreversibly attached lithium at the anode surface, i.e. the SEI. All depth profiles reveal a similar shape. An increase of lithium is detected at the anode surface, i.e. the anode-separator interphase, which might arise from surface orientation aspects or from direct lithium accumulations.[243]

In deeper anode regions (> 3 mg cm^{-2}) the signal decreased, resembling the Gaussian shape of the NDP detection response function. All signals are cut at a depth of about 5.7 mg cm^{-2}, which is the maximum depth limit for detection of ^{3}H charged particles in this setup. The inflection point, which resembles the anode-Cu current collector interphase,[243] is situated around 6.0 ± 0.7 mg cm^{-2} and lies outside of the detection range. In the bulk regime (0.5 – 3 mg cm^{-2}), a homogenous Li distribution was observed, indicating a homogenous distribution of the SEI. This correlates to the concept of the SEI as a protective layer with similar thickness covering all anode particles. The signal shape agrees well to reports of NDP data on post-mortem Si/C anodes.[77]

At all formation rates, a major portion of the SEI was formed after 2 cycles. This enhanced indications from the cycling data for the electrolyte to form a homogenous and comparable SEI also at accelerated formation rates. With increasing charge – discharge rates, the immobilized lithium was found to increase in a similar manner for all cycling rates, without changing the signal shape. This indicates a continuous growth of the SEI with minor dependence on the cycling rate. While the capacity-fade increased with rising cycling rate, the SEI growth was found similar for both cycling paths, which indicates a significant influence from separate aging effects.

A further comparison of cycling studies and NDP data, requires direct calculation of irreversible capacity losses at cycle numbers studied with NDP. Results are presented in the supplementary materials. As the C-rate was changed after 2 cycles for some cells, the discharge capacities of these studied cells dropped with varying amount due to the limited C-rate stability of the cells, which gives an artificial signal shift of the irreversible capacity loss signal after two cycles. Given knowledge about the C-rate levels at the 0.1C, 1C and 2C rate of non-laminated and laminated cells can be used to correct this inevitable signal shift at the data points at two cycles. Corrected datasets are shown in Fig. 6.3.
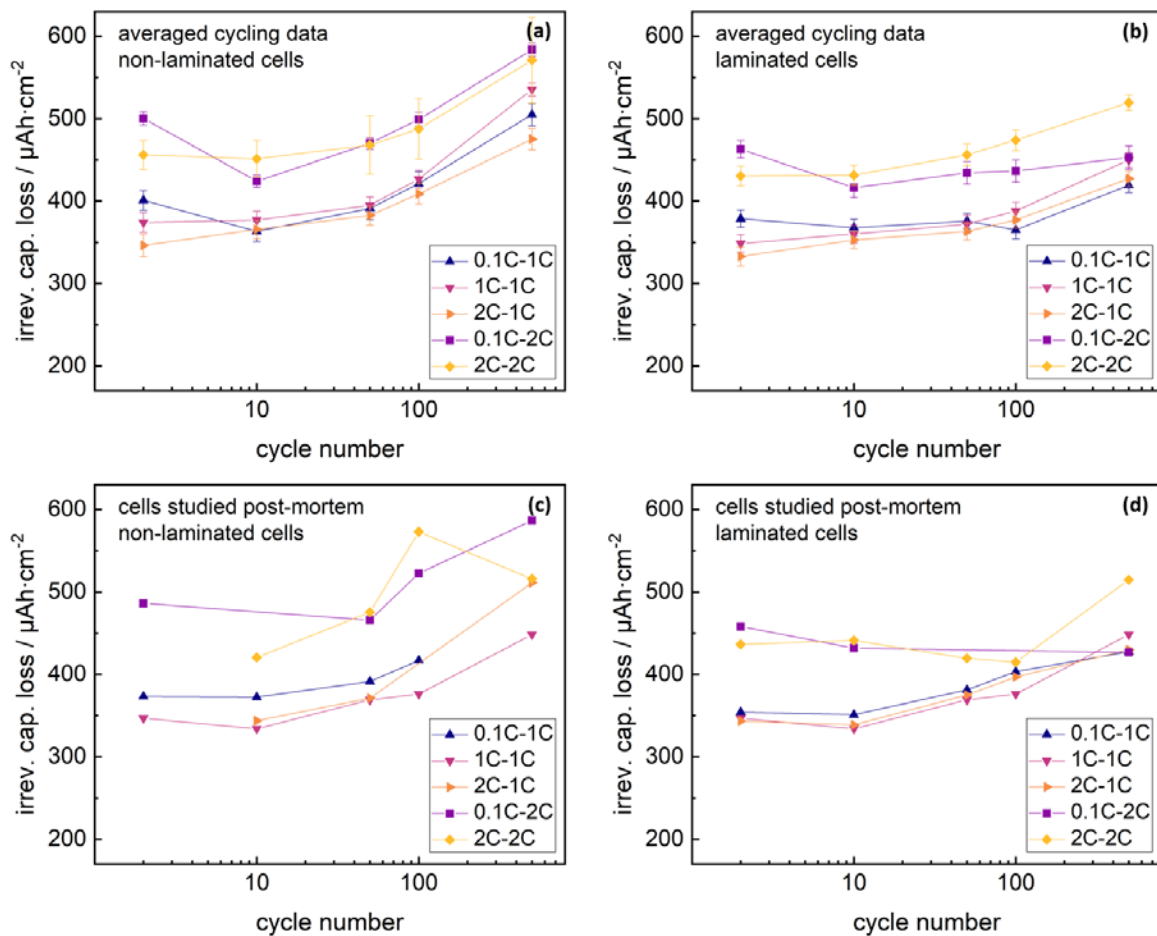
Fig. 6.3: Active lithium loss of non-laminated/laminated cells calculated from capacity-fade in cycling test; data at 2 cycles corrected with C-rate corrective term; (a,b) active lithium loss from non-laminated/laminated cells given by

average cycling test data, error bars indicated; (c,d) active lithium loss from non-laminated/laminated cells given by exemplary cycling test data from cells studied post-mortem with neutron depth profiling (NDP).

For precise analysis, the active lithium loss of the exemplary cell series studied post-mortem (Fig. 6.3c, d) was compared to the averaged active lithium loss signals (Fig. 6.3a, b) arising from the analysis of all cycled cells at the respective assembly mode, formation rate and cycling rate. Averaged signals for the irreversible capacity losses correlated to the discharge capacity trends shown in Fig. 6.1. Irreversible capacity losses of the individual cells studied post-mortem with NDP revealed similar values as the averaged datasets.

Integrating the background corrected NDP signals allows for an estimation of the lithium immobilized in the SEI, and consequently for a capacity evaluation of the immobilized lithium using Faraday's law. Comparison of the measured capacity losses during cycling and lithium immobilization losses driven by SEI growth via NDP, are presented in Fig. 6.4. NDP detection range was corrected via Gaussian extrapolation as described in previous studies.[243]
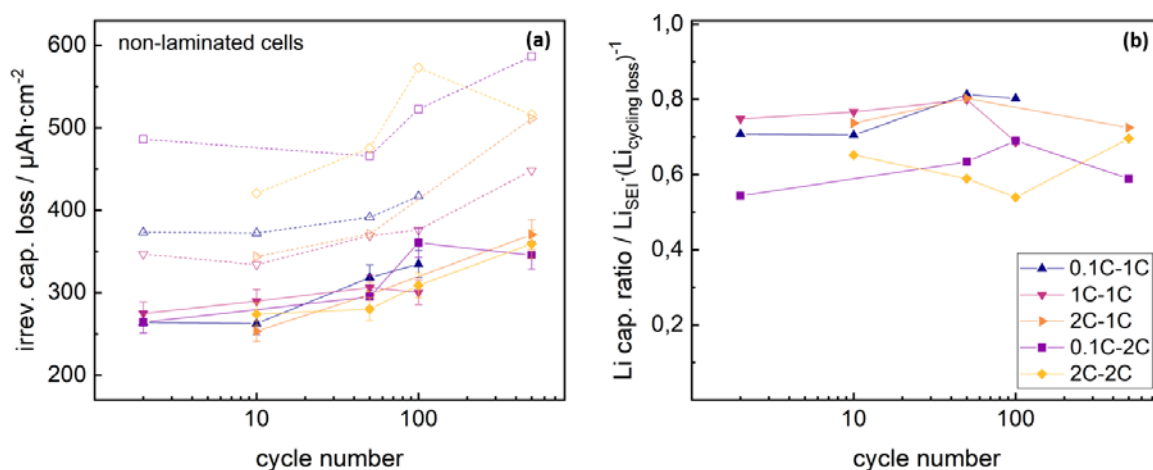
Fig. 6.4: (a) Active lithium loss of non-laminated cells calculated from capacity-fade in the cycling test (hollow symbols, dotted lines) compared to lithium bound in a solid electrolyte interphase (SEI), detected post-mortem with NDP (solid symbols, solid lines) and (b) irreversibly lost lithium fraction bound in SEI.

Lithium immobilization lay at similar levels for all formation and cycling rates, and increased with cycling analogous to the total irreversible capacity loss signals. Lithium immobilization within the SEI reflected 70 – 80% of the total capacity losses for non-laminated cells cycled at 1C rate, compared to 55 – 70% for cells cycled with 2C rate. Differences in the SEI loss capacity ratio for the 1C or 2C cycling rate might arise from different C-rate drops of the cells. The residual capacity losses of the non-laminated graphite-NMC 111 cells, aside from lithium immobilization in the SEI, might arise from increasing kinetic limitations due to ongoing changes in the crystal lattice of the NMC cathode particles.[91,94] Again, no significant influence from the formation rate was visible.

Discharged anode-separator stacks from laminated cells were studied post-mortem with NDP after varied formation rate (0.1C, 1C and 2C), cycling rate (1C and 2C) and cycle numbers (2, 10, 50, 100 and 500). Raw data are presented in the supplementary materials. The additional material of the laminated separator

reduces the maximum depth in the anode accessible with ^{3}H particles. However, the SEI accumulation in the superior layer of the anode-separator stack could be tracked and compared to non-laminated anodes. Integrating the NDP signal arising from superior anode fractions both from laminated and non laminated cells allowed for a quantification of lithium immobilized in the examined anode fractions. Datasets are shown in Fig. 6.5.
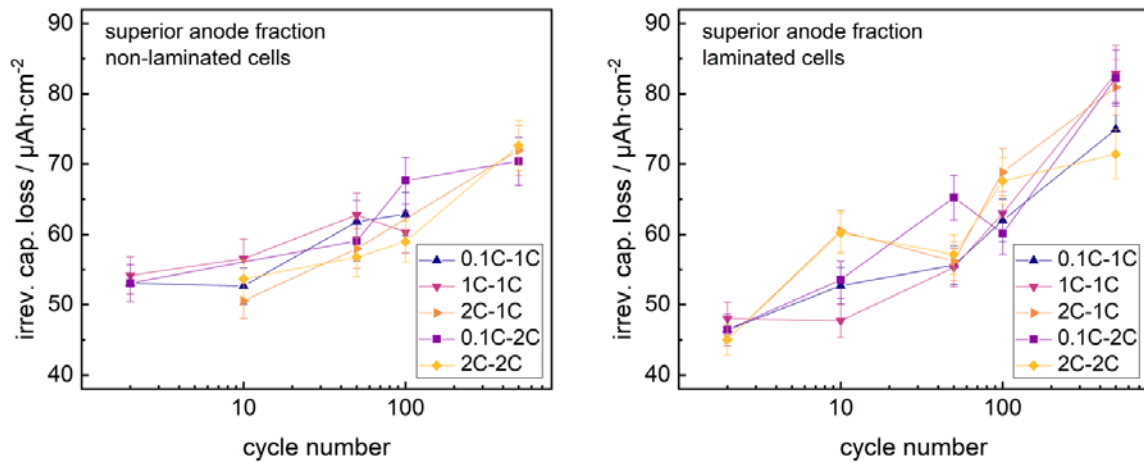
Fig. 6.5: Comparative lithium fractions in graphite anodes, comparing (a) rinsed graphite anode (non-laminated) and (b) rinsed anode/separator stack (laminated), detected post-mortem with NDP; data analysis restricted to comparative depth sector within all graphite anodes.

Both laminated and non-laminated cells revealed similar lithium immobilization (increasing with cycle number) for all formation and cycling rates.

This trend in lithium immobilization in superior anode fractions indicates no clear correlation with the capacity losses found in the cycling studies. The signal discrepancy either indicates non-homogenous SEI growth with electrode depth for laminated cells, or significant influence of separate aging phenomena.

6.3.3 Surface resistance growth phenomena

Graphite-NMC single cells were studied with electrochemical impedance spectroscopy along cycling in non-laminated and laminated state. Nyquist plots of datasets and fitting curves are shown in Fig. 6.6.
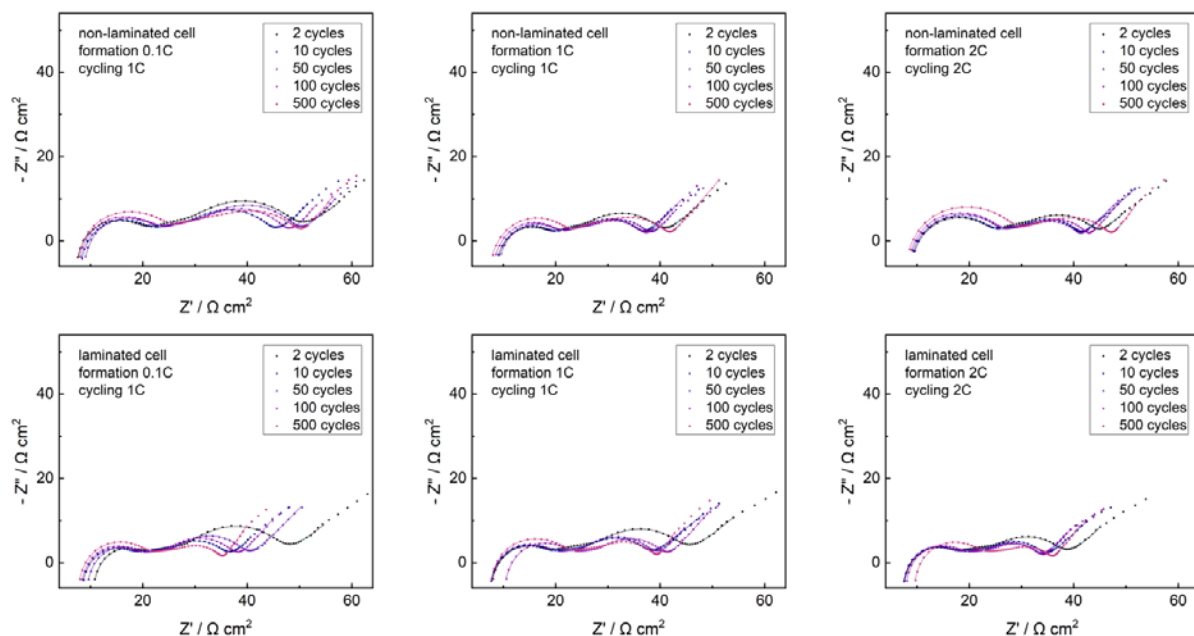
Fig. 6.6: Impedance measurements of non-laminated/laminated cells: electrochemical impedance spectroscopy (EIS; 50 kHz – 10 mHz) along cycling test (500 cycles total) after varied formation rate (2 initial cycles); fitting curves indicated as solid lines; data points at 940 Hz and 0.104 Hz highlighted in pale blue; data normalized to geometric electrode area.

All Nyquist datasets reveal similar structure of the EIS response, correlating to our previous studies.[74] The highest frequency domains were dominated by inductive effects, resulting from the EIS setup environment. Three subsequent semicircles arise from surface resistance phenomena, the anode charge-transfer reaction and cathode charge-transfer reaction, respectively. The lowest frequency responses were governed by solid-state diffusion characteristics, splitting into closed and open Warburg type data. The surface resistance semicircle increased with cycling for all cells. The highlighted data point set at 940 Hz lay close to the minimum between the 1st and 2nd semicircle for all datasets, with no shift along cycling. Analogously, the highlighted data point set at 0.104 Hz lay in the closed Warburg regime, close to the 3rd semicircle, with no shift along cycling. This indicates negligible changes in the time constants with cycling for all cells, what agrees well with literature.[74,374] Further information can be extracted using EIS fit analysis, excluding open Warburg data points due to the structure of the chosen equivalent circuit fit model. Fit parameter trends and equivalent circuit fit models are shown in Fig. 6.7.
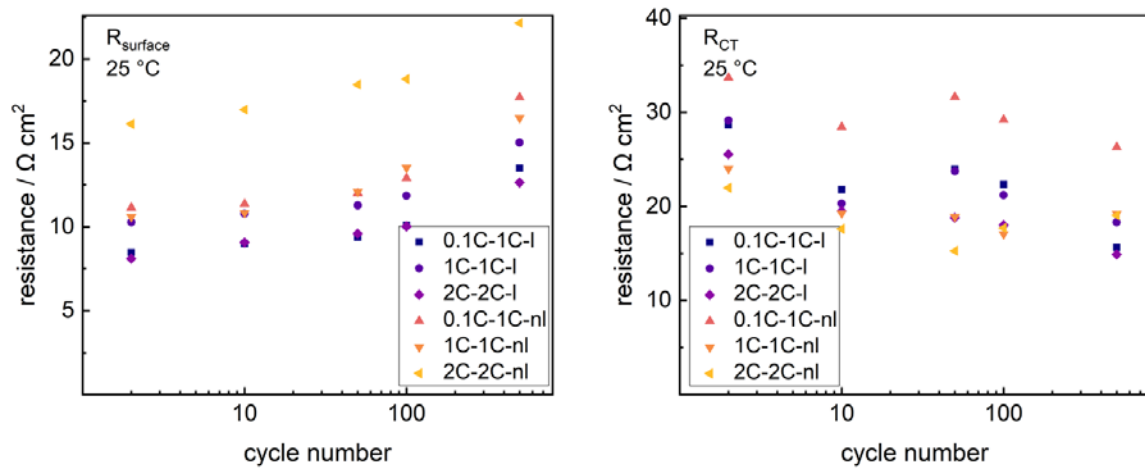
Fig. 6.7: EIS resistance fit parameters of laminated and non-laminated single cells along cycling test (500 cycles total) after varied formation rate (2 initial cycles); equivalent circuit model indicated; data normalized to geometric electrode area; (a) trend of surface resistance; (b) trend of anode and cathode charge-transfer resistance sum.

Due to strong overlapping of graphite charge-transfer semicircle and NMC charge-transfer semicircle, only the sum of both charge-transfer resistances can be detected precisely. The charge-transfer resistance revealed no clear trend with cycling for any cell. The capacitance fit parameters for graphite semicircles, NMC charge-transfer semicircles and surface resistance semicircle are shown in the supplementary materials. Laminated cells show reduced surface resistances ($\approx 8 \ \Omega \cdot cm^2$, $\approx 10 \ \Omega \cdot cm^2$ and $\approx 8 \ \Omega \cdot cm^2$) after 2 cycles for all formation rates (0.1C, 1C and 2C), compared to non-laminated cells ($\approx 11 \ \Omega \cdot cm^2$, $\approx 11 \ \Omega \cdot cm^2$ and $\approx 6 \ \Omega \cdot cm^2$), which was shown to arise from cathode optimization effects by the lamination technique. [74]The surface resistance increased with cycling for all cells. As the starting condition of the surface resistance was purely defined on cathode porosity and cathode contact situation aspects, valid information on aging phenomena along cycling can only be extracted from the normalized surface resistance. Therefore, surface resistance trends were normalized to changes from the starting value after 2 cycles. Comparison of the normalized surface resistance trends and discharge capacity trends of the respective cells, are shown in Fig. 6.8.
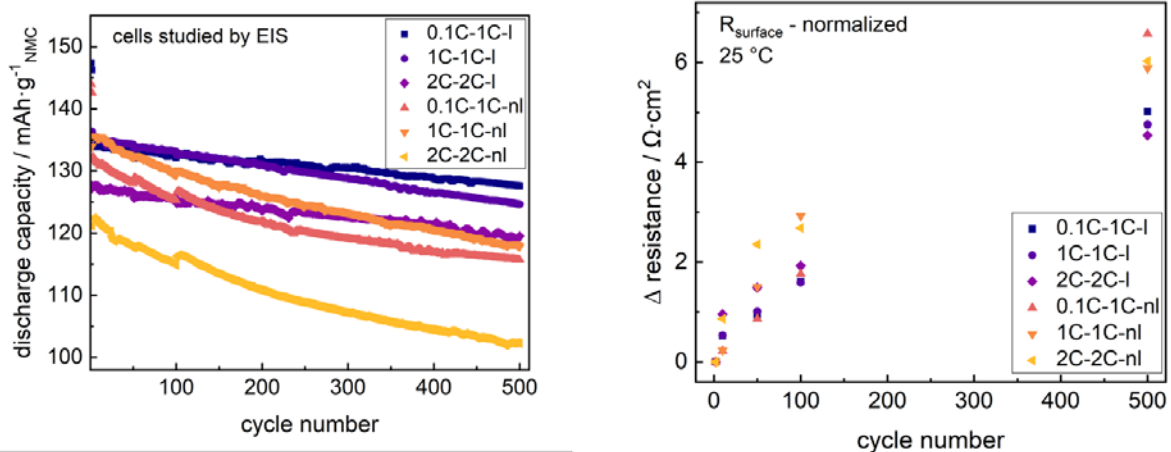
Fig. 6.8: Discharge capacity data and normalized surface resistance fit parameters of non-laminated/laminated cells along cycling test (500 cycles total) after varied formation rate (2 initial cycles).

Both non-laminated cells cycled at 1C reveal similar capacity-fade, reaching 88.2% (0.1C formation) and 87.1% (1C formation), respectively, of the maximum capacity after 500 cycles. The cell formed and cycled at 2C dropped to 84.0%. The substantial capacity fading clearly correlated to the increase in surface resistance of $+6.5\ \Omega\cdot cm^2$ (0.1C formation, 1C cycling), $+5.8\ \Omega\cdot cm^2$ (1C formation, 1C cycling) and $+6.0\ \Omega\cdot cm^2$ (2C formation, 2C cycling) after 500 cycles.

Laminated cells reduce the capacity-fade losses for all formation and cycling rates, revealing 95.2% (0.1C formation, 1C cycling), 92.2% (1C formation, 1C cycling) and 93.8% (2C formation, 2C cycling) remaining capacity after 500 cycles for the studied formation rates and cycling rates. The surface resistance increased ($+5.0\ \Omega\cdot cm^2$, $+4.7\ \Omega\cdot cm^2$, $+4.5\ \Omega\cdot cm^2$) and was lowered for the laminated cells at the respective formation and cycling modes.

As is well known from the literature, the surface resistance changes along cycling reflect both SEI growth as well as further surface resistance aspects like electrode-current collector contacts,[225] without further setup normalization like cathode lamination,[74] temperature decrease[224] or the introduction of reference electrodes.[232,233] As found from the NDP studies, the SEI growth in superior anode fractions was similar for all formation and cycling rates both in non-laminated and laminated state. This clearly indicates the reduction in capacity-fade of laminated cells at fast-formation, to arise either from non-homogenous SEI growth or further surface resistance impacts like reduced electrode delamination effects.

6.4   Materials and methods

6.4.1   Materials

For assembly of both cathodes and anodes, commercially available battery grade $LiNi_{1/3}Mn_{1/3}Co_{1/3}O_2$ (NM-3102h, BASF TODA America, Battle Creek, USA) and graphite (MAGE3, HITACHI CHEMICAL, Sakuragawa, Japan) were used as active materials, with polyvinylidene difluoride (PVDF; Solef® 5130, SOLVAY, Milan, Italy) as a binder and a series of carbonaceous conductive additives (Super C65, KS6L, SFG6L, IMERYS, Bodio, Switzerland). The solvent used was N-methyl-pyrrolidone (NMP, Overlack, Mönchengladbach, Germany). The electrolyte consisted of 1 M $LiPF_6$ in EC:EMC 3:7 (Selectilyte LP57, BASF, Florham Park, USA) with 2 wt% VC (Vinylene Carbonate E, BASF) were used as electrolyte components. For the pouch cell setup, a self-standing inorganic filled alumina/PVDF-HFP separator (67:33) was stacked with the electrodes. An aluminum foil (20 µm, GELON LIB, Hong Kong, China) and a copper foil (15 µm, GELON LIB) served as current collectors for cathodes and anodes, respectively. All materials were used as received.

6.4.2   Electrode preparation

Anode slurries were processed by blending graphite (MAGE3, 90 wt%), binder polymer (PVDF, 7 wt%), carbon black (Super C65, 2 wt%) and conductive graphite (SFG6L, 1 wt%) with NMP to have a solid content of 46 wt%. Processing of cathode slurries was done by mixing the active material (NMC 111, 93 wt%), binder (PVDF, 3 wt%), carbon black (Super C65, 3 wt%) and conductive graphite (KS6L, 1 wt%) with NMP to give a final solid content of 60 wt%. A planetary mixer (TX-2, INOUE, Isehara, Japan) was used for mixing of electrode slurries. Electrode slurries were cast onto current collectors by doctor-blade technique in a roll-to-roll process. Electrodes were dried in a two-stage drying tunnel at 135 – 150 °C. Active mass loadings of anode and cathode electrodes were ≈ 4.4 mg·cm^{-2} (1.57 mAh·cm^{-2}) and ≈ 8.7 mg·cm^{-2} (1.35 mAh·cm^{-2}), respectively. In all full cells, balancing of cathodes: anodes was ≈ 1:1.16.

6.4.3   Pouch cell preparation

The cathode, anode and separator were punched (5 × 8 cm^2, 5.4 × 8.4 cm^2 and 5.8 × 8.8 cm^2) and stacked to form single cells in the pouch cell configuration; the setup was described in detail in our previous studies.[73,74] For the fully laminated condition, cathode-separator-anode stacks were additionally laminated into single stacks by using a roll laminator (BLE 282 D, MANZ Italy, Bologna, Italy) with a line force of 157 N·cm^{-1}, roll speed at 1.4 m·min^{-1} and temperatures within 100 – 120 °C. The stacks were partially sealed in pouch foil and dried under vacuum at 110 °C for 12 h. In an argon filled glovebox (MB20, H_2O and O_2 content < 0.1 ppm, MBraun, Garching, Germany) all single cell stacks were filled with a 1000 µL electrolyte before vacuum sealing. Cells rested at room temperature for 24 h before formation.

6.4.4 Electrochemical characterisation

Charge/discharge cycles were performed with a battery test system (CTS-LAB, BaSyTec, Asselfingen, Germany), using the constant current and constant voltage (until the current dropped below 0.05C rate) modes for the charging step and CC-mode for the discharge step. The voltage range was adjusted to 3.0 V – 4.2 V. C-rates for formation and aging cycles were calculated according to the NMC weight in the cell, using the nominal NMC capacity of 155 mAh·g^{-1}, given by the supplier.

The error bars in the NDP spectra were derived from the systematic uncertainties of the setup and the calibration, as well as the statistical uncertainties of the measurement using the common rules of error propagation. For cycling studies, at least 3 cells for each formation rate and cycling rate were studied for 500 cycles, in addition to cells stopped at lower cycle numbers for post-mortem analysis.

Indicated error bars represent the standard deviation between these cells. Separate cell sets were prepared and studied via EIS.

All EIS measurements were controlled by a potentiostat (PGSTAT204, Metrohm Autolab, Filderstadt, Germany) in a climate chamber (INCU-Line® IL 68R, VWR, Ismaning, Germany) at a constant temperature of 25 °C. EIS analysis along cycling was performed by charging the cells up to 3.6 V/3.7 V/3.8 V depending on the current C-rate 0.1C/1C/2C, followed by a controlled relaxation time of 2 h in open circuit voltage previous to each EIS measurement. EIS measurements were done in the potentiostatic mode in a frequency range of 50 kHz – 10 mHz and an adjusted amplitude of 10 mV$_{rms}$. Data fitting was performed using Z-fit implemented in the BT-Lab software (BT-Lab V1.55, BioLogic SAS via GAMEC, Illingen, Germany).

6.4.5 Post-mortem characterisation

For preparation of the post-mortem analysis, pouch cells were opened and disassembled in an argon filled glovebox. For laminated stacks, only the cathode was pulled off the anode-separator stack, for non-laminated stacks, the graphite anode was directly extracted. All extracted anode/anode-separator samples were rinsed using EMC and subsequently dried under argon atmosphere in order to remove lithium residuals from the electrolyte. For NDP measurements, circular samples with a diameter of 14 mm were punched out from the central parts of the anode sheets. The anode/anode-separator samples were studied at the N4DP setup at the PGAA facility of the Heinz Maier-Leibnitz Zentrum in Garching, Germany.[77,243,352,385] The anode/anode-separator samples were assembled in a vacuum chamber (10^{-5} mbar) facing the collimated cold neutron beam (12.6 mm^2, 3×10^9 ncm^{-2}·s^{-1}) at an angle of 45 °. The cold neutron beam was adjusted to hit central parts of the anode/anode-separator samples; details on the specialized NDP setup and the specialized electrode sample holder were described in previous studies.[243,352] Each sample was individually measured for 15 min. A nominal 7.5 µm thick Kapton® separation foil (DuPont, Wilmington, USA) was used to suppress signals from ^{4}He particles of the ^{6}Li(n,^{3}H)^{4}He reaction.

6.5   Conclusion

Graphite-NMC single cells were studied at accelerated formation rates in non-laminated and laminated state by means of cycling, EIS and NDP. Increasing the formation rate up to 1C rate revealed no increase in capacity-fade, SEI growth or surface resistance growth for any cell. Increasing the formation rate up to 2C, increased the capacity-fade spreading for non-laminated cells, while SEI growth and surface resistance growth revealed negligible changes.

Laminated cells exhibited reduced capacity fading at all formation rates and cycling rates, which correlated with a significant reduction in surface resistance growth. As the SEI was shown to grow similar in superior anode fractions both in non-laminated and laminated state, the reduction in capacity-fade either indicates non-homogenous SEI growth or significant reduction of further surface resistance phenomena for laminated cells at fast-formation.

Conflicts of interest

The authors declare no conflict of interest. The funders had no role in the design of the study; in the collection, analyses, or interpretation of data; in the writing of the manuscript, or in the decision to publish the results.

6.6   Supplementary Materials

The following are available online at http://www.mdpi.com/2313-0105/6/2/21/s1.

6.6.1 Irreversible capacity loss calculation
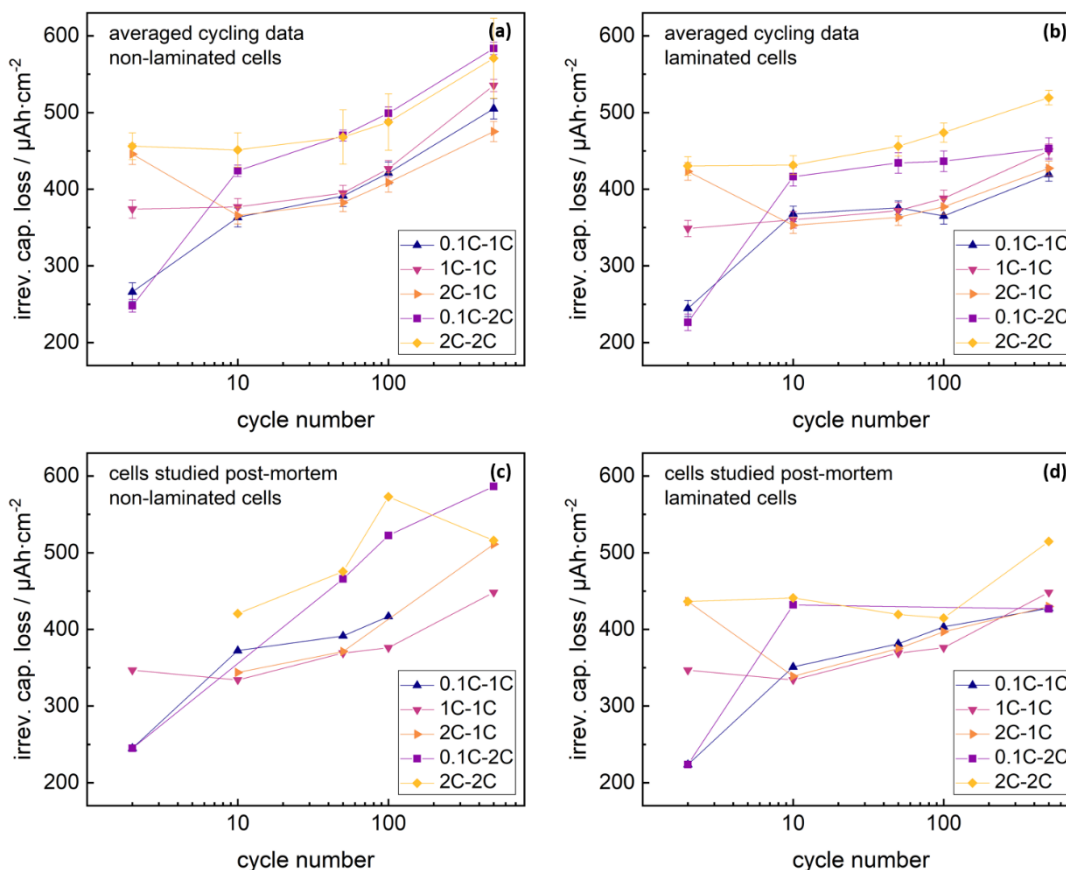
Fig. 6.9: Active lithium loss of non-laminated/laminated cells calculated from capacity-fade in cycling test; data at 2 cycles non-corrected; (a) and (b) active lithium loss from non-laminated/laminated cells given by average cycling test data, error bars indicated; (c) and (d) active lithium loss from non-laminated/laminated cells given by exemplary cycling test data from cells studied post-mortem with NDP.
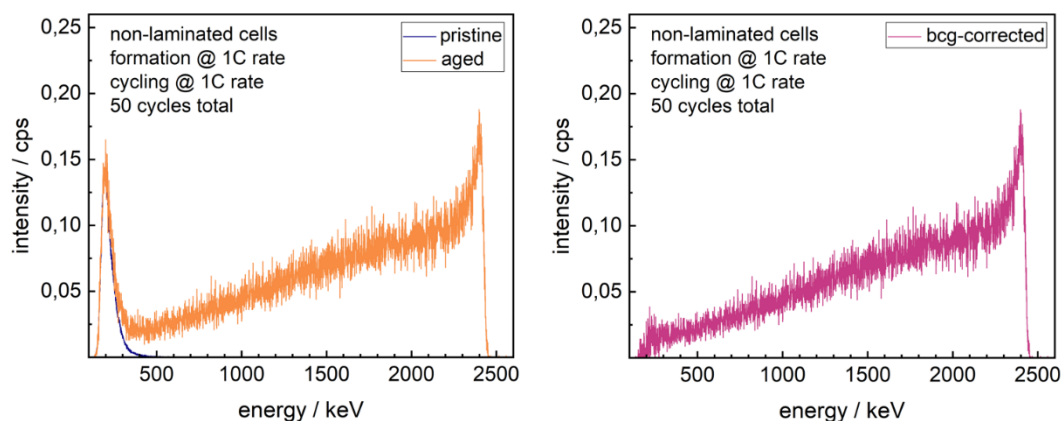
Fig. 6.10: Exemplary background correction; NDP energy spectra of pristine non-laminated anode and non-laminated anode after 50 cycles at 1C rate.

6.6.2 NDP energy spectra – background corrected
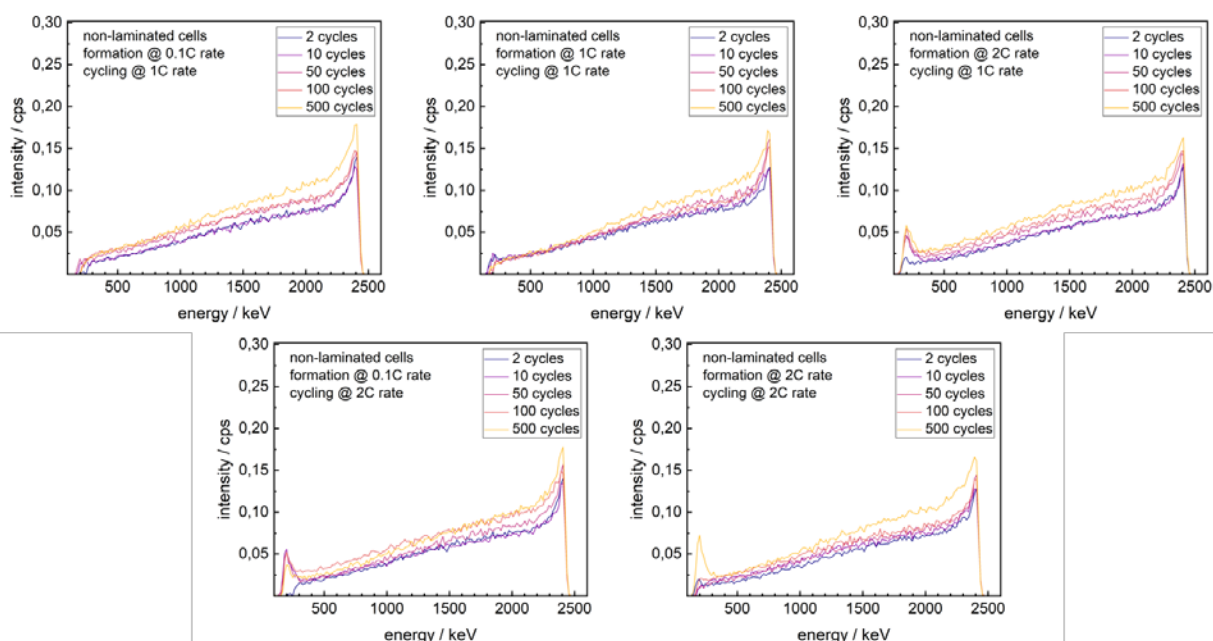
Fig. 6.11: Change of background-corrected NDP energy spectra of delithiated graphite anodes along cycling, extracted from non-laminated cells along cycling test (500 cycles total) after varied formation rate (2 initial cycles); datasets of 10 consecutive data points grouped.
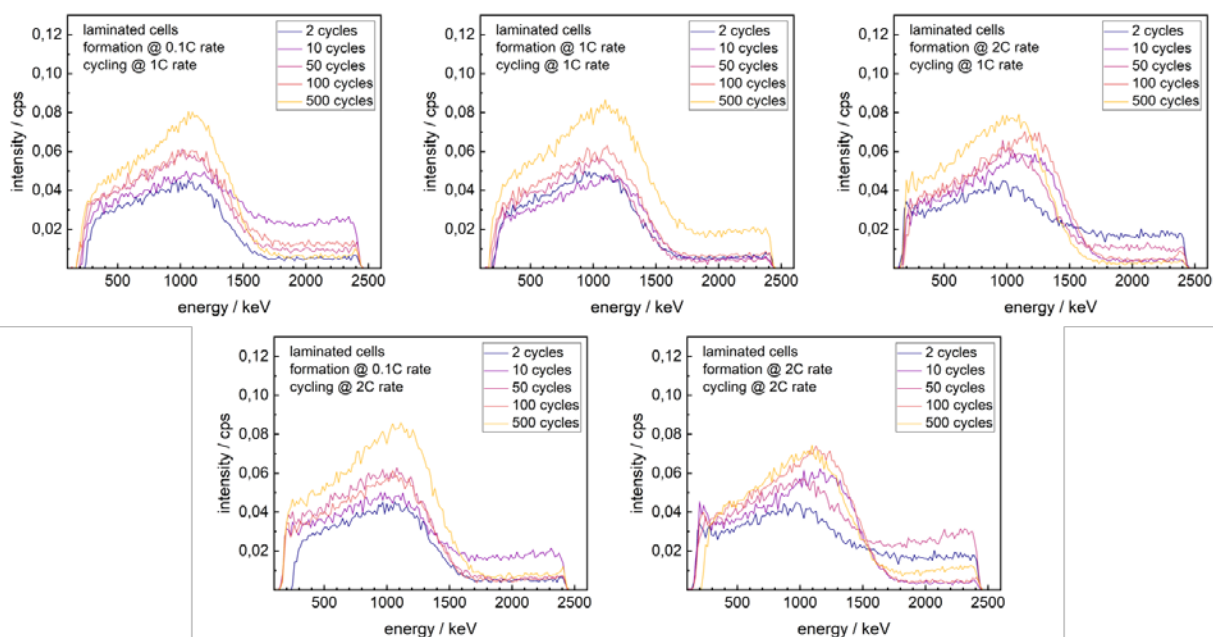
Fig. 6.12: Change of background-corrected NDP energy spectra of delithiated anode/separator stacks along cycling, extracted from laminated cells along cycling test (500 cycles total) after varied formation rate (2 initial cycles) ; datasets of 10 consecutive data points grouped.

6.6.3 EIS fit analysis – capacitance fit parameters
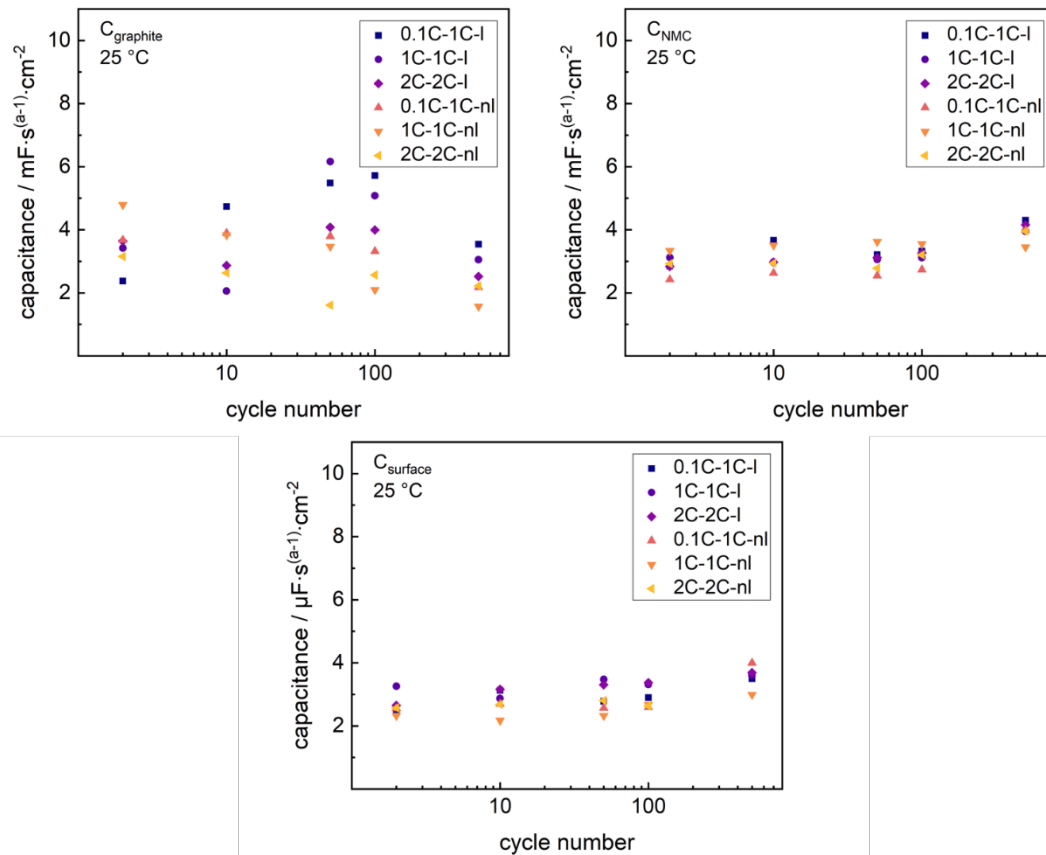
Fig. 6.13: EIS capacitance fit parameters of laminated and non-laminated single cells along cycling test (500 cycles total) after varied formation rate (2 initial cycles); data normalized to geometric electrode area.

7   Conclusion

The electrode-separator lamination technique was comprehensively studied upon microscopical, morphological, and electrochemical influences on Lithium Ion Batteries, using laminable, non-calendered electrodes and a laminable separator as exemplary setup architecture.

A drastic reduction in overall pore volume of the cathode-separator-anode stack ($\approx 66\,\%$) was allocated to a reorganization of the electrode-separator interface. While maintaining essential interface channels, the separator links to the electrode surface by enclosing electrode particles at microscopic level. The reorganization of the electrode-separator interface was demonstrated to possibly replace effects of permanent cell compression on the C-rate stability ($+ 17\,\%$ at 5 C-rate) of lithium ion cells, in case of appropriate lamination at both cathode-separator and anode-separator interface.

Electrochemical Impedance Spectroscopy revealed a significant reduction of the surface resistance of graphite-NMC 111 single cells down to a minimum level ($16\,\Omega\cdot cm^{-2} \to 6\,\Omega\cdot cm^{-2}$), arising from lamination at the cathode-separator interface. Effects were found very similar to known surface resistance reduction effects of cathode calendering. The surface resistance minimization was used as a normalization technique, allowing for detailed studies on the Solid Electrolyte Interphase by EIS even in two-electrode-geometry. Improved fast-charging capability of laminated cells was assigned to arise from reduced SEI growth along long-term cycling at accelerated charging rates.

For laminated cells, a reduction of long-term capacity fading of single cells ($\approx 44\%$ after 500 cycles) after fast-formation (2 C-rate) was found. Post-mortem Neutron Depth Profiling of cycled graphite anodes revealed similar amount and growth of SEI in superior anode fractions along fast-formation and cycling, both for laminated and non-laminated cells. Ex-situ EIS studies of graphite-NMC 111 single cells along fast-formation and cycling indicated a significant reduction in surface resistance growth to correlate with reduced capacity fading of laminated cells.

This lead to the conclusion, that the improved behaviour of laminated cells after fast-formation either arises from non-homogenous SEI growth or from separate surface resistance growth effects.

To conclude, the lamination technique should be of major interest for realization of fast-chargeable systems in EVs, as well as for significant cost reduction at the formation step in state-of-the-art production of LIBs.

8 References

1. Winter, M.; Barnett, B.; Xu, K.; *Chem. Rev.* **2018**, *118*, 11433–11456.

2. Yoshino, A.; *Angew. Chem. Int. Ed Engl.* **2012**, *51*, 5798–5800.

3. Kuribayashi, I.; *A Nameless Battery with Untold Stories;* KEE Corporation: Yokosuka, **2015**, ISBN 9784990861223.

4. Blomgren, G.E.; *J. Electrochem. Soc.* **2017**, *164*, A5019-A5025.

5. Yazami, R.; Touzain, P.; *J. Power Sources* **1983**, *9*, 365–371.

6. Goodenough, J.B.; Mizushima, K.; *Electrochemical cell with new fast ion conductors*, *United States Patent* **1981**, US4302518A.

7. Mizushima, K.; Jones, P.C.; Wiseman, P.J.; Goodenough, J.B.; *Materials Research Bulletin* **1980**, *15*, 783–789.

8. Mizushima, K.; JONES, P.; WISEMAN, P.; Goodenough, J.B.; *Solid State Ion.* **1981**, *3-4*, 171–174.

9. Whittingham, M.S.; *Chalcogenide battery*, *United States Patent* **1976**, US4009052A.

10. Barai, A.; Uddin, K.; Dubarry, M.; Somerville, L.; McGordon, A.; Jennings, P.; Bloom, I.; *Prog. Energ. Combust.* **2019**, *72*, 1–31.

11. Dunn, B.; Kamath, H.; Tarascon, J.-M.; *Science* **2011**, *334*, 928–935.

12. Fritz R. Kalhammer; Bruce M. Kopf; David Herman Swan; Vernon P. Roan; Michael P. Walsh; *State of California Air Resources Board, Sacramento, California* **2007**.

13. Thackeray, M.M.; Wolverton, C.; Isaacs, E.D.; *Energy Environ. Sci.* **2012**, *5*, 7854.

14. Manzetti, S.; Mariasiu, F.; *Renew. Sust. Energ. Rev.* **2015**, *51*, 1004–1012.

15. Han, X.; Ouyang, M.; Lu, L.; Li, J.; Zheng, Y.; Li, Z.; *J. Power Sources* **2014**, *251*, 38–54.

16. Mikolajczak, C.; Kahn, M.; White, K.; Long, R.T.; *Lithium-Ion batteries hazard and use assessment;* Springer: Boston, Mass., New York, NY, **2011**, ISBN 9781461434856.

17. Rahimzei, E.; Michaelis, S.; Kampker, A.; Heimes, H.; Lienemann, C.; Offermanns, C.; Kehrer, M.; Thielmann, A.; Hettesheimer, T.; Neef, C.; et al.; *VDMA Roadmap Batterieproduktionsmittel 2030 - Update 2018*. https://battprod.vdma.org/viewer/-/v2article/render/26974821 **2018** (accessed on 25 January 2021).

18. Thielmann, A.; Neef, C.; Hettesheimer, T.; Döscher, H.; Wietschel, M.; Tübke, J.; *Energiespeicher-Roadmap (Update 2017). Hochenergie-Batterien 2030+ und Perspektiven zukünftiger Batterietechnologien*. https://www.isi.fraunhofer.de/content/dam/isi/dokumente/cct/lib/Energiespeicher-Roadmap-Dezember-2017.pdf **2017** (accessed on 25 January 2021).

19. Kitajou, A.; Kobayashi, E.; OKADA, S.; *Electrochemistry* **2015**, *83*, 885–888.

20. Li, K.; Cao, L.; Huang, Z.; Chen, L.; Chen, Z.; Fu, C.; *J. Power Sources* **2017**, *344*, 25–31.

21. Xie, A.; Ma, C.-A.; Wang, L.; Chu, Y.; *Electrochim. Acta* **2007**, *52*, 2945–2949.

22. Zhao, W.; Zhong, G.; Zheng, J.; Zheng, J.; Song, J.; Gong, Z.; Chen, Z.; Zheng, G.; Jiang, Z.; Yang, Y.; *ACS Appl. Mater. Interfaces* **2018**, *10*, 3522–3529.

23. Liu, C.; Neale, Z.G.; Cao, G.; *Mater. Today* **2016**, *19*, 109–123.

24. Padhi, A.K.; *J. Electrochem. Soc.* **1997**, *144*, 1188.

25. Yabuuchi, N.; Ohzuku, T.; *J. Power Sources* **2003**, *119-121*, 171–174.

26. Yamada, A.; Chung, S.C.; Hinokuma, K.; *J. Electrochem. Soc.* **2001**, *148*, A224.

27. Chung, D.D.L.; *J. Mater. Sci.* **2002**, *37*, 1475–1489.

28. Dahn, J.; *Phys. Rev. B* **1991**, *44*, 9170–9177.

29. Lu, X.; Zhao, L.; He, X.; Xiao, R.; Gu, L.; Hu, Y.-S.; Li, H.; Wang, Z.; Duan, X.; Chen, L.; Maier, J.; Ikuhara, Y.; *Adv. Mater.* **2012**, *24*, 3233–3238.

30. Senyshyn, A.; Dolotko, O.; Mühlbauer, M.J.; Nikolowski, K.; Fuess, H.; Ehrenberg, H.; *J. Electrochem. Soc.* **2013**, *160*, A3198-A3205.

31. Verde, M.G.; Baggetto, L.; Balke, N.; Veith, G.M.; Seo, J.K.; Wang, Z.; Meng, Y.S.; *ACS Nano* **2016**, *10*, 4312–4321.

32. Xu, G.; Han, P.; Dong, S.; Liu, H.; Cui, G.; Chen, L.; *Coord. Chem. Rev.* **2017**, *343*, 139–184.

33. Gao, G.; Dang, W.; Wu, H.; Zhang, G.; Feng, C.; *J. Mater. Sci.: Mater. Electron.* **2018**, *29*, 12804–12812.

34. Jian, Z.; Lu, X.; Fang, Z.; Hu, Y.-S.; Zhou, J.; Chen, W.; Chen, L.; *Electrochem. Commun.* **2011**, *13*, 1127–1130.

35. Lu, J.S.; Maggay, I.V.B.; Liu, W.R.; *Chem. Commun.* **2018**, *54*, 3094–3097.

36. Di He; Wu, T.; Wang, B.; Yang, Y.; Zhao, S.; Wang, J.; Yu, H.; *Chem. Commun.* **2019**, *55*, 2234–2237.

37. Zhang, C.; Wu, C.; Zhang, Z.; Shen, Y.; Liu, W.; *Trans. Tianjin Univ.* **2020**, *26*, 142–147.

38. Zhang, P.B.; You, Y.; Wang, C.; Fang, X.H.; Ren, W.; Yang, L.Y.; Chen, X.Y.; *IOP Conf. Ser.: Earth Environ. Sci.* **2019**, *354*, 12079.

39. Bierenbaum, H.S.; Isaacson, R.B.; Druin, M.L.; Plovan, S.G.; *Ind. Eng. Chem. Prod. Res. Dev.* **1974**, *13*, 2–9.

40. Druin, M.L.; Loft, J.T.; Plovan, S.G.; *Novel open-celled microporous film*, *United States Patent* **1974**, US3801404.

41. Isaacson, R.B.; Bierenbaum, H.S.; *Process for preparing microporous film*, *United States Patent* **1971**, US3558764.

42. Hamano, K.; Yoshida, Y.; Shiota, H.; Shiraga, S.; Aihara, S.; Murai, M.; Inuzuka, T.; *Lithium Ion Secondary Battery*, *United States Patent* **2003**, US6664007B2.

43. Kim, K.J.; Kwon, H.K.; Park, M.-S.; Yim, T.; Yu, J.-S.; Kim, Y.-J.; *Phys. Chem. Chem. Phys.* **2014**, *16*, 9337–9343.

44. Kim, S.S.; Lloyd, D.R.; *J. Membr. Sci.* **1991**, *64*, 13–29.

45. Lee, J.; Lee, C.-L.; Park, K.; Kim, I.-D.; *J. Power Sources* **2014**, *248*, 1211–1217.

46. Lee, T.; Kim, W.-K.; Lee, Y.; Ryou, M.-H.; Lee, Y.M.; *Macromol. Res.* **2014**, *22*, 1190–1195.

47. Liang, X.; Yang, Y.; Jin, X.; Huang, Z.; Kang, F.; *J. Membr. Sci.* **2015**, *493*, 1–7.

48. Liu, H.; Xu, J.; Guo, B.; He, X.; *Ceram. Int.* **2014**, *40*, 14105–14110.

49. Liu, Q.; Xia, M.; Chen, J.; Tao, Y.; Wang, Y.; Liu, K.; Li, M.; Wang, W.; Wang, D.; *Electrochim. Acta* **2015**, *176*, 949–955.

50. Luo, W.; Zhou, L.; Fu, K.; Yang, Z.; Wan, J.; Manno, M.; Yao, Y.; Zhu, H.; Yang, B.; Hu, L.; *Nano Lett.* **2015**, *15*, 6149–6154.

51. Shi, C.; Zhang, P.; Chen, L.; Yang, P.; Zhao, J.; *J. Power Sources* **2014**, *270*, 547–553.

52. Xu, Q.; Kong, Q.; Liu, Z.; Zhang, J.; Wang, X.; Liu, R.; Yue, L.; Cui, G.; *RSC Adv.* **2014**, *4*, 7845.

53. Yeon, D.; Lee, Y.; Ryou, M.-H.; Lee, Y.M.; *Electrochim. Acta* **2015**, *157*, 282–289.

54. Buhrmester, C.; Chen, J.; Moshurchak, L.; Jiang, J.; Wang, R.L.; Dahn, J.; *J. Electrochem. Soc.* **2005**, *152*, A2390.

55. Buhrmester, C.; Moshurchak, L.M.; Wang, R.L.; Dahn, J.; *J. Electrochem. Soc.* **2006**, *153*, A1800.

56. Buhrmester, C.; Moshurchak, L.; Wang, R.L.; Dahn, J.; *J. Electrochem. Soc.* **2006**, *153*, A288.

57. Chen, J.; Buhrmester, C.; Dahn, J.; *Electrochem. Solid-State Lett.* **2005**, *8*, A59.

58. Chen, R.; Wu, F.; Li, L.; Guan, Y.; Qiu, X.; Chen, S.; Li, Y.; Wu, S.; *J. Power Sources* **2007**, *172*, 395–403.

59. Chen, Z.; Wang, Q.; Amine, K.; *J. Electrochem. Soc.* **2006**, *153*, A2215.

60. Croce, F.; *J. Electrochem. Soc.* **1996**, *143*, 154.

61. Dahn, J.; Jiang, J.; Moshurchak, L.M.; Fleischauer, M.D.; Buhrmester, C.; Krause, L.J.; *J. Electrochem. Soc.* **2005**, *152*, A1283.

62. Dominey, L.A.; Koch, V.R.; Blakley, T.J.; *Electrochim. Acta* **1992**, *37*, 1551–1554.

63. Kasnatscheew, J.; Streipert, B.; Röser, S.; Wagner, R.; Cekic Laskovic, I.; Winter, M.; *Phys. Chem. Chem. Phys.* **2017**, *19*, 16078–16086.

64. Ming, J.; Li, M.; Kumar, P.; Lu, A.-Y.; Wahyudi, W.; Li, L.-J.; *ACS Energy Lett.* **2016**, *1*, 529–534.

65. Schwenke, K.U.; Solchenbach, S.; Demeaux, J.; Lucht, B.L.; Gasteiger, H.A.; *J. Electrochem. Soc.* **2019**, *166*, A2035-A2047.

66. Tan, S.; Zhang, Z.; Li, Y.; Li, Y.; Zheng, J.; Zhou, Z.; Yang, Y.; *J. Electrochem. Soc.* **2013**, *160*, A285-A292.

67. Täubert, C.; Fleischhammer, M.; Wohlfahrt-Mehrens, M.; Wietelmann, U.; Buhrmester, T.; *J. Electrochem. Soc.* **2010**, *157*, A721.

68. Zhang, S.S.; *J. Power Sources* **2006**, *163*, 567–572.

69. Pfleging, W.; Pröll, J. J. Mater. Chem. A, 2(36), 14918-14926; *J. Mater. Chem. A* **2014**, *2*, 14918–14926.

70. *Handbuch Lithium-Ionen-Batterien;* Korthauer, R., Ed.; Springer Berlin Heidelberg: Berlin, Heidelberg, **2013**, ISBN 978-3-642-30652-5.

71. Zheng, H.; Tan, L.; Liu, G.; Song, X.; Battaglia, V.S.; *J. Power Sources* **2012**, *208*, 52–57.

72. Zheng, H.; Li, J.; Song, X.; Liu, G.; Battaglia, V.S. Electrochimica Acta, 71, 258-265; *Electrochim. Acta* **2012**, *71*, 258–265.

73. Frankenberger, M.; Singh, M.; Dinter, A.; Jankowksy, S.; Schmidt, A.; Pettinger, K.-H.; *J. Electroanal. Chem.* **2019**, *837*, 151–158.

74. Frankenberger, M.; Singh, M.; Dinter, A.; Pettinger, K.-H.; *Batteries* **2019**, *5*, 71.

75. Frankenberger, M.; Trunk, M.; Seidlmayer, S.; Dinter, A.; Dittloff, J.; Werner, L.; Gernhäuser, R.; Revay, Z.; Märkisch, B.; Gilles, R.; Pettinger, K.-H.; *Batteries* **2020**, *6*, 21.

76. *Handbook of battery materials;* Besenhard, J.O., Ed.; Wiley-VCH: Weinheim, New York, **1999**, ISBN 9783527611676.

77. Wetjen, M.; Trunk, M.; Werner, L.; Gernhäuser, R.; Märkisch, B.; Revay, Z.; Gilles, R.; Gasteiger, H.A.; *J. Electrochem. Soc.* **2018**, *165*, A2340-A2348.

78. Jossen, A.; Weydanz, W.; *Moderne Akkumulatoren richtig einsetzen*, 2. überarbeitete Auflage; Cuvillier Verlag: Göttingen, **2019**, ISBN 3736999453.

79. Bramnik, N.N.; Bramnik, K.G.; Nikolowski, K.; Hinterstein, M.; Baehtz, C.; Ehrenberg, H.; *Electrochem. Solid-State Lett.* **2005**, *8*, A379.

80. Nam, K.-W.; Yoon, W.-S.; Zaghib, K.; Yoon Chung, K.; Yang, X.-Q.; *Electrochem. Commun.* **2009**, *11*, 2023–2026.

81. Ouyang, C.; Shi, S.; Wang, Z.; Huang, X.; Chen, L.; *Phys. Rev. B* **2004**, *69*, 1188.

82. Julien, C.M.; Mauger, A.; Zaghib, K.; *J. Mater. Chem.* **2011**, *21*, 9955.

83. Satyavani, T.; Ramya Kiran, B.; Rajesh Kumar, V.; Srinivas Kumar, A.; Naidu, S.V.; *Eng. Sci. Technol. Int J.* **2016**, *19*, 40–44.

84. Malik, R.; Burch, D.; Bazant, M.Z.; Ceder, G.; *Nano Lett.* **2010**, *10*, 4123–4127.

85. Gao, J.; Shi, S.-Q.; Li, H.; *Chinese Phys. B* **2016**, *25*, 18210.

86. Bak, S.-M.; Hu, E.; Zhou, Y.; Yu, X.; Senanayake, S.D.; Cho, S.-J.; Kim, K.-B.; Chung, K.Y.; Yang, X.-Q.; Nam, K.-W.; *ACS Appl. Mater. Interfaces* **2014**, *6*, 22594–22601.

87. Noh, H.-J.; Youn, S.; Yoon, C.S.; Sun, Y.-K.; *J. Power Sources* **2013**, *233*, 121–130.

88. Jung, R.; Metzger, M.; Maglia, F.; Stinner, C.; Gasteiger, H.A.; *J. Electrochem. Soc.* **2017**, *164*, A1361-A1377.

89. Koyama, Y.; Tanaka, I.; Adachi, H.; Makimura, Y.; Ohzuku, T.; *J. Power Sources* **2003**, *119-121*, 644–648.

90. Yin, S.-C.; Rho, Y.-H.; Swainson, I.; Nazar, L.F.; *Chem. Mater.* **2006**, *18*, 1901–1910.

91. Buchberger, I.; Seidlmayer, S.; Pokharel, A.; Piana, M.; Hattendorff, J.; Kudejova, P.; Gilles, R.; Gasteiger, H.A.; *J. Electrochem. Soc.* **2015**, *162*, A2737-A2746.

92. Kasnatscheew, J.; Rodehorst, U.; Streipert, B.; Wiemers-Meyer, S.; Jakelski, R.; Wagner, R.; Laskovic, I.C.; Winter, M.; *J. Electrochem. Soc.* **2016**, *163*, A2943-A2950.

93. Kasnatscheew, J.; Evertz, M.; Streipert, B.; Wagner, R.; Klöpsch, R.; Vortmann, B.; Hahn, H.; Nowak, S.; Amereller, M.; Gentschev, A.-C.; Lamp, P.; Winter, M.; *Phys. Chem. Chem. Phys.* **2016**, *18*, 3956–3965.

94. Kasnatscheew, J.; Evertz, M.; Streipert, B.; Wagner, R.; Nowak, S.; Cekic Laskovic, I.; Winter, M.; *J. Power Sources* **2017**, *359*, 458–467.

95. Gireaud, L.; Grugeon, S.; Laruelle, S.; Yrieix, B.; Tarascon, J.-M.; *Electrochem. Commun.* **2006**, *8*, 1639–1649.

96. Li, Z.; Huang, J.; Yann Liaw, B.; Metzler, V.; Zhang, J.; *J. Power Sources* **2014**, *254*, 168–182.

97. Steiger, J.; Kramer, D.; Mönig, R.; *J. Power Sources* **2014**, *261*, 112–119.

98. Kim, C.; Norberg, N.S.; Alexander, C.T.; Kostecki, R.; Cabana, J.; *Adv. Funct. Mater.* **2013**, *23*, 1214–1222.

99. Zhao, B.; Zikry, M.A.; *Polymer* **2015**, *57*, 1–11.

100. Kataoka, K.; Takahashi, Y.; Kijima, N.; Akimoto, J.; Ohshima, K.; *J. Phys. Chem. Solids* **2008**, *69*, 1454–1456.

101. Colin, J.-F.; Godbole, V.; Novák, P.; *Electrochem. Commun.* **2010**, *12*, 804–807.

102. Sun, X.; Radovanovic, P.V.; Cui, B.; *New J. Chem.* **2015**, *39*, 38–63.

103. Ohzuku, T.; Iwakoshi, Y.; Sawai, K.; *J. Electrochem. Soc.* **1993**, *140*, 2490–2498.

104. Persson, K.; *Materials Data on LiC6 (SG:191) by Materials Project*, United States: N. p., **2016**, doi:10.17188/1273021.

105. Amin, R.; Chiang, Y.-M.; *J. Electrochem. Soc.* **2016**, *163*, A1512-A1517.

106. Amin, R.; Ravnsbæk, D.B.; Chiang, Y.-M.; *J. Electrochem. Soc.* **2015**, *162*, A1163-A1169.

107. Molenda, J.; Ojczyk, W.; Marzec, J.; *J. Power Sources* **2007**, *174*, 689–694.

108. Satyavani, T.; Ramya Kiran, B.; Rajesh Kumar, V.; Srinivas Kumar, A.; Naidu, S.V.; *Eng. Sci. Technol. Int J.* **2016**, *19*, 40–44.

109. Vikram Babu, B.; Vijaya Babu, K.; Tewodros Aregai, G.; Seeta Devi, L.; Madhavi Latha, B.; Sushma Reddi, M.; Samatha, K.; Veeraiah, V.; *Results Phys.* **2018**, *9*, 284–289.

110. Dominko, R.; Gaberscek, M.; Drofenik, J.; Bele, M.; Pejovnik, S.; Jamnik, J.; *J. Power Sources* **2003**, *119-121*, 770–773.

111. Chi, Z.-X.; Zhang, W.; Cheng, F.-Q.; Chen, J.-T.; Cao, A.-M.; Wan, L.-J.; *RSC Adv.* **2014**, *4*, 7795.

112. Jiang, W.; Wu, M.; Liu, F.; Yang, J.; Feng, T.; *RSC Adv.* **2017**, *7*, 44296–44302.

113. Raj, H.; Sil, A.; *Ionics* **2018**, *24*, 2543–2553.

114. Spahr, M.E.; Goers, D.; Leone, A.; Stallone, S.; Grivei, E.; *J. Power Sources* **2011**, *196*, 3404–3413.

115. Hasegawa, K.; Noda, S.; *J. Power Sources* **2016**, *321*, 155–162.

116. Maryam, M.; Suriani, A.B.; Shamsudin, M.S.; Rusop, M.; *Adv. Mat. Res.* **2012**, *626*, 289–293.

117. Endo, M.; Kim, Y.; Hayashi, T.; Nishimura, K.; Matusita, T.; Miyashita, K.; Dresselhaus, M.; *Carbon* **2001**, *39*, 1287–1297.

118. Wang, Q.; Su, F.; Tang, Z.; Ling, G.; Yang, Q.-H.; *New Carbon Mater.* **2012**, *27*, 427–432.

119. *Lithium-Ion Batteries: Basics and Applications;* Korthauer, R., Ed.; Springer Berlin Heidelberg: Berlin, Heidelberg, **2018**, ISBN 9783662530702.

120. Müller, M.; Pfaffmann, L.; Jaiser, S.; Baunach, M.; Trouillet, V.; Scheiba, F.; Scharfer, P.; Schabel, W.; Bauer, W.; *J. Power Sources* **2017**, *340*, 1–5.

121. Morasch, R.; Landesfeind, J.; Suthar, B.; Gasteiger, H.A.; *J. Electrochem. Soc.* **2018**, *165*, A3459-A3467.

122. Markevich, E.; Salitra, G.; Aurbach, D.; *Electrochem. Commun.* **2005**, *7*, 1298–1304.

123. Hausbrand, R.; Cherkashinin, G.; Ehrenberg, H.; Gröting, M.; Albe, K.; Hess, C.; Jaegermann, W.; *Mat. Sci. Eng. B* **2015**, *192*, 3–25.

124. Buqa, H.; Holzapfel, M.; Krumeich, F.; Veit, C.; Novák, P.; *J. Power Sources* **2006**, *161*, 617–622.

125. Carvalho, D.V.; Loeffler, N.; Kim, G.-T.; Marinaro, M.; Wohlfahrt-Mehrens, M.; Passerini, S.; *Polymers (Basel)* **2016**, *8*.

126. Giorgio, F. de; Laszczynski, N.; Zamory, J. von; Mastragostino, M.; Arbizzani, C.; Passerini, S.; *ChemSusChem* **2017**, *10*, 379–386.

127. Lee, J.-H.; Lee, S.; Paik, U.; Choi, Y.-M.; *J. Power Sources* **2005**, *147*, 249–255.

128. Toigo, C.; Singh, M.; Gmeiner, B.; Biso, M.; Pettinger, K.-H.; *J. Electrochem. Soc.* **2020**, *167*, 20514.

129. Starke, B.; Seidlmayer, S.; Dolotko, O.; Gilles, R.; Pettinger, K.-H.; *Energies* **2017**, *10*, 2135.

130. Starke, B.; Seidlmayer, S.; Jankowsky, S.; Dolotko, O.; Gilles, R.; Pettinger, K.-H.; *Sustainability* **2017**, *9*, 888.

131. Giorgio, F. de; La Monaca, A.; Dinter, A.; Frankenberger, M.; Pettinger, K.-H.; Arbizzani, C.; *Electrochim. Acta* **2018**, *289*, 112–119.

132. Bigoni, F.; Giorgio, F. de; Soavi, F.; Arbizzani, C.; *J. Electrochem. Soc.* **2017**, *164*, A6171-A6177.

133. Gordon, R.; Orias, R.; Willenbacher, N.; *J Mater Sci* **2020**, *55*, 15867–15881.

134. Schälicke, G.; Landwehr, I.; Dinter, A.; Pettinger, K.-H.; Haselrieder, W.; Kwade, A.; *Energy Technol.* **2020**, *8*, 1900309.

135. Bockholt, H.; Haselrieder, W.; Kwade, A.; *ECS Trans.* **2013**, *50*, 25–35.

136. Arora, P.; Zhang, Z.J.; *Chem. Rev.* **2004**, *104*, 4419–4462.

137. Kannan, D.R.R.; Terala, P.K.; Moss, P.L.; Weatherspoon, M.H.; *Int. J. Electrochem.* **2018**, *2018*, 1–7.

138. Fukutsuka, T.; Koyamada, K.; Maruyama, S.; Miyazaki, K.; Abe, T.; *Electrochim. Acta* **2016**, *199*, 380–387.

139. Wang, Y.; Yin, C.; Song, Z.; Wang, Q.; Lan, Y.; Luo, J.; Bo, L.; Yue, Z.; Sun, F.; Li, X.; *Materials (Basel, Switzerland)* **2019**, *12*.

140. Lee, T.; Lee, Y.; Ryou, M.-H.; Lee, Y.M.; *RSC Adv.* **2015**, *5*, 39392–39398.

141. Xiang, Y.; Li, J.; Lei, J.; Liu, D.; Xie, Z.; Qu, D.; Li, K.; Deng, T.; Tang, H.; *ChemSusChem* **2016**, *9*, 3023–3039.

142. Springer, B.C.; Frankenberger, M.; Pettinger, K.-H.; *PLoS ONE* **2020**, *15*, e0227903.

143. Peled, E.; *J. Electrochem. Soc.* **1979**, *126*, 2047.

144. Xu, K.; *Chem. Rev.* **2004**, *104*, 4303–4417.

145. Schneider, Alan A., Moser, James R.; *Primary cells and iodine containing cathodes therefor*, *United States Patent* **1972**, US3674562.

146. Fraioli, A.V.; Barber, W.A.; Feldman, A.M.; *Composite paper electrode for a voltaic cell*, *United States Patent* **1970**, US3551205.

147. Skarstad, P.M.; Coury, A.J.; Untereker, D.F.; *Battery cathodes*, *United States Patent* **1972**, US4393125.

148. Fong, R.; *J. Electrochem. Soc.* **1990**, *137*, 2009.

149. Haynes, W.M.; *CRC Handbook of Chemistry and Physics*, 95th ed.; CRC Press: Hoboken, **2015**, ISBN 9781482208672.

150. Newman, J.; Thomas-Alyea, K.E.; *Electrochemical Systems*, 3rd ed.; Wiley-Interscience: s.l., **2004**, ISBN 9780471477567.

151. *Handbook of batteries;* Linden, D., Ed., 2nd ed.; McGraw-Hill: New York, **1995**, ISBN 9780070379213.

152. Schmidt, M.; Heider, U.; Kuehner, A.; Oesten, R.; Jungnitz, M.; Ignatiev, N.; Sartori, P.; *J. Power Sources* **2001**, *97-98*, 557–560.

153. Ue, M.; *J. Electrochem. Soc.* **1995**, *142*, 2577.

154. Walker, C.W.; *J. Electrochem. Soc.* **1996**, *143*, L80.

155. Wiemers-Meyer, S.; Winter, M.; Nowak, S.; *Phys. Chem. Chem. Phys.* **2016**, *18*, 26595–26601.

156. Waller, F.J.; Barrett, A.G.M.; Braddock, D.C.; Ramprasad, D.; McKinnell, R.M.; White, A.J.P.; Williams, D.J.; Ducray, R.; *J. Org. Chem.* **1999**, *64*, 2910–2913.

157. Naoi, K.; *J. Electrochem. Soc.* **1999**, *146*, 462.

158. Ue, M.; *J. Electrochem. Soc.* **1997**, *144*, 2684.

159. Ue, M.; Murakami, A.; Nakamura, S.; *J. Electrochem. Soc.* **2002**, *149*, A1572.

160. Xu, K.; Angell, C.A.; *Electrochim. Acta* **1995**, *40*, 2401–2403.

161. Jaumann, T.; Balach, J.; Langklotz, U.; Sauchuk, V.; Fritsch, M.; Michaelis, A.; Teltevskij, V.; Mikhailova, D.; Oswald, S.; Klose, M.; Stephani, G.; Hauser, R.; Eckert, J.; Giebeler, L.; *Energy Storage Mater.* **2017**, *6*, 26–35.

162. Nie, M.; Demeaux, J.; Young, B.T.; Heskett, D.R.; Chen, Y.; Bose, A.; Woicik, J.C.; Lucht, B.L.; *J. Electrochem. Soc.* **2015**, *162*, A7008-A7014.

163. Wang, D.Y.; Sinha, N.N.; Burns, J.C.; Aiken, C.P.; Petibon, R.; Dahn, J.; *J. Electrochem. Soc.* **2014**, *161*, A467-A472.

164. Wang, D.Y.; Xia, J.; Ma, L.; Nelson, K.J.; Harlow, J.E.; Xiong, D.; Downie, L.E.; Petibon, R.; Burns, J.C.; Xiao, A.; Lamanna, W.M.; Dahn, J.; *J. Electrochem. Soc.* **2014**, *161*, A1818-A1827.

165. Rago, N.D.; Basco, J.K.; Vu, A.; Li, J.; Hays, K.; Sheng, Y.; Wood, D.L.; Bloom, I.; *J. Power Sources* **2019**, *435*, 1–7.

166. Xu, K.; *Chem. Rev.* **2014**, *114*, 11503–11618.

167. Wang, B.; Qu, Q.T.; Xia, Q.; Wu, Y.P.; Li, X.; Gan, C.L.; van Ree, T.; *Electrochim. Acta* **2008**, *54*, 816–820.

168. Xiao, L.; Ai, X.; Cao, Y.; Yang, H.; *Electrochim. Acta* **2004**, *49*, 4189–4196.

169. Moshurchak, L.M.; Buhrmester, C.; Dahn, J.; *J. Electrochem. Soc.* **2005**, *152*, A1279.

170. Moshurchak, L.M.; Buhrmester, C.; Dahn, J.; *J. Electrochem. Soc.* **2008**, *155*, A129.

171. Herreyre, S.; Huchet, O.; Barusseau, S.; Perton, F.; Bodet, J.M.; Biensan, P.; *J. Power Sources* **2001**, *97-98*, 576–580.

172. Zhang, S.; Xu, K.; Jow, T.; *J Solid State Electrochem* **2003**, *7*, 147–151.

173. Zhang, S.; Xu, K.; Allen, J.; Jow, T.; *J. Power Sources* **2002**, *110*, 216–221.

174. *ProZell – Das Kompetenzcluster zur Batteriezellproduktion*. https://www.prozell-cluster.de/ (accessed on 28 February 2021).

175. Mayer, J.K.; Almar, L.; Asylbekov, E.; Haselrieder, W.; Kwade, A.; Weber, A.; Nirschl, H.; *Energy Technol.* **2020**, *8*, 1900161.

176. Haarmann, M.; Haselrieder, W.; Kwade, A.; *Energy Technol.* **2020**, *8*, 1801169.

177. Kim, K.M.; Jeon, W.S.; Chung, I.J.; Chang, S.H.; *J. Power Sources* **1999**, *83*, 108–113.

178. Lee, G.-W.; Ryu, J.H.; Han, W.; Ahn, K.H.; Oh, S.M.; *J. Power Sources* **2010**, *195*, 6049–6054.

179. Landesfeind, J.; Eldiven, A.; Gasteiger, H.A.; *J. Electrochem. Soc.* **2018**, *165*, A1122-A1128.

180. Landesfeind, J.; Ebner, M.; Eldiven, A.; Wood, V.; Gasteiger, H.A.; *J. Electrochem. Soc.* **2018**, *165*, A469-A476.

181. Landesfeind, J.; Hattendorff, J.; Ehrl, A.; Wall, W.A.; Gasteiger, H.A.; *J. Electrochem. Soc.* **2016**, *163*, A1373-A1387.

182. Dreger, H.; Bockholt, H.; Haselrieder, W.; Kwade, A.; *J. Electron. Mater.* **2015**, *44*, 4434–4443.

183. Matsumoto, A.; Fujie, F.; Okada, H.; *BINDER RESIN FOR SECONDARY BATTERY ELECTRODES, BINDER RESIN COMPOSITION FOR SECONDARY BATTERY ELECTRODES USING SAME, SLURRY FOR SECONDARY BATTERY ELECTRODES, ELECTRODE FOR SECONDARY BATTERIES, AND SECONDARY BATTERY*, *United States Patent* **2019**, US20190067698.

184. Pettinger, K.-H.; Kampker, A.; Hohenthanner, C.-R.; Deutskens, C.; Heimes, H.; vom Hemdt, A.; *Lithium-ion cell and battery production processes*. In *Lithium-Ion Batteries: Basics and Applications*; Korthauer, R., Ed.; Springer Berlin Heidelberg: Berlin, Heidelberg, **2018**; 211–226, ISBN 9783662530702.

185. Hawley, W.B.; Li, J.; *J. Energy Storage* **2019**, *25*, 100862.

186. Kang, H.; Lim, C.; Li, T.; Fu, Y.; Yan, B.; Houston, N.; Andrade, V. de; Carlo, F. de; Zhu, L.; *Electrochim. Acta* **2017**, *232*, 431–438.

187. Andrew van Bommel; Ranjith Divigalpitiya; *J. Electrochem. Soc.* **2013**, *159*.

188. Meyer, C.; Bockholt, H.; Haselrieder, W.; Kwade, A. Journal of Materials Processing Technology, 249, 172-178; *J. Mater. Process. Technol.* **2017**, *249*, 172–178.

189. Oladimeji, C.F.; Moss, P.L.; Weatherspoon, M.H.; *Adv. Chem.* **2016**, *2016*.

190. Sheng, Y.; Fell, C.R.; Son, Y.K.; Metz, B.M.; Jiang, J.; Church, B.C.; *Front. Energy Res.* **2014**, *2*, 56.

191. Zhijia Du; R. A. Dunlap; M. N. Obrovac; *J. Electrochem. Soc.* **2014**, *161*, A1698-A1705.

192. Müller, S.; Eller, J.; Ebner, M.; Burns, C.; Dahn, J.; Wood, V.; *J. Electrochem. Soc.* **2018**, *165*, A339-A344.

193. Jaiser, S.; Friske, A.; Baunach, M.; Scharfer, P.; Schabel, W.; *Dry. Technol.* **2017**, *35*, 1266–1275.

194. Jaiser, S.; Müller, M.; Baunach, M.; Bauer, W.; Scharfer, P.; Schabel, W. Journal of Power Sources, 318, 210-219; *J. Power Sources* **2016**, *318*, 210–219.

195. Arno Kwade; Wolfgang Haselrieder; Ruben Leithoff; Armin Modlinger; Franz Dietrich; Klaus Droeder; *Nat. Energy* **2018**, *3*, 290–300.

196. Danner, T.; Singh, M.; Hein, S.; Kaiser, J.; Hahn, H.; Latz, A.; *J. Power Sources* **2016**, *334*, 191–201.

197. Singh, M.; Kaiser, J.; Hahn, H.; *J. Electrochem. Soc.* **2015**, *162*, A1196-A1201.

198. Singh, M.; Kaiser, J.; Hahn, H.; *Batteries* **2016**, *2*, 35.

199. Singh, M.; Kaiser, J.; Hahn, H.; *J. Electroanal. Chem.* **2016**, *782*, 245–249.

200. Nadimpalli, S.P.; Sethuraman, V.A.; Abraham, D.P.; Bower, A.F.; Guduru, P.R.; *J. Electrochem. Soc.* **2015**, *162*, A2656-A2663.

201. Willenberg, L.K.; Dechent, P.; Fuchs, G.; Sauer, D.U.; Figgemeier, E.; *Sustainability* **2020**, *12*, 557.

202. Pettinger, K.-H.; *Fertigungsprozesse von Lithium-Ionen-Zellen*. In *Handbuch Lithium-Ionen-Batterien*; Korthauer, R., Ed.; Springer Berlin Heidelberg: Berlin, Heidelberg, **2013**, ISBN 978-3-642-30652-5.

203. Pettinger, K.-H.; *Li-Ionen Technologie - Zellbau und industrielle Fertigung*, iPAT lecture series 2013, iPAT Institut für Partikeltechnik - Technische Universität Braunschweig, Braunschweig, **2013**.

204. Schmutz, C.N.; Shokoohi, F.K.; Tarascon, J.-M.; Warren, P.C.; *Method of making a laminated lithium-ion rechargeable battery cell*, *United States Patent* **1995**, US5470357A.

205. Babinec, S.J.; Less, G.B.; Vieau, D.; *Laminated battery cell comprising multilayer composite separator and methods for creating the same*, *United States Patent* **2014**, USOO8697290B2.

206. Gozdz, A.S.; Schmutz, C.N.; Tarascon, J.-M.; Warren, P.C.; *Method of making an electrolyte activatable lithium-ion rechargeable battery cell*, *United States Patent* **1995**, US5456000A.

207. Gozdz, A.S.; Schmutz, C.N.; Warren, C.; *Low resistance rechargeable lithium-ion battery*, *United States Patent* **1996**, US005587253A.

208. Lee, S.-K.; Cho, J.-H.; Kim, D.-H.; Ku, C.-H.; *Secondary battery unit cell having improved wettability and manufacturing method therefor*, *European Patent Application* **2018**, EP3396767A1.

209. Wood, V.; Ebner, M.O.J.; *Method for the production of electrodes and electrodes made using such a method*, *European Patent Application* **2014**, EP2793300A1.

210. Choi, E.S.; Cho, S.H.; Park, B.O.; Chung, J.B.; Kim; Dong-Myung; *Curved electrode stacked body and battery cell comprising same*, *European Patent Application* **2018**, EP2985831B1.

211. Sayre, J.R.; Risser, S.M.; Manning, A.J.; *Multifunctional cell for structural applications*, *European Patent Application* **2018**, EP2852990B1.

212. Rho, S.Y.; Choi, W.G.; Cho, H.W.; Jang, J.H.; Noh, H.T.; Kim, J.G.; *Flexible battery, manufacturing method therefor, and auxiliary battery comprising flexible battery*, *European Patent Application* **2017**, EP3190651A1.

213. Toyoda, Y.; Sasaki, T.; *Separator for secondary cell*, *European Patent Application* **2018**, EP2835844B1.

214. Uematsu, I.; Hayamizu, N.; Sakurai, N.; *Secondary battery*, *European Patent Application* **2017**, EP2899777B1.

215. Laforgue, A.; Simon, P.; Fauvarque, J.F.; Mastragostino, M.; Soavi, F.; Sarrau, J.F.; Lailler, P.; Conte, M.; Rossi, E.; Saguatti, S.; *J. Electrochem. Soc.* **2003**, *150*, A645.

216. Pettinger, K.-H.; *Slurry coating techniques*, TZE invited lectures, Technology Center for Energy - Landshut University of Applied Sciences, Ruhstorf, **2017**.

217. Barsoukov, E.; Macdonald, J.R.; *Impedance Spectroscopy, Theory, experiment, and applications*, Second edition; Wiley: Hoboken, New Jersey, **2005**, ISBN 9780471647492.

218. Macdonald, J.R.; *Solid State Ion.* **1984**, *13*, 147–149.

219. Macdonald, J.R.; *Bull. Am. Phys. Soc.* **1985**, *30*, 587.

220. Macdonald, J.R.; *J. Appl. Phys.* **1985**, *58*, 1955–1970.

221. Macdonald, J.R.; *J. Appl. Phys.* **1985**, *58*, 1971–1978.

222. McCann, J.F.; *J. Electrochem. Soc.* **1982**, *129*, 551.

223. Randles, J.E.B.; *Discuss. Faraday Soc.* **1947**, *1*, 11.

224. Momma, T.; Matsunaga, M.; Mukoyama, D.; Osaka, T.; *J. Power Sources* **2012**, *216*, 304–307.

225. Gaberscek, M.; Moskon, J.; Erjavec, B.; Dominko, R.; Jamnik, J.; *Electrochem. Solid-State Lett.* **2008**, *11*, A170-A174.

226. Liu, G.; Zheng, H.; Kim S.; Deng, Y.; Minor A. M.; Song X.; Battaglia, V.S.; *J. Electrochem. Soc.* **2008**, *155*, A887-A892.

227. Gordon, I.J.A.; Grugeon, S.; Takenouti, H.; Tribollet, B.; Armand, M.; Davoisne, C.; Débart, A.; Laruelle, S.; *Electrochim. Acta* **2017**, *223*, 63–73.

228. Jiménez Gordon, I.; Grugeon, S.; Débart, A.; Pascaly, G.; Laruelle, S.; *Solid State Ion.* **2013**, *237*, 50–55.

229. Dollé, M.; Orsini, F.; Gozdz, A.S.; Tarascon, J.-M.; *J. Electrochem. Soc.* **2001**, *148*, A85-A857.

230. Yu, P.; Popov, B.N.; Ritter, J.A.; White, R.E.; *J. Electrochem. Soc.* **1999**, *146*, 8.

231. Liu, L.; Park, J.; Lin, X.; Sastry, A.M.; Lu, W.; *J. Power Sources* **2014**, *268*, 482–490.

232. Solchenbach, S.; Pritzl, D.; Kong, E.J.Y.; Landesfeind, J.; Gasteiger, H.A.; *J. Electrochem. Soc.* **2016**, *163*, A2265-A2272.

233. Song, J.Y.; Lee, H.H.; Wang, Y.Y.; Wan, C.C.; *J. Power Sources* **2002**, *111*, 255–267.

234. MarcoTolo; *Diagram of a scanning electron microscope with English captions.* https://commons.wikimedia.org/w/index.php?curid=9643934 **2010** (accessed on 26 February 2021).

235. Muso - Own work; *EDX-scheme.svg*. https://commons.wikimedia.org/w/index.php?curid=3241031 **2007** (accessed on 26 February 2021).

236. Downing, R.G.; Lamaze, G.P.; Langland, J.K.; Hwang, S.T.; *J. Res. Natl. Inst. Stand. Technol.* **1993**, *98*, 109–126.

237. Ziegler, J.F.; Ziegler, M.D.; Biersack, J.P.; *Nucl. Instrum. Methods Phys. Res. B* **2010**, *268*, 1818–1823.

238. Oudenhoven, J.F.M.; Labohm, F.; Mulder, M.; Niessen, R.A.H.; Mulder, F.M.; Notten, P.H.L.; *Adv. Mater.* **2011**, *23*, 4103–4106.

239. Lv, S.; Verhallen, T.W.; Vasileiadis, A.; Ooms, F.; Xu, Y.; Li, Z.; Li, Z.; Wagemaker, M.; *Nat. Commun.* **2018**, *9*, 2152.

240. Harks, P.-P.R.M.L.; Verhallen, T.W.; George, C.; van den Biesen, J.K.; Liu, Q.; Wagemaker, M.; Mulder, F.M.; *J. Am. Chem. Soc.* **2019**, *141*, 14280–14287.

241. Whitney, S.M.; Biegalski, S.R.F.; Huang, Y.H.; Goodenough, J.B.; *J. Electrochem. Soc.* **2009**, *156*, A886-A890.

242. Whitney, S.M.; Biegalski, S.R.F.; Downing, G.; *J. Radioanal. Nucl. Chem.* **2009**, *282*, 173–176.

243. Trunk, M.; Wetjen, M.; Werner, L.; Gernhäuser, R.; Märkisch, B.; Revay, Z.; Gasteiger, H.A.; Gilles, R.; *Mater. Charact.* **2018**, *146*, 127–134.

244. Chen, C.; Oudenhoven, J.F.M.; Danilov, D.L.; Vezhlev, E.; Gao, L.; Li, N.; Mulder, F.M.; Eichel, R.-A.; Notten, P.H.L.; *Adv. Energy Mater.* **2018**, *8*, 1801430.

245. Arens, T.; Hettlich, F.; Karpfinger, C.; Kockelkorn, U.; Lichtenegger, K.; Stachel, H.; *Mathematik*, 2. Aufl., 1. korrigierter Nachdr; Spektrum Akad. Verl.: Heidelberg, **2013**, ISBN 9783642404726.

246. Kendall, M.G.; Stuart, A.; Ord, J.K.; *The advanced theory of statistics*, *In three volumes*, 4. ed.; Griffin: London, **1979**, ISBN 0852642555.

247. Feller, W.; *An introduction to probability theory and its applications*, 2. ed., [Nachdr.]; Wiley: S.l., **2009**, ISBN 9780471257097.

248. Johnson, N.L.; Kotz, S.; *Distributions in statistics;* Wiley: New York, **1970**, ISBN 0471446262.

249. Cox, D.R.; Hinkley, D.V.; *Theoretical statistics*, Reprint; Chapman & Hall/CRC: Boca Raton, **2000**, ISBN 0412428601.

250. Kardar, M.; *Statistical Physics of Particles;* Cambridge University Press: Cambridge, **2007**, ISBN 9780511815898.

251. Orazem, M.E.; Tribollet, B.; *Electrochemical impedance spectroscopy;* Wiley: Hoboken, NJ, **2008**, ISBN 9780470041406.

252. Peck, R.; Devore, J.L.; *Statistics*, *The exploration and analysis of data*, 7th ed.; Brooks/Cole, Cengage Learning: Australia, United States, **2012**, ISBN 9780840058010.

253. Minitab.com; *Minitab User's Manual*. https://support.minitab.com/de-de/minitab/18/help-and-how-to/statistics/basic-statistics/supporting-topics/normality/test-for-normality/ **2019** (accessed on 25 June 2021).

254. Weibull, W.; *A statistical theory of the strength of materials;* Generalstabens litografiska anstalts förlag: Stockholm, **1939**.

255. Andreas Handl; *Symmetrie und Schiefe*. https://www.andreashandl.de/wp-content/uploads/2017/05/symmetrie.pdf **2017** (accessed on 11 August 2020).

256. Minitab.com; *Minitab User's Manual*. https://support.minitab.com/de-de/minitab/20/help-and-how-to/statistics/basic-statistics/supporting-topics/normality/what-to-do-with-nonnormal-data/ **2019** (accessed on 25 June 2021).

257. Park, J.-K.; *Principles and applications of lithium secondary batteries;* Wiley-VCH: Weinheim, **2012**, ISBN 9783527650408.

258. Peled, E.; Menkin, S.; *J. Electrochem. Soc.* **2017**, *164*, A1703-A1719.

259. Peled, E.; Golodnitsky, D.; Penciner, J.; *The Anode/Electrolyte Interface*. In *Handbook of battery materials*; Besenhard, J.O., Ed.; Wiley-VCH: Weinheim, New York, **1999**, ISBN 9783527611676.

260. Edström, K.; Herstedt, M.; Abraham, D.P.; *J. Power Sources* **2006**, *153*, 380–384.

261. Soto, F.A.; Ma, Y.; La Martinez de Hoz, J.M.; Seminario, J.M.; Balbuena, P.B.; *Chem. Mater.* **2015**, *27*, 7990–8000.

262. Thevenin, J.G.; *J. Electrochem. Soc.* **1987**, *134*, 273.

263. Peled, E.; Tow, D.B.; Merson, A.; Burstein, L.; *J. New Mat. Electrochem. Syst.* **1999**, *3*.

264. Peled, E.; Tow, D.B.; Merson, A.; Gladkich, A.; Burstein, L.; Golodnitsky, D.; *J. Power Sources* **2001**, *97-98*, 52–57.

265. Thomas, M.G.S.R.; Bruce, P.G.; Goodenough, J.B.; *J. Electrochem. Soc.* **1985**, *132*, 1521.

266. Aurbach, D.; Markovsky, B.; Rodkin, A.; Levi, E.; Cohen, Y.; Kim, H.-J.; Schmidt, M.; *Electrochim. Acta* **2002**, *47*, 4291–4306.

267. Würsig, A.; Buqa, H.; Holzapfel, M.; Krumeich, F.; Novák, P.; *Electrochem. Solid-State Lett.* **2005**, *8*, A34.

268. Liu, Y.-M.; G Nicolau, B.; Esbenshade, J.L.; Gewirth, A.A.; *Anal. Chem.* **2016**, *88*, 7171–7177.

269. Pettinger, K.-H.; *Production test procedures*. In *Lithium-Ion Batteries: Basics and Applications*; Korthauer, R., Ed.; Springer Berlin Heidelberg: Berlin, Heidelberg, **2018**; 237–246, ISBN 9783662530702.

270. An, S.J.; Li, J.; Du, Z.; Daniel, C.; Wood, D.L.; *J. Power Sources* **2017**, *342*, 846–852.

271. Heimes, H.H.; Offermanns, C.; Mohsseni, A.; Laufen, H.; Westerhoff, U.; Hoffmann, L.; Niehoff, P.; Kurrat, M.; Winter, M.; Kampker, A.; *Energy Technol.* **2019**, *118*, 1900118.

272. Holtstiege, F.; Bärmann, P.; Nölle, R.; Winter, M.; Placke, T.; *Batteries* **2018**, *4*, 4.

273. Tabuchi, T.; Yasuda, H.; Yamachi, M.; *J. Power Sources* **2005**, *146*, 507–509.

274. Tabuchi, T.; Yasuda, H.; Yamachi, M.; *J. Power Sources* **2006**, *162*, 813–817.

275. Veluchamy, A.; Doh, C.-H.; Kim, D.-H.; Lee, J.-H.; Lee, D.-J.; Ha, K.-H.; Shin, H.-M.; Jin, B.-S.; Kim, H.-S.; Moon, S.-I.; Park, C.-W.; *J. Power Sources* **2009**, *188*, 574–577.

276. Zhang, X.; Qu, H.; Ji, W.; Zheng, D.; Ding, T.; Abegglen, C.; Qiu, D.; Qu, D.; *ACS Appl. Mater. Interfaces* **2020**, *12*, 11589–11599.

277. Liu, C.; Kim, N.; Rubloff, G.W.; Lee, S.B.; *Nanoscale* **2017**, *9*, 11566–11573.

278. Kim, H.J.; Choi, S.; Lee, S.J.; Seo, M.W.; Lee, J.G.; Deniz, E.; Lee, Y.J.; Kim, E.K.; Choi, J.W.; *Nano Lett.* **2016**, *16*, 282–288.

279. Fei, L.; Yoo, S.H.; Villamayor, R.A.R.; Williams, B.P.; Gong, S.Y.; Park, S.; Shin, K.; Joo, Y.L.; *ACS Appl. Mater. Interfaces* **2017**, *9*, 9738–9746.

280. Hanai, K.; Liu, Y.; Matsumura, T.; Imanishi, N.; Hirano, A.; Takeda, Y.; *Solid State Ion.* **2008**, *179*, 1725–1730.

281. Liu, N.; Hu, L.; McDowell, M.T.; Jackson, A.; Cui, Y.; *ACS Nano* **2011**, *5*, 6487–6493.

282. Sun, H.; He, X.; Ren, J.; Li, J.; Jiang, C.; Wan, C.; *Electrochim. Acta* **2007**, *52*, 4312–4316.

283. Wang, Z.; Fu, Y.; Zhang, Z.; Yuan, S.; Amine, K.; Battaglia, V.; Liu, G.; *J. Power Sources* **2014**, *260*, 57–61.

284. Yang, J.; Takeda, Y.; Imanishi, N.; Yamamoto, O.; *Electrochim. Acta* **2001**, *46*, 2659–2664.

285. Zhao, H.; Wang, Z.; Lu, P.; Jiang, M.; Shi, F.; Song, X.; Zheng, Z.; Zhou, X.; Fu, Y.; Abdelbast, G.; Xiao, X.; Liu, Z.; Battaglia, V.S.; Zaghib, K.; Liu, G.; *Nano Lett.* **2014**, *14*, 6704–6710.

286. Liu, D.; Du, F.; Pan, W.; Chen, G.; Wang, C.; Wei, Y.; *Mater. Lett.* **2009**, *63*, 504–506.

287. Liu, Y.; *Solid State Ion.* **2004**, *172*, 69–72.

288. Liu, Y.; Hanai, K.; Horikawa, K.; Imanishi, N.; Hirano, A.; Takeda, Y.; *Mater. Chem. Phys.* **2005**, *89*, 80–84.

289. Liu, Y.; Horikawa, K.; Fujiyosi, M.; Imanishi, N.; Hirano, A.; Takeda, Y.; *Electrochim. Acta* **2004**, *49*, 3487–3496.

290. Shodai, T.; *Solid State Ion.* **1999**, *122*, 85–93.

291. Sun, H.; HE, X.; LI, J.; REN, J.; JIANG, C.; WAN, C.; *Solid State Ion.* **2006**, *177*, 1331–1334.

292. Deng, K.; Han, D.; Ren, S.; Wang, S.; Xiao, M.; Meng, Y.; *J. Mater. Chem. A* **2019**, *7*, 13113–13119.

293. Ma, L.; Kim, M.S.; Archer, L.A.; *Chem. Mater.* **2017**, *29*, 4181–4189.

294. Menkin, S.; Golodnitsky, D.; Peled, E.; *Electrochem. Commun.* **2009**, *11*, 1789–1791.

295. Zhang, L.; Zhang, K.; Shi, Z.; Zhang, S.; *Langmuir* **2017**, *33*, 11164–11169.

296. Gallus, D.R.; Schmitz, R.; Wagner, R.; Hoffmann, B.; Nowak, S.; Cekic-Laskovic, I.; Schmitz, R.W.; Winter, M.; *Electrochim. Acta* **2014**, *134*, 393–398.

297. Lux, S.F.; Lucas, I.T.; Pollak, E.; Passerini, S.; Winter, M.; Kostecki, R.; *Electrochem. Commun.* **2012**, *14*, 47–50.

298. Hunter, J.C.; *J. Solid State Chem.* **1981**, *39*, 142–147.

299. Aurbach, D.; Levi, M.D.; Gamulski, K.; Markovsky, B.; Salitra, G.; Levi, E.; Heider U.; Heider, L.; Oesten, B.; *J. Power Sources* **1999**, *81-82*, 472–479.

300. Yabuuchi, N.; Makimura, Y.; Ohzuku, T.; *J. Electrochem. Soc.* **2007**, *154*, A314.

301. Shaju, K.M.; Bruce, P.G.; *Adv. Mater.* **2006**, *18*, 2330–2334.

302. Petzl, M.; Kasper, M.; Danzer, M.A.; *J. Power Sources* **2015**, *275*, 799–807.

303. Petzl, M.; Danzer, M.A.; *J. Power Sources* **2014**, *254*, 80–87.

304. Meyerson, M.L.; Sheavly, J.K.; Dolocan, A.; Griffin, M.P.; Pandit, A.H.; Rodriguez, R.; Stephens, R.M.; Vanden Bout, D.A.; Heller, A.; Mullins, C.B.; *J. Mater. Chem. A* **2019**, *7*, 14882–14894.

305. An, S.J.; Li, J.; Daniel, C.; Mohanty, D.; Nagpure, S.; Wood, D.L.; *Carbon* **2016**, *105*, 52–76.

306. Amine, K.; Chen, Z.; Zhang, Z.; Liu, J.; Lu, W.; Qin, Y.; Lu, J.; Curtis, L.; Sun, Y.-K.; *J. Mater. Chem.* **2011**, *21*, 17754.

307. Joshi, T.; Eom, K.; Yushin, G.; Fuller, T.F.; *J. Electrochem. Soc.* **2014**, *161*, A1915-A1921.

308. Komaba, S.; Kumagai, N.; Kataoka, Y.; *Electrochim. Acta* **2002**, *47*, 1229–1239.

309. Zheng, H.; Sun, Q.; Liu, G.; Song, X.; Battaglia, V.S.; *J. Power Sources* **2012**, *207*, 134–140.

310. Nakamura, T.; Okano, S.; Yaguma, N.; Morinaga, Y.; Takahara, H.; Yamada, Y.; *J. Power Sources* **2013**, *244*, 532–537.

311. Jeong, C.U.; Lee, S.-Y.; Kim, J.; Cho, K.Y.; Yoon, S.; *J. Power Sources* **2018**, *398*, 193–200.

312. Loghavi, M.M.; Askari, M.; Babaiee, M.; Ghasemi, A.; *J. Electroanal. Chem.* **2019**, *841*, 107–110.

313. Frankenberger, M.; Pettinger, K.-H.; *Zwischenbericht SurfaLIB 2018-I - project number 03ET6103C, Federal Ministry for Economic Affairs and Energy, Germany*, Ruhstorf, **2018**.

314. Pettinger, K.-H.; Frankenberger, M.; *Verbundvorhaben SurfaLIB: Verbesserte Lithium-Ionen-Batterien durch Modifikation der Elektrodenoberflächen; Teilprojekt: Prozessieren und elektrochemische Performance von strukturierten Dickschichtelektroden auf modifizierten Stromableiterfolien : Schlussbericht.* https://www.tib.eu/de/suchen/id/TIBKAT:1743681216/Verbundvorhaben-SurfaLIB-Verbesserte-Lithium-Ionen?cHash=a5fa4a39072ad9ff77ff8bcdb4b13371 **2020** (accessed on 26 January 2021).

315. Habedank, J.B.; Kraft, L.; Rheinfeld, A.; Krezdorn, C.; Jossen, A.; Zaeh, M.F.; *J. Electrochem. Soc.* **2018**, *165*, A1563-A1573.

316. Pfleging, W.; *Nanophotonics* **2018**, *7*, 549–573.

317. Mangang, M.; Seifert, H.J.; Pfleging, W.; *J. Power Sources* **2016**, *304*, 24–32.

318. Smyrek, P.; Pröll, J.; Seifert, H.J.; Pfleging, W.; *J. Electrochem. Soc.* **2016**, *163*, A19-A26.

319. Kohler, R.; Bruns, M.; Smyrek, P.; Ulrich, S.; Przybylski, M.; Pfleging, W.; *Laser annealing of textured thin film cathode material for lithium ion batteries*. In *Laser-based Micro- and Nanopackaging and Assembly IV;* SPIE LASE, **2010**, San Francisco, California, USA; SPIE; 75850O.

320. Kohler, R.; Proell, J.; Ulrich, S.; Trouillet, V.; Indris, S.; Przybylski, M.; Pfleging, W.; *Laser-assisted structuring and modification of LiCoO 2 thin films*. In *Laser-based Micro- and Nanopackaging and Assembly III;* SPIE LASE: Lasers and Applications in Science and Engineering, **2009**, San Jose, CA; SPIE; 720207.

321. Proell, J.; *J. Laser Micro Nanoeng.* **2012**, *7*, 97–104.

322. Pröll, J.; Kohler, R.; Adelhelm, C.; Bruns, M.; Torge, M.; Heißler, S.; Przybylski, M.; Ziebert, C.; Pfleging, W.; *Laser modification and characterization of Li-Mn-O thin film cathodes for lithium-ion batteries*. In *Laser-based Micro- and Nanopackaging and Assembly V;* SPIE LASE, **2011**, San Francisco, California, USA; SPIE; 79210Q.

323. Pröll, J.; Kohler, R.; Bruns, M.; Oberst, V.; Weidler, P.G.; Heißler, S.; Kübel, C.; Scherer, T.; Prang, R.; Seifert, H.J.; Pfleging, W.; *Thin film passivation of laser generated 3D micro patterns in lithium manganese oxide cathodes*. In *Laser-based Micro- and Nanopackaging and Assembly VII;* SPIE LASE, **2013**, San Francisco, California, USA; SPIE; 860807.

324. Pröll, J.; Kohler, R.; Torge, M.; Bruns, M.; Przybylski, M.; Ulrich, S.; Seifert, H.J.; Pfleging, W.; *Laser adjusted three-dimensional Li-Mn-O cathode architectures for secondary lithium-ion cells*. In *Laser-based Micro- and Nanopackaging and Assembly VI;* SPIE LASE, **2012**, San Francisco, California, USA; SPIE; 82440S.

325. Yamada, M.; Watanabe, T.; Gunji, T.; Wu, J.; Matsumoto, F.; *Electrochem* **2020**, *1*, 124–159.

326. Doberdò, I.; Löffler, N.; Laszczynski, N.; Cericola, D.; Penazzi, N.; Bodoardo, S.; Kim, G.-T.; Passerini, S.; *J. Power Sources* **2014**, *248*, 1000–1006.

327. Busson, C.; Blin, M.-A.; Guichard, P.; Soudan, P.; Crosnier, O.; Guyomard, D.; Lestriez, B.; *J. Power Sources* **2018**, *406*, 7–17.

328. Turi, E.; Ray, M.B.; *Current Collector having a Conductive Primer Layer*, *United States Patent* **1995**, US5478676.

329. Wang, R.; Li, W.; Liu, L.; Qian, Y.; Liu, F.; Chen, M.; Guo, Y.; Liu, L.; *J. Electroanal. Chem.* **2019**, *833*, 63–69.

330. Wu, H.-C.; Wu, H.-C.; Lee, E.; Wu, N.-L.; *Electrochem. Commun.* **2010**, *12*, 488–491.

331. Lepage, D.; Savignac, L.; Saulnier, M.; Gervais, S.; Schougaard, S.B.; *Electrochem. Commun.* **2019**, *102*, 1–4.

332. Swain, P.; Viji, M.; Mocherla, P.S.; Sudakar, C.; *J. Power Sources* **2015**, *293*, 613–625.

333. Frankenberger, M.; Schubert, J.; Pettinger, K.-H.; *Zwischenbericht SurfaLIB 2018-II - project number 03ET6103C, Federal Ministry for Economic Affairs and Energy, Germany*, Ruhstorf, **2019**.

334. Schubert, J.; *Neuartige Haftvermittler für Lithium-Ionen- Akkumulatoren zur Verbesserung des Stromkollektor/Aktivmaterial-Interface - Master studies Research Report 2*, Ruhstorf, **2019**.

335. Nava-Avendaño, J.; Veilleux, J.; *J. Phys. D: Appl. Phys.* **2017**, *50*, 163001.

336. Tanaka, M.; Kageyama, T.; Sone, H.; Yoshida, S.; Okamoto, D.; Watanabe, T.; *Nanomaterials (Basel)* **2016**, *6*.

337. Jiang, Q.; Zhang, H.; Wang, S.; *Green Chem.* **2016**, *18*, 662–666.

338. Major, K.; Veilleux, J.; Brisard, G.; *J. Therm. Spray Tech.* **2016**, *25*, 357–364.

339. Endo, E.; Yasuda, T.; Kita, A.; Yamaura, K.; Sekai, K.; *J. Electrochem. Soc.* **2000**, *147*, 1291.

340. Wang, J.; Zhang, Q.; Li, X.; Wang, Z.; Guo, H.; Xu, D.; Zhang, K.; *Phys. Chem. Chem. Phys.* **2014**, *16*, 16021–16029.

341. Doğan, İ.; van de Sanden, M.C.M.; *Plasma Process. Polym.* **2016**, *13*, 19–53.

342. Ding, Y.; Yamada, R.; Gresback, R.; Zhou, S.; Pi, X.; Nozaki, T.; *J. Phys. D: Appl. Phys.* **2014**, *47*, 485202.

343. Lamontagne, P.; Soucy, G.; Veilleux, J.; Quesnel, F.; Hovington, P.; Zhu, W.; Zaghib, K.; *Phys. Status Solidi A* **2014**, *211*, 1610–1616.

344. Fauchais, P.; Montavon, G.; Lima, R.S.; Marple, B.R.; *J. Phys. D: Appl. Phys.* **2011**, *44*, 93001.

345. Wang, Z.; Zhu, H.; Yang, L.; Wang, X.; Liu, Z.; Chen, Q.; *Plasma Sci. Technol.* **2016**, *18*, 424–429.

346. Han, M.; Kim, D.-W.; Kim, Y.-C.; *ACS Appl. Mater. Interfaces* **2016**, *8*, 26073–26081.

347. Chen, H.; Lin, Q.; Xu, Q.; Yang, Y.; Shao, Z.; Wang, Y.; *J. Membr. Sci.* **2014**, *458*, 217–224.

348. Fang, J.; Kelarakis, A.; Lin, Y.-W.; Kang, C.-Y.; Yang, M.-H.; Cheng, C.-L.; Wang, Y.; Giannelis, E.P.; Tsai, L.-D.; *Phys. Chem. Chem. Phys.* **2011**, *13*, 14457–14461.

349. Jeon, H.; Jin, S.Y.; Park, W.H.; Lee, H.; Kim, H.-T.; Ryou, M.-H.; Lee, Y.M.; *Electrochim. Acta* **2016**, *212*, 649–656.

350. Frankenberger, M.; Pettinger, K.-H.; *Zwischenbericht SurfaLIB 2019-II - project number 03ET6103C, Federal Ministry for Economic Affairs and Energy, Germany*, Ruhstorf, **2020**.

351. Habedank, J.B.; Kriegler, J.; Zaeh, M.F.; *J. Electrochem. Soc.* **2019**, *166*, A3940-A3949.

352. Werner, L.; Trunk, M.; Gernhäuser, R.; Gilles, R.; Märkisch, B.; Revay, Z.; *Nucl. Instrum. Methods Phys. Res. A* **2018**, *911*, 30–36.

353. Cannarella, J.; Arnold, C.B.; *J. Power Sources* **2014**, *245*, 745–751.

354. Barai, A.; Tangirala, R.; Uddin, K.; Chevalier, J.; Guo, Y.; McGordon, A.; Jennings, P.; *Journal of Energy Storage* **2017**, *13*, 211–219.

355. Jossen, A.; Weydanz, W.; *Moderne Akkumulatoren richtig einsetzen*, 1. Auflage; Ubooks-Verlag: Neusäß, **2006**, ISBN 9783741892592.

356. Nitta, N.; Wu, F.; Lee, J.T.; Yushin, G.; *Mater. Today* **2015**, *18*, 252–264.

357. Wang, Y.; Li, H.; He, P.; Hosono, E.; Zhou, H.; *Nanoscale* **2010**, *2*, 1294–1305.

358. Lee, H.; Yanilmaz, M.; Toprakci, O.; Fu, K.; Zhang, X.; *Energy Environ. Sci.* **2014**, *7*, 3857–3886.

359. Aydemir, M.; Mooy, R.; Glodde, A.; Seliger, G.; *ZWF* **2017**, *112*, 684–689.

360. Klett, M.; Eriksson, R.; Groot, J.; Svens, P.; Ciosek Högström, K.; Lindström, R.W.; Berg, H.; Gustafson, T.; Lindbergh, G.; Edström, K.; *J. Power Sources* **2014**, *257*, 126–137.

361. Rubino, R.S.; Gan, H.; Takeuchi, E.S.; *J. Electrochem. Soc.* **2001**, *148*, A1029.

362. Hirai, T.; *J. Electrochem. Soc.* **1994**, *141*, 611.

363. Kim, J.S.; Pfleging, W.; Kohler, R.; Seifert, H.J.; Kim, T.Y.; Byun, D.; Jung, H.-G.; Choi, W.; Lee, J.K.; *J. Power Sources* **2015**, *279*, 13–20.

364. Pröll, J.; Kim, H.; Piqué, A.; Seifert, H.J.; Pfleging, W.; *J. Power Sources* **2014**, *255*, 116–124.

365. Zhang, Z.; Chen, Z.; Zhang, X.; Li, Y.; Zhang, Q.; Hart, J.; Li, J.; *ECS J. Solid State Sci. Technol.* **2016**, *5*, Q3088-Q3094.

366. Barai, A.; Guo, Y.; McGordon, A.; Jennings, P.; *A study of the effects of external pressure on the electrical performance of a lithium-ion pouch cell*. In *2013 International Conference on Connected Vehicles and Expo;* ICCVE, **2013**, Las Vegas, USA; IEEE; 295–299.

367. Ning, G.; Haran, B.; Popov, B.N.; *J. Power Sources* **2003**, *117*, 160–169.

368. Geng, X.; Guo, H.; Wang, C.; Cheng, M.; Li, Y.; Zhang, H.; Huo, H.; *J. Mater. Sci.: Mater. Electron.* **2018**, *29*, 19207–19218.

369. Lee, M.-J.; Lho, E.; Oh, P.; Son, Y.; Cho, J.; *Nano Res.* **2017**, *10*, 4210–4220.

370. Zhang, J.; Yue, L.; Kong, Q.; Liu, Z.; Zhou, X.; Zhang, C.; Xu, Q.; Zhang, B.; Ding, G.; Qin, B.; Duan, Y.; Wang, Q.; Yao, J.; Cui, G.; Chen, L.; *Sci. Rep.* **2014**, *4*, 3935.

371. Lim, D.G.; Chung, D.-W.; Kohler, R.; Pröll, J.; Scherr, C.; Pfleging, W.; Garcia, R.E.; *J. Electrochem. Soc.* **2014**, *161*, A302-A307.

372. Gu, Y.; Wang, W.-W.; Li, Y.-J.; Wu, Q.-H.; Tang, S.; Yan, J.-W.; Zheng, M.-S.; Wu, D.-Y.; Fan, C.-H.; Hu, W.-Q.; Chen, Z.-B.; Fang, Y.; Zhang, Q.-H.; Dong, Q.-F.; Mao, B.-W.; *Nat. Commun.* **2018**, *9*, 1339.

373. Stroe, D.I.; Swierczynski, M.; Stan, A.I.; Knap, V.; Teodorescu, R.; Andreasen, S.J.; *Diagnosis of lithium-ion batteries state-of-health based on electrochemical impedance spectroscopy technique*. In *Proceedings of the 2014 IEEE Energy Conversion Congress and Exposition;* ECCE, **2014**, Pittsburgh, USA; IEEE; 4576–4582.

374. Waag, W.; Käbitz, S.; Sauer, D.U.; *Appl. Energy* **2013**, *102*, 885–897.

375. Levi, M.D.; Dargel, V.; Shilina, Y.; Aurbach, D.; Halalay, I.C.; *Electrochim. Acta* **2014**, *149*, 126–135.

376. Landesfeind, J.; Pritzl, D.; Gasteiger, H.A.; *J. Electrochem. Soc.* **2017**, *164*, A1773-A1783.

377. Pritzl, D.; Landesfeind, J.; Solchenbach, S.; Gasteiger, H.A.; *J. Electrochem. Soc.* **2018**, *165*, A2145-A2153.

378. Ovejas, V.; Cuadras, A.; *Batteries* **2018**, *4*, 43.

379. Huang, J.; Zhe, L.; Zhang, J.; Song, S.; Lou, Z.; Wu, N.; *J. Electrochem. Soc.* **2015**, *162*, A585-A595.

380. Hesse, H.; Schimpe, M.; Kucevic, D.; Jossen, A.; *Energies* **2017**, *10*, 2107.

381. Wood, D.L.; Li, J.; Daniel, C.; *J. Power Sources* **2015**, *275*, 234–242.

382. Peled, E.; *J. Electrochem. Soc.* **1998**, *145*, 3482.

383. Winter, M.; Appel, W.K.; Evers, B.; Hodal, T.; Möller, K.-C.; Schneider, I.; Wachtler, M.; Wagner, M.R.; Wrodnigg, G.H.; Besenhard, J.O.; *Monatsh. Chem.* **2001**, *132*, 473–486.

384. Pinson, M.B.; Bazant, M.Z.; *J. Electrochem. Soc.* **2013**, *160*, A243-A250.

385. Revay, Z.; Kudějová, P.; Kleszcz, K.; Söllradl, S.; Genreith, C.; *Nucl. Instrum. Methods Phys. Res. A* **2015**, *799*, 114–123.

List of acronyms

AM	active material
BET	Brunauer-Emmett-Teller
CE	counter electrode
CEI	cathodic Solid Electrolyte Interphase
CMC	sodium carboxymethylcellulose
CNT	carbon nanotube
CPE	Constant Phase Element
DEC	diethyl carbonate
DMC	dimethyl carbonate
DOD	Depth of Discharge
EC	ethylene carbonate
EDX	Energy Dispersive X-ray analysis
EIS	Electrochemical Impedance Spectroscopy
EMC	ethyl methyl carbonate
EV	electric vehicle
FEC	fluoroethylene carbonate
FE–SEM	Field-Emission Scanning Electron Microscope
GEIS	Galvanostatic Electrochemical Impedance Spectroscopy
GN	graphene nanosheets
IAM–ESS	Institute for Applied Materials – Energy Storage Systems
KIT	Karlsruhe Institute of Technology
LFMP	$LiFe_{1/3}Mn_{2/3}PO_4$
LFP	$LiFePO_4$
LIB	Lithium Ion Battery
LiFSI	$Li^+[N(SO_2CF)_2]^-$
LiTFSI	$Li^+[N(SO_2CF_3)_2]^-$
LNMO	$LiNi_{0.5}Mn_{1.5}O_4$
LTO	$Li_4Ti_5O_{12}$
MLZ	Heinz Maier-Leibnitz Zentrum
NCA	$LiNi_{16/20}Co_{3/20}Al_{1/20}O_2$
NDP	Neutron Depth Profiling

NMC 111	$LiNi_{1/3}Mn_{1/3}Co_{1/3}O_2$
NMC 532	$LiNi_{5/10}Mn_{3/10}Co_{2/10}O_2$
NMC 622	$LiNi_{6/10}Mn_{2/10}Co_{2/10}O_2$
NMC 811	$LiNi_{8/10}Mn_{1/10}Co_{1/10}O_2$
NEP	N-ethyl pyrrolidone
NMP	N-methyl pyrrolidone
N4DP	Neutron-based four-Dimensional Profiling
PC	propylene carbonate
PE	polyethylene
PEIS	Potentio Electrochemical Impedance Spectroscopy
PGAA	Prompt Gamma-Ray Activation Analysis
PP	polypropylene
PSE	periodic table of elements
PVDF	polyvinylidene difluoride
RE	reference electrode
SBR	styrene-butadiene rubber
SEI	Solid Electrolyte Interphase
SEM	Scanning Electron Microscopy
SI	Supplementary Information
SOC	State of Charge
TEC	Chair of Technical Electrochemistry
TZE	Technology Center for Energy
TUM	Technical University of Munich
UAS Landshut	University of Applied Sciences Landshut
VC	vinylene carbonate
VGCF	vapor grown carbon fiber
WE	working electrode

List of symbols

c	concentration
C_{DL}	double layer capacitance
$D_{\pm}$	binary diffusion coefficient
$E\{x\}$	expectation
f	frequency
f_{Ah}	charging factor
F	Faraday constant
i	current
$\hat{\imath}$	momentary current
j	imaginary number
$i_{charge/discharge}$	charge/discharge current
m_{AM}	limiting active material mass
q_{Ah}	coulombic efficiency
$Q_{discharge-momentary}$	momentary discharge capacity
$Q_{discharge-total}$	total discharge capacity
Q_{meas}	measured capacity
$Q_{nominal}$	nominal capacity
Q_{spec}	specific capacitiy
R_{CT}	charge-transfer resistance
R_{DC}	internal resistance
R_{S}	solvent resistance
s_{x}	standard error
t	time
t_{+}	transference number
u	voltage
$\hat{u}$	momentary voltage
$V_{components,minimal}$	minimum volume of components
V_{pores}	pore volume
V_{real}	real volume
z_{+}	cation charge
Z	complex resistance / impedance
$\hat{Z}$	momentary resistance
Z_{W}	Warburg Element

$\gamma_\pm$	activity coefficient
γ_x	skewness
ε	porosity
κ	electrical conductivity
μ_x	mean
υ_0	kinematic viscosity
υ_+	cation stoichiometric number
σ_x^2	variance
σ_x	standard deviation
τ	tortuosity
φ	potential
ϕ_0	time dependent phase angle
ϕ_Z	impedance phase angles
ϕ_u	voltage phase angle
ϕ_i	current phase angle
ω	angular frequency

List of figures

List of tables

Reprint Permissions

Copyright Clearance Center | RightsLink®

Home | Help | Email Support | Sign in | Create Account

ELSEVIER

Laminated Lithium Ion Batteries with improved fast charging capability

Author:
Martin Frankenberger,Madhav Singh,Alexander Dinter,Sebastian Jankowksy,Alexander Schmidt,Karl-Heinz Pettinger

Publication: Journal of Electroanalytical Chemistry

Publisher: Elsevier

Date: 15 March 2019

BACK | CLOSE WINDOW

https://doi.org/10.1016/j.jelechem.2019.02.030

EIS Study on the Electrode-Separator Interface Lamination

by Martin Frankenberger * , Madhav Singh , Alexander Dinter and Karl-Heinz Pettinger

Technology Center for Energy, University of Applied Sciences Landshut, Wiesenweg 1, D-94099 Ruhstorf, Germany

* Author to whom correspondence should be addressed.

View Full-Text   Download PDF   Browse Figures   Cite This Paper

Abstract

This paper presents a comprehensive study of the influences of lamination at both electrode-separator interfaces of lithium-ion batteries consisting of $LiNi_{1/3}Mn_{1/3}Co_{1/3}O_2$ cathodes and graphite anodes. Typically, electrode-separator lamination shows a reduced capacity fade at fast-charging cycles. To study this behavior in detail, the anode and cathode were laminated separately to the separator and compared to the fully laminated and non-laminated state in single-cell format. The impedance of the cells was measured at different states of charge and during the cycling test up to 1500 fast-charging cycles. Lamination on the cathode interface clearly shows an initial decrease in the surface resistance with no correlation to aging effects along cycling, while lamination on both electrode-separator interfaces reduces the growth of the surface resistance along cycling. Lamination only on the anode-separator interface shows up to be sufficient to maintain the enhanced fast-charging capability for 1500 cycles, what we prove to arise from a significant reduction in growth of the solid electrolyte interface. View Full-Text

Keywords: lithium-ion battery; lamination; electrochemical impedance spectroscopy; fast-charging capability; lifetime
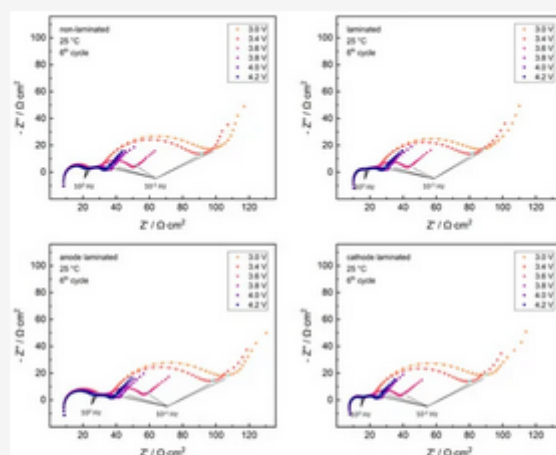
▼ Show Figures

Figure 1

SEI Growth Impacts of Lamination, Formation and Cycling in Lithium Ion Batteries

by ⬛ Martin Frankenberger [1,*] ✉ ⓘⒹ, ⬛ Markus Trunk [2,3] ✉, ⬛ Stefan Seidlmayer [3] ✉ ⓘⒹ, ⬛ Alexander Dinter [1] ✉, ⬛ Johannes Dittloff [2] ✉, ⬛ Lukas Werner [2] ✉, ⬛ Roman Gernhäuser [2] ✉ ⓘⒹ, ⬛ Zsolt Revay [3] ✉, ⬛ Bastian Märkisch [2] ✉, ⬛ Ralph Gilles [3] ✉ and ⬛ Karl-Heinz Pettinger [1] ✉

[1] Technology Center for Energy, University of Applied Sciences Landshut, 94099 Ruhstorf, Germany

[2] Physics Department, Technical University of Munich, 85748 Garching, Germany

[3] Heinz Maier-Leibnitz Zentrum, Technical University of Munich, 85748 Garching, Germany

* Author to whom correspondence should be addressed.

[View Full-Text] [Download PDF] [Browse Figures] [Cite This Paper]

Abstract

The accumulation of solid electrolyte interphases (SEI) in graphite anodes related to elevated formation rates (0.1C, 1C and 2C), cycling rates (1C and 2C), and electrode-separator lamination is investigated. As shown previously, the lamination technique is beneficial for the capacity aging in graphite-$LiNi_{1/3}Mn_{1/3}Co_{1/3}O_2$ cells. Here, surface resistance growth phenomena are quantified using electrochemical impedance spectroscopy (EIS). The graphite anodes were extracted from the graphite NMC cells in their fully discharged state and irreversible accumulations of lithium in the SEI are revealed using neutron depth profiling (NDP). In this post-mortem study, NDP reveals uniform lithium accumulations as a function of depth with lithium situated at the surface of the graphite particles thus forming the SEI. The SEI was found to grow logarithmically with cycle number starting with the main formation in the initial cycles. Furthermore, the EIS measurements indicate that benefits from lamination arise from surface resistance growth phenomena aside from SEI growth in superior anode fractions. View Full-Text

Keywords: lithium-ion battery; electrochemical impedance spectroscopy; neutron depth profiling; lamination; formation; solid-electrolyte-interphase; lifetime
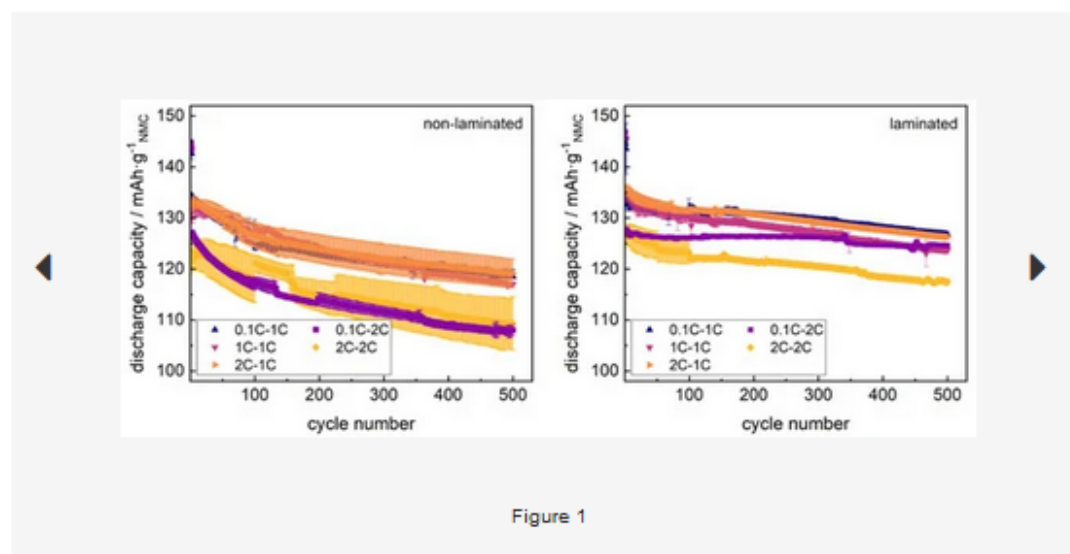
▼ Show Figures

Figure 1

https://doi.org/10.3390/batteries6020021

List of publications

Manuscripts

1. **Frankenberger, M.**; Mock, C.; Schälicke, G; Ophey, J.; Landwehr, I.; Rössler, S.; Hagemeister, J.; Kaden, N.; Holeczek, H.; Kwade, A.; Pettinger, K.-H.; Plasma-modification of electrodes in NMC622/graphite single cells, **2022**, *in preparation*.

2. Toigo, C.; **Frankenberger, M.**; Billot, N.; Pscherer, C.; Stumper, B.; Distelrath, F.; Schubert, J.; Pettinger, K.-H.; Arbizzani, C.; Improved $Li_4Ti_5O_{12}$ electrodes by modified current collector surface. *Electrochim. Acta* **2021**, *392*, 138978.

3. **Frankenberger, M.**; Trunk, M.; Seidlmayer, S.; Dinter, A.; Dittloff, J.; Werner, L.; Gernhäuser, R.; Revay, Z.; Märkisch, B.; Gilles, R.; Pettinger, K.-H.; SEI Growth Impacts of Lamination, Formation and Cycling in Lithium Ion Batteries *Batteries* **2020**, *6*, 21.

4. Springer, B. C.; **Frankenberger, M.**; Pettinger, K.-H.; Lamination of Separators to Electrodes using Electrospinning *PLoS ONE* **2020**, *15*, e0227903.

5. **Frankenberger, M.**; Singh, M.; Dinter, A.; Pettinger, K.-H.; EIS Study on the Electrode-Separator Interface Lamination *Batteries* **2019**, *5*, 71.

6. **Frankenberger, M.**; Singh, M.; Dinter, A.; Jankowksy, S.; Schmidt, A.; Pettinger, K.-H.; Laminated Lithium Ion Batteries with improved fast charging capability *J. Electroanal. Chem.* **2019**, *837*, 151–158.

7. Giorgio, F. de; La Monaca, A.; Dinter, A.; **Frankenberger, M.**; Pettinger, K.-H.; Arbizzani, C.; Water-processable $Li_4Ti_5O_{12}$ electrodes featuring eco-friendly sodium alginate binder *Electrochim. Acta* **2018**, *289*, 112–119.

Conference talks

1. *SEI growth influences at Li-Ion cells caused by formation, cycling and lamination revealed using NDP*, MLZ User Meeting 2019 (December 10th, 2019) in Munich, Germany.

Poster presentations

1. **Frankenberger, M.**; Singh, M.; Dinter, A.; Pettinger, K.-H.; EIS study on rapid lamination for Lithium Ion Batteries; Poster at Batterieforum Deutschland 2020, Berlin, Germany.

2. **Frankenberger, M.**; Singh, M.; Pettinger, K.-H.; Effect of inactive materials on performance of thick electrodes for Lithium Ion Batteries; Poster at Advanced Battery Power 2018, Münster, Germany.